Università degli Studi di Napoli Federico II

Dottorato di Ricerca in

Ingegneria Strutturale, Geotecnica e Rischio Sismico

THESIS FOR THE DEGREE OF DOCTOR OF PHILOSOPHY

Degradation effects on structural safety

of masonry walls

by
Felice Saviano

Advisor: Prof. Ing. Gian Piero Lignola

Scuola Politecnica e delle Scienze di Base
Dipartimento di Strutture per l'Ingegneria e l'Architettura

Degradation effects on structural safety of masonry walls

Ph.D. Thesis presented
for the fulfillment of the Degree of Doctor of Philosophy
in Ingegneria Strutturale, Geotecnica e Rischio Sismico
by
Felice Saviano

March 2023

Approved as to style and content by

____

Prof Gian Piero Lignola, Advisor

Università degli Studi di Napoli Federico II
Ph.D. Program in Ingegneria Strutturale, Geotecnica e Rischio Sismico
XXXV cycle - Chairman: Prof. Iunio Iervolino

www.dist.unina.it/dottorati-di-ricerca/dottorati

Candidate's declaration

I hereby declare that this thesis submitted to obtain the academic degree of Philosophiæ Doctor (Ph.D.) in Ingegneria Strutturale, Geotecnica e Rischio Sismico is my own unaided work, that I have not used other than the sources indicated, and that all direct and indirect sources are acknowledged as references. Parts of this dissertation have been published in international journals and/or conference articles (see list of the author's publications at the end of the thesis).

Napoli, March 10, 2023

Felice Saviano

____

Abstract

Assessing the vulnerability of buildings exposed to various climate conditions, which can severely influence durability and long-term performance, is a challenging topic in both research and engineering practice. Degradation affects all types of buildings across the world, differing in the timing and manifestation, for which specific rehabilitation measures are required. Most of the research activity in the last decades, was focused on seismic actions, even if analysis and rehabilitation against gravity loads represent a major challenge especially for historical buildings, mainly if degradation is the main reason for safety reduction.
In this framework, this thesis aims at the quantitative assessment of the effects of aging and material degradation on structural safety. In order to reproduce a geometric degradation of mortar joint, tests have been carried out by reducing mortar joint's width to simulate a typical form of aging in masonry, without an attempt to model the physical processes of material aging. Tests have concerned in a first phase both small scale masonry wallets of brick and tuff masonry then in a second phase full-scale unreinforced masonry (URM) walls with an opening were tested under different load schemes. Both in plane and out of plane loads were considered.In terms of in plane loading, a severe risk for existing buildings is represent by settlement at the base, on the other hand, out of plane load is significant to account for walls not being firmly connected to horizontal structures with uncounteracted horizontal forces. A further challenge has been the development of numerical analyses to simulate the capacity and behaviour of such walls against ageing effect with a calibration based on the experimental results from axial and diagonal-compression tests. Numerical models of wallets and full scale walls calibrated by using the experimental data confirmed the strength analytical envelopes, the failure mode and remarked the influence of the mechanical properties and their variations. In fact, refined numerical FEM models supported the analytical modelling approach, including a refinement of the spandrels failure criteria, modifying those devoted to piers.

Keywords: Ageing, Settlement, Out of plane load, Masonry, Numerical and analytical modelling, Experimental tests

Sintesi in lingua italiana

La valutazione della vulnerabilità degli edifici esposti a diverse condizioni climatiche, che possono influenzare severamente la durabilità e le prestazioni a lungo termine, è un tema impegnativo sia nella ricerca che nella pratica ingegneristica. Il degrado colpisce tutti i tipi di edifici in tutto il mondo, con tempi e manifestazioni diverse, per le quali sono necessarie misure di ristrutturazione specifiche. La maggior parte dell'attività di ricerca negli ultimi decenni è stata incentrata sulle azioni sismiche, anche se la progettazione e la messa in sicurezza per i carichi gravitazionali, rappresentano una sfida importante in modo particolare per gli edifici storici, soprattutto se il degrado è la ragione principale della riduzione della sicurezza.

In questo quadro, la tesi mira alla valutazione quantitativa degli effetti dell'invecchiamento naturale e del degrado dei materiali sulla sicurezza strutturale. Per riprodurre il degrado geometrico del giunto di malta, sono stati eseguiti test riducendo la larghezza del giunto di malta al fine di simulare una tipica forma di invecchiamento della muratura, senza tentare di modellare i processi fisici di invecchiamento del materiale. Le prove hanno riguardato in una prima fase pareti in muratura di mattoni e tufo in scala ridotta e in una seconda fase sono state testate sotto diversi schemi di carico pareti in scala reale in muratura non rinforzata (URM) con un'apertura. Sono stati considerati sia carichi nel piano che fuori paiano. Per l'azione nel piano, un grave rischio per gli edifici esistenti è rappresentato da un cedimento fondale, mentre il carico fuori piano è significativo per le pareti che non sono saldamente collegate alle strutture orizzontali, con forze orizzontali non contrastate. Un'ulteriore sfida è stata lo sviluppo di analisi numeriche per simulare la capacità e il comportamento di tali pareti in relazione all'effetto dell'invecchiamento, con una calibrazione basata sui risultati sperimentali delle prove di compressione assiale e diagonale. I modelli numerici dei pannelli e delle pareti in scala reale, calibrati utilizzando i dati sperimentali, hanno confermato gli inviluppi analitici di resistenza, le modalità di rottura e evidenziato l'influenza delle proprietà meccaniche e delle loro variazioni nei confronti del degrado. Infatti, i raffinati modelli numerici FEM hanno affiancato l'approccio analitico, che ha incluso un perfezionamento dei criteri di rottura dei pannelli di fascia, modificando quelli previsti per i pannelli di maschio.

Parole chiave: Invecchiamento, Cedimento, Carico fuori piano, Muratura Modellazione numerica e analitica, Test sperimentali.

Acknowledgements

The author's work has been carried out in the framework of the PRIN 2017 (Progetti di Rilevante Interesse Nazionale) DETECT-AGING "*Degradation Effects on sTructural safEty of Cultural heriTAGe constructions through simulation and health monitorING*" (Grant No. 201747Y73L).

Ringraziamenti

Ringrazio il mio tutor, il Prof. Ing. Gian Piero Lignola, che mi ha dato l'opportunità di partecipare a questo programma di dottorato. La sua guida in questi anni mi ha permesso di ampliare le conoscenze scientifiche. Grazie per il costante aiuto e per essermi stato accanto nel mio percorso di ricerca. La sua dedizione e compiacenza alla ricerca mi hanno sempre spronato a dare il massimo e superare i miei limiti. La sua gentilezza e onestà sono rare.

Appaiono scontati i ringraziamenti ai miei genitori per gli sforzi profusi nel corso di questi anni, per consentirmi di tagliare quest'importante traguardo, più appropriati sono invece i ringraziamenti nei loro confronti per la pazienza e la capacità di sopportare i tanti momenti di stanchezza, di stress ed esaurimento.

Un grande grazie va alle mie sorelle, per aver appoggiato le mie scelte ed essermi state vicine sempre.

Sento di rivolgere un affettuoso ringraziamento a tutti i miei amici. Gli eventi ci portano a percorrere strade differenti ma questo non avrà nessun effetto sul legame che ci unisce.

Ringrazio tutti coloro che mi sono stati vicini in questi anni, e anche chi è andato via; i tanti bei momenti passati insieme mi hanno senza dubbio permesso di trovare le energie necessarie per proseguire nel mio percorso.

Inoltre, un ringraziamento particolare è rivolto ai miei colleghi del quarto piano, per il supporto, penso ricambiato, che mi hanno dato in tutto questo tempo condividendo piaceri e difficoltà e instaurando un'amicizia che spero continuerà nel tempo.

List of Figures

List of Tables

Contents

Chapter 1

Background of Masonry structures

1.1. Background and Framework

Masonry buildings are a significant part of the worldwide built heritage, including most of European cultural heritage buildings.

The structural assessment of historical masonry buildings is a complex task because of several motivations, such as a significant variability in geometric and mechanical properties of masonry that are rather difficult to be characterised, and nonlinear behaviour of structural systems under different loading conditions. The structural analysis contributes to conservation of historical buildings, including diagnosis, reliability assessment and design of intervention, oriented to grant an efficient and respectful conservation of monuments and historical buildings [1]. Non exhaustive or incorrect structural analysis can lead to ineffective interventions.

Through their life structures are exposed to varying climate conditions which can severely influence durability and long-term performance.

Masonry is widely a topic of interest for researchers, because the mechanical properties of masonry constituents and assemblages are highly variable both for intrinsic spatial characteristics [2], [3] (type of matrix, quality of units, presence of mortar joints) but also due to variations in the quality of workmanship, environmental conditions during construction and service life, which include high moisture, temperature cycles and the presence of salts. Changes caused by these factors affect the performance of the structures, so it is important to understand how degradation mechanism affects structural components to be taken into account to assess the vulnerability of such buildings.

Degradation affects all types of buildings across the world, differing in the timing and manifestation of anomalies, for which specific rehabilitation measures are required.

Also reinforced concrete (RC) buildings are affected by signs of degradation as well as hidden defects, even if constructed in recent times regardless of environmental zone, urban or industrial areas, where in the latter results a significant concentration of carbon dioxide, carbonation-corrosion prevails due to a significant concentration of carbon dioxide in the environmental pollution. Reinforcement corrosion may be induced by the penetration of chloride ions, producing the so called ‘‘pitting corrosion”, or by the carbonation process of concrete cover. On the other hand, chloride-induced corrosion is of utmost importance in structures exposed to marine environments.

The deterioration of concrete as well as the progressive corrosion of reinforcing bars may lead to significant changes in the safety coefficients. Erduran et al.[4] presented models intended at simulating the evolution (generally stepwise linear in time) of relevant geometric properties, such as effective concrete cover thickness and radius loss in steel rebars. As for the member-scale analysis, N-M interaction curves drawn for RC section in the various stages of their degradation configuration show that degradation leads to significant reduction in terms of section capacity subjected to normal stresses and concrete cover can delay the development of degradation, influenced by the environmental conditions which the element is exposed to.

Numerical investigation of the environmental effects on the seismic behaviour of RC structures was described in [5], where the progressive deterioration of RC structures over time implies the reduction of their load bearing capacity and, also the shift of the failure mechanism from the ductile to the brittle type.

For existing RC and masonry structures exposed to aggressive conditions, engineering interest has increased in the evaluation of their remaining safety and serviceability over time [6], [7].

The characteristics of the mortar are a key factor in controlling the height of rising damp and the amount of subsequent evaporation. For a brick wall, a high permeability mortar gives moisture content of 15 to 20 w_t% whereas a low permeability mortar gives only 1 to 3 w_t% as described in [8].

Foraboschi et al. demonstrated (in [9]) that moisture significantly reduces the compression strength of a brick; the greater the moisture content the lower compression strength, all other condition being equal, in particular salt concentration inside the brick. Moreover, the experimental results demonstrate that salts together with moisture significantly reduce brick compression strength, while salts without moisture increase brick compression strength. However, the crystallization of these salts can cause subflorescence and efflorescence inside the bricks, which eventually reduce the compression strength of the bricks and the masonry.

Analysis of mortar loss and spalling on structural safety for a masonry arch aqueduct is described in [10], where it is claimed that the influence of dispersed loss is less than those of concentrated loss. With reference to the location of degradation, mortar loss at the vault is most dangerous, followed by the arch shoulder, and then the arch foot part.

Masonry can be regarded as a very hard to be described building materials both for the mechanical properties and his behaviour. Heterogeneity composition of this material represents the first issue in the mechanical behaviour, which is usually based on the collaboration between mortar joints and block units, with the exception of the dry-jointed masonry structures which are also widely spread. Ultimately, masonry behaviour necessarily depends on the mechanical properties of the components and on the masonry bond (arrangement of the stones).

Most of the research activity on vulnerability and damage assessment of masonry buildings was focused on seismic actions, even if analysis and rehabilitation against gravity loads represents a major challenge especially for historical buildings, even before earthquakes.

Walls are fundamental structural elements in masonry buildings and can be understood mainly as a compressive element providing an appropriate support to vaults, domes and arches. When connected and correctly

constructed, walls represent the major structural element able to face in-plane actions from gravity load to wind and seismic events.
The investigation of the serviceability condition is a fundamental topic, in the case of masonry structures especially, and the serviceability limit states are worth to be studied with numerical analyses, e.g. crack control and differential movement.

The in-plane behaviour of masonry walls has been widely investigated from both the experimental and the theoretical points of view. Failure of wall regarding gravity load can be divided in :
-"in-plane" where the flexural controlled failure mode is characterised by flexural vertical cracks at pier, horizontal cracking at pier tops and bases, and a compression crushing at plastic hinge locations, typically in solid walls without openings , while the frequently noted shear controlled failure modes concerning the sliding along a mortar joint (step joint or bed joint) or diagonal cracking through bricks, in either spandrels or piers, typically in perforated walls, .e.g. when subjected to settlement of the foundation soil.
-"out-of-plane", mostly because flexural stresses produced by arch and vault thrusts.

Potential failure mechanisms in spandrel panels are almost equal to those of piers (with different level and orientation, with respect to bed joints, of axial load), as mentioned before, sliding shear, diagonal cracking, and flexural toe crushing [11],[12], but ageing development a rather different nonlinear response may produce, with a flexural to shear failure mode transition as the degradation level increased. Degradation, as a form of decay and physical-mechanical alteration of constituent materials, is also a potential cause of vulnerability that, in the event of a seismic event, but not limited to, can affect the response of the building.
In this contest appears that knowledge of ageing effects plays an important role for engineering development affecting both design stages (for the development of new types of strengthening systems and techniques) and the implementation of structural health monitoring

systems (to predict the residual lifetime of structures). A significant challenge is still open with respect to damage phenomena.

The present thesis is framed within the activities of the research project DETECT-AGING “Degradation Effects on sTructural safEty of Cultural heriTAGe constructions through simulation and health monitorING”, funded by the Italian Ministry of Education, Universities and Research (MIUR). The project aims to develop a new analytical-instrumental approach aimed at the quantitative assessment of the effects of aging and material degradation on structural safety of cultural heritage (CH), with particular reference to masonry structures. Through the combined use of structural models and health monitoring (SHM), indications and operative tools will be provided for the identification and quantification of structural damage, for the management of built cultural heritage especially that are a significant part of the worldwide built.

Structural health monitoring, aimed at reducing epistemic and aleatory uncertainties in the assessment process, will be mainly supported by computationally efficient models, such as Equivalent Frame (EF) essentially limiting the use of refined 3D FEM.

This project also developed a sustainable management strategy for CH at the quantitative assessment of the effects of aging and material degradation on structural safety that aims to evaluate the ability to identify, locate and eventually quantify degradation-induced damage, through a joint processing of monitoring and structural simulations for pro-active risk prevention.

The Consortium is composed by four Research Unit (RU): RU1 (Naples), coordinated by Prof. Lignola and Prof. Parisi focuses on degradation effect modelling: from the material scale to the whole structure with experimental test on brick and tuff walls and full-scale unreinforced masonry (URM) wall with an opening tested under different loading conditions, in plane and out of plane, both new prototype and damaged and intrinsically degraded panels made of URM at the construction stage, i.e. with imperfections; RU2 (Genova) coordinated by Prof. Cattari deals with modelling at structural element scale (EF models), reliability of simplifications by comparison with results from nonlinear detailed FE models (accounting for aleatory and epistemic uncertainties); RU3 (Perugia) coordinated by Prof. Ubertini is working on development of new SHM systems for historic masonry structures aimed at revealing, localizing and possibly quantifying a structural damage caused by material degradation; RU4 (Bologna) coordinated by Prof. Buratti deals with estimation of effects of aleatory and epistemic uncertainties on the results of numerical simulations with experimental full-scale prototype building as testbed for the SHM and damage identification techniques.

DETECT-AGING is a three-year project, started on 1st of September of 2019 and is now ending with the publication of the final deliverables, after an extension due to Covid19 delays.

1.2. Motivation of research

It's really undeniable the expressive force conveyed by masonry construction, as an arch, a tower or a dome, which leads us to preserve as unquestionable heritage for the community

Masonry constructions are massive structures and their safety and stability are mainly provided by geometry and geometric proportions of the building. These concepts were clear to old workers, consolidated through successive experiences, trials and errors,

In a lot of seismic regions around the world the masonry buildings have not been designed to hold up the appropriate seismic load with structural walls of these buildings principally designed to resist only gravity loads [13]. Indeed, ancient historical buildings were constructed following the so-called “rule of thumb” (based on the experience from previous built structure) and they were not capacity designed such as today.

A lot of strengthening techniques has been implemented in the last decades to enhance the structural response of masonry constructions [14]–[17], which led to increased awareness of the importance of preserving historic buildings not only in scientific community but also being fully implemented in different country environmental policies.

Furthermore, these structures have been designed and built in periods with no regulations, specific methodologies and calculation tools, favouring a design approach based more on the intuition and experience (e.g. geometrical rules).
The design approaches, which guarantee stability and performance for the buildings, less frequently were applied to the ordinary buildings.
The use of numerical or analytical models is not simple, given the fragile architectural and structural context, especially for the use of the Performance-Based Assessment (PBA) which assumes a set of Performance Levels that a specific structure can exhibit against defined hazard levels.
The correct identification of mechanical parameters plays a crucial role for a good accuracy of modelling results. In last years, al lot of researchers have been dealing with experimental studies on both masonry walls and masonry walls strengthened with composites subjected to ageing due to environmental conditions during construction and service life, which include high moisture, temperature cycles and the presence of salts.
An initial numerical study was performed to evaluate the influence of the variability in mechanical properties of wall masonry and to quantify the effect of degradation at the wall scale through a statistics-based sensitivity analysis and subsequent regression analysis [18]. Numerical analysis results indicate how the degradation is not only the reason of a capacity loss in terms of stiffness and resistance, but it also affects the expected failure mode, changing from flexural failure to either a mixed or shear failure.

In order to reproduce a geometric degradation of mortar joint, tests have been carried out by reducing mortar joint’s width to simulate a typical form of aging in masonry, without an attempt to model the physical processes of material aging. The objective of this research was to quantify the performance of two masonry typologies: brick and tuff masonry.

-The former type was studied for evaluating aging effect from the level of material to the scale of component and so to define a simple tool to support the prediction of structural capacity, which can also be used for real-scale prototype building test, that will be carried out by UR4 in the research project.

-Tuff masonry was carried out to investigate in-plane and out-plane behaviour of unreinforced tuff masonry walls with door opening in the centre (URM) when subjected to gravity load with foundation movements or with transversal force.

Masonry behaviour necessarily depends on the mechanical properties of the components, being masonry a composite material, so in order to fully characterize masonry properties, a comprehensive testing program was set-up using destructive testing through uniaxial and diagonal compression test.

Briefly, the following tests, carried out at the Laboratory of department of Structures for Engineering and Architecture, University of Naples Federico II, have been conducted:

-four uniaxial and diagonal compression test on brick masonry, where for each load condition, half of test was on aged specimens

-four uniaxial and diagonal compression test on tuff masonry, where for each load condition, half of test was on aged specimens;

-two in-plane URM test subjected to gravity load and settlement of the pier, one test in intact and one test for the deteriorated configuration;

-two out-plane URM test, one test in intact and one test for the deteriorated configuration.

A challenging task in this field is represented by the ability to develop numerical analyses to simulate the capacity behaviour of such a structure against ageing effect in order to analyse the structural vulnerability and design effective solutions to protect them. Several modelling approaches exist in literature, each one of them trying to better simulate the very hard structural behaviour of a material like masonry.

It was of particular interest to investigate:

-Mechanical characterization of brick and tuff masonry under compression test with the aim of obtaining their complete behaviour, enabling the determination of the elastic modulus, strength and fracture properties.

-the effects of aging and material degradation on structural safety in terms of mechanical properties

-The in-plane strength and deformation capacity of perforated unreinforced masonry (URM)

- Review the test result using the DIANA Finite Elements program.

- The relationship between the analysis and the experiment.

The final goal of the present work is to provide useful information for the mechanics of existing stone masonry buildings, allowing the assessment of sophisticated nonlinear analysis models and the safety assessment of buildings.

As a future work, the experience gathered on the mechanics of the masonry walls under in- and out-plane loading can be of great advantage in the decision process related to the strengthening possibilities of ancient structures to face the seismic action not dealt with in this context.

1.3. Thesis outline

The thesis outline is here reported:

Chapter 2. The dissertation starts with a full description of the experimental program to investigate how aging and degradation impact the structural capacity of masonry walls, starting from the masonry assemblage small scale of brick and tuff masonry wallets to a full-scale unreinforced masonry (URM) wall with an opening. This chapter is dedicated to the description of the results obtained by experimental tests, with a fundamental comparison between the two configurations tested of intact and degraded masonry, used to simulate a geometric degradation.

Chapter 3. In this chapter the main experimental outcomes are discussed. with reference also to the theoretical considerations by performing an experimental-theoretical comparison. For the settlement load, building damage criteria based on critical displacement parameters are proposed.

Chapter 4. This Chapter is dedicated to the description of the results obtained by numerical evaluations using the FEM software DIANA FEA

10.4. The research outcomes have been also validated with the FEM simulations in terms of both global load vs displacement, and damage pattern.

Chapter 5. Conclusive remarks and further developments of the carried out work in this Chapter are described, focusing on the effect of degradation at the different scales considered in this project and on the different effects of degradation at different loading conditions of real scale masonry walls.

Chapter 2

Experimental Program: From the design to the main experimental outcomes

2.1. Abstract

The results of a research project carried out on masonry brick and tuff panels with degradation in masonry joints are presented. The experimental part of the project consists of laboratory tests, the prototypes made of both single and double leaf stone walls made of common bricks and other with tuff and natural hydraulic lime mortar, were performed respectively for uniaxial and diagonal compression test, with the arrangement of masonry units for single-leaf and double leaf walls reported in Figure 1. In addition, test on aged specimen, where the physical processes of material aging was not attempted but reproducing only a final state, have been carried out. In particular geometric degradation of mortar joint was performed by reducing their width to simulate a typical form of aging in masonry. Figure 1. also reported the dimensions of tuff unreinforced masonry wall (URM) with an opening tested under in-plane and out-plane loads.

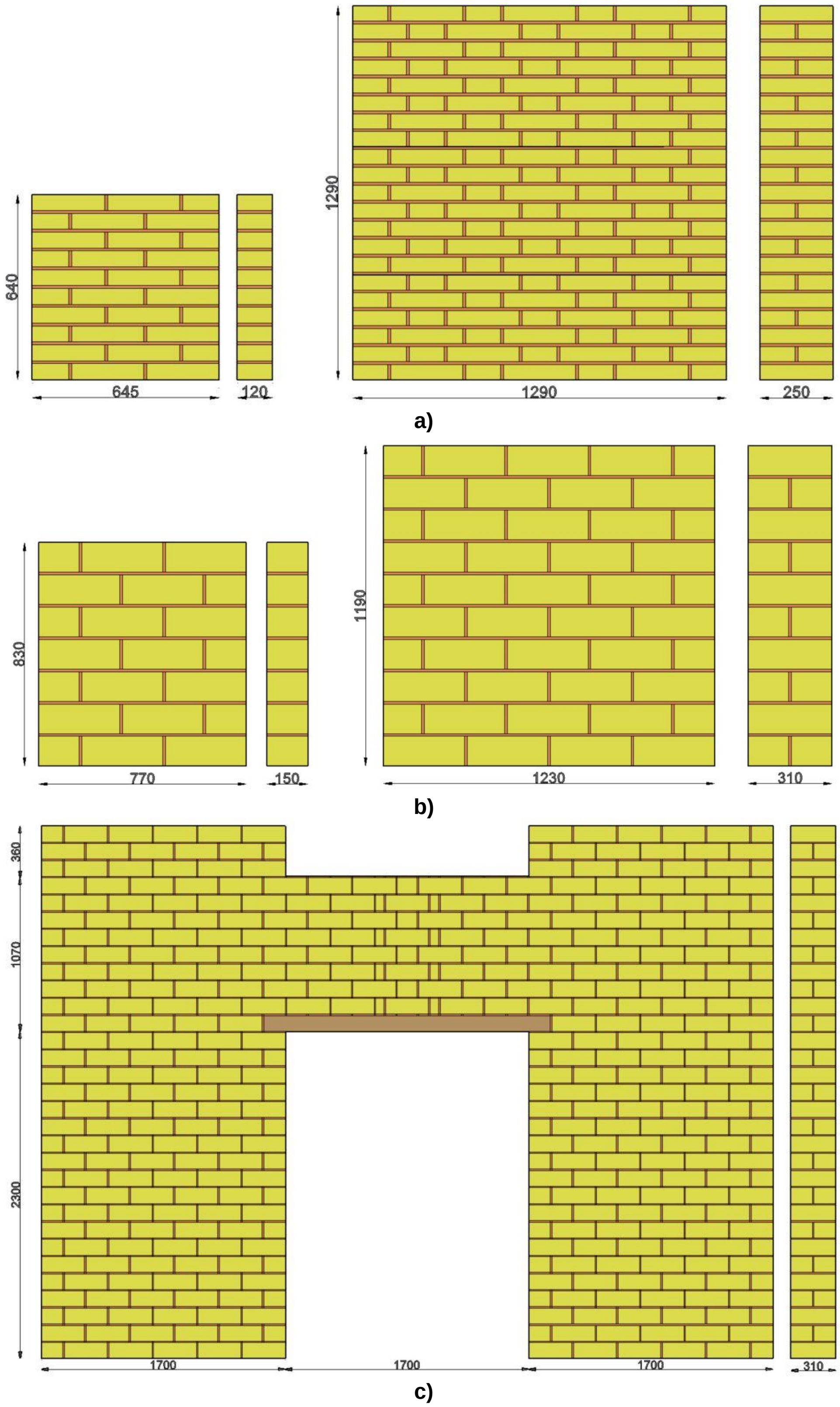

Figure 1. Dimensions of the specimens and masonry bond pattern for: a) brick masonry subjected to uniaxial and diagonal compression loads with single-leaf and double leaf respectively; b) tuff masonry subjected to uniaxial and diagonal compression loads with single-leaf and double leaf respectively; c) tuff URM tested under in-plane and out-plane loads.

2.2. Experimental program for bricks masonry

Within the framework of the DETECT-AGING research project, an experimental program was undertaken. The main aim was to investigate how aging and degradation influences the structural capacity of masonry walls, starting from the masonry assemblage scale where experimental tests focused on variations in Young's and shear moduli of masonry as well as its compressive and shear strengths. Accordingly, the experimental program included a set of characterization tests to assess the mechanical properties of masonry. Four masonry wallets were tested under simple uniaxial compression, whereas other four specimens were subjected to diagonal compression tests. The former set of specimens were made of single-leaf clay brick masonry (CBM), whereas specimens tested in diagonal compression consisted of double-leaf CBM. To simulate masonry in existing buildings, CBM was made of common clay bricks and natural hydraulic lime mortar. Half of each set of CBM wallets was fabricated with mortar joints being characterized by reduced area, in order to simulate potential effects of CBM degradation in the form of geometric joint alterations on each side of the specimen.

Diagonal compression tests allow the panel a free deformation, since its four sides are free from any kind of constraints so this situation may be assumed to be representative of masonry spandrels in which the vertical compression stress may be considered equal to zero and the effect of confinement is very limited. Although this type of test is not univocal as it has given rise to different interpretations in the literature, it is a useful tool for studying the behaviour and shear resistant capacity of masonry.

Conversely, this study of an experimental nature, aims to evaluate the effects of degradation at the smallest scale of masonry, with particular reference to monotonic actions attributable to static loads.

2.2.1. Description and mechanical properties of brick masonry materials

The selection of materials and construction techniques was driven by the aim of recreating conditions that are representative of historical masonry buildings. Clay brick masonry was fabricated in laboratory, according to a running bond pattern. Clay bricks were produced with soft mud technology and were characterized by a nominal size of 250x120x55 mm^3, showing an old-like geometry with rounded edges that allows the recreation of historical brickworks in several countries such as Italy.

The masonry joints were nominally 10-mm-thick and filled with a premixed hydraulic mortar composed by natural hydraulic lime (NHL) with 1:4 water/binder ratio by weight (i.e., 6.25 L of water per 25 kg of lime) and fine sand, resulting into a low-performance lime mortar. The mortar composition was designed in a way to reproduce the main features of old mortar types in historical masonry buildings.

The bricks had mean unit weight w = 15.40 kN/m^3, with mechanical properties determined by means of experimental results on prismatic samples 40x40x160 mm^3 according to UNI 8942-3 standard [19]. The mean flexural strength f_{fb}=7.38 (CoV = 9.30%), was obtained by means of three-point bending while the mean compressive strength f_{cb} =20.79 MPa (with coefficient of variation CoV = 19.09%) was determined on the halves of the specimens after bending tested under flexure. According to technical product declarations by the mortar manufacturer, the premixed hydraulic mortar was classified as M2.5 (corresponding to mean compressive strength of mortar f_{cm} = 2.52 MPa) according to Eurocode 6 [20] and Italian Building Code [21]. During the construction of each masonry wallet, mortar prisms (40x40x160mm^3 in size) were prepared and tested under three-point bending according to EN 1015-11 standard [22]. Using the same procedure for characterization of bricks, the two parts of each prismatic specimen after flexural rupture close to the mid cross section were individually tested under uniaxial compression.

Table 1 outlines the mean values and CoV for both compressive and flexural tensile strengths of mortar and bricks.

All specimens were cured for 28 days at standard levels of relative humidity and temperature.

Table 1. Mechanical properties of masonry constituents*.

Material	Statistic	f_c	f_f
Clay brick	Mean value [MPa]	20.79	7.38
	CoV	19.09%	9.30%
		(8)	(4)
NHL mortar	Mean value [MPa]	2.52	0.96
	CoV	27.32%	19.57%
		(12)	(6)

* f_c and f_f indicate compressive and flexural strengths of either material; bracketed figures denote the number of specimens for each experimental test.

2.2.2. Geometry and fabrication of specimens

The specimens tested under simple compression were characterized by a single-leaf masonry assemblage with overall size equal to 645x640x120 mm^3,in agreement with other experiments carried out in the past [23] and 10 masonry layers (Figure 2.a). By contrast, the specimens tested under diagonal compression were fabricated according to a double-leaf masonry pattern with overall size equal to 1290x1290x250 mm^3 in agreement with standard ASTM [24] and other studies[25], [26]. Regarding the masonry fabrication, the bricks were wetted in water before their installation in contact with the mortar. The specimens with artificial degradation (abbreviated as 'deteriorated specimens' hereinafter in contrast to 'intact specimens' with fully mortared joints) were made of partially filled mortar joints, as shown in Figure 2.b. In those specimens, the amount of mortared joint area can be deduced according to the ratio s/t between the full width of the mortared joint (*s*) and the total thickness of the wallet (*t*). The fabrication of deteriorated specimens was carefully controlled so that *s/t* was equal on average to 33% and 24% in specimens to be tested in simple and diagonal compression, respectively.

a)

b)

Figure 2. Pictures of specimens to be tested under (a) simple compression and (b) diagonal compression

A beam of high strength and stiffness, used for testing procedure, has been placed on the top of the specimen made perfectly flat by the application of a layer of mortar, to remove surface roughness and ensure a uniform distribution of the load and a smooth contact surface during the uniaxial compression test. For each of the two specimen configurations (i.e., intact and deteriorated), strain-sensing piezoresistive bricks denoted as ‘smart bricks’ in previous papers [27]–[29] were integrated in the specimens to assess their ability to monitor the stress/strain progress for structural health monitoring (SHM) applications. The specimens with smart bricks are labelled with final letter ‘m’. Intact specimens included three smart bricks in both front and rear leaves of the masonry, whereas only the front leaf of deteriorated specimens was equipped with three smart bricks (Figure 3).

The novel sensors are made of fiber-reinforced clay-based material mixing fresh clay with stainless steel micro fibers to supply the intrinsic piezoresistivity of the clay matrix. So smart bricks provide variations in their electrical outputs when mechanically strained under compression loads. A detailed description of smart brick operating principle can be found in [27], [28], [30]. (Figure 4).

Figure 3. Smart bricks pattern for diagonal compression test: a) Intact; b) Deteriorated

a)

b)

Figure 4. Masonry bond pattern for diagonal compression test with smart bricks for configuration: a) intact; b) deteriorated

2.2.3. Experimental setups and testing procedures

2.2.3.1. Uniaxial compression for brick masonry

The experimental setup for simple compression tests consisted of a universal testing machine Italsigma: the machine consists of a rigid steel base, equipped with T-slots for mounting the test equipment and specimen restraints, four columns located at the vertices of a rectangle, fixed in the base and a movable beam, which slides along the four columns. An actuator is mounted on the beam, allowing both monotonic and cyclic loading displacement-controlled tests up to a maximum stroke of 75 mm and force control up to 3000 kN in compression and 2400 kN in tension.

Each specimen was thus placed on the basement of the testing machine and equipped with a rigid steel I-beam on top, in order to allow an almost uniform distribution of pressures. (Figure 5)

Load was transferred to the specimen via spherical hinge, interposed between the load plate of the actuator and the upper beam of the panel keeping the resultant force centred on the wall section.

All specimens were tested under monotonically increasing displacement up to failure, assuming a displacement rate equal to 0.01 mm/s to ensure effective monitoring of cracks and to fully measure the nonlinear behaviour of masonry including post-peak strain softening.

The first couple of specimens with intact conditions was labelled as CB_A_1 and CB_A_2, whereas their deteriorated counterparts were labelled as CB_A_1_D and CB_A_2_D, using symbol D to indicate a deteriorated condition.

According to previous investigations, measurement devices were installed in the central region of both specimen sides so that measurements were not affected by local effects on top and at the bottom of the specimen. Deformations were measured by three inductive linear variable differential transformers (LVDTs) as follows: two LVDTs per side were parallel to the loading direction, and the other was orthogonal to the loading direction. All LVDTs were connected only to bricks, according to provisions by EN1052-1 standard [31].

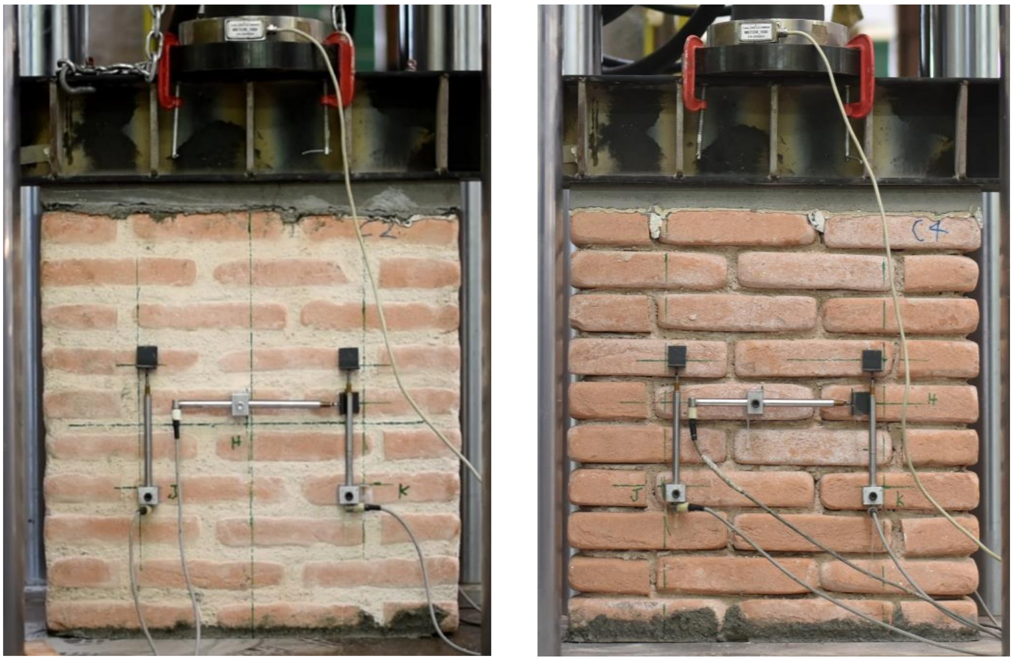

a) b)

Figure 5. Experimental setups of specimens subjected to simple compression in configuration (a) intact and (b) deteriorated.

2.2.3.2. Diagonal compression for brick masonry

Diagonal compression tests were carried out to investigate the in-plane shear behaviour of different double-leaf specimens with the same type of masonry assemblage. Diagonal compression tests, indirect type test compared to shear-compression test, are preferred compared to the latter, because the former is simpler to realize with limited cost and duration for set-up procedure, but on the other hand their interpretation is more uncertain with different approaches available in literature to calculate mechanical parameters of masonry used in analytical models.

a)

b)

Figure 6. Experimental setups of specimens subjected to diagonal compression in configuration (a) intact and (b) deteriorated.

Four URM panels with global dimensions 1292x1290x250 mm^3 were tested, two intact labelled CB_D_1; CB_D_2_m and the other deteriorated specimens CB_D_1_D; CB_D_2_D_m, final letter ‘m’ stands for the specimens with smart bricks, following the same approach for uniaxial compression test with a ratio between the full width of the mortar strips and the total thickness equal to 24% on average (Figure 6).

Testing procedures involved rotation of the URM wall panel by 45° and once centred in the machine frame the specimen was instrumented, and then subjected to in-plane diagonal loading along one of the wall’s diagonals.

Diagonal compression tests were carried out with displacement control up to failure, using the same universal testing machine described for simple compression tests (see Sect. 2.2.3.1) and the same displacement rate (i.e., 0.01 mm/s).

Load was applied on top corner of each specimen by means of two complex L-shaped elements (i.e., steel shoes), which derived from the assembly of steel plates with suitable thickness to avoid local crushing of masonry. Those loading shoes were thus installed on opposite corners of each specimen, along the diagonal line so that the eccentricity between loading direction and such diagonal line was minimized. It is noted that quick-setting anti-shrinkage mortar was filled locally between the steel shoes and the free surface of the specimen to ensure effective bond and transfer mechanism of local pressures.

Diagonal load was transferred to the specimen via spherical hinge, capable of absorbing any out-of-plane deformations of the panels during testing, placed between the actuator and the load cell.

The diagonal compression test was stopped when approximately 50% of peak force was reached on the post-peak softening branch of the force–displacement diagram.

On each side, relative vertical and horizontal displacements were measured by linear variable differential transformers (LVDTs) with gage length g = 400 mm, so as not to have localized effects in the centre, bearing in mind that ASTM E 519-07 does not provide standard gage lengths for LVDTs.

Smart bricks measures are not elaborated in this study as it is subject matter of UR3 “Department of Civil and Environmental Engineering, University of Perugia” involved in the DETECT-AGING research project.

2.2.4. Results of simple compression tests for brick masonry

Macro vertical cracks spread on the panels surfaces mainly on the brick-and-mortar vertical joints with a successive spalling substantially uniform over the whole specimen, always characterized also by the splitting phenomenon (Figure 7.b-d). The failure mechanism of the wallets started with vertical splitting shortly before the maximum load was reached. For intact specimens, vertical cracks spread along the head joints and bricks starting from the edges of the specimen, when the splitting phenomenon is triggered, up to the inner zone (Figure 7.a). On the other hand, extensive cracking occurred in the central zone for the deteriorated specimens, even in the range of small deformations (Figure 7.c). Strain gauges placed at central zone reveal that until crushing the wallet behaviour is quasi-elastic, without relevant increasing of the compression stress till the failure.

Progressive opening of the cracks caused the detachment of sensors during the test, affecting the readings of the LVDTs on the post-peak softening branch for some specimens.

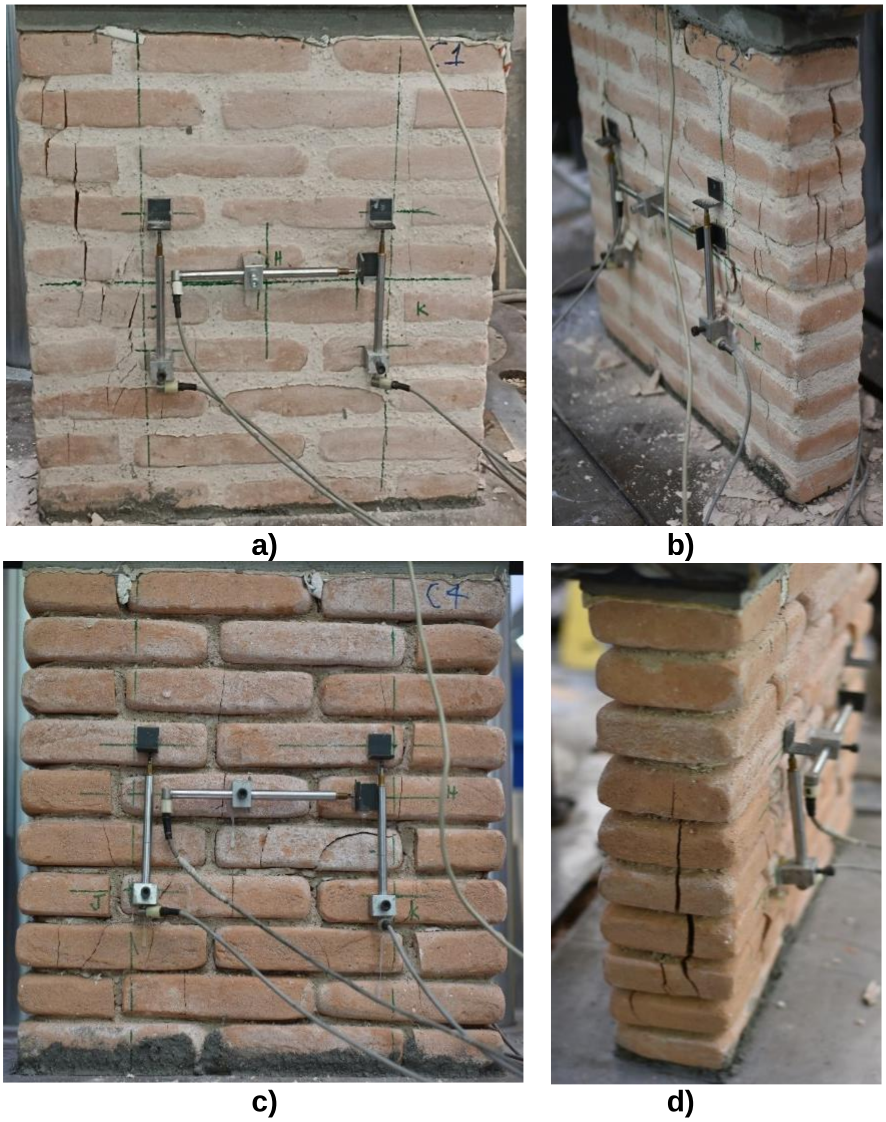

Figure 7. Crack pattern of masonry prism in compression for intact specimens: a) frontal and b) transverse views; deteriorated specimens c) frontal and d) transverse views.

Uniaxial load tests can be assumed to produce a uniform stress distribution over the section, so the compressive strength σ_c can be calculated as ratio between the applied load and the gross area of the cross section (σ_c = N_u/A). Engineering axial strains were computed by dividing the average value of LVDT readings by their gauge length [32]. Figure 8 shows the experimental stress–strain curves, denoting by ε_H and ε_V the horizontal and vertical axial strains, respectively.

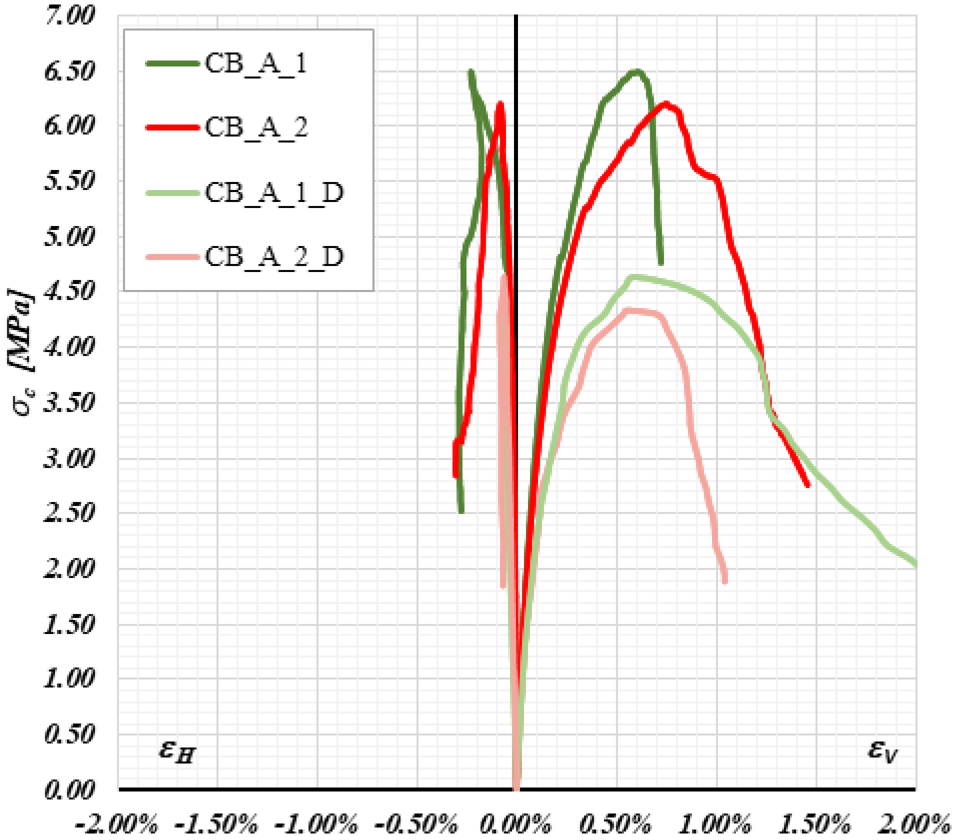

Figure 8. Experimental stress-strain curves of specimens subjected to uniaxial compression test.

Table 2 provides a summary of the main experimental results related to the following properties: peak compressive strength (σ_p), the vertical and horizontal strains at peak strength (ε_{Vp} and ε_{Hp}), Young's modulus, and Poisson ratio ($\nu_m = -\varepsilon_H/\varepsilon_V$), were reported. Alternative estimates of Young's modulus were derived, as follows: chord modulus (E_c) [33] evaluated between 5% and 30% of peak compressive strength; secant modulus corresponding to one-third of peak compressive strength ($E_{1/3}$), according to European standards and codes [20], [21]]; and secant modulus corresponding to half of peak compressive strength ($E_{1/2}$), according to previous studies [23].That modus operandi was motivated by the need to identify the best estimate of Young's modulus, removing local effects due to initial lack of effective contrast between the specimen and testing machine.

Table 2. Summary of simple compression test results

Specimen configuration	Specimen	σ_p	ε_{Vp}	ε_{Hp}	E_c	$E_{1/3}$	$E_{1/2}$	ν
		[MPa]	[×10^{-3}]	[×10^{-3}]	[MPa]	[MPa]	[MPa]	[–]
Intact	CB_A_1	6.49	6.06	2.33	3725	3863	3148	0.25
	CB_A_2	6.20	7.51	0.83	3224	3788	2890	0.20
	Average	6.35	6.78	1.58	3475	3825	3019	0.22
Deteriorated	CB_A_1_D	4.34	5.51	0.74	2671	2968	2299	0.38
	CB_A_2_D	4.64	5.85	0.64	2450	2888	2283	0.36
	Average	4.49	5.68	0.69	2561	2928	2291	0.37

Intact wallets show stress–strain curves linear up to approximately 50% of peak compressive strength, which was followed by a change in slope in the remaining part of pre-peak nonlinear rising branch.

CB_A_1 reached higher compressive strength at similar vertical deformation of panel CB_A_2. After reached the peak, panel CB_A_1 showed a sudden drop of load-carrying capacity differently from panel CB_A_2.

The average values obtained for intact specimens showed compressive strength, σ_p = 6.35 MPa which results in good agreement with the values provided by the Italian Code for brick masonry, elastic modulus E = 3475 MPa and Poisson ratio ν = 0.22. The modulus of elasticity of masonry was correlated with the masonry compressive strength and was found to be E=547 σ_p which agrees well with the values provided by Codes [21], [34]. A different value was found for aged specimens, about E= 570 σ_p with compressive strength equal to 4.49 MPa.

The reduction of joint filling by an average of 33% leads to a similar compression strength reduction (29%) while elastic modulus is subjected to a slightly lower reduction (26%). Deteriorated specimens exhibit a lower resistance, a more pronounced non-linear pre-peak phase, with a sudden change in slope and a post-peak softening tail rather long especially for panel CB_A_2_D. The compression strength and modulus of elasticity were lower than those of intact specimens while Poisson ratio higher, due to a stress state acting on a reduced mortar layer resulting in increased deformability. Despite the aged state, masonry reveals the capacity of

sustaining loading, so this deformation capacity may play a significant role in safety assessment of structures.
Geometric degradation of mortar joint was performed by reducing their width. Reduction of joint width for aged specimens under simple compression test, has a direct effect, *i.e.,* proportional to filling compared to the nominal value, on masonry properties both compression strength and elastic modulus, so mortar joint can be seen as the weak link in the chain for masonry under axial load.

2.2.5. Results of diagonal compression tests for brick masonry

Figure 9-Figure 10 show the crack patterns of the four walls after failure.
The wallets presented a relatively brittle behaviour. Failures were characterized by shear-sliding mainly involving both bed and head joints along the compressed diagonal and only rarely some bricks were broken, with patterns qualitatively similar and, in almost all cases, a final diagonal main crack connected both loaded corners with a small difference for panels CB_D_1, where cracks appeared almost simultaneously along the full length at peak load and failure plane ran through a greater surface compared to other case which would explain the higher shear strength causing a sudden full separation of the panel into two pieces.
The cracks involved the full thickness and were visible on both faces of the walls. The opening of the central diagonal cracks caused a premature detachment of sensors in some tests and affected the readings of the LVDTs on the post-peak softening branch of the force–displacement diagram.
The behaviour of solid brick URM evidenced a sudden drop in resistance after the occurrence of the diagonal crack, especially for specimens with smart bricks integrated, both intact and deteriorated mortar joints, conserving a very residual resistance (see Figure 11).
The unreinforced panels without smart bricks, CB_D_1 and CB_D_1_D were characterized by a similar behaviour up to about 30% of the

maximum shear strength when for CB_D_1_D wall the mortar geometric variation caused a stiffness drop resulting higher deformability and shear strength decrease.

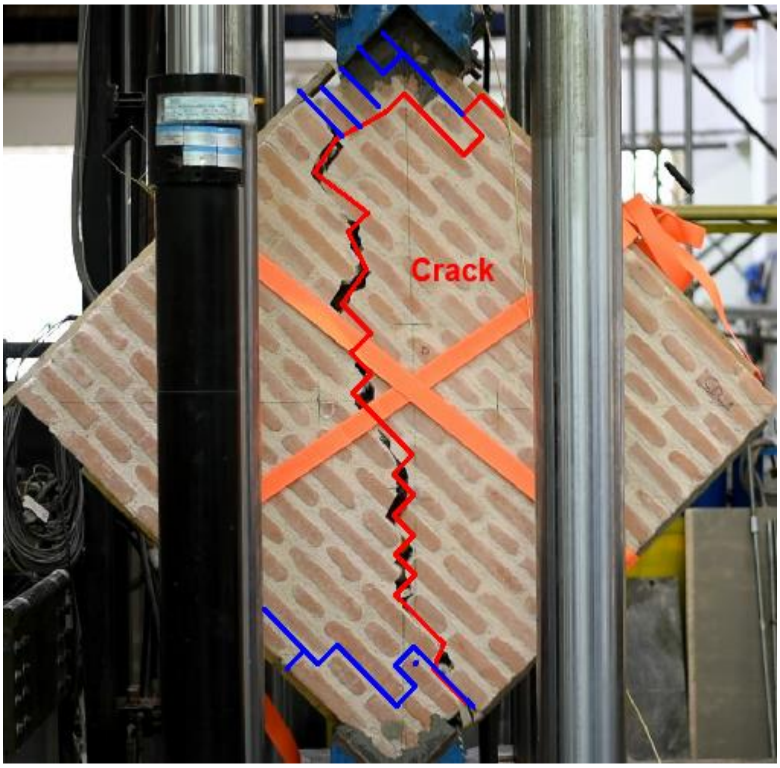

a)

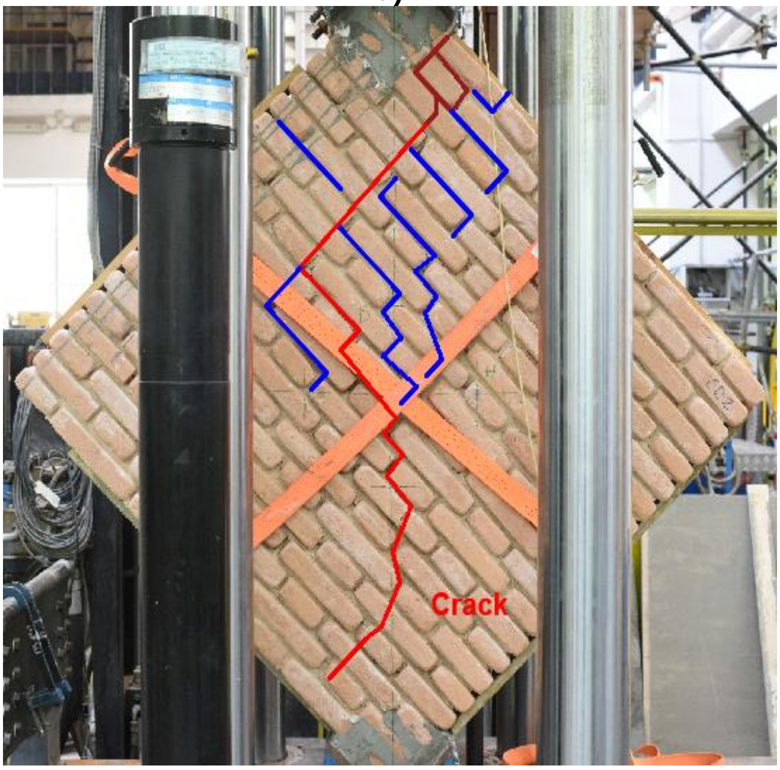

b)

Figure 9 Crack pattern of specimens: a) CB_D_1; b) CB_D_1_D;

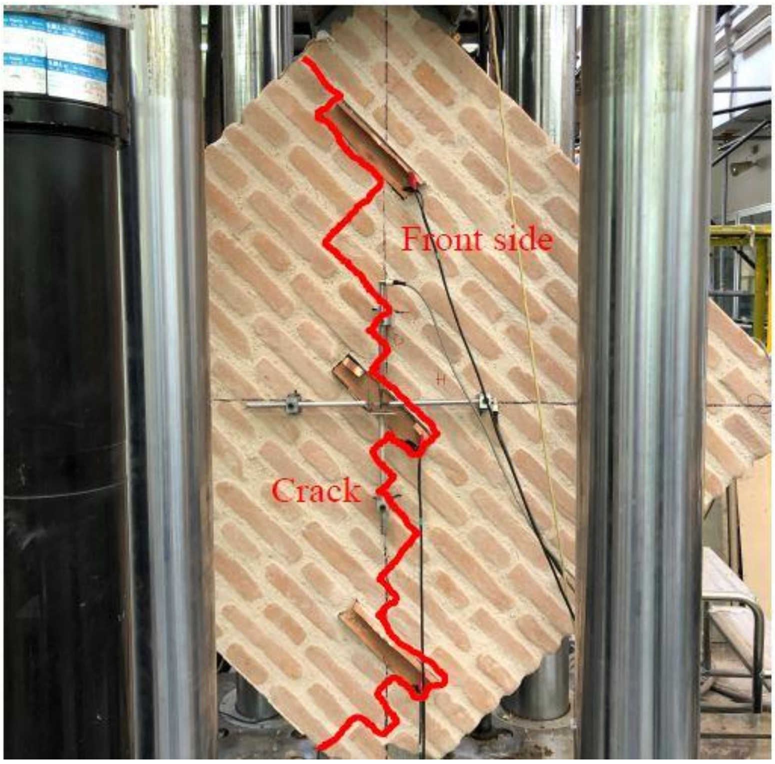

c)

d)

Figure 10 Crack pattern of specimens: c) CB_D_2_m; b) CB_D_2_D_;

For specimens with integrated smart bricks, on the other hand, the load increased almost linearly with the imposed displacement until a sudden load drop occurred. The behaviour of the specimens was similar, with the $\tau - \gamma$ curves that followed one another closely up to the end of the test with difference in shear strength. The geometric defect effect was very limited by smart bricks that have added an inherent weak spot to masonry with a further worsening of shear strength when smart bricks are integrated both in its front and rear sides.

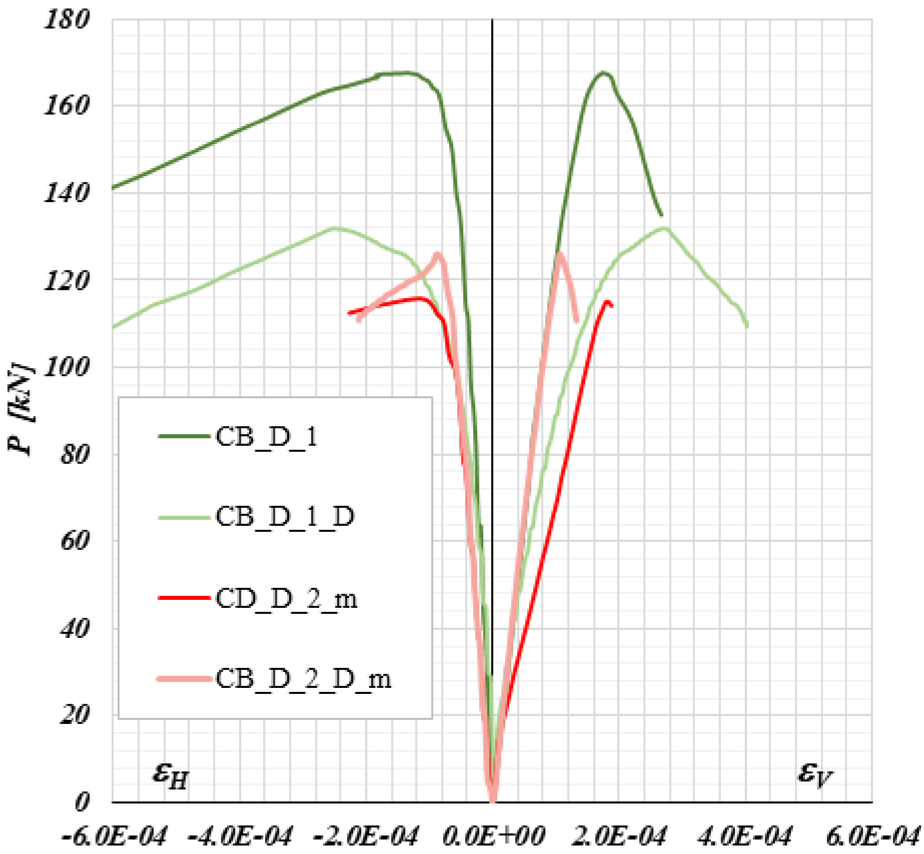

Figure 11. Experimental load-strain curves for the four specimens.

2.2.6. Significant mechanical parameters of brick masonry

According to ASTM E519-2010 [24] (abbreviated as ASTM hereinafter) and RILEM TC-76-LUMB2010 [35] (abbreviated as RILEM hereinafter) specifications, masonry shear strength could be evaluated starting from the maximum applied diagonal compressive load P and the section area A of the specimen, multiplied by a factor depending on the interpretation model used which provides a wide range of variability of shear strength.
According to the ASTM standard, diagonal compression introduced a pure shear stress state and, in these conditions, the Mohr circle of the stress state is centred in its origin (see Eqs (1))
Shear stress τ_0 of masonry, equal to the principal tensile stress σ_I and tensile strength $f_t$of masonry at applied load P was determined by using the following equations (1) and (2):

$$\sigma_I = -\sigma_{II} = \tau_0 = f_t \quad (1)$$

$$\tau_0 = \frac{P}{A \cdot \sqrt{2}} \quad (2)$$

where A is the cross section of the panel, determined as the average of the width (w) and height (h) of the specimen multiplied by its thickness (t) ($i.e. A = \frac{(w+h)}{2} \cdot t$).
On the other hand, RILEM instructions provide another description of stress state inside a masonry panel subjected to diagonal compression, where the shear stress τ is coupled with normal component σ in the center of the panel. It was obtained by Frocht [36] by modelling the masonry panel as if it is an isotropic and homogeneous material and running a linear elastic analysis and he found that the stress state at the centre of the specimen is not a pure shear state, so the Mohr's circle corresponding to the specimen is not centred in the shear stress versus normal stress plane with different value for f_t the tensile strength of masonry (Eqs.(3)), and τ_0 the pure shear strength (Eqs.(4)):

$$f_t = \sigma_I = 0.5\,\frac{P}{A} \quad (3)$$

$$\tau_0 = 0.88\frac{P}{A} \quad (4)$$

More recent finite element analysis confirmed that the pure shear stress is only a theoretical condition which does not consider the redistribution of stresses [37]–[39].

Both ASTM's and Frocht's instructions, lead to different estimations of the tensile strength of masonry, but also of the acting shear stresses and the shear strength at zero compressive stress.

At each given displacement test, the tensile strengths of each wall were evaluated with Equations (2) and (4) corresponding to the different approaches of ASTM E519 and Frocht.

According to Italian code [21] and [34] tensile strength of masonry f_t can be assumed equal to the maximum diagonal applied load divided by twice the cross section area A of the wall when diagonal compression tests are carried out, but no indication about the evaluation of the shear strength is given by code. So adopting the Turnšek and Čačovič [12] the shear strength at zero confining stress is expressed as $\tau_0 = f_t/1.5$.

From the result of diagonal compression tests, it is possible to obtain a wide range of variability of the pure shear strength, according to different approaches [39].

Similarly, strain measurements from LVDTs were retrieved by considering the following relations (Eqs. (5) and (6)):

ΔV_1, ΔV_2 are the relative displacements measured in the front and rear sides of a specimen, respectively, along the direction parallel to the applied load;

ΔH_1, ΔH_2 are the displacements measured in the front and rear sides of a specimen, respectively, along the direction orthogonal to the applied load, and g is the baseline measurement of the LVDTs (equal to 400mm) [40], [41].

$$\varepsilon_v = \frac{\Delta V_1 + \Delta V_2}{2g} \quad \varepsilon_h = \frac{\Delta H_1 + \Delta H_2}{2g} \tag{5}$$

$$\gamma = \varepsilon_v + \varepsilon_h \tag{6}$$

Table 3 presents a summary of the experimental results from diagonal compression tests on the four tests and indicates the registered values of maximum load P_{max} x and the calculated values of tensile strength f_t and shear modulus $G_{1/3}$ as secant modulus between the origin and the stress equal to 30% of peak shear strength and the corresponding shear strain. The need of delving into the interpretation of the diagonal test outcomes is evident in the light of the obtained average results especially for specimens with integrated smart bricks.

The analysis of the shear–average strain curves highlight the influence of the smart bricks both for intact and deteriorated specimens, with a limited post-peak softening branch and a lower peak load compared to panels without smart bricks, as already mentioned before.

Table 3. Summary of diagonal compression test results.

Specimen	**Series**	**P_{max}** [kN]	**Standard**	**$G_{1/3}$** [MPa]	**τ_o** [MPa]	**f_t** [MPa]
Intact	CB_D_1	167.83	ASTM	2400	0.37	0.37
			RILEM	2750	0.47	0.26
	CB_D_2_m	116.03	ASTM	1166	0.25	0.25
			RILEM	1484	0.32	0.18
	Average	141.93	ASTM	1783	0.31	0.31
			RILEM	2117	0.40	0.22
Deteriorated	CB_D_1_D	132.00	ASTM	2296	0.29	0.29
			RILEM	2679	0.37	0.20
	CB_D_2_D_m	126.05	ASTM	1890	0.28	0.28
			RILEM	2406	0.35	0.20
	Average	129.02	ASTM	2093	0.28	0.28
			RILEM	2545	0.36	0.20

Considering the influence of the smart bricks on the panel behaviour, stress state was defined by considering only the net cross section of masonry removing the smart brick length in case of smart bricks specimen both front and rear sides, while half-length in case of aged specimen (with smart bricks only on a side).

In these conditions the Mohr circle defined at the peak load, for specimens with integrated smart bricks, both intact and deteriorated, is comparable with the ones tested without innovative sensor. (Figure 12)

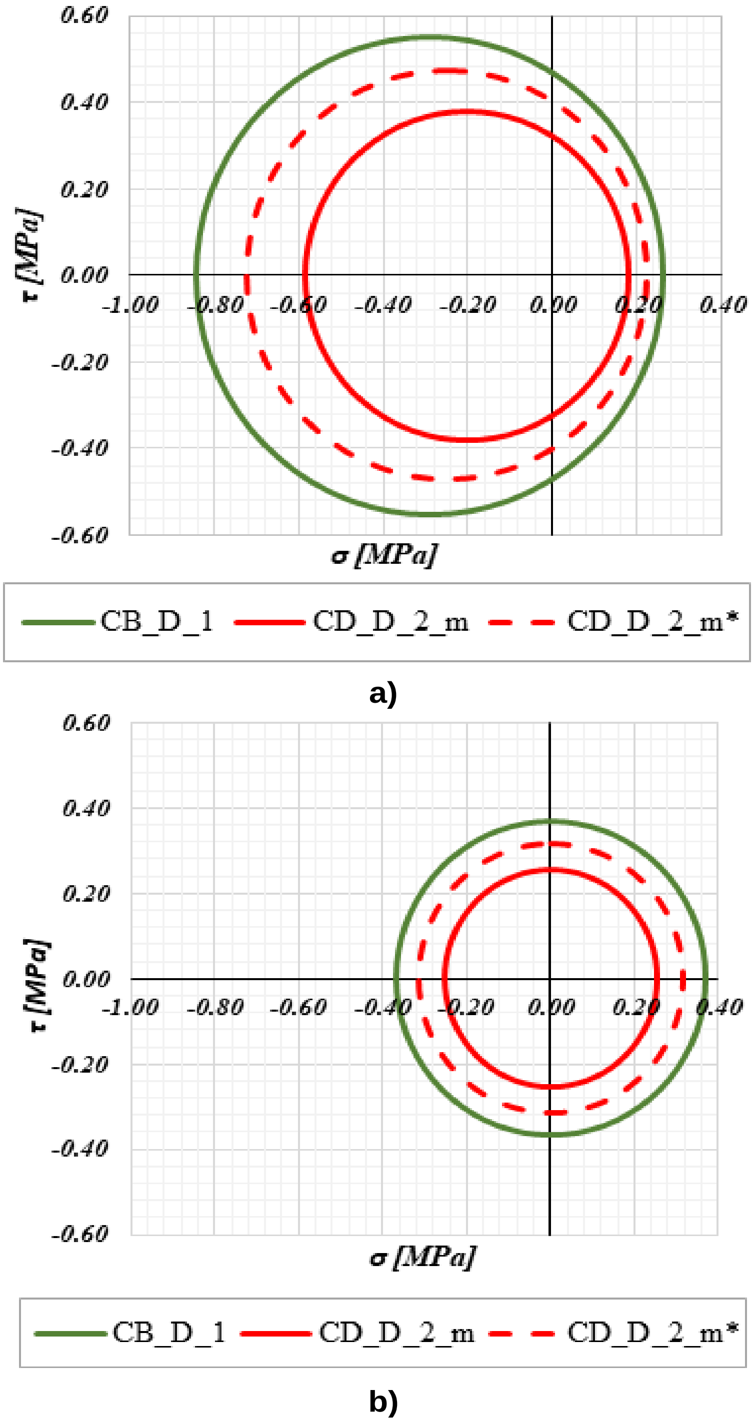

Figure 12. Mohr circles considering smart bricks influence according to different standards: (a) RILEM; (b) ASTM.

Consequently, new values of the main outcomes in terms of shear strength and stiffness are summarized in Table 4 complying with RILEM TC 76 and ASTM E 519, separately.

Table 4. Updated results of diagonal compression tests

Specimen configuration	Specimen	P_{max} [kN]	Standard	$G_{1/3}$ [MPa]	τ_o [MPa]	f_t [MPa]
Intact	CB_D_1	167.83	ASTM	2400	0.37	0.37
			RILEM	2750	0.47	0.26
	CB_D_2_m*	116.03	ASTM	1446	0.32	0.32
			RILEM	1840	0.40	0.22
	Average	141.93	ASTM	1923	0.34	0.34
			RILEM	2295	0.43	0.24
Deteriorated	CB_D_1_D	132.00	ASTM	2296	0.29	0.29
			RILEM	2679	0.37	0.20
	CB_D_2_D_m*	126.05	ASTM	2093	0.31	0.31
			RILEM	2664	0.39	0.22
	Average	129.02	ASTM	2195	0.30	0.30
			RILEM	2672	0.38	0.21

Very close values of the shear stress were achieved by specimens with same mortar geometric configuration, particularly for aged specimens, so the exceedance of tensile shear strength occurs at the same stress state, but the presence of smart brick limits the force of the panel, or based on the result of diagonal compression test the maximum vertical load P, and the capacity in terms of deformation. This highlights that, based on the size of the masonry specimens under investigation, a lower number of smart bricks could be used to prevent significant influence of those sensors on the characterization of mechanical behaviour. This may play a key role in SHM applications, where the layout and number of sensors should be correctly designed to allow correct interpretations of data.

The formulation provided by ASTM led to the following mean values of peak shear strength at zero confining stress and tensile strength: $\tau_0 = f_t = 0.34\ MPa$ in the case of intact specimens and $\tau_0 = f_t = 0.30\ MPa$ in the case of deteriorated specimens.

Data processing according to RILEM provided the following mean values of peak shear strength at zero confining stress and tensile strength: $\tau_0 = 0.43\ MPa$, $f_t = 0.24\ MPa$ in the case intact specimens and $\tau_0 = 0.38\ MPa$, $f_t = 0.21\ MPa$ in those deteriorated.

The shear modulus of rigidity $G_{1/3}$ was calculated as secant modulus between the origin and the stress equal to 30% of peak shear strength and the corresponding shear strain, to define a nominal slope of the elastic branch of τ–γ diagram.

The secant modulus defined in this way is representative of an initial state of the panel, i.e., not cracked. A representative value of the cracked condition is derived.

As masonry is a material without a distinct yield point, the concept of pseudo-ductility can be extended to describe its behaviour, so this requires defining an idealized bilinear diagram for the experimental τ- γ curve. Two methodologies were implemented for computation of γ_y, γ_u and τ_u.as depicted in Figure 13.

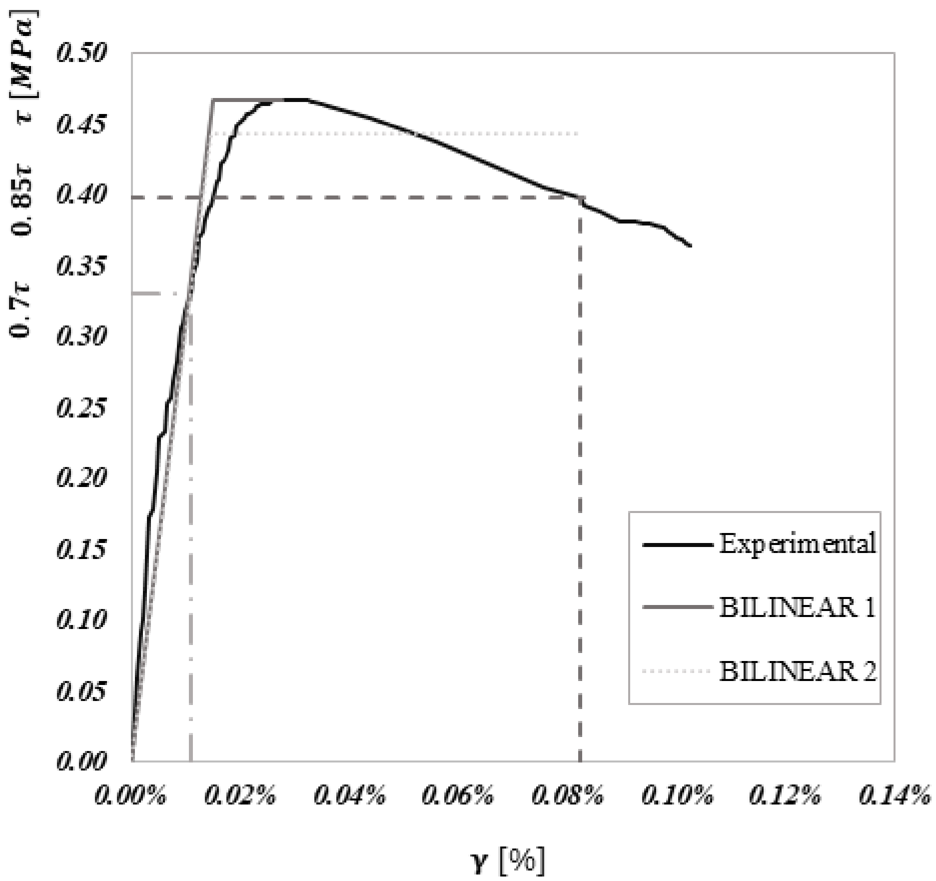

Figure 13. Bilinear idealization of shear stress versus shear strain diagram.

In the first method, “Bilinear 1” the ultimate shear stress τ_u was defined as the experimental value to the peak shear stress on the experimental τ-γ diagram and the corresponding shear strain was defined as the γ_u for the idealized bilinear. Therefore γ_y was derived assuming equal areas below idealized τ- γ diagram and the experimental till the peak.

In the second method “Bilinear 2” the ultimate shear strain γ_u was associated with a 15% strength drop on the post-peak softening branch while γ_y and τ_u were defined by using a secant modulus from the origin of the experimental τ- γ curve to 70% of τ_{max}.. Ultimate shear strain was set to the strain recorded at the 15% of the peak stress because specimens embedded with smart bricks failed before the shear stress dropped to the 80% of the peak stress.

For both approaches the elastic shear modulus G_e was defined as $G_e = \tau_u/\gamma_y$ and only for the idealized bilinear with the second method, shear strain ductility factor μ_γ was defined as $\mu_\gamma = \gamma_u/\gamma_y$.

Pseudo-ductility concept under diagonal compression condition is not univocal in the literature and must take into account the specific behaviour manifested by the type of masonry [26].

In Table 5 are listed the mechanical parameters related to shear modulus of rigidity and shear strain ductility.

Table 5.Main capacity features of intact and deteriorated wallets.

Specimen configuration	Specimen	Approach	Standard	G_e [MPa]	μ_γ -
Intact	CB_D_1	Bilinear 1	ASTM	1831	
			RILEM	2331	
		Bilinear 2	ASTM	1897	4.61
			RILEM	2414	4.61
	CB_D_2_m*	Bilinear 1	ASTM	1362	
			RILEM	1734	
		Bilinear 2	ASTM	1336	2.83
			RILEM	1701	2.83
	Average	Bilinear 1	ASTM	1596	
			RILEM	2032	
		Bilinear 2	ASTM	1616	3.72
			RILEM	2057	3.72
Deterioated	CB_D_1_D	Bilinear 1	ASTM	1233	
			RILEM	1570	
		Bilinear 2	ASTM	1329	4.68
			RILEM	1692	4.68
	CB_D_2_D_m*	Bilinear 1	ASTM	2066	
			RILEM	2630	
		Bilinear 2	ASTM	2189	4.60
			RILEM	2786	4.60
	Average	Bilinear 1	ASTM	1650	
			RILEM	2100	
		Bilinear 2	ASTM	1759	4.64
			RILEM	2239	4.64

Deteriorated specimens exhibit a lower resistance, with a long post-peak softening tail despite the reduced section, but unlike the case of compression test, diagonal test reveals a change in mechanical properties less proportional to the section reduction

The shear strength was lower than those of intact specimens, on average by 13 % while for the shear elastic modulus, neglecting the intact wallet with six smart bricks because of lower value for his brittle behaviour, the reduction was comparable.

Despite the aged state, masonry reveals also a deformation capacity in term of ductility ratios μ_γ = 4.64 equal to the case of intact specimen CD_D_1, so aging effect does not seem to affect post-peak behaviour.

Definitively, reduction of joint width, for aged specimens under diagonal compression test, is mitigated by the brick units interlocking with a less direct effect of filling width on masonry properties especially for shear elastic modulus.

2.2.7. Comparison between experimental results

The global behaviour of walls under in-plane loading was recorded for each load test as presented in the previous section and a summary of capacity features were collected in Table 2,3,5 where compressive and shear strength are related to the type of mortar joints filling. Indeed, test on aged specimen, where the physical processes of material aging was not attempted but reproducing only a final state, were simulated by reducing mortar joints filling compared to the nominal value.

Capacity features were computed both with reference to the gross area (obtaining engineering stresses expressed with the subscript $_{eng}$) and with reference to the net area of the cross section, (obtaining true stresses expressed with the subscript $_{true}$) to evaluate possible combined mechanical and geometrical effects due to the aging.

In Figure 14 dimensional and normalized plots are reported from compression test values: picture a) and b) have on the vertical axis the $\sigma_{c,eng}$ compressive strength and $E_{c,eng}$ chord modulus computed with reference to the gross area, normalized with respect to the corresponding value of the maximum experimental intact panel CD_A_1(i.e. $\tilde{\sigma}_{c,eng}$ and $\tilde{E}_{c.eng}$), while on the horizontal axis the gross area A and the mortar joint loss MJL compared to the intact panel.

Local-global data sets were used to develop linear regression models for their use in structural safety assessment of masonry structures.

Regressions are characterized by a coefficient of determination R^2 equal to 0.975 and 0.848 respectively for prediction of $\tilde{\sigma}_{c,eng}$ compressive strength reduction and that of $E_{c,eng}$ elastic modulus given mortar joint filling, indicating a satisfactory goodness of fitting data. The reduction of joint filling by an average of 33% leads to a similar compression strength reduction (29%) while elastic modulus is subjected to a slightly lower reduction (26%).

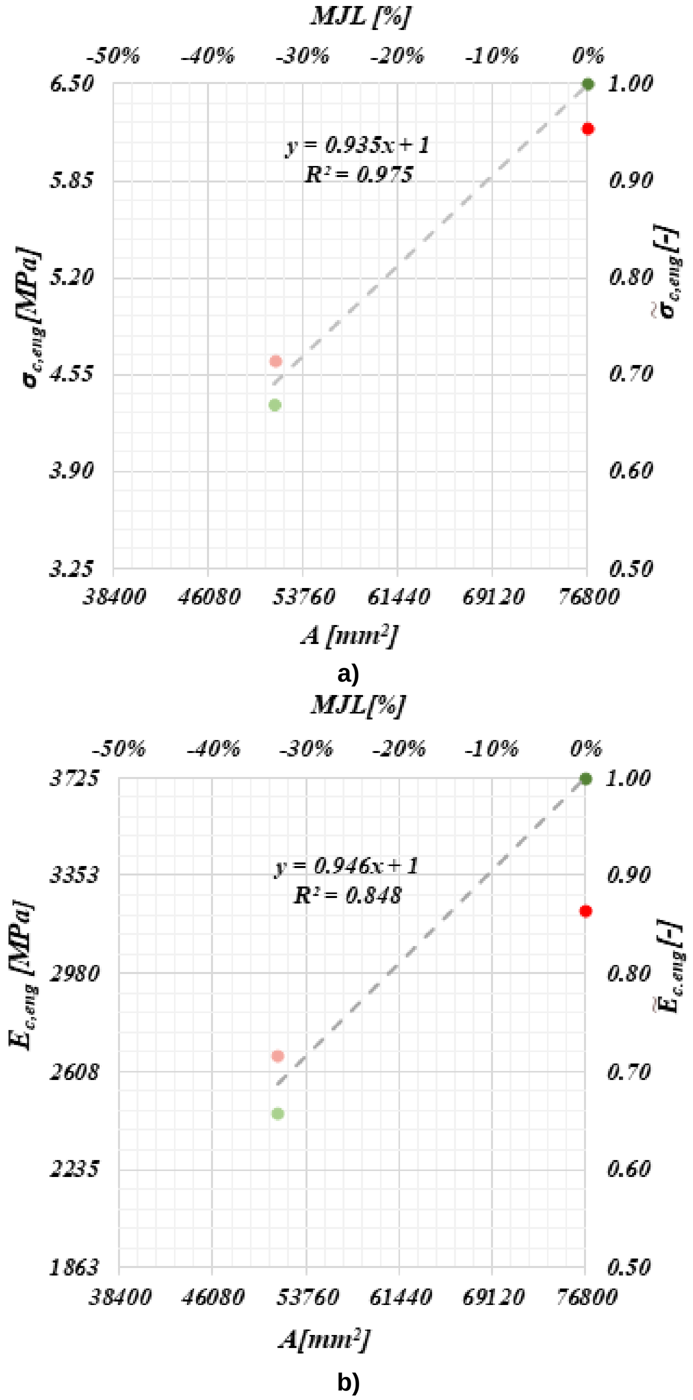

Figure 14. Regression models for prediction of a) compressive strength reduction given mortar joint loss; b) elastic modulus reduction given mortar joint loss.

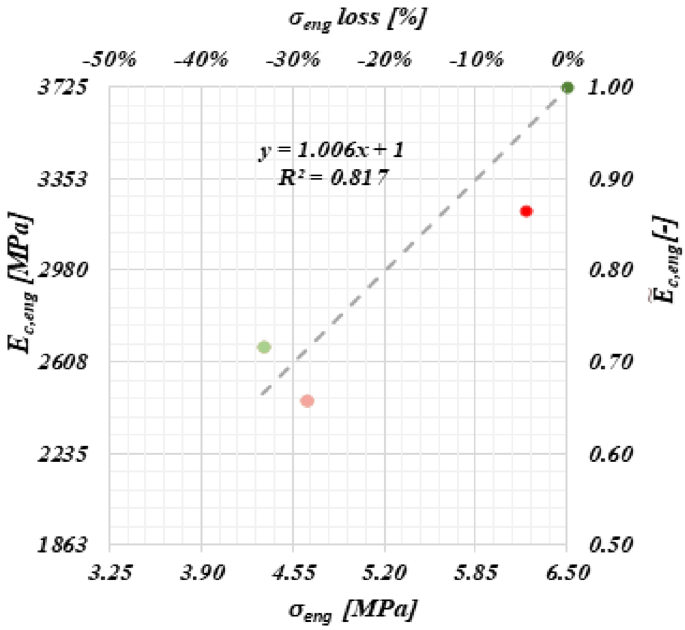

c)

Figure 15.Regression models for prediction of c) elastic modulus reduction given compressive masonry strength loss.

Compressive strength is usually used as main local property of masonry, so another correlation has been defined in Figure 15 between $\tilde{E}_{c,eng}$ normalized elastic stiffness and $\tilde{\sigma}_{c,eng}$ compressive strength loss with a satisfactory goodness of coefficient R^2 equal to 0.817. In this way, regression model allows the estimation of the conditional mean value of elastic modulus reduced given the loss of the compressive masonry strength related to material degradation, and hence after that the loss of section area is known.

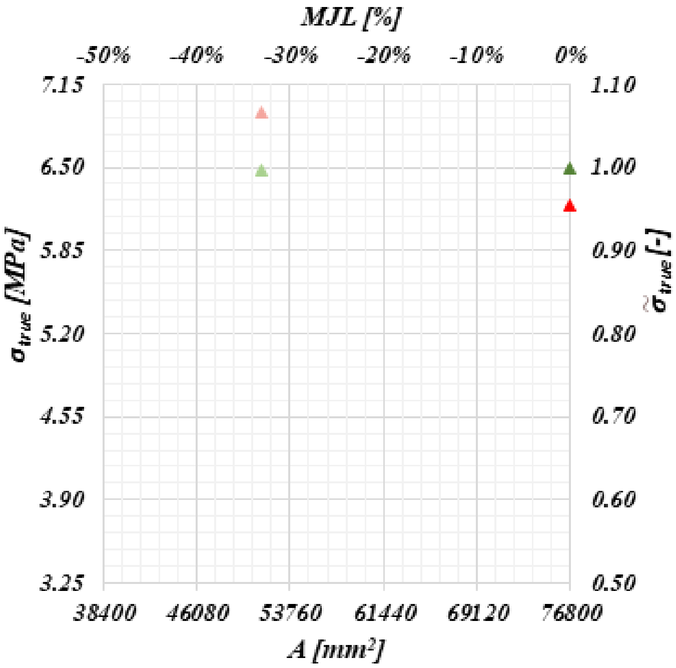

a)

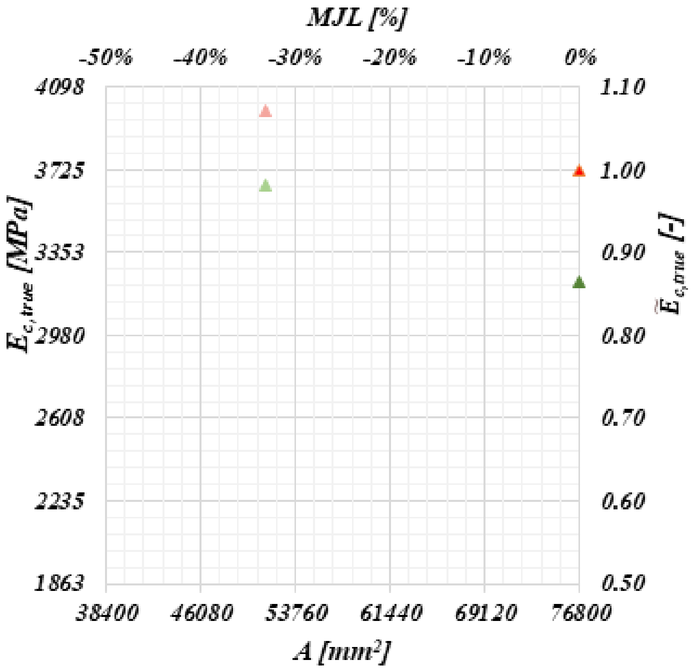

b)

Figure 16. Trends of a) true compressive strength given mortar joint loss; b) true elastic modulus given mortar joint loss; c) true elastic modulus reduction given true compressive masonry strength variation.

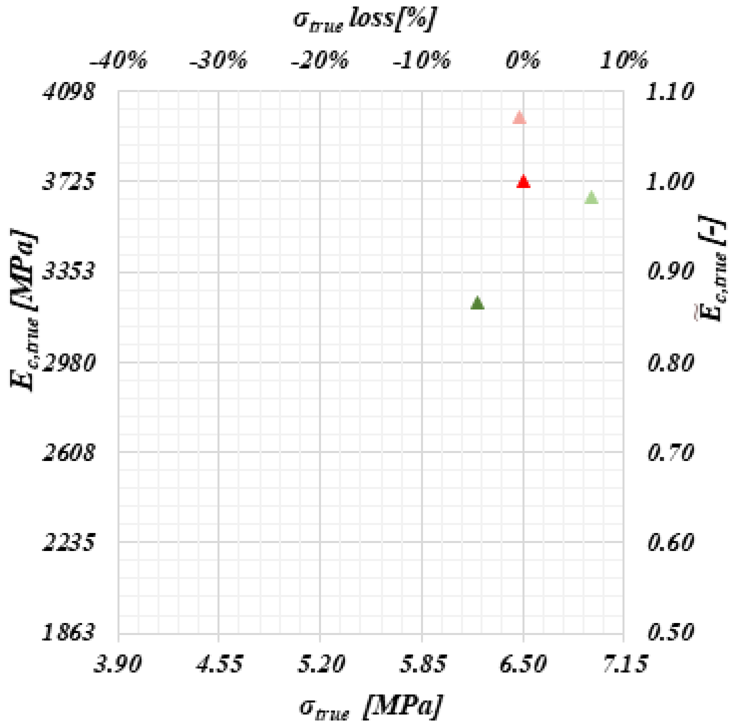

Figure 17. Trends of true elastic modulus reduction given true compressive masonry strength variation.

In Figure 16 and Figure 17 same plots of previous figures are reported with reference to true capacity features.(*i.e.* $\tilde{\sigma}_{true}$ *and* $\tilde{E}_{c,true}$.). As shown, in the case of deteriorated specimens, recorded load changes are only due to geometric effect because referring to the net cross-section the stress state is identical to that of intact specimens, as well for elastic modulus. When brittle phenomena occur resulting in geometric variation of the initial section, although the true tensional state remains almost unchanged the peak load capacity only changes due to the presence of geometric effects. The correlation between $\tilde{E}_{c,true}$ elastic modulus and $\tilde{\sigma}_{true}$ compressive strength suggests an average ratio between the two properties of 560.

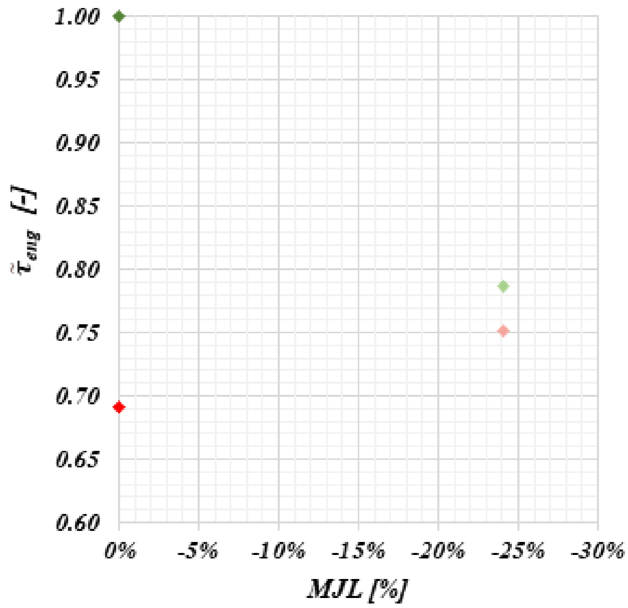

a)

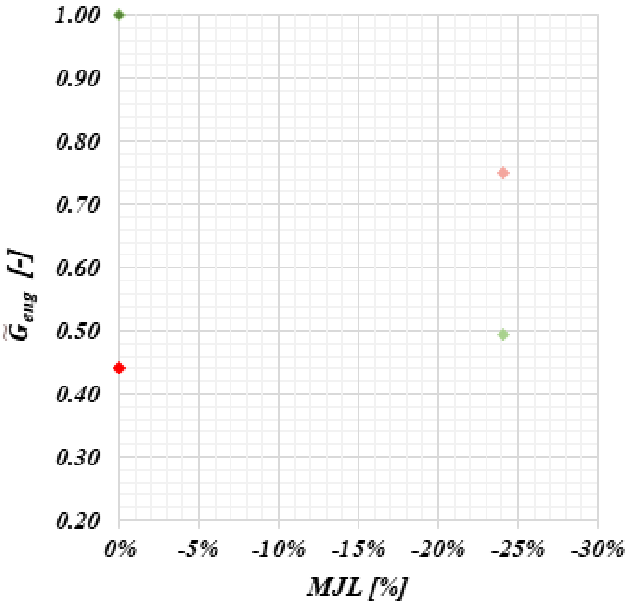

b)

Figure 18. Trends of a) true shear strength given mortar joint loss; b) true shear elastic modulus given mortar joint loss.

In Figure 18 dimensional and normalized plots are reported from diagonal compression test values: picture a) and b) have on the vertical axis τ_{eng} the engineering shear strength and G_{eng} shear elastic modulus, normalized with respect to the corresponding value of the maximum experimental integrity panel CD_D_1 (*i.e.* $\tilde{\tau}_{eng},$ and $\tilde{G}_{eng}$), while on the horizontal axis the gross area A and the mortar joint loss MJL compared to the intact panel.

As already noted in the previous section, the presence of the smart bricks had a non-negligible effect on the behaviour of the wall panels.

For intact condition, the presence of six smart bricks resulted in a significant reduction in strength and modulus of elasticity. The same effects are recorded in the case of deteriorated panels, where the number of smart bricks, i.e., 3, has led to lower deviations than in those without sensors. For this reason, new plots reported in Figure 19 were defined by considering only the net cross section of masonry removing the smart brick section, as already argued in the previous section. From pictures a and b, mortar joint loss by an average of 25% leads to a similar $\tilde{\tau}_{eng}$ shear strength reduction (20%) while $\tilde{G}_{eng}$ shear elastic modulus is subjected to a lower reduction (10%). It is worth noting that while for $\tilde{\tau}_{eng}$ shear stress wallets with innovative sensors show a comparable value, for the G_{eng} shear elastic modulus the intact wallet with six smart bricks shows a value significantly lower than that recorded for the deteriorated specimen with three sensors.

So, another interesting correlation has been defined in Figure 20.a between average $\tilde{G}_{eng}$ normalized shear stiffness values for deteriorated specimens (for intact configuration, CD_D_1_m was neglected for the reasons described above) and average $\tilde{\tau}_{eng}$ shear strength loss. In this way, regression model allows the estimation of the conditional mean value of shear modulus reduced due to the loss of the shear stress related to material degradation, and hence after that the loss of section area is known.

The last correlation (Figure 20.b) has been defined considering the average values, with reference to the $\tilde{E}_{eng}$ elastic modulus and $\tilde{G}_{eng}$ shear modulus values. More specifically, this regression model allows the estimation of the conditional mean value of shear modulus normalized given the variation of normalized elastic modulus related to material degradation, and hence after that the loss of compressive strength of masonry constituents is known.

These regressions provide all capacity characteristics to be included in analytical or FEM models when the compressive strength is known and the effect of geometric degradation on the behaviour of masonry buildings subjected to gravitational and seismic loads has to be investigated.

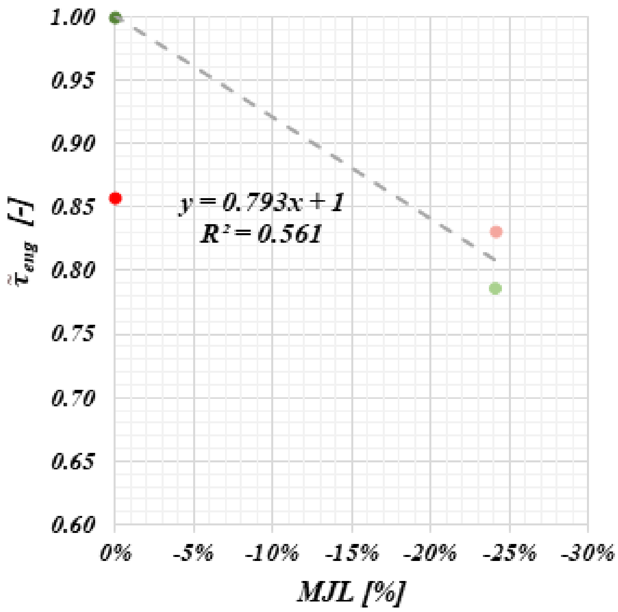

a)

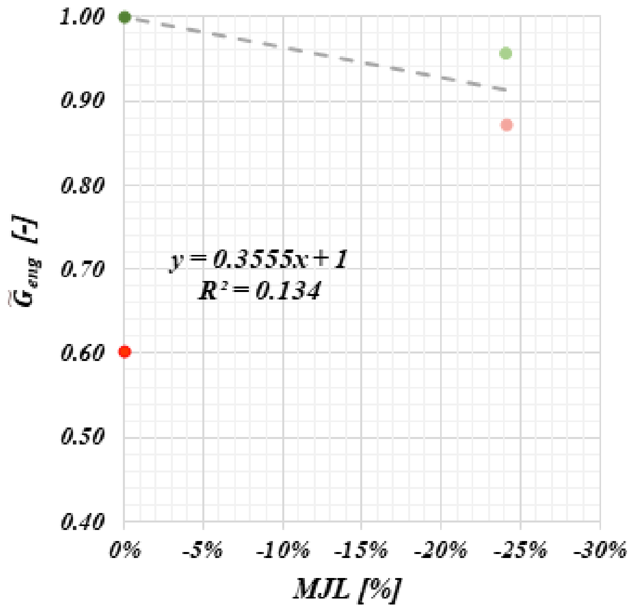

b)

Figure 19. Regression models for prediction of a) shear stresses reduction given mortar joint loss; b) shear elastic modulus reduction given mortar joint loss.

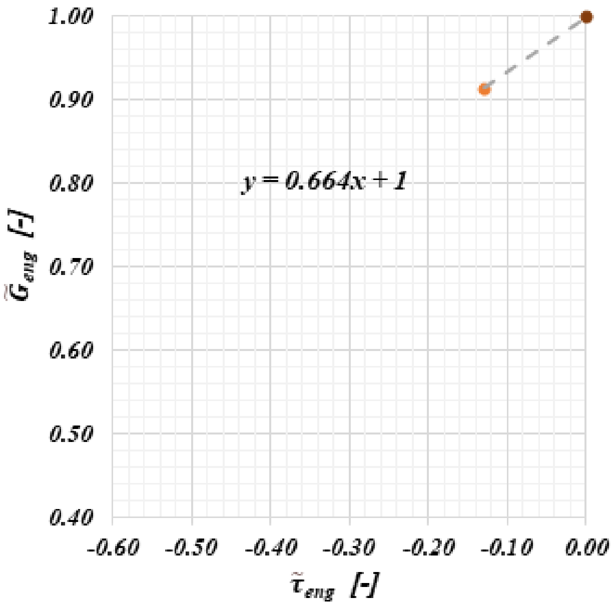

a)

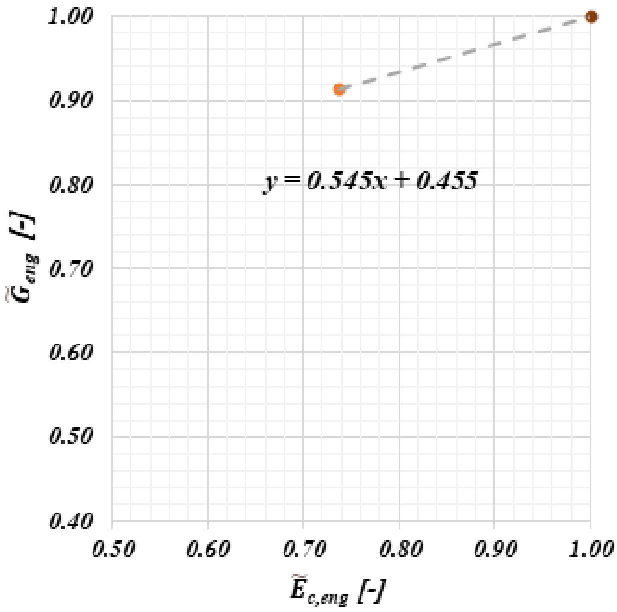

b)

Figure 20. Regression models for prediction of a) shear elastic modulus reduction given shear stresses loss; b) normalized shear modulus given normalized elastic modulus.

Even if these analyses are limited to this typology of brick masonry, model prediction can also be carried out on other types of masonry walls, which can develop different behaviour depending on their different material properties.

2.3. Description and mechanical properties of tuff masonry materials

Tuff masonry was fabricated in laboratory, according to a running bond pattern. Tuff was characterized by a nominal size of 300x150x110 mm^3, while masonry joints were nominally 10-mm-thick and filled with a premixed hydraulic mortar composed by natural hydraulic lime (NHL) with 1:5 water/binder ratio by weight (i.e., 5.25 L of water per 25 kg of lime) and fine sand, resulting into a low-performance lime mortar. The mortar composition was designed in a way to reproduce the main features of old mortar types in historical masonry buildings.

The stone had mechanical properties determined by means of experimental tests on six cubic tuff stones samples 75x75x75 mm^3 for compressive strength, according to [42]

The mean compressive strength f_{cb} = 4.30 MPa (with coefficient of variation CoV = 12.90%). The modulus of elasticity of the tuff stones was determined from tests on six prismatic specimens with dimensions 75X75X150 mm^3 and was equal to 2098 MPa (CoV=3.95%) [43]. Ten tuff specimens of dimensions 50x75x300 mm^3 were tested for flexural strength [44]. The mean flexural strength f_{fb} was equal to 0.85 (CoV = 3.34%). According to technical product declarations by the mortar manufacturer, the premixed hydraulic mortar was classified as M2.5 (corresponding to mean compressive strength of mortar f_{cm} = 2.5 MPa) according to Eurocode 6 [20] and Italian Building Code [21]. During the construction of each masonry wallet, mortar prisms (40x40x160mm^3 in size) were prepared and tested under three-point bending according to EN 1015-11 standard [22]. The two parts of each prismatic specimen after flexural failure close to the mid cross section were individually tested under uniaxial compression.

Table 6 outlines the mean values and CoV for both compressive and flexural tensile strengths of mortar and tuff.

All specimens were cured for 28 days at standard levels of relative humidity and temperature.

Table 6. Mechanical properties of masonry constituents*.

Material	Statistic	f_c	f_f
Tuff	Mean value [MPa]	4.30	0.85
	CoV	12.60%	3.34%
		(6)	(10)
NHL mortar	Mean value [MPa]	2.82	0.80
	CoV	10.27%	5.96%
		(12)	(6)

* f_c and f_f indicate compressive and flexural strengths of either material; bracketed figures denote the number of specimens for each experimental test.

2.3.1. Geometry and fabrication of specimens

The specimens tested under simple compression were characterized by a single-leaf masonry assemblage with overall size equal to 770x830x150 mm^3, while the another one double-leaf masonry assemblage with overall size equal to 770x830x310 mm^3, in agreement with other experiments carried out in the past [23] with 10 masonry layers (Figure 21.a). By contrast, the specimens tested under diagonal compression were fabricated according to a double-leaf masonry pattern with overall size equal to 1190x1230x310 mm^3 in agreement. with standard ASTM [24] and other studies[25], [26]. Regarding the masonry fabrication, the bricks were wetted with water before their installation in contact with the mortar. The specimens with artificial degradation (abbreviated as 'deteriorated specimens' hereinafter in contrast to 'intact specimens' with fully mortared joints) were made of partially filled mortar joints, as shown in Figure 21.b. In those specimens, the amount of mortared joint area can be deduced according to the ratio *s/t* between the full width of the mortared joint (*s*) and the total thickness of the wallet (*t*). The fabrication of deteriorated specimens was carefully controlled so that *s/t* was equal on average from 36% to 10% in specimens to be tested in simple compression and from 20% to 10% for the ones tested in diagonal compression.

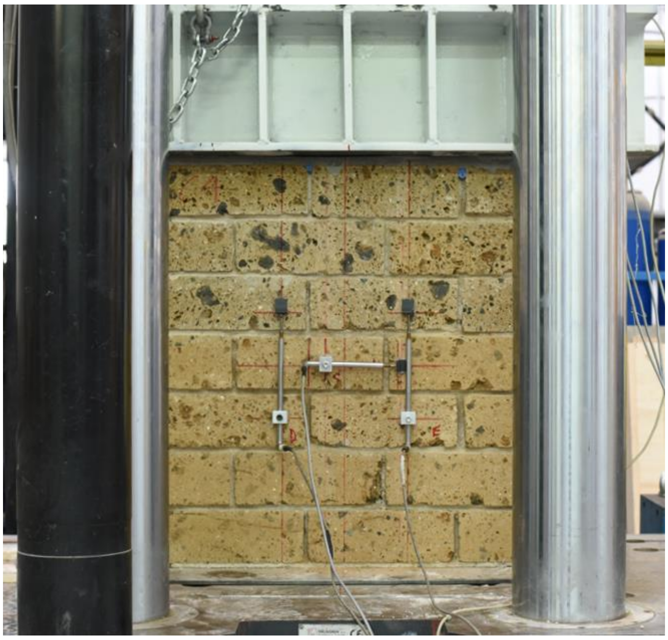

a)

b)

Figure 21.Pictures of specimens to be tested under (a) simple compression and (b) diagonal compression

2.3.2. Experimental program for tuff masonry

Also for tuff masonry, as illustrated before for bricks (see Sect. 2.2), an experimental program was carried out. The comprehensive testing program was set-up using destructive testing through uniaxial and diagonal compression test. Experimental tests focused on variations in

Young’s and shear moduli of masonry as well as its compressive and shear strengths, to inspect how tuff masonry reacts to a change due to ageing influence.

The assessment of tuff masonry’s mechanical properties, through these set of characterization tests, has been vital to understand how degradation effects from the scale of material up to the scale of component have an effect on to the scale of structure

In the following paragraphs, in fact, they will also be shown tests on full-scale unreinforced structures in degraded conditions, where degradation does not always trig to an unsafe effect compared to intact conditions.

Four masonry wallets were tested under simple uniaxial compression, whereas other four specimens were subjected to diagonal compression tests. The former set of specimens were made of single-leaf tuff masonry (TM) in number of three and one test on double-leaf TM, whereas specimens tested in diagonal compression consisted only of double-leaf TM. To simulate masonry in existing buildings, TM was made of common yellow tuff stones from a quarry near Viterbo, Italy, and natural hydraulic lime mortar. Half of each set of TM wallets was fabricated with mortar joints being characterized by reduced area, in order to simulate potential effects of TM degradation in the form of geometric joint alterations on each side of the specimen.

2.3.3. Experimental setups and testing procedures

2.3.3.1. Uniaxial compression for tuff masonry

The experimental setup for simple compression tests consisted of a universal testing machine Italsigma, with the full characterization reported in Sect.2.2.3.1

Test required a rigid steel I-beam on top, to allow an almost uniform distribution of pressures. (Figure 22)

All specimens were tested under monotonically increasing displacement up to failure, assuming a displacement rate equal to 0.01 mm/s to ensure effective monitoring of cracks and to fully measure the nonlinear behaviour of masonry including post-peak strain softening.

The only specimen with intact condition was labelled as TM_A_1, TM_A_2_D for the single-leaf tuff masonry and TM-DL_A_D for the one double-leaf, using final symbol D to indicate a deteriorated condition.

Deformations were measured by three inductive linear variable differential transformers (LVDTs) as follows: two LVDTs per side were parallel to the loading direction, and the other was orthogonal to the loading direction. All LVDTs were connected only to tuff, according to provisions by EN1052-1 standard [31].

a) b)

Figure 22.Experimental setups of specimens subjected to simple compression in configuration (a) intact and (b) deteriorated.

2.3.3.2. Diagonal compression for tuff masonry

Diagonal compression tests were carried out to investigate the in-plane shear behaviour of different double-leaf specimens with the same type of tuff masonry assemblage.

The two intact specimens with intact condition were labelled TM_D_1; TM_D_2 and the other deteriorated specimens TM_D_1_D; TM_D_2_D following the same approach for uniaxial compression test with a ratio between the full width of the mortar strips and the total thickness from 20% to 10% on average (Figure 23).

Testing procedures involved rotation of the URM wall panel by 45° and once centred in the machine frame the specimen was instrumented, and then subjected to in-plane diagonal loading along one of the wall's diagonals.

Diagonal compression tests were carried out with displacement control up to failure, using the same universal testing machine described for simple compression tests (see Sect. 2.3.3.1) and the same displacement rate (i.e., 0.01 mm/s). Load test procedure was the same as that used for bricks masonry test. (see Sect. 2.2.3.2)

The diagonal compression test was stopped when approximately a 50% of peak force drop was reached on the post-peak softening branch of the force–displacement diagram.

On each side, relative vertical and horizontal displacements were measured by linear variable differential transformers (LVDTs) with gage length g = 400 mm, not to have localized effects in the centre, bearing in mind that ASTM E 519-07 does not provide standard gage lengths for LVDTs.

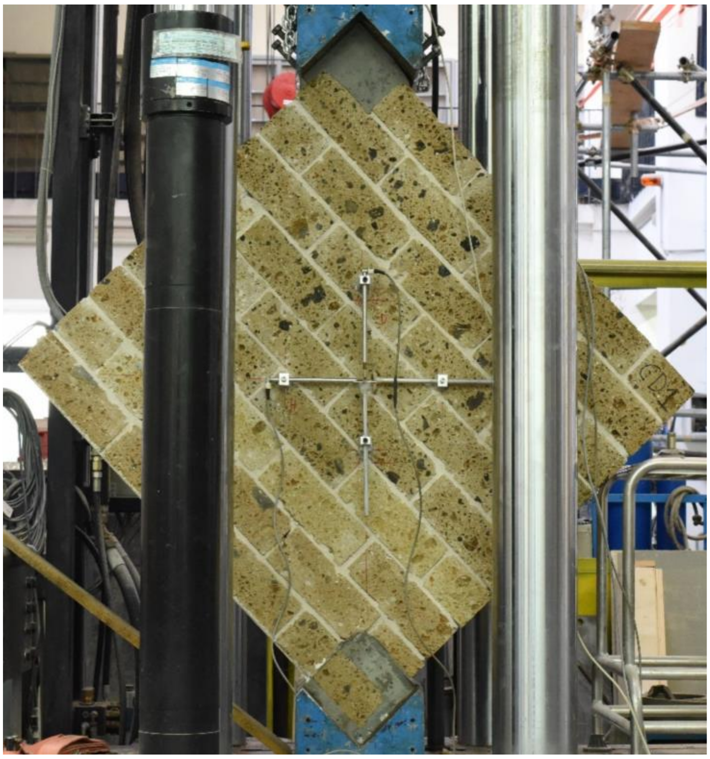

a)

b)

Figure 23. Experimental setups of specimens subjected to diagonal compression in configuration (a) intact and (b) deteriorated.

2.3.4. Results of simple compression tests for tuff masonry

At the load peak, macro vertical cracks spread on the panels surfaces mainly on the tuff-and-mortar vertical joints with a successive spalling substantially uniform over the whole specimen while consequently the load-carrying capacity deteriorated until the end of the test (Figure 24.a.c). The failure mechanism of the wallets started with vertical splitting shortly before the maximum load was reached. For intact specimen, vertical cracks spread along the head joints and tuff starting from the edges of the specimen, when the splitting phenomenon is triggered, up to the inner zone. On the other hand, extensive cracking occurred in the central zone for the deteriorated specimens, even in the range of small deformations, followed by lateral flaking of vertical courses and faces spalling off. For intact specimen a restrained splitting phenomenon was observed, while for those deteriorated, a limited material ejection was recorded (Figure 24.b.d).

Splitting along the thickness is a failure mode of masonry subjected to axial compression and is due to the difference between elastic properties of masonry units and those of mortar. The enhanced masonry deformability, due to unfully filled mortar joints, may have not fully involved tuff's stiffness.

Strain gauges placed at central zone reveal that, before crushing, the tuff behaviour is quasi-elastic, without relevant increasing of the compression stress till the failure. Progressive opening of the cracks caused the detachment of sensors during the test, affecting the readings of the LVDTs both for elastic and post-peak softening branch, for some specimens.

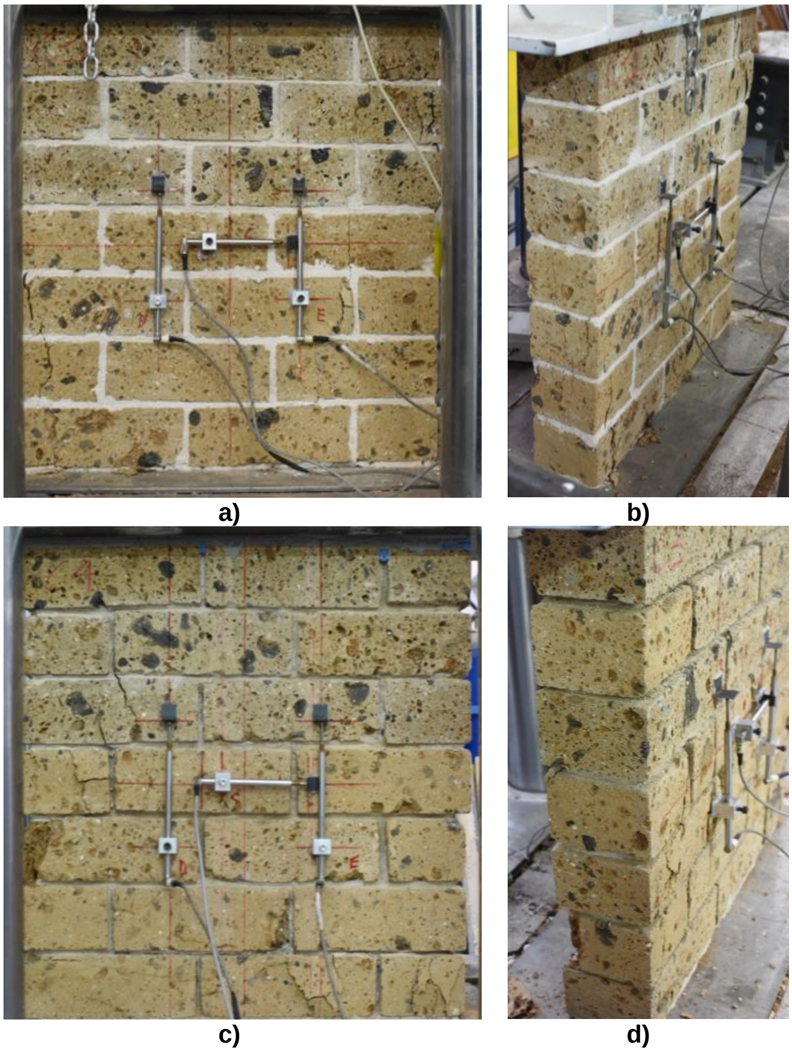

Figure 24. Crack pattern of masonry prism in compression for intact specimens a) frontal and b) transverse views; deteriorated specimens c) frontal and d) transverse views.

Uniaxial load tests can be assumed to produce a uniform stress distribution over the section, so the compressive strength σ_c can be calculated as the ratio between the applied load and the gross area of the cross section ($\sigma_c = N_u/A$). Engineering axial strains were computed by dividing the average value of LVDT readings by their gauge length [32]. Figure 25 shows the experimental stress–strain curves, denoting by ε_H and ε_V the horizontal and vertical axial strains, respectively.

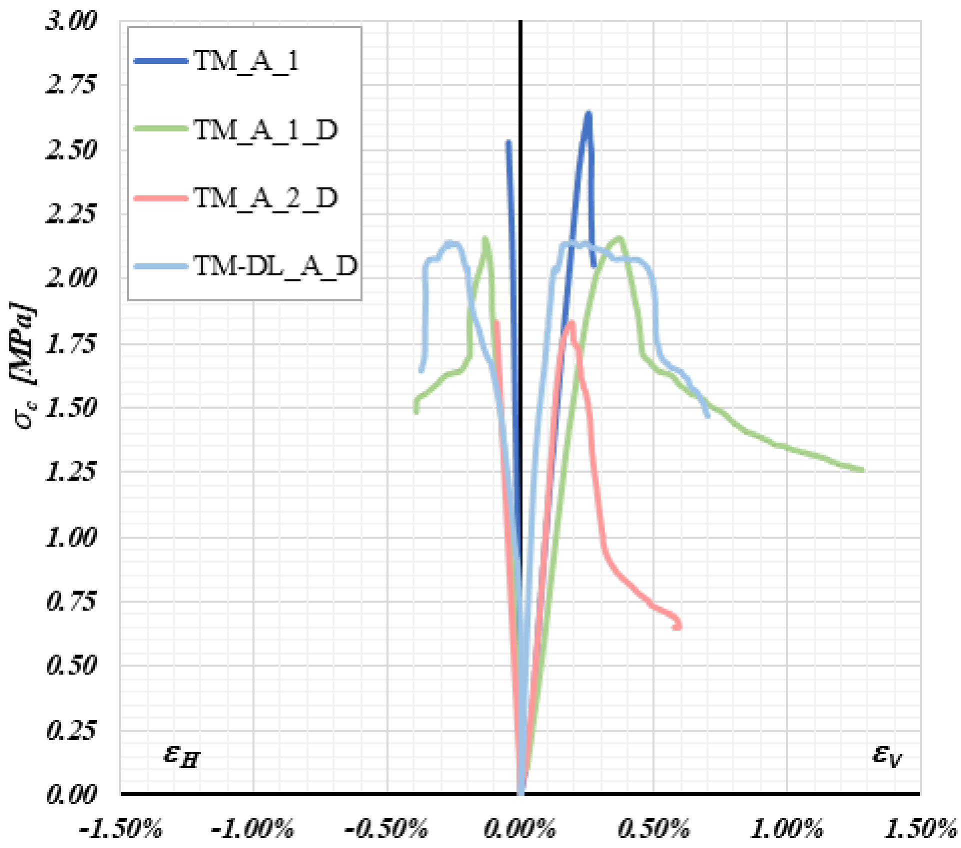

Figure 25. Experimental stress-strain curves of specimens subjected to uniaxial compression test

Table 7 provides a summary of the main experimental results related to the following properties: peak compressive strength (σ_p), the vertical and horizontal strains at peak strength (ε_{Vp} and ε_{Hp}), Young's modulus, and Poisson ratio ($\nu_m = -\varepsilon_H/\varepsilon_V$). Alternative estimates of Young's modulus were derived, as follows: chord modulus (E_c) [33] evaluated between 5% and 30% of peak compressive strength; secant modulus corresponding to one-third of peak compressive strength ($E_{1/3}$), according to European standards and codes [20], [21]; and secant modulus corresponding to half of peak compressive strength ($E_{1/2}$), according to previous studies [23].That modus operandi was motivated by the need to identify the best estimate of Young's modulus, removing local effects due to initial lack of effective contrast between the specimen and testing machine.

Table 7. Summary of simple compression test results

Specimen configuration	Specimen	σ_p	ε_{Vp}	ε_{Hp}	E_c	$E_{1/3}$	$E_{1/2}$	ν_C
		[MPa]	[×10^{-3}]	[×10^{-3}]	[MPa]	[MPa]	[MPa]	[–]
Intact	TM_A_1	2.64	2.54	-0.47	1424	1063	1109	0.16
Deteriorated	TM_A_1_D	2.16	3.63	-1.30	890	721	768	0.25
	TM_A_2_D	1.83	1.88	-0.28	1056	979	1081	0.24
	TM-DL_A_D	2.14	1.89	-2.66	1216	1106	1172	0.20
	Average	2.04	2.47	-1.41	1054	935	1007	0.23

Intact wallets show stress–strain curves linear up to approximately 40% of peak compressive strength, which was followed by a change in slope in the remaining part of the pre-peak nonlinear rising branch.

After the peak was reached, panel TM_A_1 showed a sudden drop of load. The value obtained for intact specimen showed compressive strength, σ_p = 2.64 MPa which results in good agreement with the values provided by the Italian Code for tuff masonry, elastic modulus E = 1424 MPa and Poisson ratio ν = 0.16. The modulus of elasticity of masonry was correlated with the masonry compressive strength and was found to be E=539 σ_p which agrees well with the values provided by Codes [21], [34]. A different value was found for aged specimens, about E= 516 σ_p with compressive strength equal to 2.04 MPa.

The reduction of joint filling by an average of 36% leads to a similar compression strength and elastic modulus reduction Deteriorated specimens exhibit a lower compression strength and modulus of elasticity than those of intact specimens while Poisson ratio is higher, due to a stress state acting on a reduced mortar layer resulting in increased deformability. Despite the aged state, masonry reveals the capacity of sustaining loading, where a direct effect, *i.e.,* proportional to filling compared to the nominal value of joint width was observed on masonry properties both compression strength and elastic modulus. Mortar joint can be seen as the weak link of the chain for masonry under axial load, so strengthening with trimmed joints seal can be useful to face gravity action.

2.3.5. Results of diagonal compression tests for tuff masonry

The wallets presented a relatively brittle behaviour and Figure 26-Figure 29 show the crack patterns of the four walls after failure. First cracks appeared at the upper corner of the panels and then progressed throughout the masonry assemblage by increasing deformation. Failures were characterized by shear-sliding involving both bed and head joints along the compressed diagonal with patterns qualitatively similar and, in almost all cases, a final diagonal main crack connected both loaded corners.

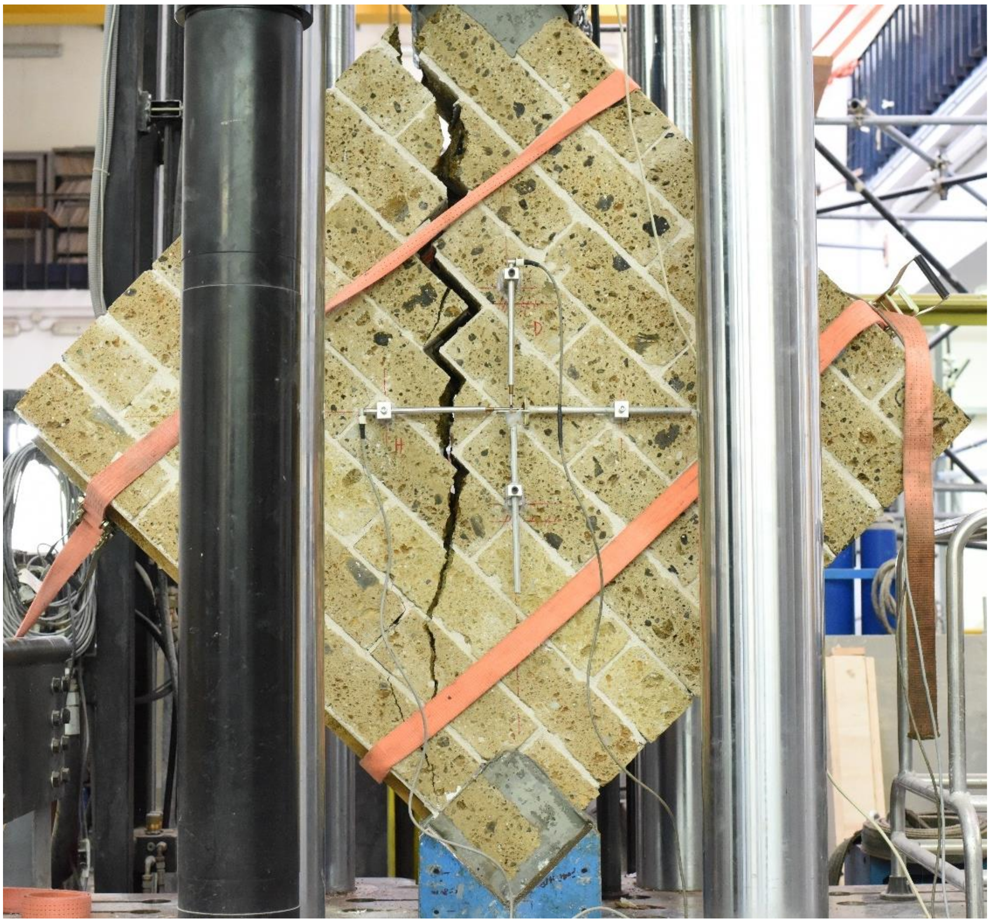

Figure 26. Crack pattern of specimen TM_D_1

Slight differences for intact panels were observed, for TM_D_1 specimen some masonry stone in the central part were broken but peak load was lower compared to other intact case. This could be explained by combination of material properties variability with assemblage inhomogeneity and considering that collapse of masonry wallets subjected to diagonal compression test is generally governed by tensile strength of bricks located in the central part.

Figure 27. Crack pattern of specimen TM_D_2

The cracks involved the full thickness and were visible on both faces of the walls. The opening of the central diagonal cracks caused a premature detachment of sensors in some tests, and affected the readings of the LVDTs on the post-peak softening branch of the force–displacement diagram.

The behaviour of solid brick URM evidenced a sudden drop in resistance after the occurrence of the diagonal crack for a couple of each configuration (intact and deteriorated mortar joints) (see Figure 30).

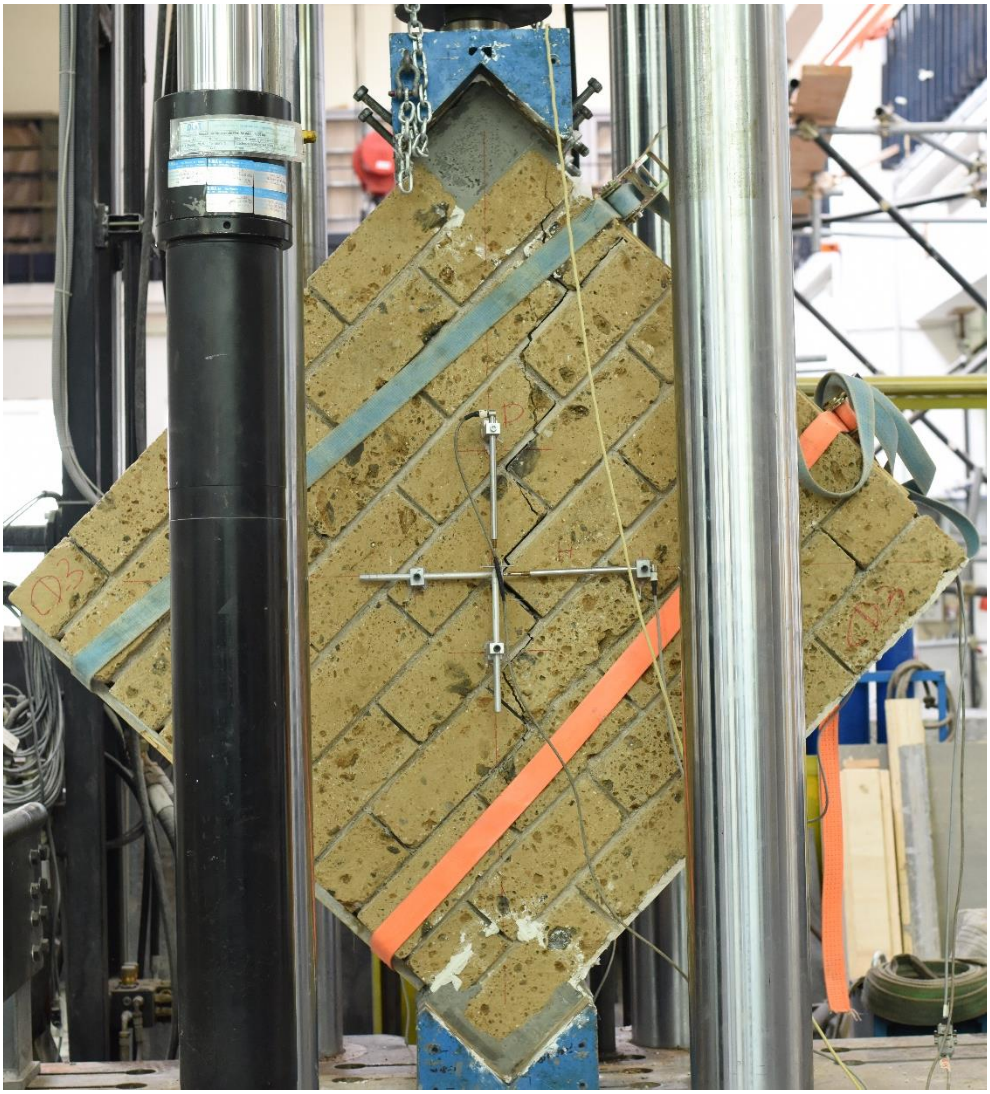

Figure 28 Crack pattern of specimen TM_D_1_D

The behaviour of the specimens was similar, with the τ–γ curves that followed one another closely up to the end of the test with differences in shear strength.

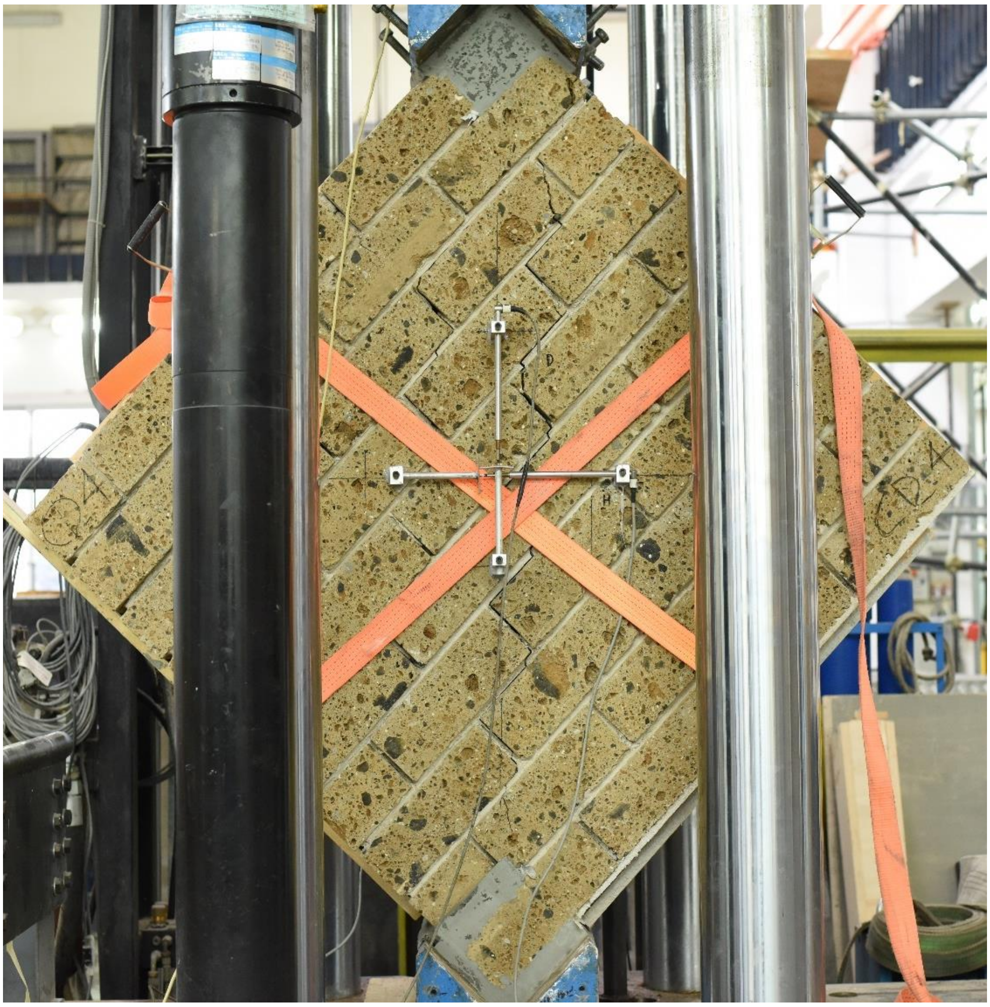

Figure 29. Crack pattern of specimen TM_D_2_D

The deteriorated panels, TM_D_1 and TM_D_1_D were characterized by a similar behaviour up to about 35% of the maximum shear strength when for TM_D_1_D wallet the mortar geometric variation caused a stiffness drop resulting in higher deformability and shear strength decrease.

TM_D_2_D wallet, despite a geometric degradation of mortar by 10% on average, showed the better result in terms of shear strength, as a result of the epistemic and aleatory uncertainties in material properties variability. It's really noteworthy, the two specimen configurations (intact and deteriorated) have a similar two-by-two behaviour, in terms of elastic stiffness (see TM_D_1/TM_D_1_D and TM_D_2/TM_D_2_D)

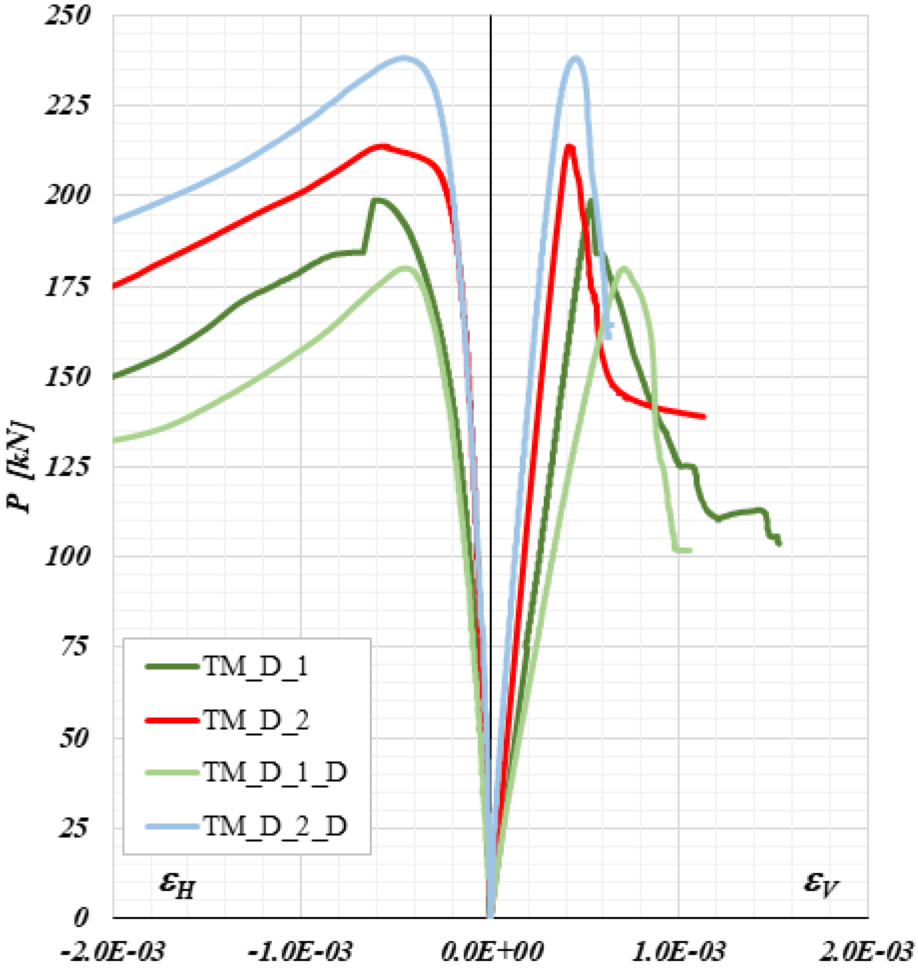

Figure 30.Experimental load-strain curves for the four specimens

2.3.6. Significant mechanical parameters of tuff masonry

From the results of diagonal compression tests, it is possible to obtain a wide range of variability of the pure shear strength, according to different approaches [39].

Masonry shear strength, according to ASTM E519-2010 and RILEM TC-76-LUMB2010 specifications, as described before for brick masonry test, were used for the identification of mechanical parameters

According to the ASTM standard, shear stress τ_0 and tensile strength f_t of masonry, were determined by using the equations (1) and (2):

On the other hand, according to RILEM instructions, these latter were calculated by equations (3), and (4).

Similarly, strain measurements from LVDTs were retrieved by considering the following relations (Eqs.(5) and (6)).

Table 8 presents a summary of the experimental results from diagonal compression tests on the four wallets and indicates the registered values of maximum load P_{max}, the calculated values of shear stress τ_0, tensile strength f_t and shear modulus $G_{1/3}$ as secant modulus between the origin and the stress equal to 30% of peak shear strength and the corresponding shear strain.

Table 8. Summary of diagonal compression test results

Specimen configuration	Specimen	P_{max} [kN]	Standard	$G_{1/3}$ [MPa]	τ_o [MPa]	f_t [MPa]
Intact	TM_D_1	198.85	ASTM	534	0.37	0.37
			RILEM	664	0.47	0.27
	TM_D_2_	213.77	ASTM	769	0.40	0.40
			RILEM	957	0.50	0.28
	Average		ASTM	651	0.39	0.39
			RILEM	810	0.48	0.28
Deteriorated	TM_D_1_D	180.02	ASTM	444	0.34	0.34
			RILEM	553	0.42	0.24
	TM_D_2_D	238.33	ASTM	1071	0.45	0.45
			RILEM	1333	0.56	0.32
	Average		ASTM	758	0.39	0.39
			RILEM	943	0.49	0.28

Very close values of the shear stress were achieved by specimens with same mortar geometric configuration, particularly for intact specimens, so the exceedance of tensile shear strength occurs at the same stress state, with comparable values as well as maximum vertical load P, and the capacity in terms of deformation.

The formulation provided by ASTM led to the following mean values of peak shear strength at zero confining stress and tensile strength: $\tau_0 = f_t = 0.39\ MPa$ in the case of intact specimens as well as in the case of deteriorated specimens, these latter conditioned by TM_D_2_D peculiar result.

Data processing according to RILEM provided the following mean values of peak shear strength at zero confining stress and tensile strength: $\tau_0 = 0.48\, MPa$, $f_t = 0.28\, MPa$ in the case of intact specimens and $\tau_0 = 0.49\, MPa$, $f_t = 0.28\, MPa$ in those deteriorated.

The shear modulus of rigidity $G_{1/3}$ was calculated as secant modulus between the origin and the stress equal to 30% of peak shear strength and the corresponding shear strain, to define a nominal slope of the elastic branch of τ–γ diagram.

Pseudo-ductility concept under diagonal compression condition is not univocal in the literature and must take into account the specific behaviour manifested by the type of masonry [26].

Two methodologies were implemented for the computation of γ_y, γ_u and τ_u.as depicted in Figure 13. (see Sect. 2.2.6)

In the first method, "Bilinear 1" the ultimate shear stress τ_u was defined as the experimental value at the peak shear stress on the experimental τ-γ diagram and the corresponding shear strain was defined as the γ_u for the idealized bilinear. Therefore γ_y was derived assuming equal areas underneath idealized τ- γ diagram and the experimental up to the peak.

In the second method "Bilinear 2" the ultimate shear strain γ_u was associated with a 20% strength drop on the post-peak softening branch while γ_y and τ_u were defined by using a secant modulus from the origin of the experimental τ- γ curve to 70% of τ_{max}. Ultimate shear strain was set to the strain recorded at the 20% of the peak according to current criteria for the definition of ultimate limit state of load-bearing masonry walls and buildings, especially in lateral loading conditions.

For both approaches the elastic shear modulus G_e was defined as $G_e = \tau_u / \gamma_y$ and, only for the idealized bilinear with the second method, shear strain ductility factor μ_γ was defined as $\mu_\gamma = \gamma_u / \gamma_y$.

In Table 9 the mechanical parameters are listed related to shear modulus of rigidity and shear strain ductility.

Table 9.Main capacity features of intact and deteriorated wallets.

Specimen configuration	Specimen	Approach	Standard	G_e [MPa]	μ_γ -
Intact	TM _D_1	Bilinear 1	ASTM	498	
			RILEM	619	
		Bilinear 2	ASTM	483	3.53
			RILEM	601	3.53
	TM _D_2	Bilinear 1	ASTM	702	
			RILEM	874	
		Bilinear 2	ASTM	739	5.65
			RILEM	920	5.65
	Average	Bilinear 1	ASTM	600	
			RILEM	747	
		Bilinear 2	ASTM	611	4.59
			RILEM	761	4.59
Deterioated	TM _D_1_D	Bilinear 1	ASTM	429	
			RILEM	533	
		Bilinear 2	ASTM	394	3.19
			RILEM	490	3.19
	TM_D_2_D	Bilinear 1	ASTM	895	
			RILEM	1114	
		Bilinear 2	ASTM	819	5.54
			RILEM	1020	5.54
	Average	Bilinear 1	ASTM	662	
			RILEM	824	
		Bilinear 2	ASTM	607	4.36
			RILEM	755	4.36

Deteriorated specimens exhibit a lower resistance, but unlike the case of compression test, diagonal test reveals a change in mechanical properties less proportional to the section reduction.

The shear strength was lower than that of intact specimens, on average by 13 % neglecting the deteriorated wallet TM_D_2_D because of the off-trend behaviour.

Despite the aged state, masonry also reveals a deformation capacity in terms of ductility ratios μ_γ = 4.36 equal to the case of intact specimen, so aging effect does not seem to affect their post-peak behaviour.

Also for tuff wallets under diagonal compression test, joint mortar reduction, for aged specimens, is mitigated by the tuff units meshing with a less straightforward effect to filling width on masonry properties especially for shear elastic modulus.

2.3.7. Comparison between experimental results

The global behaviour of walls under in-plane loading was recorded for each load test as presented in the previous section and a summary of capacity features were collected in Table 8,and Table 9 where compressive and shear strength are related to the type of mortar joints filling. Indeed, test on aged specimen, where the physical processes of material aging was not attempted but reproducing only a final state, were simulated by reducing mortar joints filling compared to the nominal value.

Capacity features were computed both with reference to the gross area (obtaining engineering stresses expressed with the subscript $_{eng}$) and with reference to the net area of the cross section, (obtaining true stresses expressed with the subscript $_{true}$) to evaluate possible combined mechanical and geometrical effects due to the aging.

In Figure 31 dimensional and normalized plots are reported from compression test values: Figures a) and b) have on the vertical axis the $\sigma_{c,eng}$ compressive strength and $E_{c,eng}$ chord modulus computed with reference to the gross area, normalized with respect to the corresponding value of the experimental intact panel TM_A_1 (i.e. $\tilde{\sigma}_{c,eng}$ and $\tilde{E}_{c.eng}$), while on the horizontal axis the gross area A and the mortar joint loss MJL compared to the intact panel.

Local-global data sets were used to develop linear regression models for their use in structural safety assessment of masonry structures. Regressions are characterized by a coefficient of determination R^2 equal to 0.862 and 0.965 respectively for prediction of $\tilde{\sigma}_{c,eng}$ compressive strength reduction and that of $E_{c,eng}$ elastic modulus given mortar joint filling, indicating a satisfactory goodness of fitting data. The reduction of joint filling by an average of 31% leads to a similar compression strength and elastic modulus reduction

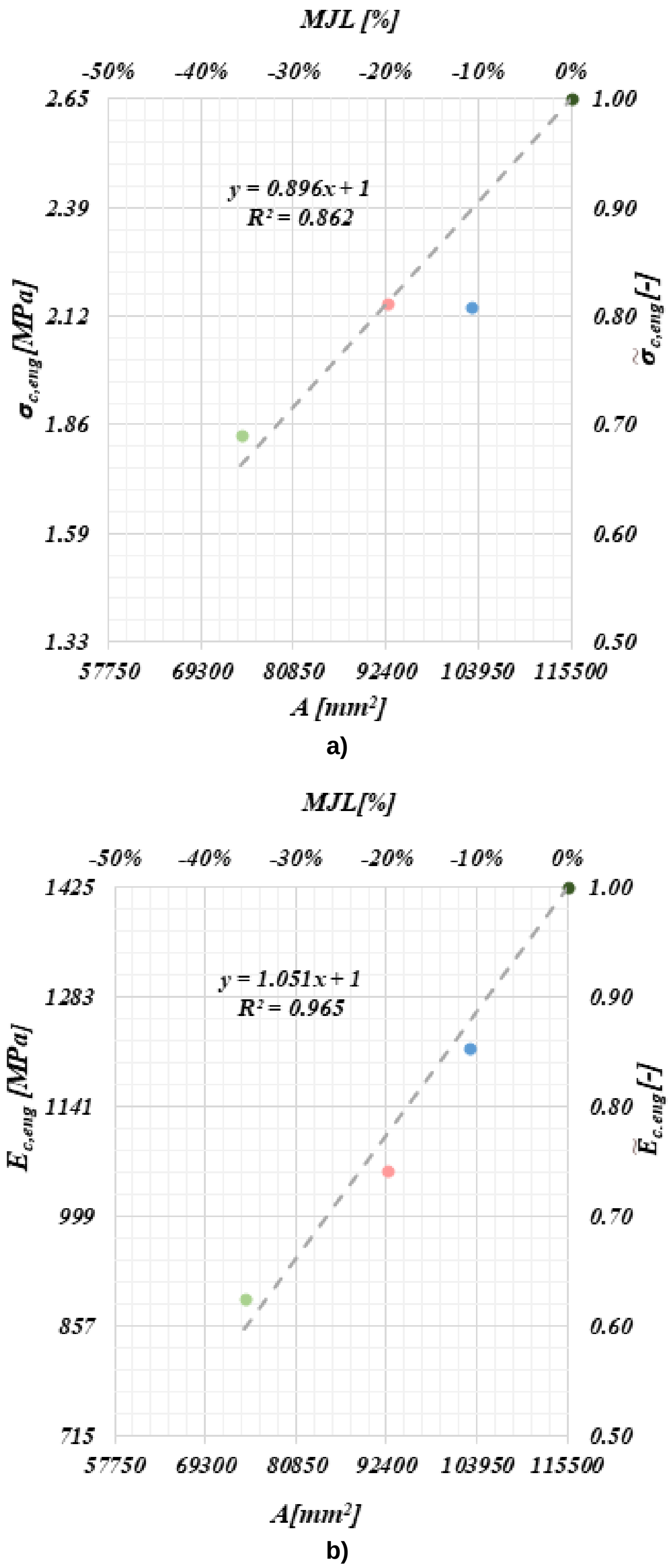

Figure 31. Regression models for prediction of a) compressive strength reduction given mortar joint loss; b) elastic modulus reduction given mortar joint loss.

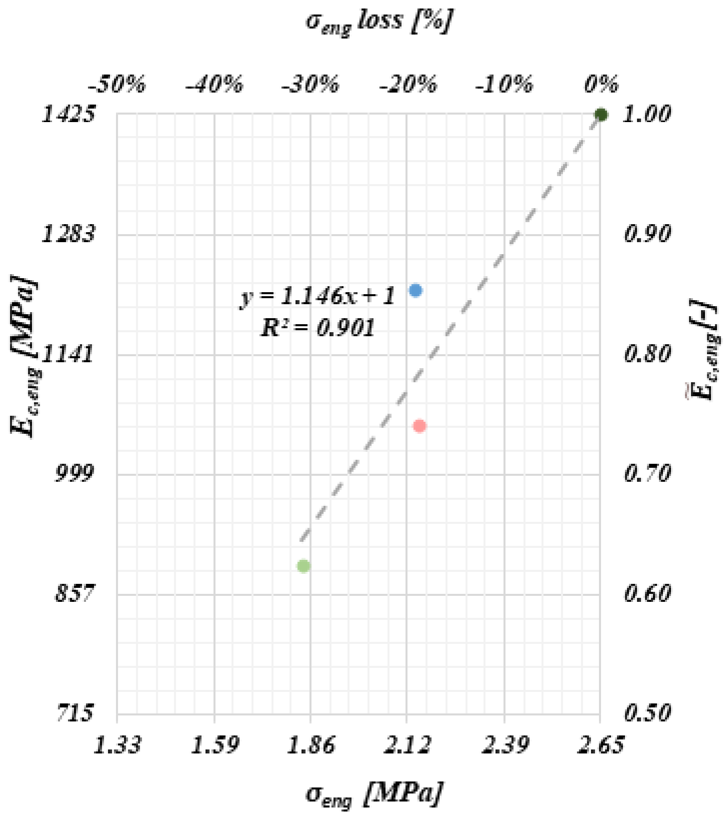

c)

Figure 32.Regression models for prediction of c) elastic modulus reduction given compressive masonry strength loss.

Compressive strength is usually used as main local property of masonry, so another correlation has been defined in Figure 32 between $\tilde{E}_{c,eng}$ normalized elastic stiffness and $\tilde{\sigma}_{c,eng}$ compressive strength loss with a satisfactory goodness of coefficient R^2 equal to 0.901. In this way, regression model allows the estimation of the conditional mean value of elastic modulus reduced according to the loss of the compressive masonry strength related to material degradation, hence after that the loss of section area is known.

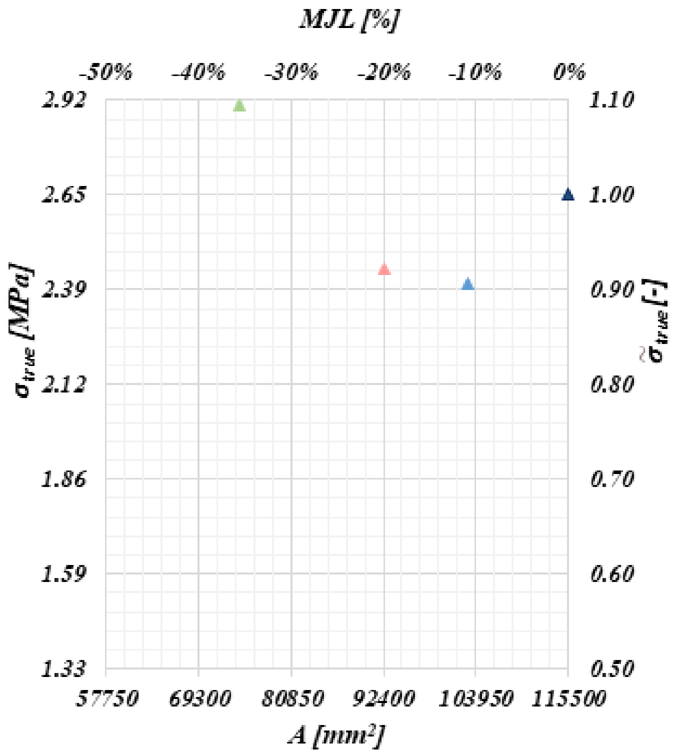

a)

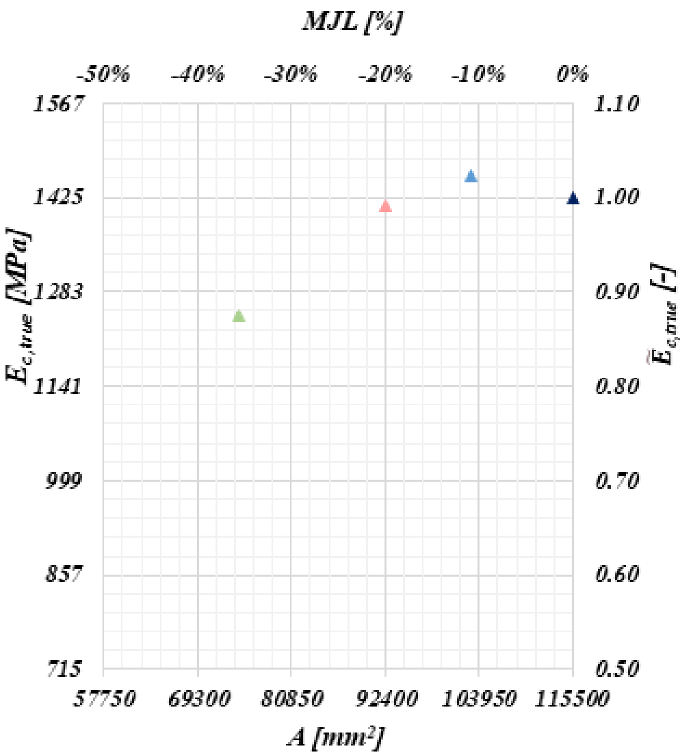

b)

Figure 33. Trends of a) true compressive strength given mortar joint loss; b) true elastic modulus given mortar joint loss.

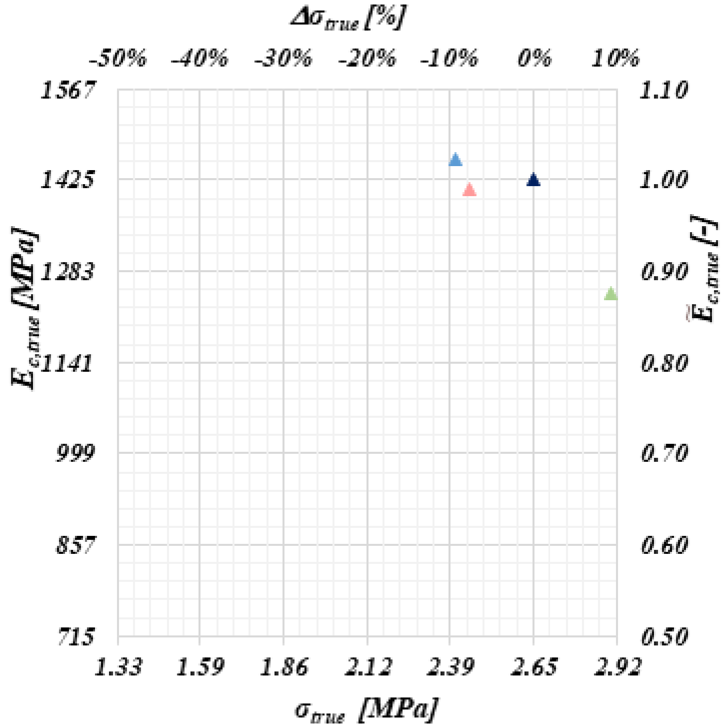

Figure 34. Trends of true elastic modulus reduction given true compressive masonry strength variation.

In Figure 33 and Figure 34 same plots of previous figures are reported with reference to true capacity features (*i.e.* $\tilde{\sigma}_{true}$ *and* $\tilde{E}_{c,true}$*.).* As shown, in the case of deteriorated specimens, recorded load changes are only due to geometric effect because referring to the net cross-section the stress state is identical to that of intact specimens, as well for elastic modulus. When degradation phenomena occur resulting in geometric variation of the initial section, although the true tensional state remains almost unchanged, the peak load capacity only changes due to the presence of geometric effects.

The correlation between $\tilde{E}_{c,true}$ elastic modulus and $\tilde{\sigma}_{true}$ compressive strength suggests an average ratio between the two properties of 530.

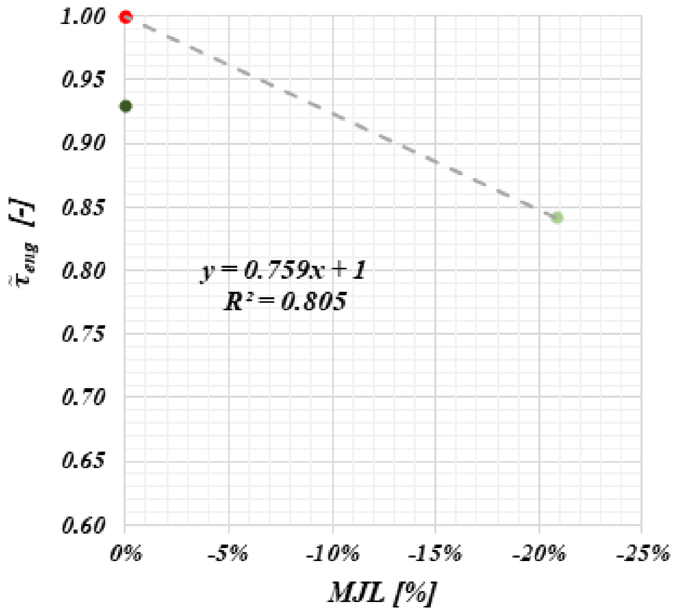

a)

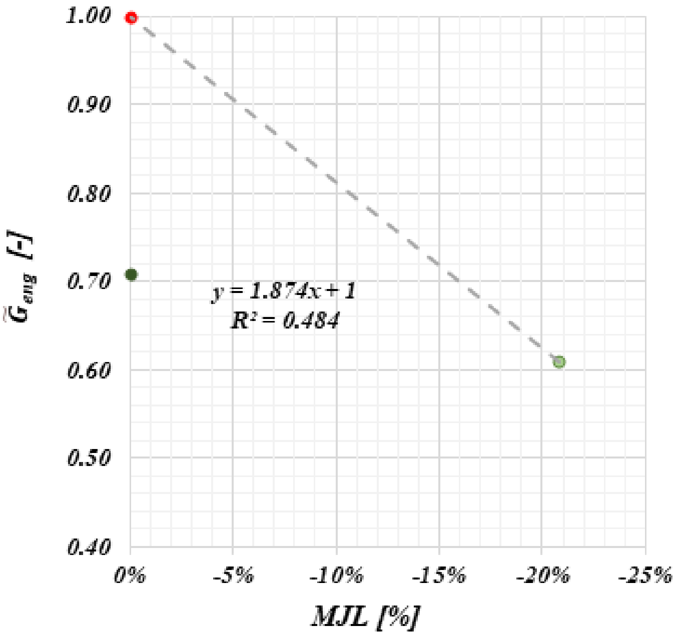

b)

Figure 35. Regression models for prediction of a) shear stresses reduction given mortar joint loss; b) shear elastic modulus reduction given mortar joint loss.

In Figure 35 dimensional and normalized plots are reported from diagonal compression test values: picture a) and b) have on the vertical axis τ_{eng} the engineering shear strength and G_{eng} shear elastic modulus, normalized with respect to the corresponding value of the maximum experimental intact panel TM_D_2(i.e. $\tilde{\tau}_{eng}$, and $\tilde{G}_{\text{eng}}$), while on the horizontal axis the gross area A and the mortar joint loss MJL compared to the intact panel.

As already noted in the previous section, TM_D_2_D specimen with a different behaviour, likely due to aleatory uncertainties in material properties variability, was excluded from regression models listed below. From Figures a and b, mortar joint loss by an average of 20% leads to a similar $\tilde{\tau}_{\text{eng}}$ shear strength reduction (15%) while $\tilde{G}_{\text{eng}}$ shear elastic modulus is subjected to a higher reduction (40%). But it's noted a significant dispersion within experimental intact groups, resulting in substantial differences in wallet mechanical performance. This was particularly evident in terms of shear elastic modulus.

So, another interesting correlation has been defined in Figure 36.a between average $\tilde{G}_{\text{eng}}$ normalized shear stiffness values, (deteriorated specimens TM_D_2_D was neglected for the above described reasons) and average $\tilde{\tau}_{\text{eng}}$ shear strength loss.

In this way, the regression model allows the estimation of the conditional mean value of reduced shear modulus given the loss of the shear stress related to material degradation, and hence after that, the loss of section area is known.

The last correlation (Figure 36.b) has been defined considering the average values, with reference to the $\tilde{E}_{\text{eng}}$ elastic modulus and $\tilde{G}_{\text{eng}}$ shear modulus values. More specifically, this regression model allows the estimation of the conditional mean value of normalized shear modulus given the variation of normalized elastic modulus related to material degradation, and hence after that the loss of compressive strength of masonry constituents is known.

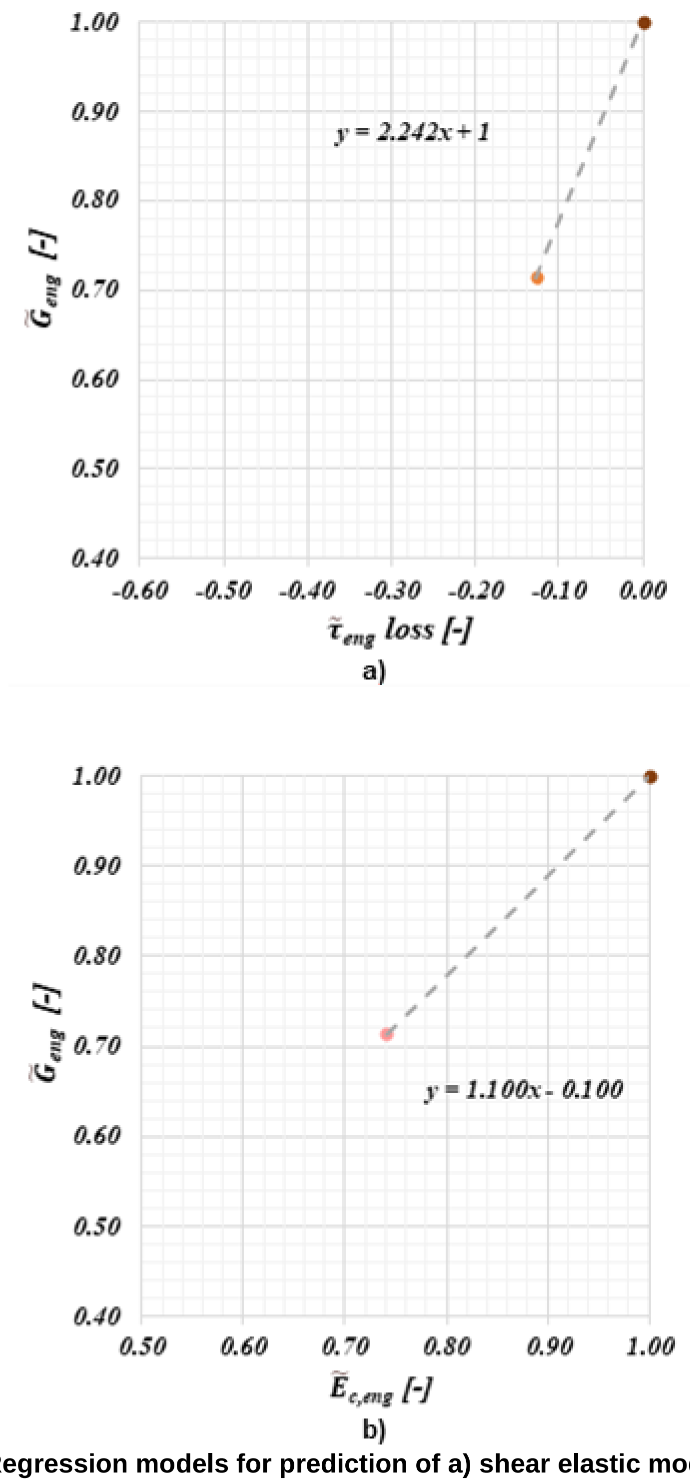

Figure 36. Regression models for prediction of a) shear elastic modulus reduction given shear stresses loss; b) normalized shear modulus given normalized elastic modulus.

These regressions provide all capacity characteristics to be included in analytical or FEM models when the compressive strength is known and the effect of geometric degradation on the behaviour of masonry buildings subjected to gravitational and seismic loads is to be investigated.

2.4 Settlement testing of unreinforced masonry

This part of the thesis presents the results of a laboratory test carried out on a full-scale unreinforced masonry wall (URM) with an opening subjected to a differential settlement. Specific attention was paid to aging effect, so two configurations have been adopted, intact and deteriorated such as previous described simple and diagonal compression test. The main objective of this study is to make available accurate and reliable experimental data to be used as validation of numerical results.

It was observed that masonry structures subjected to foundation movements usually develop typical failure patterns when they are affected by ground movements at the base, depending on the portion of the structure involved in the movements, the type of differential settlement pattern. Figure 37 shows a series of typical damage patterns for specific masonry types, such as façades, corners, connection, arches and vaults [45].

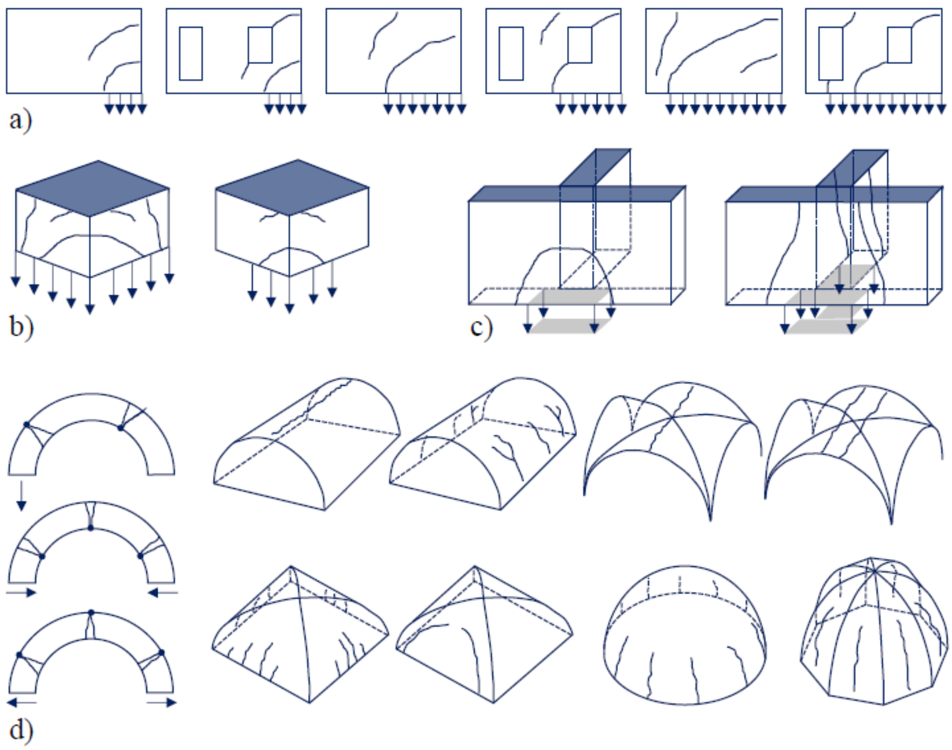

Figure 37. Damage patterns for masonry structures subjected to settlements: (a) Façade with and without openings; (b) buildings corner connections; (c) T-connections; (d) arches, vaults and domes.

Korff [46] noted that buildings with load bearing walls are more vulnerable to damage than buildings with frame structure. For the same vertical displacement, frame structures can accommodate differential displacements by deformation of the beams, whereas load bearing walls need to bend, which leads to cracking more easily. This situation led to a 20/25% lower tolerable relative rotation and settlement for load bearing walls.

Buildings under specific loading condition can move, crack, deform, tilt with damage depending on their construction type, stiffness, openings and joint [46].

Possible causes of building deformation are self-weight, temperature changes, moisture content changes or settlements. Settlements can be seen as subsequent to environmental changes. Environmental conditions that can cause settlement are due to soil characteristics, changes in groundwater level or mining activities, causing vibration and deep subsidence, changes in neighbouring buildings, vibration due to traffic and construction of new roads or structures [47].

These deformations lead too strain which in turn may cause important damage to the structure with possible tilt. Tilt phenomena are characterized by a rigid body motion of building portion under settlement load. Building deformation due to differences in settlement over the extent of a building may cause several types of damage.

The most likely deformation modes are the hogging and sagging mode (see Figure 38).

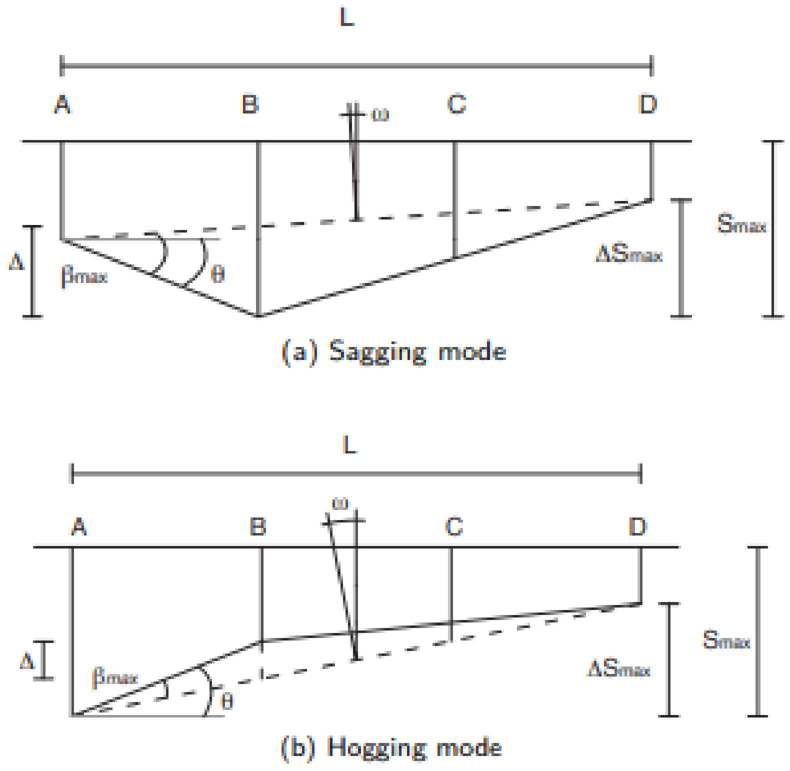

Figure 38. Deformation mode due to settlement

The former is characterized by sides of the building with greater slump than the average, while in the latter mode, greater slump is at the centre of the building.

Building deformation can be specified in more detail into several modes, such as shear and bending deformation as well as elongations and shortening (Figure 39).

Generally, a combination of deformation modes occurs simultaneously. When settlement affects the building, tensile strains occur due to bending deformation and diagonal strains due to shear deformation, generally both at the same time.

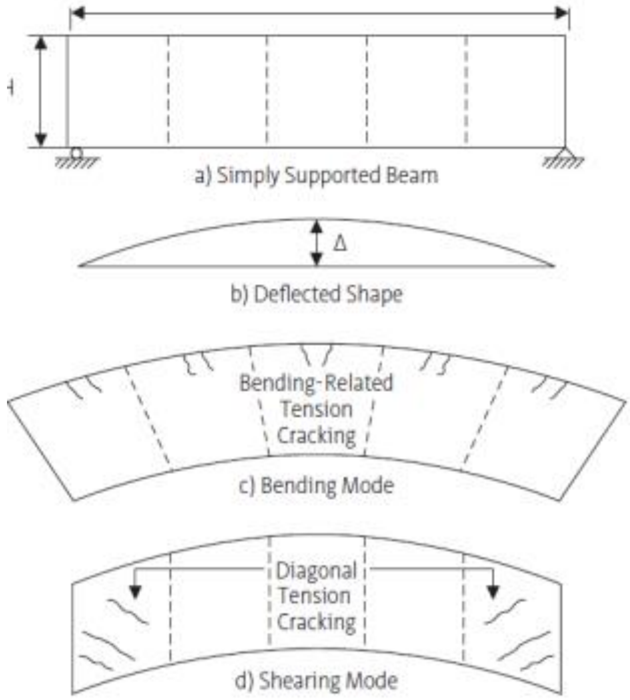

Figure 39. Overview of deformations in buildings and related damage. Boscardin & Cording [48]

2.4.1 As-Built Specimen Geometry

The tuff units used for URM had the same dimensions of those employed for the tested tuff wallets previously described, such as the mortar joints with a thickness of 10 mm.

According to technical product declarations by the mortar manufacturer, the premixed hydraulic mortar was classified as M2.5 (corresponding to mean compressive strength of mortar f_{cm} = 2.5 MPa). Mechanical properties of the constituent mortar system materials were first determined through laboratory tests. During the construction of each URM, mortar prisms (40x40x160mm^3 in size) were prepared and tested under three-point bending according to EN 1015-11 standard [22]. The two parts of each prismatic specimen after flexural failure close to the mid cross section were individually tested under uniaxial compression.

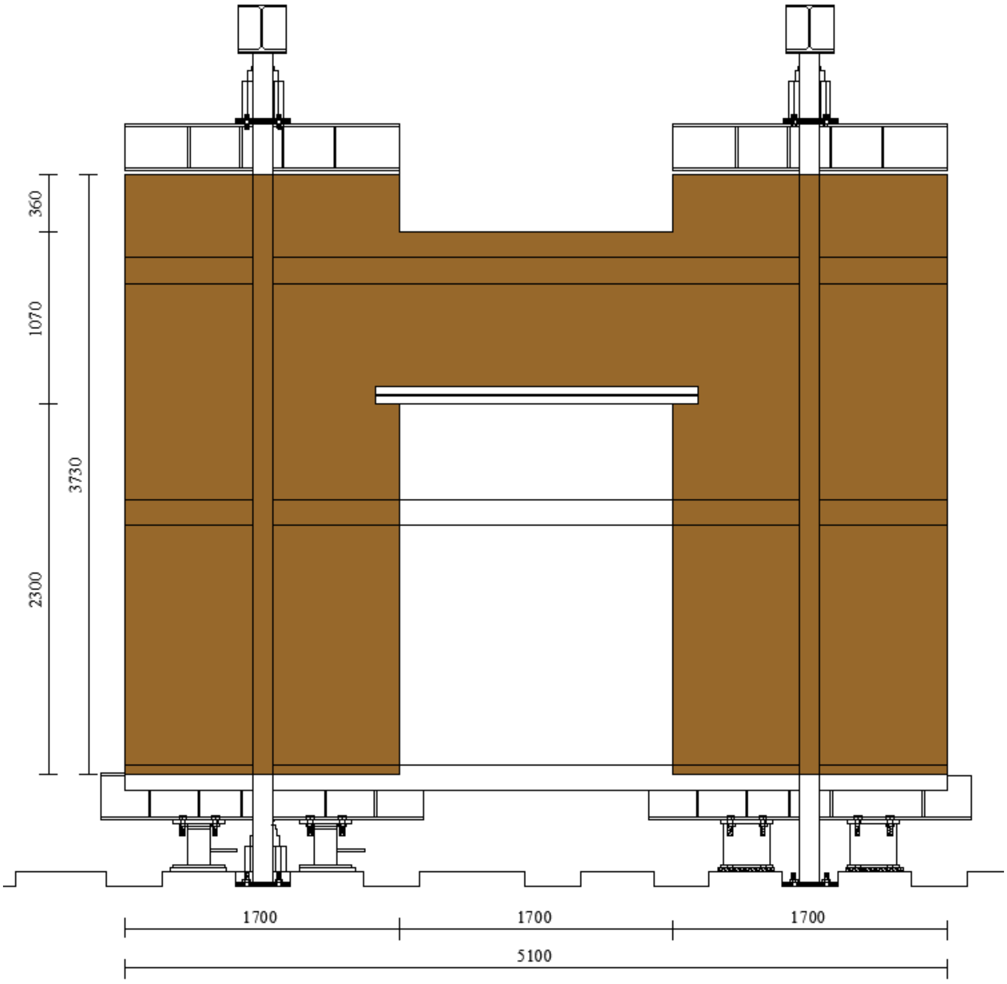

Figure 40. Dimensions of tested URM (in mm)

The wall was globally 5.10 m long, 3.73 m high, and 0.31 m thick, composed by two piers connected by a spandrel panel. Both piers and spandrel panel had a length of 1.70 m, whereas the height of the latter was equal to 1.07 m including the wooden lintel, that has a bond length of 150 mm at both sides of the spandrel (Figure 40). URM can be seen as a representative part of a building type structure, so the presence of the other overlying storyes, is assumed through the transferred load from three masonry layers constructed over the spandrel. The brickwork is arranged in a stretchers bond pattern with all stones laid as stretchers and half-bats at the beginning or at the end of alternate courses (Figure 41).

The fabrication of deteriorated URM was controlled so that *s/t* was equal on average to 20%, such as for wallets tested in diagonal compression.

A joint study on masonry behaviour in degraded conditions was carried out with UR3 Perugia, within the framework of the DETECT-AGING research project. In the SHM framework, the damage modelling strategy within the finite element method FEM plays an important role in the implementation of automatic damage detection algorithms, allowing the development of simplified macro-element models from FEM [18].

The challenge in the DETECT-AGING framework, is to correctly identify when damage detected through SHM measurements is caused by, for example, structural deterioration; and with structural models, to develop numerical analyses to analyse the structural vulnerability for the quantification of structural damage. A configuration of accelerometers was used on the URM deteriorated specimen with eleven devices useful to assess the decay of frequency and modal form (Figure 42). Results of the SHM measurements are not elaborated in this thesis as it is the subject matter of UR3 “Department of Civil and Environmental Engineering, University of Perugia” activity.

2.4.2 Test Setup and Instrumentation

The bearing support system is designed to allow the pier to move along the vertical axis. A reaction system was installed to apply vertical load to the masonry wall. The system consisted of two transverse steel frames located at the centrelines of the masonry piers and allowed to apply vertical load by hydraulic jacks put in contrast with the cap beams of the transverse frames. Rigid steel beams were placed between the jacks and masonry joint to get a uniform distribution of normal stresses simulating gravity loads on the specimen.

Figure 41. Experimental setup of intact URM under settlement load

The piers were supported by I-shaped steel profiles. Beams were connected to the laboratory strong floor bolted to a Ω-shaped steel frame from the fixed piers side. On the other side of the wall the beam was movable with free displacements along the horizontal and vertical directions,. This steel support is composed by two pieces, which can be compared to a “nut” and a “screw”: the nut consists of a steel plate, bolted to the beam supporting the piers, with a threaded hollow tube which is screwed onto the threaded solid tube welded to the other side. The two parts were spaced out during the URM construction phase and screwed with an external tube. The rotation of the parts allows to simulate in this way the settlement at the foot of the masonry piers.

Polytetrafluoroethylene (PTFE) layers were placed between the steel plate and the laboratory strong floor to prevent any frictional resisting force at the interface.

Three steel beams were bolted to the columns of the transverse frames at both sides of the URM to prevent potential out-of-plane failure modes.

In addition, a steel L-system, in turn bolted to the laboratory floor slab, was installed near to the beam moveable support, as guides to allow pier moving along the vertical axis and to prevent torsional effect of the steel beam. Also in this case, PTFE layers were placed between the steel L-system and the other steel beam.

Deformations were measured by inductive linear variable differential transformers (LVDTs) and string potentiometers as follows: LVDTs were placed at the end cross sections of the spandrel and pier panels at each side to obtain information about flexural deformations. Potentiometers were mounted along the diagonals of spandrel and joint panels. The progression of the test was controlled by the maximum displacement applied to the moveable beam and measured through two LVDTs placed on opposite sides.

For intact configuration, load variation due to settlement was read by the strain gauges applied to the steel supports at the base of the fixed piers side. The strain gauge is a sensor in which the elastic deformation of the steel supports is reflected in the variation of the element's load. The collapse of the masonry wall is induced by the progressive settlement of the movable pier and the collapse load is evaluated through the base reaction at failure. The progressive load change is measured by the strain gauge's variation which corresponds to the increasing support reaction, until the failure, related to vertical displacement at the bottom of the pier (frontal side of Figure 41).

So, according to the adopted assumptions, wall failure is attained as the decreasing support reaction becomes stable or resumes its initial value so that increments in displacement do not produce load change at the fixed support.

Figure 42. Experimental setup of deteriorated URM under settlement load

For the deteriorated wall, the set-up configuration was the same as intact one. The settlement loading was applied through a servocontrolled hydraulic actuator (with cell load capacity of 100 kN and stroke ±50 mm) placed between the steel beam and the laboratory strong floor. This cell was employed to get real-time measurements of the vertical force applied to the pier (Figure 42).

The tests on the masonry wall consisted of two stages for both configuration (*i.e.,* intact and deteriorated): in the first stage, vertical forces of 200 kN were applied to the piers by the hydraulic jacks to simulate gravity loads; in the second, the wall was subjected to in-plane settlement loading through a steel support or, servocontrolled hydraulic actuator whereas the vertical forces on the piers were kept constant.

The settlement was applied in 5 steps of 3 mm (corresponding to nut thread pitch) reaching a final displacement of 15 mm (corresponding to a spandrel drift ratio, θ, of approximately 0.9%) for intact configuration and while for the deteriorated one, the actuator was applied to increase displacements at a constant rate of 0.01 mm/s up to a displacement at the actuator of 35 mm (corresponding to a spandrel drift ratio, θ, of approximately 2%). Load and deformation measurements were stopped at 3,9,15mm to allow the data acquisition and identification from the accelerometers.

2.4.3 Damage Patterns and analysis of the Experimental Force-Displacement Curves

Both intact and deteriorated URM show a crack pattern typical of a spandrel panel subjected to bending moment, with a vertical crack arising at the top near the interface zone between spandrel section and joint panel located on fixed pier.

When cracks are produced by foundation structural distortion they tend to be concentrated in areas where maximum structural distortion occurs, or at the weak points in the structure.

Figure 43 and Figure 44 show the damage pattern observed after the settlement test on the intact URM, with vertical cracks owing to flexure occurred at the end sections of the spandrel panel. The initial cracks grow and propagate on each side of the spandrel panel. It is noted that cracks are small at one end and wider at the other, often seen both on the inside and outside the building.

Figure 43. Crack pattern at 15mm of settlement applied to intact URM, frontal side

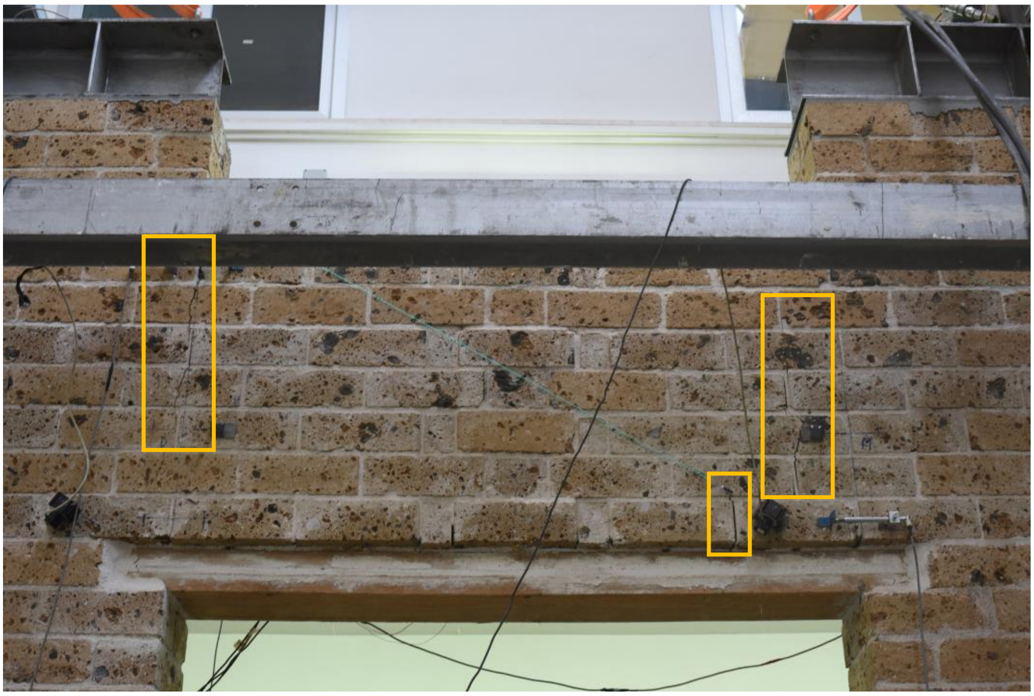

Figure 44. Crack pattern at 15mm of settlement applied to intact URM, back side

For intact URM, vertical loading induced damage especially to the spandrel panel without involving the piers. The curve shows a first change in slope after 1,5 mm of settlement, at the onset of the first hairline cracks, located at the right corners of the openings. Visible cracks to the naked eye were recorded at very advanced displacements

The exact location of the cracks is strongly dependent on the position of the opening, which induce stress localization at their corners and define the weakest cross sections.

The deteriorated URM spandrel panel, on each side, was painted in white to facilitate the damage monitoring. Although flexural failure of the spandrel was still detected also at greater displacement levels, compared to intact test, fracture propagation in the spandrel panel diverged from the pattern observed during the previous test, resulting in vertical cracking spreading toward the moveable pier (Figure 45,Figure 46). Nevertheless, splitting of the masonry wasn't detected in the pier section cross. The crack pattern is characterised by initial hairline cracks evolving in macro cracks. For increasing values of the vertical displacement, the rotation of the left part increases, leading to a complete separation with cracks on both sides.

Wooden lintel supported the masonry above and constrained the spandrel panel in transmitting the applied load between the piers

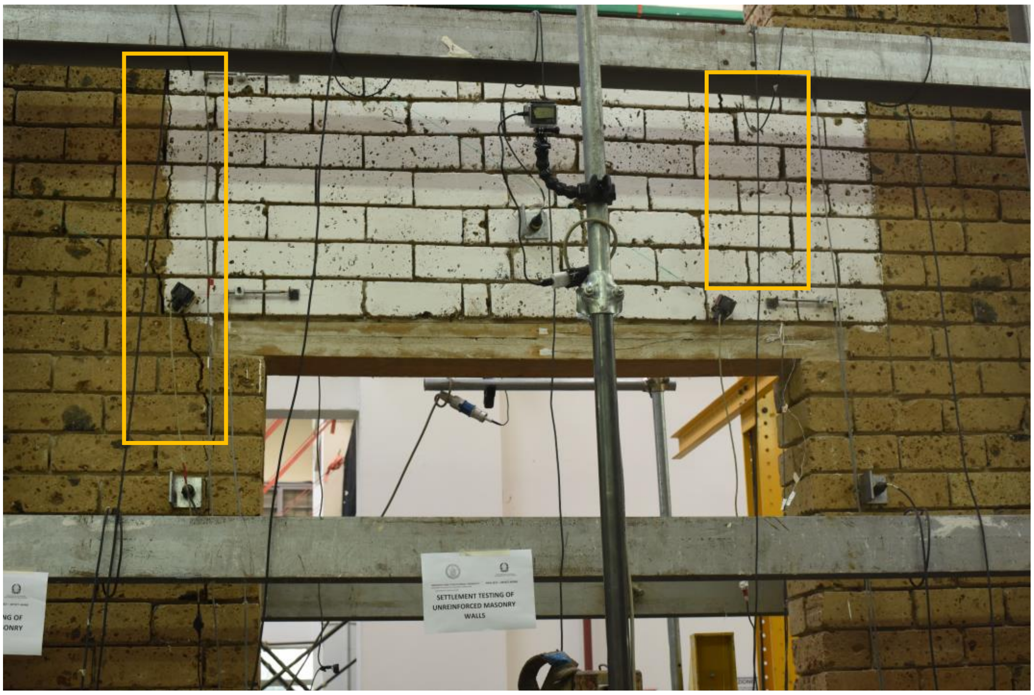

Figure 45. Crack pattern at 35mm of settlement applied to deteriorated URM, frontal side

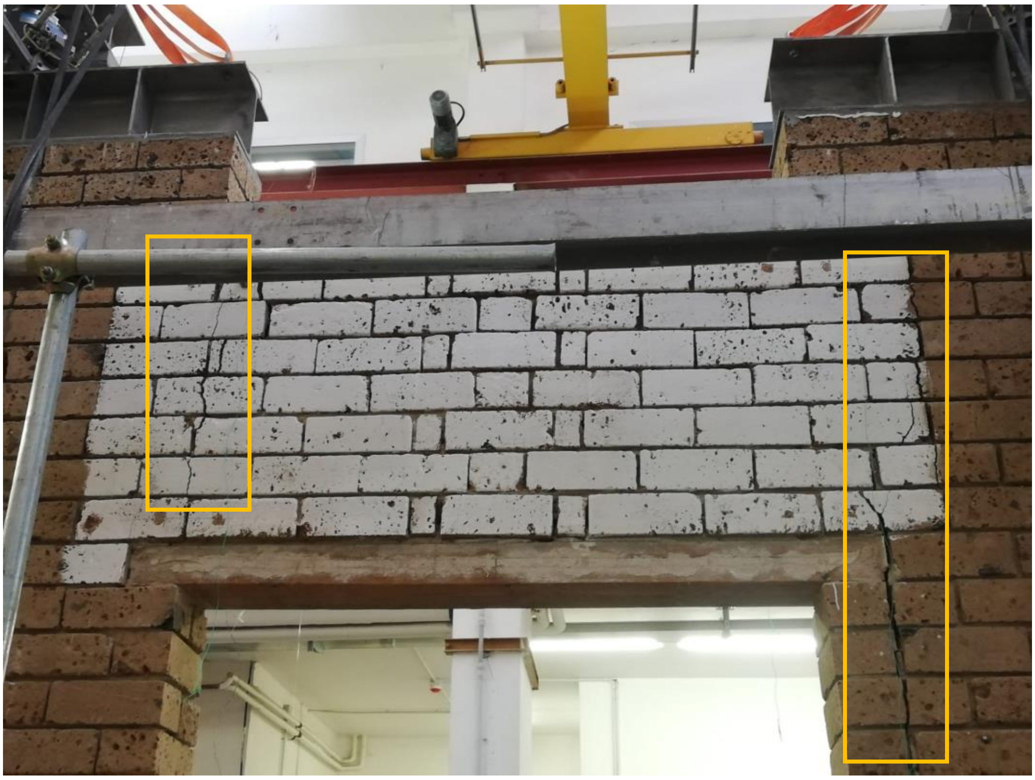

Figure 46. Crack pattern at 35mm of settlement applied to deteriorated URM, back side

Crack pattern development for deteriorated specimen, characterized by macro cracks, is linked to the wooden lintel sliding. The exceedance of the adhesion capacity in the interface zone with the tuff is a direct consequence of the spandrel resistant mechanism.

Spandrel shear V_{sp}, from a global equilibrium, is considered equal to the axial force N_{pr} acting on the pier subjected to settlement, given by the gravitational force and the load arising as a result of the imposed settlement δs, minus the contribution of the initial load. Despite its greater deformability, the deteriorated URM, after the peak load is reached, (Figure 47), shows a residual shear in the spandrel because of a residual resistance mechanism that involves the formation of a diagonal compression strut in the spandrel panel.

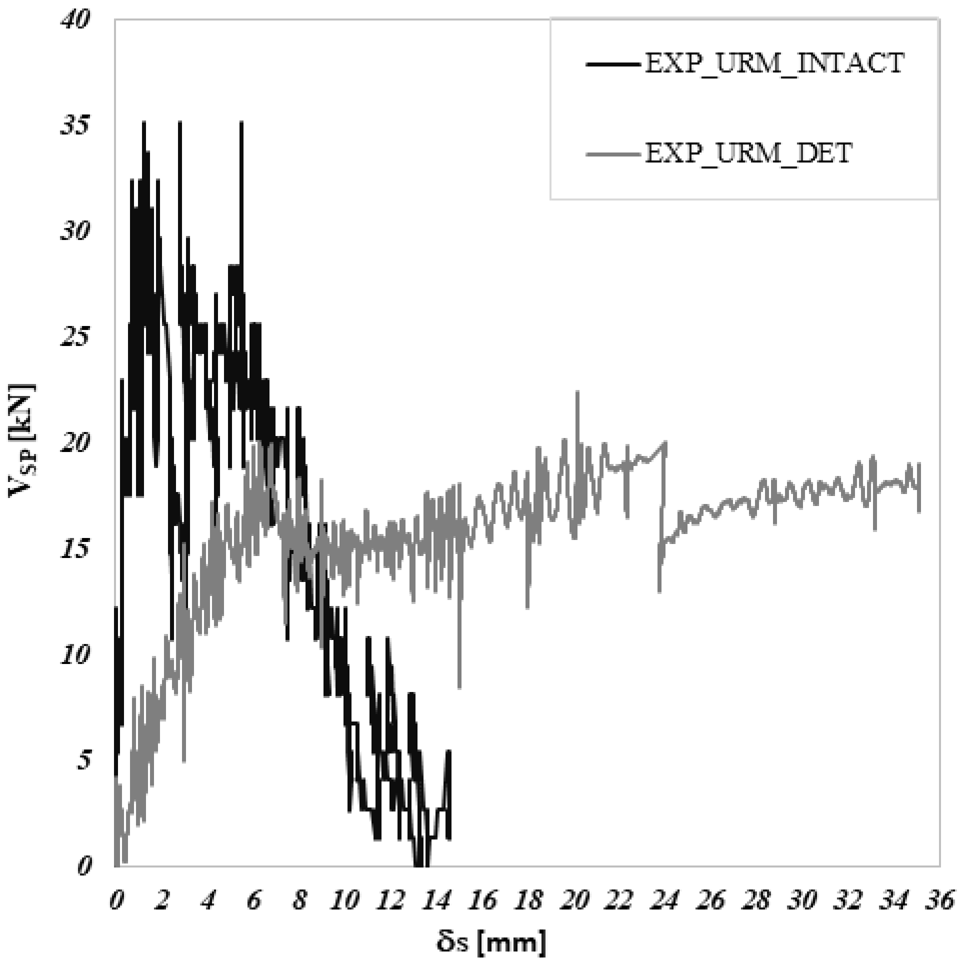

Figure 47.Spandrel shear versus differential displacement for intact and deteriorated URM

Even though cracking occurred in the spandrel at an advanced state, also affecting the moveable pier, the compression diagonal strut allowed spandrel to continuously transfer load. Conversely, in the intact URM condition, following the cracking, the spandrel is no longer able to transfer load, behaving like a horizontal pendulum. As a result, the two piers behave as separate cantilevers, bringing gravitational load only.

From LVDT displacement values on either sides of the beam supporting the moveable pier, differences can be seen in the two tests (Figure 48,Figure 49).

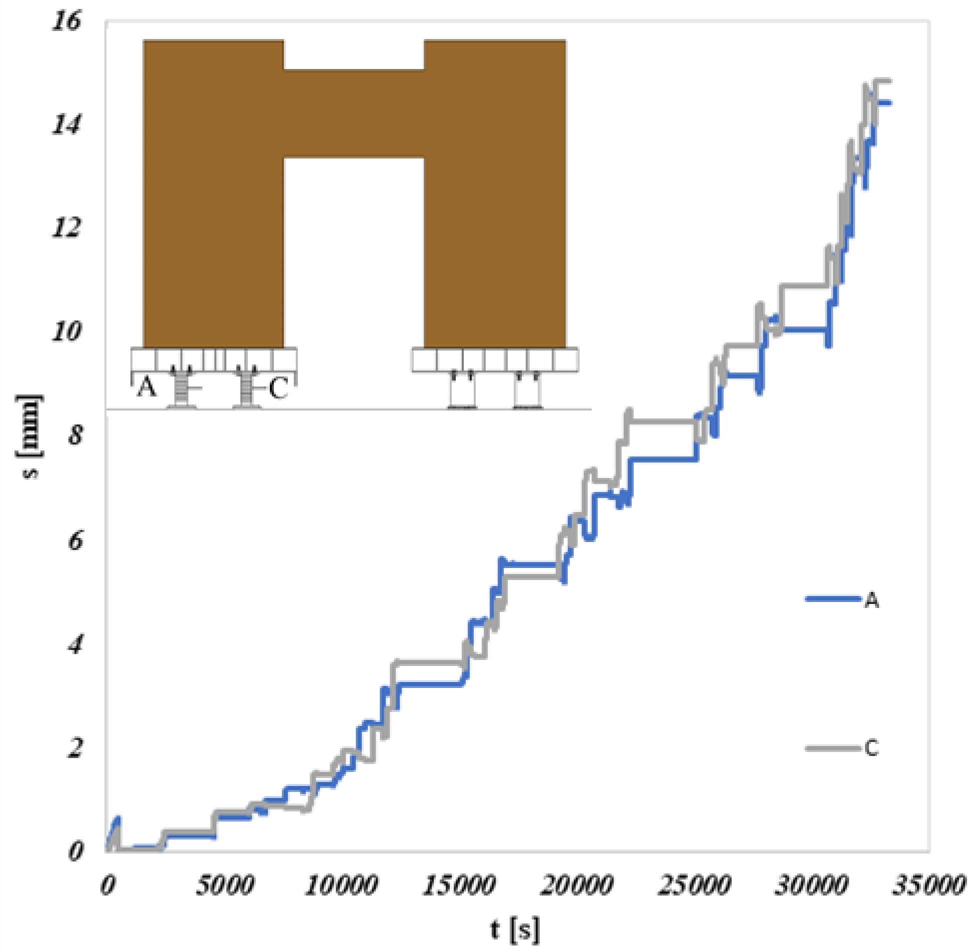

Figure 48. Displacement trend recorded by LVDTs at the sides of the movable beam for intact URM

In the intact URM, beam displacement is uniform, *i.e*. the same value is recorded by the LVDT, unlike the deteriorated URM. In the former, at the beginning, the differences in displacement values are negligible, and become noticeable only at higher displacements when the peak force is already reached resulting in sagging deformation mode. In the deteriorated URM, the greater displacements of the outside compared to the inside resulted in hogging deformation mode.

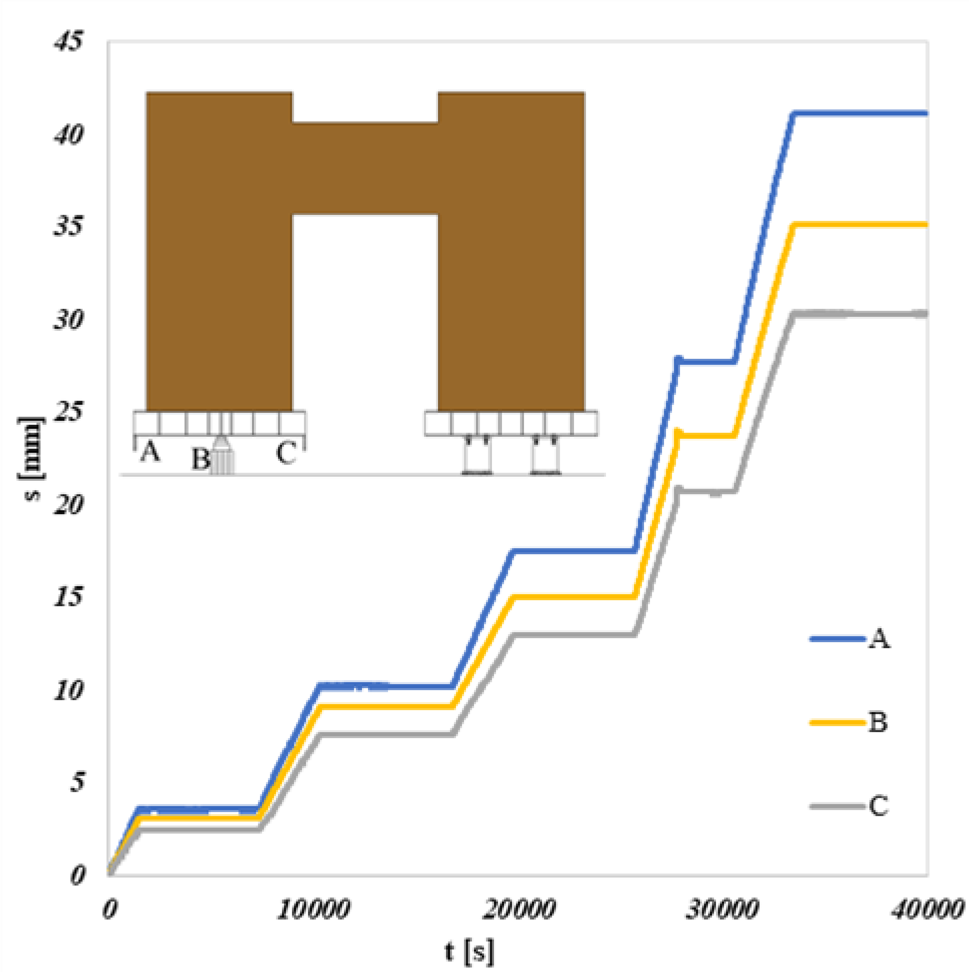

Figure 49. Displacement trend recorded by LVDTs at the sides of the movable beam for deteriorated URM

This deformation mode could be related to the unfully filled mortar joints, and as a result of the gravitational load this triggered a higher interlocking on the outer side, due to increased joint deformability. This defined a preferential pathway for the failure. Cracks array confirm the mechanical interlocking occurring at the crack interface during the in-plane deformation of the spandrel. The crack state impacted the response of deteriorated URM, since cracks supplied additional strength and deformation capacity to resist loads by means of interlocking engaged by the array of edge-notched cracks (cohesive cracks) favoured by the larger initial deformability of the mortar joints, which developed into a diagonal compression strut.

Although the geometric degradation implies a reduction of the peak load strength, URM exhibits a not negligible residual strength, that also for other actions, *i.e.* earthquakes, can give a benefit for the seismic evaluation.

In the next chapter (Section 3) displacement and mechanical parameters are introduced, useful for understanding in detail the different behaviour exhibited by the two URM configurations.

2.5 Out-of-plane testing of unreinforced masonry wall

This part of the thesis presents the results of a laboratory test carried out on a full-scale unreinforced masonry wall (URM) with an opening subjected to a progressive damage induced by increasing out-of-plane loading conditions. As previously described for other tests, two configurations have been adopted, *i.e.,* intact and deteriorated to pay attention on aging effect. The main objective of this study is to improve the understanding of failure mechanisms occurring when URM walls are subjected to horizontal forces by analysing and discussing failure modes and their out-of-plane capacity and make available accurate and reliable experimental data to be used as validation of numerical models.

Existing URM buildings tend to be more vulnerable than new buildings, not only because they have been designed to little or no seismic loading requirements, but also because the façade may separate from transverse walls and overturn or fail by bending, not being firmly connected to horizontal structures [49].

The vulnerability of masonry walls under out-of-plane loads is one of the main causes of earthquake induced damage, but not only. In general, horizontal forces generated from roofs, arches, and vaults not counteracted by appropriate structural elements can lead to out-of-plane mechanisms similar to the effects of seismic actions. Therefore, flexural collapse may occur in slender masonry panels and/or panels restrained far apart from orthogonal walls.

The strength assessment of existing URM structures is important due to the large number of buildings designed without due consideration to wind and earthquake loading.

For URM walls subjected to out-of-plane loading, several key factors, must be considered: support conditions, masonry material, random variability of masonry; and the cause of out-of-plane loading.

According to the support condition, if the upper and lower edges of the wall are restrained between rigid supports, such as walls built inside a reinforced concrete frame, then significant in-plane arching can develop resulting in increased load capacity. (Figure 50.i). A wall fixed only on vertical sides and with reduced restraint along its base will undergo one-way horizontal bending (Figure 50.ii). For all other factors being equal, these walls generally show greater capacities than vertically spanning walls. For walls with at least two adjacent supported sides, two-way bending will occur (Figure 50.iii), further increasing the capacity.

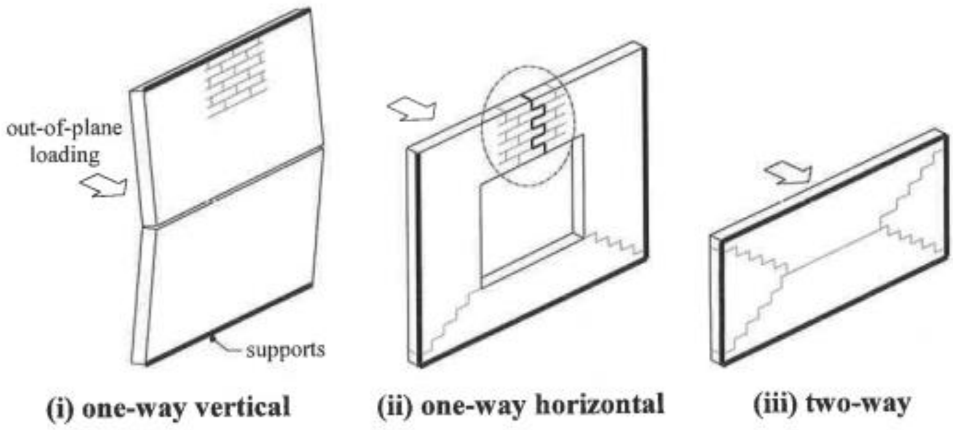

Figure 50. Out of plane bending mechanism [50]

Masonry is a composite material consisting of units and mortar, it is markedly non-homogeneous and anisotropic, showing distinct directional properties due to the planes of weakness created by the mortar joints so this influences also the different bending mechanisms. In addition, the factors affecting variability include inherent variation in materials, variation in manufacturing processes, unit and mortar properties (surface conditions, porosity, moisture content and suction rate).

For the cause of out-of-plane loading, for seismic loading, out-of-plane bending arises as a result of the inertia forces caused by the transverse horizontal component of the ground motion [51].

For multi-storey buildings, the inertial forces are higher for upper storeys, that are the weak elements in the seismic load path of URM for the inadequate out-of-plane bending strength, because of a combination of higher out-of-plane loading and a lower level of axial loading, which produces stabilising moments and acts to strengthen the walls [52].

However, it is not excessively conservative to assume that the out-of-plane load, which may be directly related to ground acceleration, is uniform over the storey heigh.

Walls subjected to out-of-plane loading are known as “flexural walls” because the flexure is the predominant action. The out-of-plane behaviour is considerably more complex than in-plane behaviour of walls, because in the former the tensile strength in horizontal flexure can be several times greater than the strength in vertical flexure [53].

This difference can occur because the vertical flexure depends basically on the tensile bond strength of the unit mortar interface of the bed joints, whereas the horizontal flexure depends on the friction resistance of the bed joints and on the tensile bond strength at vertical joint interfaces.

In unreinforced masonry walls supported on four sides, the vertical bending moment at mid-height of the wall induces tensile stresses perpendicular to the bed joints. When these stresses are higher than the tensile strength, a horizontal crack initiates and the behaviour of the cracked wall depends upon the orthogonal flexural strength of the masonry. The crack propagates along the bed joints and the mechanism is immediately formed (Figure 50.iii). On the contrary, when the horizontal flexural strength is greater than its vertical strength, a crack propagates along the bed joints under constant load and a stable state is reached with two sub-panels, each simply supported along three sides and free along the cracked bed joint, with a final diagonal crack.

In the experimental carried out activity, URM simulates perimeter building walls where the progressive release of steel tying, or the punctual load of arches, pushes URM to an out-of-plane load, resulting in bending mechanism. Progressive release of steel tying can be seen also as a degradation effect of previous (historical) retrofit interventions.

2.5.1 As Built Specimen Geometry

The URM has the same geometry of the wall subjected to settlement load, hence more details can be found in Sect 2.4.1. The wall was globally 5.10 m long, 3.73 m high, and 0.31 m thick, composed by two piers connected by a spandrel over an opening. Both piers and spandrel panel had a length of 1.70 m, spandrel height equal to 1.07 m .(Figure 51). The same professional mason built them, in order to prevent differences in hand work and mortar workability among different specimens. In this way the same geometric URM was tested under in-plane and out-plane loads (even if it was built in different days).

The tuff units used for URM had the same dimensions of those employed for the tested tuff wallets previously described, such as the mortar joints with a thickness of 10 mm.

According to technical product declarations by the mortar manufacturer, the premixed hydraulic mortar was classified as M2.5 (corresponding to mean compressive strength of mortar f_{cm} = 2.80 MPa). Mechanical properties of the constituent mortar system materials were first determined through laboratory tests on mortar prisms (40x40x160mm^3 in size). Prisms were tested under three-point bending according to EN 1015-11 standard with the two parts of each prismatic specimen after flexural failure tested under uniaxial compression.

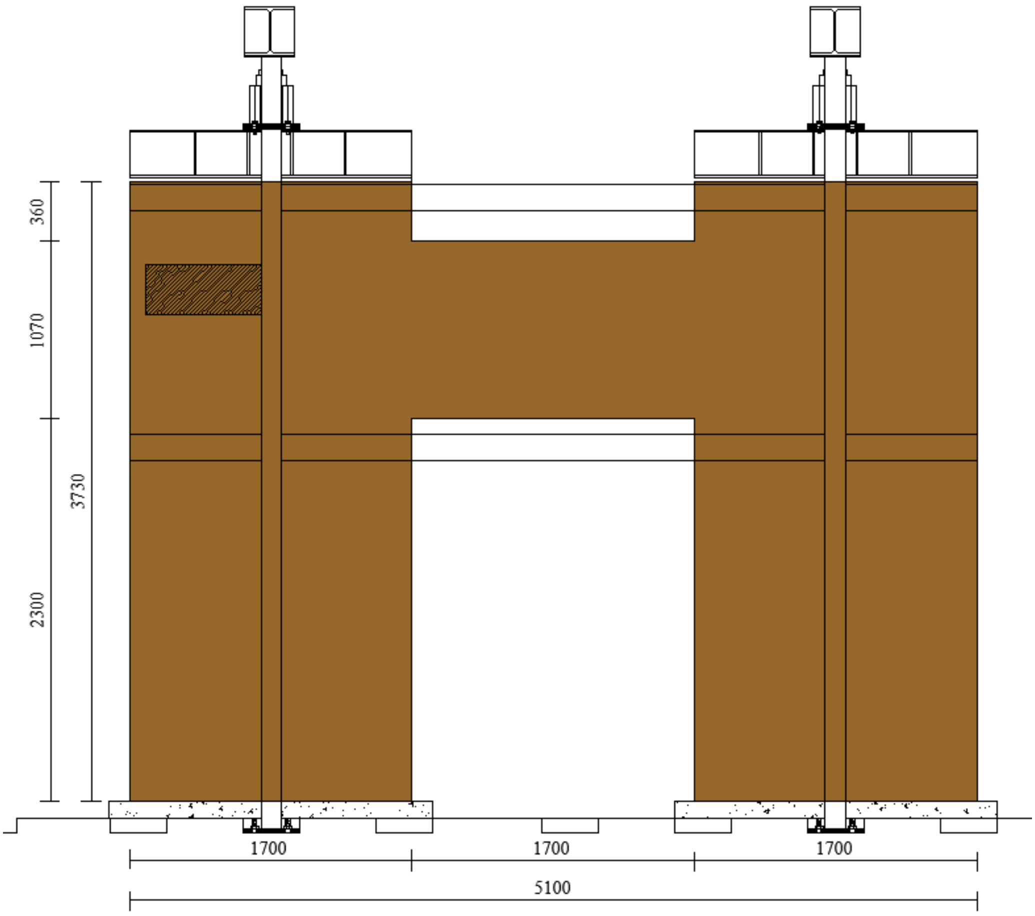

Figure 51. Dimensions of tested URM (in mm)

The fabrication of deteriorated URM was controlled so that *s/t* was equal on average to 20%, such as for wallets tested in diagonal compression.

A joint study on masonry behaviour in degraded conditions was carried out with UR3 Perugia, within the framework of the DETECT-AGING research project.

The challenge is to correctly identify damage detected through SHM measurements and correlate the development of damage on the wall to decay of its natural frequencies and mode shapes. This is significant because it can be identified even before damage may have occurred in a building being visible to the naked eye, in order to define an alarm threshold.

The URM specimen was instrumented with a dense network of uniaxial seismic accelerometers mounted on supporting steel plates anchored to the tuff stones, useful to assess the decay of frequency and modal form

(Figure 53). Results of the SHM measurements are not elaborated in this thesis as it is the subject matter of UR3 “Department of Civil and Environmental Engineering, University of Perugia” activity.

2.5.2 Test Setup and Instrumentation

Since the evaluation of the out-of-plane behaviour of strengthened walls requires two different types of actions combined simultaneously, applied along vertical and horizontal directions, a designed set-up was used, capable of applying horizontal forces to the wall together with a constant vertical axial stress.

Test setup is consistent with that similar previously described for settlement load, but with some differences. The reaction system consisted of two transverse steel frames located at the centrelines of the masonry piers and allowed to apply vertical load by hydraulic jacks in contrast with the cap beams of the transverse frames, reused from settlement test. A uniform distribution of normal stresses simulating gravity loads on the specimen was ensured by rigid steel beams placed between the jacks and masonry joint panels.

To rigidly connect the specimen to the laboratory strong floor, RC beams with dimensions 2000 x 310 x 200 mm^3 were built below the piers. The lateral loading was applied through a horizontal servocontrolled hydraulic actuator (maximum capacity of 500 kN and stroke of 250 mm) bolted to a non prismatic reaction wall fixed to the laboratory slab through four steel bars, each pretensioned at 400 kN. The horizontal actuator was anchored to the masonry wall by means of two perforated steel plates by means of two steel bars aimed at applying force at the opposite end of the specimen to push the structure and to pull back the specimen to its initial position at the end of the test. A load cell with capacity of 100 kN was positioned between the central part of the horizontal actuator and its rigid end plate to get real-time measurements of the actual horizontal force applied to the URM (Figure 52).

Polytetrafluoroethylene (PTFE) layers were placed between the hydraulic jack and the beam of the transverse frames to prevent any frictional resisting force at the interface and to ensure that the hydraulic vertical jacks followed the displacement induced by the horizontal actuator.

Two steel beams were bolted to the columns of the transverse frames at both sides of the URM to prevent potential brittle collapses. In addition, on the opposite side to the actuator, steel ties in turn bolted to the laboratory floor slab were placed over the two columns of the steel frame not to impair the test results, but only to act as safety bracing frame (see Figure 53).

The tests on the masonry wall consisted of two stages for both configurations (*i.e.,* intact and deteriorated): in the first stage, vertical forces of 400 kN were applied to the piers by the hydraulic jacks to simulate gravity loads. The vertical compressive force N of 400 kN approximately corresponds to a dimensionless axial force on the piers equal to $\eta = 0{,}28$, being obtained from

$$\eta = \frac{N}{Bsf_c} \tag{7}$$

In which B,s are the length and thickness of the piers, respectively and f_c the compressive strength of masonry.

The value of the compressive force, chosen for the tests, is compatible with the condition in which a wall could be because of the service permanent and accidental weights.

In the second stage, the wall was subjected to out-plane displacements systematically imposed through the servocontrolled hydraulic actuator whereas the vertical forces on the piers were kept constant.

Two initial displacement cycles (load/unload) between 0 and 3 mm were applied on the specimen to reach good contrast between wall and actuator. Then the lateral loading test was carried out by applying monotonically increasing displacements.

Figure 52. Experimental setup of intact URM under out-plane load, frontal side

Deformations were measured by inductive linear variable differential transformers (LVDTs) and string potentiometers as follows: LVDTs were placed at the end cross sections of the spandrel and pier panels at each side to obtain information about flexural deformations. Potentiometers were mounted to control the maximum out plane displacement of the piers: two for the loaded pier and one for the fixed pier

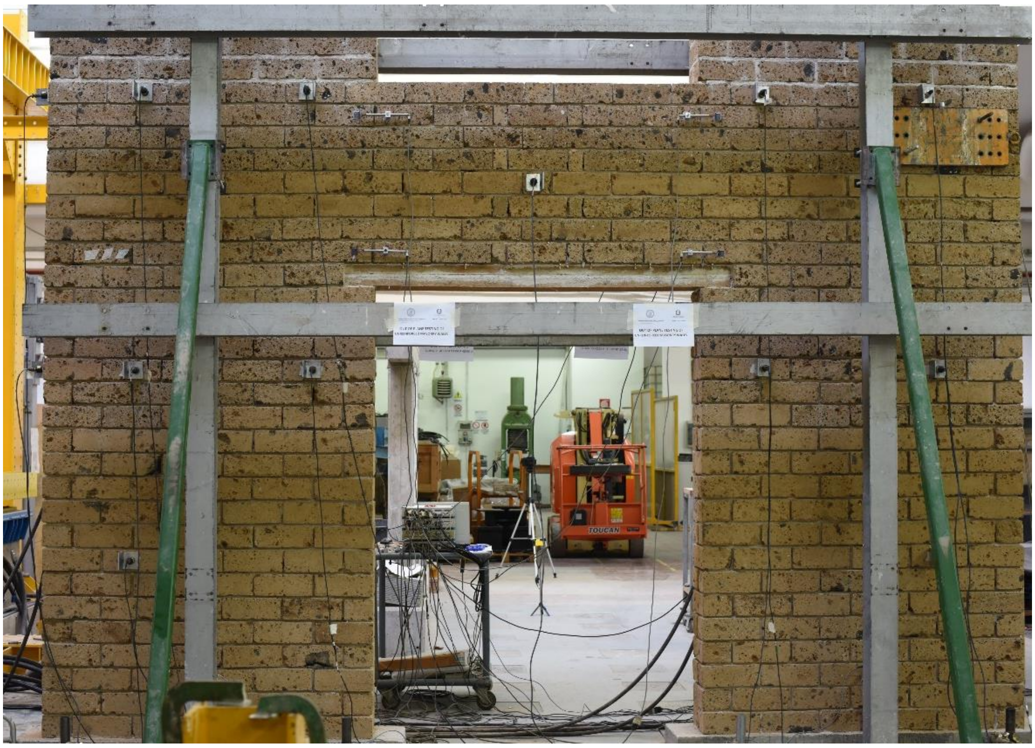

Figure 53. Experimental setup of deteriorated URM under out of plane load, back side

For the deteriorated wall, the set-up configuration was the same as the intact one The lateral force at the actuator was applied to increase displacements at a constant rate of 0,05 mm/s. up to a displacement reading at the actuator of 128,85 mm (corresponding to a spandrel -horizontal- drift ratio, θ, of approximately 7%) even if the load drop was not very significant, the test was stopped due to the significant drift. For the deteriorated wall, the actuator was moved up to a displacement reading at the actuator of 94,30 mm (corresponding to a spandrel -horizontal- drift ratio, θ, of approximately 5.5%), obtained for a lateral force drop higher than 45%. Peak force was achieved at displacement of 91.50 mm and 55.45, respectively for intact and deteriorated URM corresponding to a spandrel drift ratio, θ, of approximately 5.4% and 3.3%). However, these high values of drift were obtained for a mid-high axial load as reported later in Sect 3.3.

For deteriorated URM equipped with a dense network of uniaxial seismic accelerometers, load and deformation measurements were stopped at 3,9,18,27,36,58 mm to perform Ambient Vibration Tests (AVTs), by data acquisition from the sensors.

2.5.3 Damage Patterns and analysis of the Experimental Force-Displacement

The damage patterns observed at the end of the out-of-plane tests for the two URM configurations are shown from Figure 54 toFigure 67 with a final cracking pattern showing a vertical crack from the top towards the bottom near the interface zone between spandrel section and joint panel, characteristic of the out-of-plane bending failure mode. with some differences for the two configurations. Diagonal stepped cracks had affected the loaded pier passing through the whole thickness, showing the formation of a clear overturning mechanism for intact configuration also completely enveloping the spandrel panel (Figure 54,Figure 55,Figure 61) unlike the deteriorated one. For the latter, hairline cracks located at mid-height of loaded pier, visible after a careful inspection, were recorded at very advanced displacements only on frontal side. The uncompleted development of this crack explained the lack of diagonal crack in the spandrel (Figure 62,Figure 63,Figure 67).

Damage to the spandrel panel after the monotonic test on the URM can be observed in Figure 56, Figure 57 and Figure 62,Figure 63 respectively for the two configurations. For the intact one, spandrel panel presented a first diagonal stepped cracking for a displacement corresponding to about 80 % of the peak load. However, this pattern was found to be only on the frontal side (Figure 60,Figure 61). As the displacement progressed, there was a drop in load that can be attributed reasonably to the splitting phenomenon (Figure 59). When the load increased again, a vertical crack from top towards the bottom at the right of the back side was found at 50.3mm. Also these cracks didn’t pass through the whole thickness. At the onset of peak load, a complete diagonal stepped crack interested the spandrel and loaded pier on both sides. The pier, at the end of test, exhibited a moderate crushing at corners with material ejection, Figure 58.

URM failure was attained as the load became stable, which is recorded with the attainment of the flexural strength on the spandrel section near the pier not directly affected by the out-of-plane displacement, on both sides.

Figure 59 shows a detail of the transverse splitting that started to develop at mid-test. It is expected to be caused by high compression forces acting along the mortar bed joints that induce a significant strength reduction in the masonry capacity.

Figure 54. Crack pattern for intact URM, frontal side

Figure 55. Crack pattern for intact URM, back side

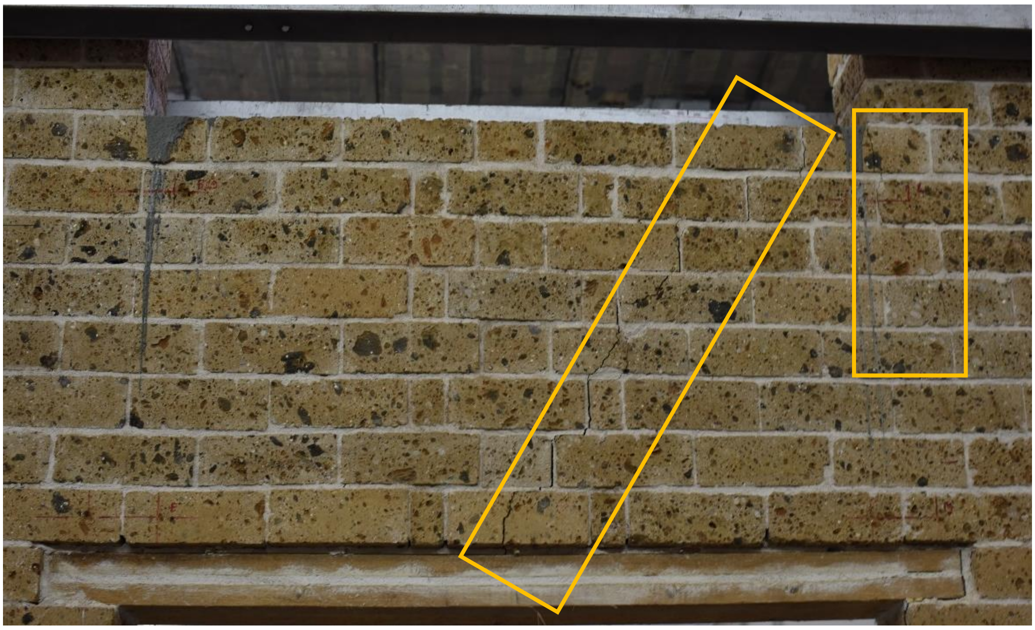

Figure 56. Crack pattern for spandrel, intact URM, frontal side

Figure 57. Crack pattern for spandrel, intact URM, back side

Figure 58. Crack pattern for loaded pier, intact URM, back side

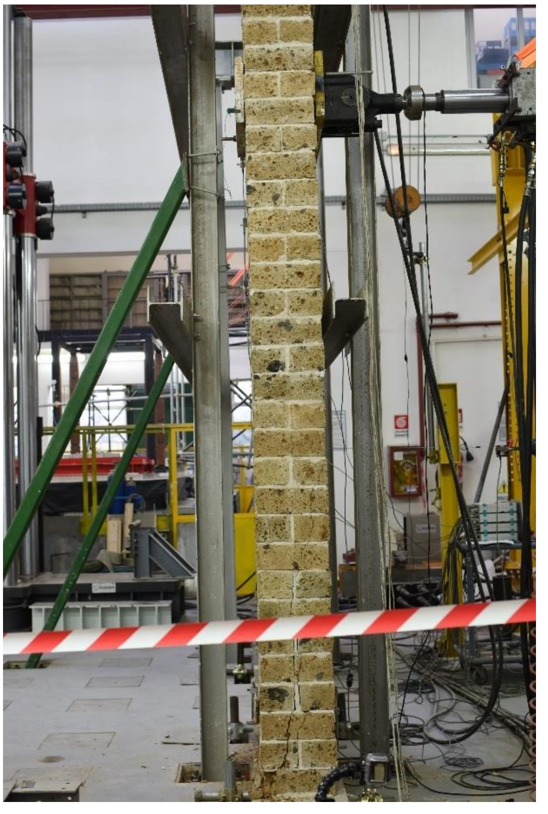

Figure 59. Crack pattern, intact URM, lateral view

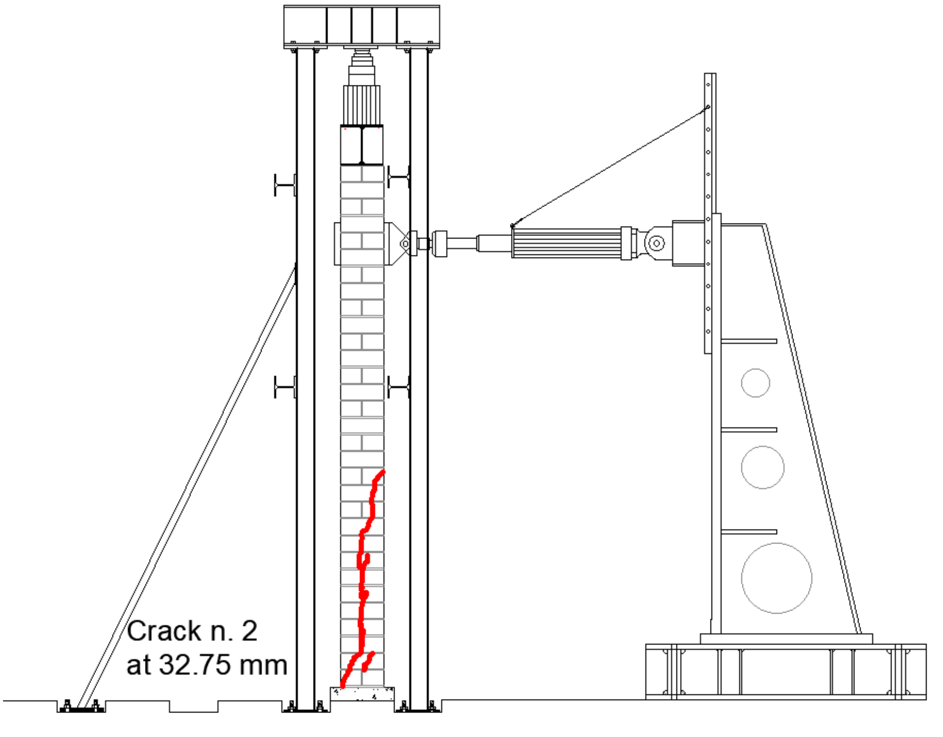

Figure 60. Crack pattern at 32.75mm displacement for intact URM, transversal view

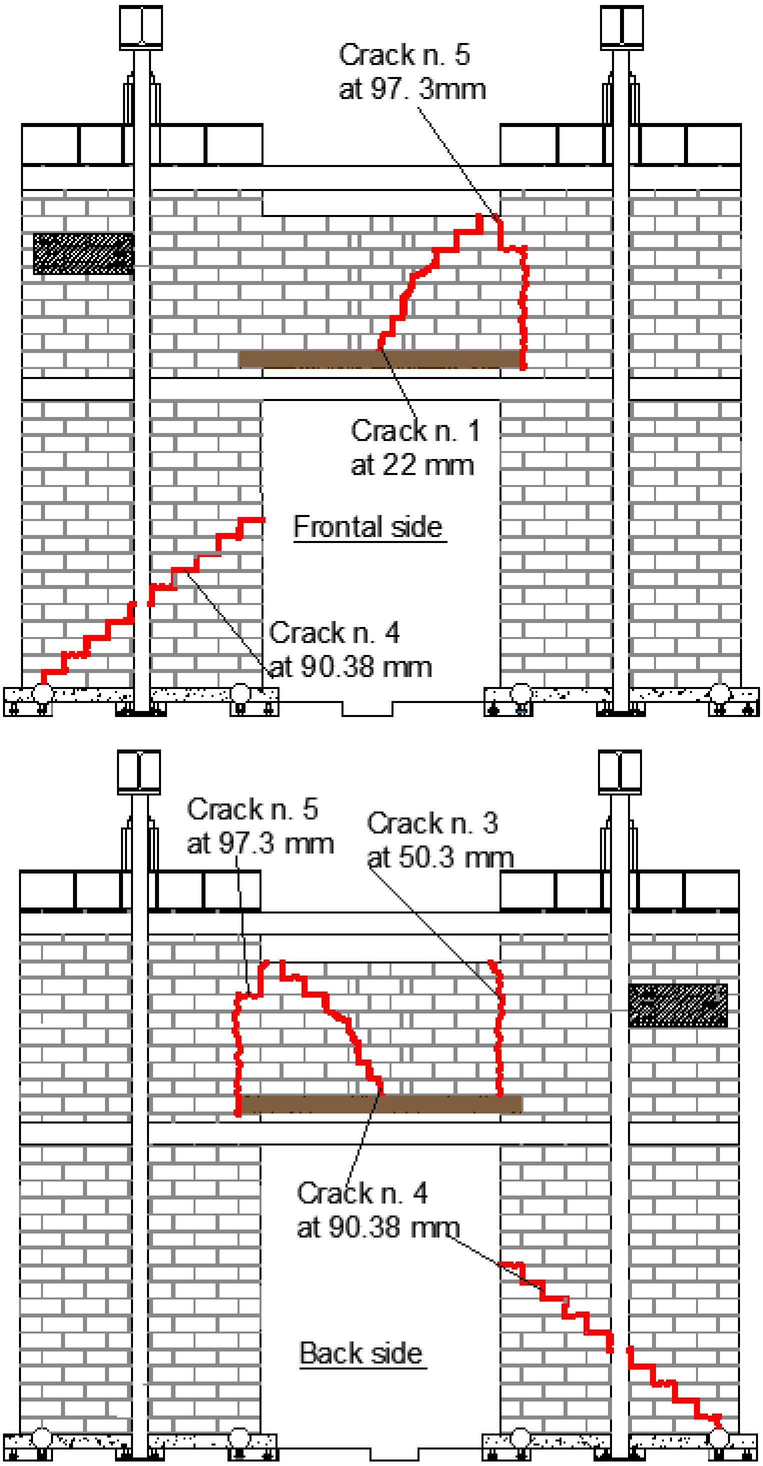

Figure 61. Crack pattern at different displacements for intact URM, frontal and back side

Damage pattern observed after the out of plane test on the deteriorated URM is shown form Figure 63 to Figure 65, with vertical cracks owing to the flexure occurred at the end sections of the spandrel panel. The initial cracks grow and propagate on each side of the spandrel panel, with a final involvement of the loaded pier, as well.

Wooden lintel supported the masonry above and constrained the spandrel panel in transmitting the applied load between the piers. Although the low anchorage length, lintel played an important role in the load transfer between the piers because it forced the masonry of the spandrel panel to absorb and to dissipate input energy.

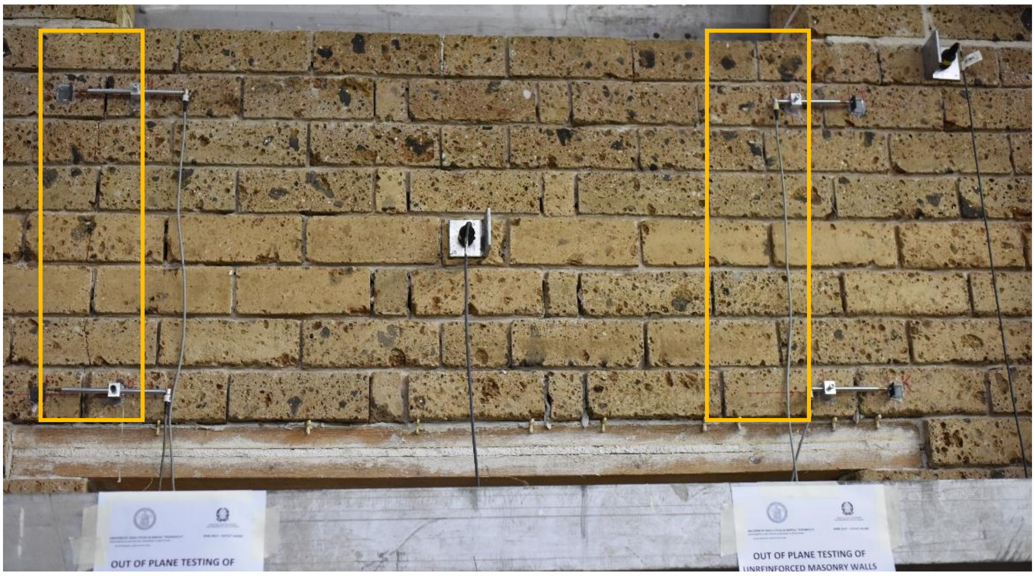

Figure 62. Crack pattern for spandrel, deteriorated URM, frontal side

Figure 63. Crack pattern for spandrel, deteriorated URM, back side

Figure 64. Crack pattern ,deteriorated URM, lateral view

Figure 65. Crack pattern of loaded pier with details, deteriorated URM, frontal side.

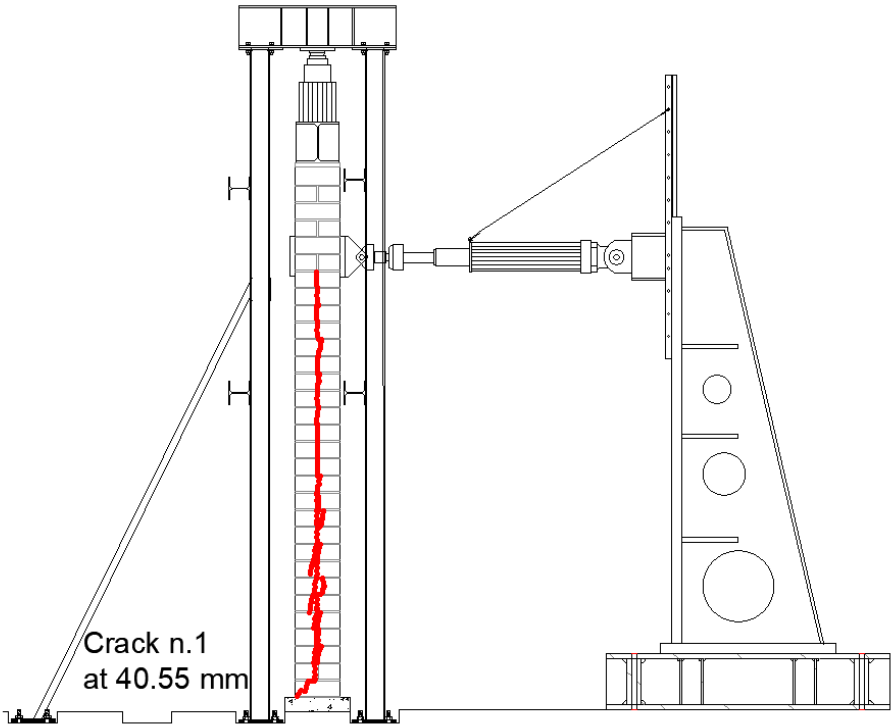

Figure 66. Crack pattern at 40.55mm displacement for deteriorated URM, transversal view

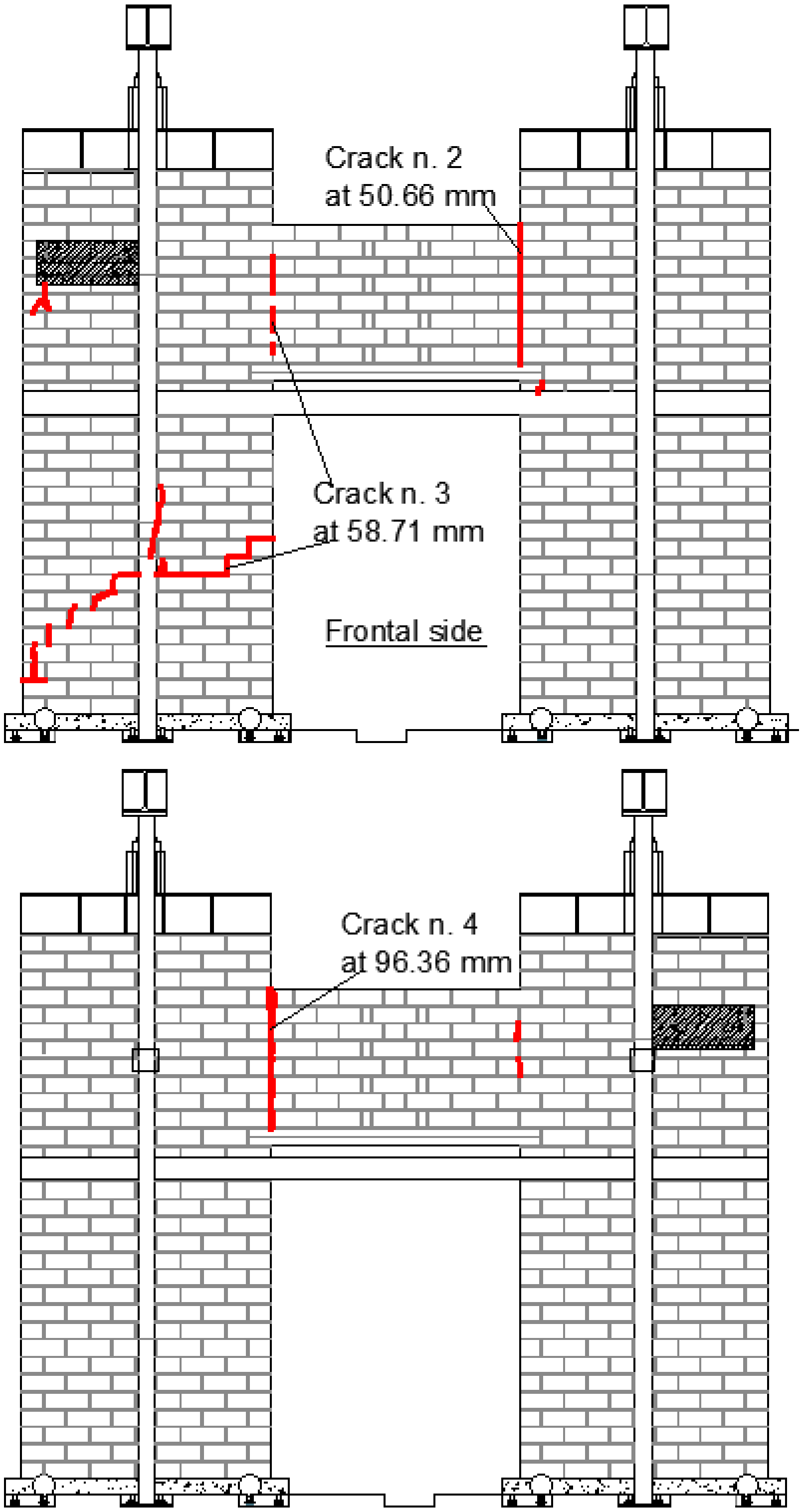

Figure 67. Crack pattern at different displacements for deteriorated URM, frontal and back side

Deteriorated URM shows a comparable behaviour to that of the intact test, in terms of overall capacity (Figure 68).

Deteriorated URM didn’t exhibit any visible crack before a displacement of about 40.55 mm where splitting phenomenon induces the first crack in the thickness of the outer part of the loaded pier (see Figure 66). As the test continued, cracks development concerned more than half the height of the pier, with moderate openings.

New cracks consecutively developed on the URM, affecting mainly the spandrel panel (Figure 62,Figure 63). The peak of the out-of-plane force was reached about at 58 mm of out-of-plane displacement, with the attainment of the flexural strength on the spandrel section. Unlike intact URM, a residual load-bearing capacity is shown, with a complete crack visible on both spandrel sides and hairline cracks located at mid-height of the loaded pier, recorded only on frontal side, Figure 65. Splitting crack development affected the inner side of the loaded pier. At an out-of-plane displacement of 93.36 mm, corresponding to a force equal to 19.90 kN, the test ended.

Deteriorated URM, showed a different behaviour in terms of stiffness at about 3 mm, due to its greater deformability (Figure 68) with a residual shear after the peak lateral load is reached also for significant displacement.

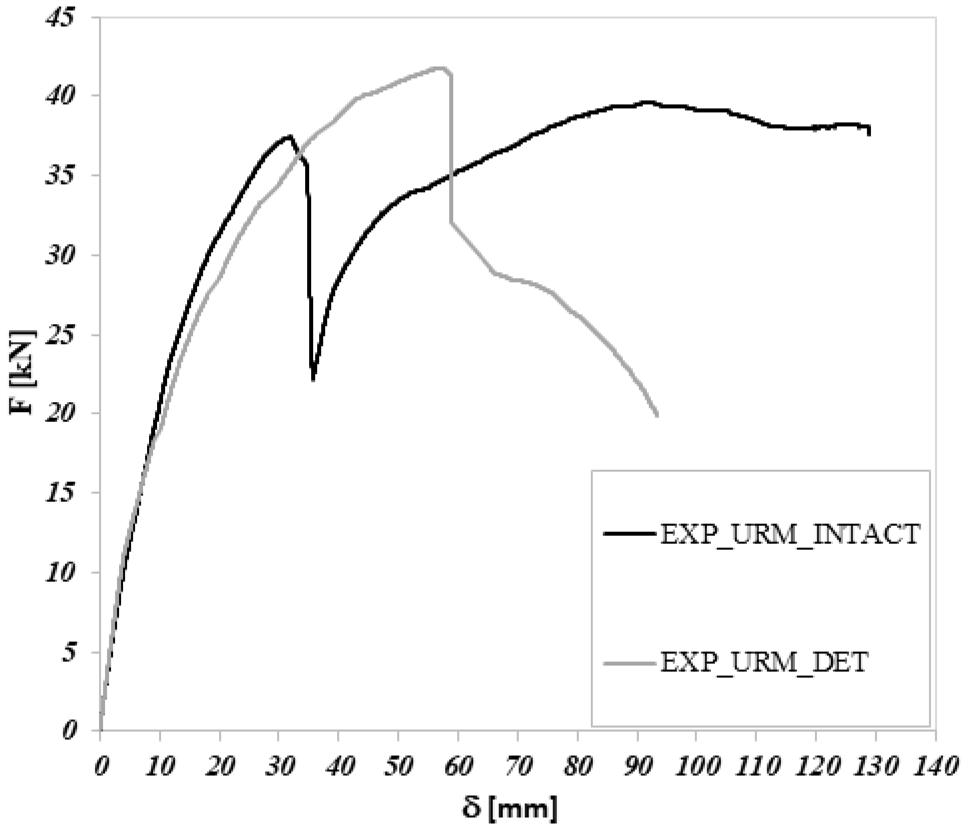

Figure 68.Lateral load versus displacement out-of-plane for intact and deteriorated URM

The geometric degradation impacted the response of deteriorated URM, since it prevented the overturning moment from being triggered, however, the achievement of flexural capacity was such as to achieve collapse.

Splitting had a key role for the two configurations: for the intact one, it initially interrupted the overturning mechanism, resulting in a considerable displacement for which peak out of plane force is reached.

In the second case, splitting didn't allow the overturning mechanism, but masonry spandrel fully achieved flexural strength at the interface, resulting in a good overall capacity of the URM. The latter shows a more brittle behaviour than the former with a higher aggravation for seismic conditions where energy dissipation is crucial to prevent the effect of ground shaking. In the next chapter (Sect. 3.3) a theoretical model is introduced, useful for understanding in detail the different behaviour exhibited by the two URM configurations.

Chapter 3

Experimental-Theoretical Comparison

3.1. Abstract

Ancient masonry buildings are often characterized by high seismic vulnerability, due to low tensile strength. Particularly for the spandrel panel, tensile strength could have a key role for the assessment of buildings. In this background, the numerical analyses provide important information about the structural behaviour of such elements. However, the use of refined numerical FEM models can be always adopted as a support of an analytical modelling approach. Spandrel behaviour, part of URM substructures, was studied for the different load and degradation conditions. Spandrels are usually modelled as piers, but rotated by 90°, and boundary conditions are very different from those of piers, so transposing the experimental results of piers to the spandrels without failure criteria modifications can be inconsistent.

In this background, an analytical modelling approach for capacity assessment is presented.

For the settlement load, building damage criteria based on critical displacement parameters, namely deflection ratio, horizontal strain, and twist, are proposed.

3.2. Settlement test

Building deformation can be specified in more detail into several modes, such as shear and bending deformation as well as elongations and shortening. Definition used in this thesis work are explained in the following. Annex H of Eurocode 7 [54] define the critical displacement parameters , with regard to Figure 69.

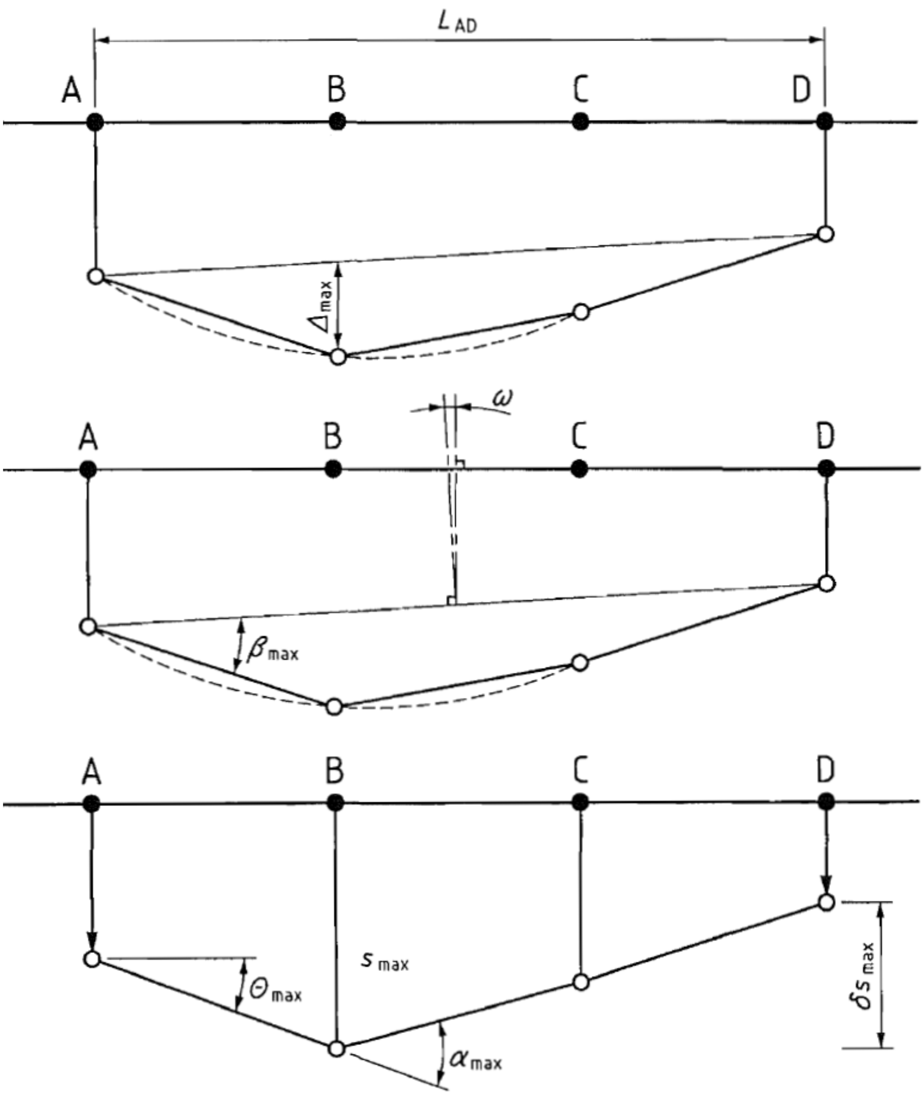

Figure 69. Explanation of the displacement parameters

Given a settlement, S is the vertical displacement of a point:

- the differential settlement δs is the difference between the settlements of two points;
- the relative deflection Δ is the maximum displacement between the settlement profile of two points and a straight line connecting them;
- the deflection ratio Δ/L is the ratio of the relative deflection between two points to the length between them;
- the rotation θ is the gradient of a straight line connecting two points;
- the tilt ω is the body rotation of the part of the structure defined by two points;
- the angular distortion β (or relative rotation) is the rotation of the straight line connecting two points relative to their tilt.

Different displacement values are suggested in the literature, for assessing damage on buildings induced by settlements .

Polshin & Tokar [55] define limits for wall in terms of deflection ratio, Δ/L relating them to the building length, where for L/H<=2 a threshold value between 1/3300 and 1/2500 was suggested (with L and H, length and height of the wall, respectively).

Meyerhof [56] follows stricter criteria and define safe limits for unreinforced bearing walls in hogging and sagging mode and also for open steel and concrete frame buildings. The limit value for angular distortion β for hogging and sagging of unreinforced loadbearing walls was set to 1/2000 and 1/1000, respectively.

The Eurocode 7 [54] establishes limiting values for foundation movements of ordinary and new constructions For open load bearing or continuous brick walls, the maximum allowed angular distortion varies between 1/2000 and 1/300. A limit value of 1/500 is acceptable for many structures, to prevent the occurrence of a serviceability limit state. As noted in the literature resistance offered by the foundations makes the sagging deformation mode less sensitive than the hogging one, so that limit values of displacement parameters have to be halved for the hogging mode.

Burland [57] argued that the onset of cracking in a building due to soil deformation may be in the order of $\varepsilon = 0.5 \times 10^{-3}$.

An important development by Boscardin and Cording [48], by joining the results for angular distortion from Skempton [58], Polshin & Tokar, Meyerhof with the tensile strain criterion from Burland, defines a zone, Figure 70, in which negligible damage can occur with horizontal stretching of the building ε in the order of $0.5x10^{-3}$ or with angular distortion β in the order of $1x10^{-3}$. Their study assumes buildings as simply supported beams with 6.40 m length with L/H=1, so the ratio L/H=1 can be considered conservative and these results are valid for L/H >1.

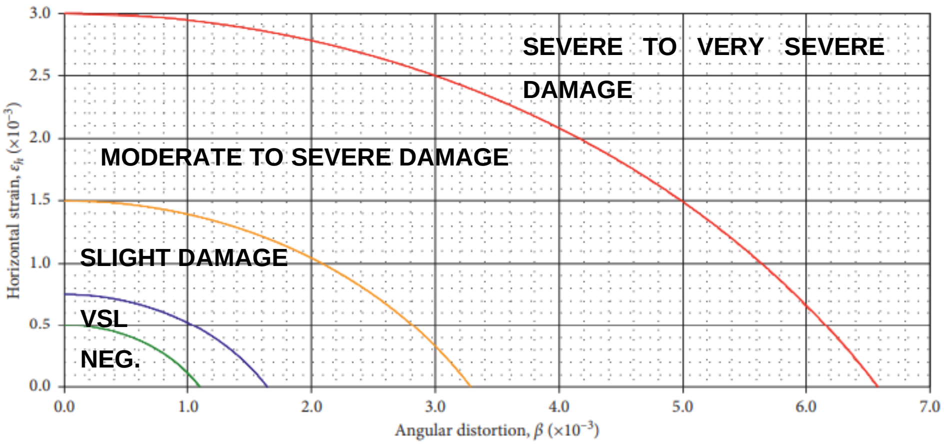

Figure 70. Relationship between angular distortion and horizontal strain. Boscardin & Cording [48]

Cording and Son [59] updated Boscardin and Cording's work, to get a lateral strain independent on L/H, E/G and the position of neutral axis (with E and G bending and shear stiffness of the wall respectively).

According to van Staalduinen and laboratory tests [60] it was showed that elongation at which the extremely absorbable bending tensile stress occurs in masonry can be higher, in the order of $1x10^{-4}$. Also the laboratory tests were conditioned to have weaker masonry so damage growth could be studied in the test setup.

Compared to these laboratory tests, the criteria mentioned in Boscardin and Cording and Son thus imply higher acceptable strains. The criteria used in practice, apparently, accept a slight exceedance of the allowable stress in the masonry. At microlevel, indeed some form of crack may have occurred in a building while it is not yet visible to the naked eye.

These values should not be considered as rigid rules since the performance of buildings may depend on many factors such as material properties, environmental conditions, foundation types [61].

The criteria used for damage identification for URM presented in this thesis, are found to be angular distortion β and horizontal strain ε, introduced by Boscardin and Cording and later refined by Son. The criteria are well accepted internationally in order to assess damage to masonry buildings by settlements.

Burland and Wroth [57] for the evaluation of tensile strains for a given deflected shape of the building foundations, hence obtain the deflection ratio Δ/L at which cracking is initiated; introduced the equivalent beam approach, where the building is represented by an elastic rectangular deep beam of length L and height H. Authors considered two extreme modes: bending only about a neutral axis at the center and shearing only. In the case of bending only, the cracks are related to the bending strain ε_b occurring in the top fibre, whereas in the case of shearing only, the diagonal cracks are due to the shear strain ε_d caused by shear deformations. In general, both modes of deformation will occur simultaneously, and it is necessary to calculate both bending and shear strains to ascertain which type is the limiting one.

The expression for the maximum bending strain ε_b and the maximum shear strain ε_d, in function of deflection ratio Δ/L are the following equations (8) and (9):

$$\varepsilon_b = 4.8 \cdot \frac{H}{L} \cdot \frac{\Delta}{L} \tag{8}$$

$$\varepsilon_d = 2 \cdot \frac{\Delta}{L} \tag{9}$$

The displacement parameters, angular distortion β, horizontal strain ε, and deflection ratio Δ/L are reported in Table 10 for each of the two URM configurations, at different phases of the test. For the deflection ratio Δ/L, the Polshin & Tokar limit *i.e.*, between 3.03x10-^{4} and 4.00 x10-^{4} were found to be exceeded from the peak load to the end of test for both configurations, as well as cracks are small, at the onset of the first hairline cracks, and wider after.

Table 10. Displacement parameters for intact and deteriorated URM

TEST	*Phase* [-]	Δ/L [-]	β [rad]	ε_b [-]	ε_d [-]
Intact	Peak Load	1.31E-04	3.49E-04	4.08E-04	2.63E-04
	End	9.80E-04	2.97E-03	3.04E-03	1.96E-03
Deteriorated	Peak Load	1.29E-04	1.75E-04	4.02E-04	2.59E-04
	Diagonal strut	5.30E-04	1.05E-03	1.65E-03	1.06E-03
	End	1.38E-03	2.62E-03	1.93E-03	1.24E-03

Angular distortion β and horizontal strain ε, as a result of the settlement, were used together to assess building damage with the zones defined by Boscardin and Cording (Figure 70). Intact URM was found to be from negligible damage at the peak load, to very severe damage when spandrel was no longer able to transfer load, behaving like a horizontal pendulum.

Also deteriorated URM was found to be from negligible/visible damage at the peak load, to the beginning of severe damage when diagonal strut occurs with a severe damage zone at the end.

Hogging mode exhibited by deteriorated URM showed a deflection ratio higher than the intact one when failure was attained as well as for other displacement parameters as angular distortion β and horizontal strain ε.

3.2.1. Theoretical model

A theoretical analysis of spandrel panel was performed to assess the failure mode. In the frame of a macroelement idealization of the subassemblage, two pier panels with a length of 170 cm and an effective height of 230 cm (i.e., an aspect height to length ratio of 1.35) and a spandrel panel with a length of 170 cm and a height of 96 cm (i.e., an aspect length to height ratio of 1.77) were identified.

A stress-based approach, according to the current building codes, such as Italian code [21], [34] and other scientific literature [11], [62]–[64] were used to evaluate the nominal lateral strength of the URM spandrel panel. Masonry strength was assumed as the minimum between those associated with the following failure modes: toe crushing; diagonal tension cracking; stair-stepped diagonal sliding; and bed-joint sliding, where the first failure mode is flexure-controlled while the others are shear controlled.

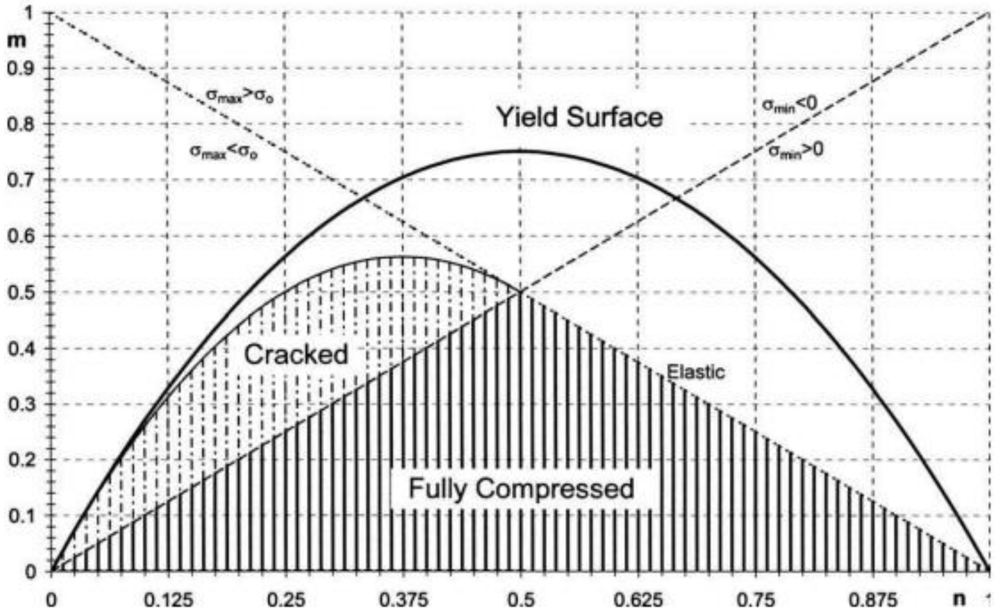

Figure 71. Normalized interaction diagram m,n for flexure mode of rectangular cross section. Lignola et al. [64]

The basic assumptions refer to the material behaviour and the no-tension is the assumption usually adopted in the engineering problems for masonry structures. Masonry is considered as a no-tensile resistant homogeneous material with elastic perfectly plastic behaviour in compression, defined by a peak strain ε_{mo}, an ultimate strain ε_{mu} with a strength f_c

The compressive strength of masonry was assumed to be 85% of the actual one, which was $f_c = 2.65\ MPa$ according to the uniaxial compression tests on tuff masonry wallets previously shown (see Sect. 2.3.4).

The flexural strength V_f defined by a yielding surface, Figure 71, is provided by the equation:

$$V_f = B^2 s \frac{\sigma_0}{2H_{eff}}(1-\frac{\sigma_0}{0.85 f_c}) \tag{10}$$

Formulation depends on the geometry of the walls (the length B, the height H, the thickness s of the pier) and on the vertical compressive stress σ_0.

Figure 71 also shows the elastic and cracked limit state for a rectangular cross section. For the elastic limit state, section never cracks so limit condition is characterized by a tension at most equal to the ultimate compression stress and on the opposite side at most equal to zero.

In the cracking limit state, instead a portion of the cross section is in tension and cracked, while the reacting portion is always in compression (maximum stress is equal to the compressive strength).

For regular masonry walls made of regular arrangements of units bonded with horizontal and vertical mortar joints, the following equations for shear strength, both based on the well-known Mohr–Coulomb criterion, are provided:

$$V_s = B' s \frac{f_{v0}+\mu\sigma_0}{\gamma_m} \tag{11}$$

$$V_{sd} = \frac{Bs}{b}(f'_{v0}+\mu'\sigma_0) \quad f'_{v0} = \frac{f_{v0}}{1+\mu\varphi};\ \mu' = \frac{\mu}{1+\mu\varphi};\ \varphi = \frac{2h_b}{b_b}; \tag{12}$$

Equation (11) is provided for predicting the V_s shear strength in the case of sliding along horizontal joints while equation (12), formulated by [65], is provided in the case of sliding along diagonal stepped cracks in the mortar V_{sd}. In the equation (11) the partial safety coefficient γ_m appears, but it is discarded in experimental evaluations. In the formulation (11) μ is the friction coefficient and f_{v0} is the cohesion, defined as 'local' parameters, in Equation (11) the 'global' parameters f'_{v0} and μ' are used to account for the interlocking between the units expressed by parameter φ, which depends on the units height h_b and length b_b. In addition to equation (12), the Commentary to the Italian code [34] specifies that the achievement of the tensile strength of the block is set as an upper bound for the shear capacity. Equation (9) also depends on the shape factor b that according to the Commentary to the Italian code [34], is herein assumed equal to the in-plane slenderness of the panel $b = \lambda = H/B$ but limited to the range

1.0–1.5. Equation (9) also depends on the compressive strength of masonry f_c, and on the effective height H_{eff}, assumed as the shear length and, thus, equal to 0.5 H in the case of double-fixed constraint, while B is the uncracked length of the end sections of the walls.

For irregular masonry (the irregularities occur in the arrangements of units and mortar) the in-plane shear resistance of the wall, which can only occur for diagonal shear failure, is provided by the following formulation, based on the Turnšek and Čačovič model, and involving the tensile strength of masonry f_t:

$$V_t = Bs\frac{f_t}{b}\sqrt{1+\frac{\sigma_0}{f_t}} \qquad (13)$$

with the mechanical and geometrical parameters introduced before.

The values of shear strength τ_0 ,tensile strength f_t refer to the diagonal compression tests on tuff masonry wallets previously shown (see Sect.2.3.6), while for the other mechanical parameters, values of f_{v0} and μ used for the numerical predictions, have been obtained from [66].

Flexure in piers produces tensile stresses normal to the bed joints of masonry, conversely, flexure in spandrels produces tensile stresses normal to the head joints, therefore the structural response of these elements is different considering that masonry is an anisotropic material. Moreover, the intersections between piers and spandrel, namely the joint panels, supplied a further effect of confinement and a moderate axial load to the spandrel. This last observation suggests that transposing the experimental results of piers to the spandrels, by adopting the same failure criteria, without modifications, can be inconsistent.

The main effects of f_t tensile strength on the performance of the masonry were studied in the course of time by different authors [67]–[69].

Particularly for the spandrel panel, tensile strength could have a key role for the assessment of buildings. In contrast to the case of piers, the compressive strength domain for spandrel can be determined by taking into account the tensile strength (f_{ttd}) that is generated in the end sections as a result of interlocking with the adjacent masonry portions. The failure mechanisms may involve the tensile strength of the blocks f_{btd} or occur by sliding along the horizontal joints; the horizontal tensile strength is therefore given by the expression:

$$f_{ttd} = \min\left(\frac{f_{btd}}{2}; f_{v0} + \frac{\mu\,\sigma_0}{\varphi}\right) \quad (14)$$

According to best knowledge of author also for f_{v0} there must be considered the interlocking effect expressed by φ. Compressive stress σ_0 on horizontal joints in the spandrel end section can be considered as half the vertical normal compressive stress in the pier.

The compressive strength of spandrel can be defined as half of masonry one, according to [70], in the following indicated as f_h as it refers to resistance in the horizontal direction $f_h = 0.5\ f_c$ .Taking into account the tensile strength, flexural strength V_f was defined by the following equation introduced in [71]

$$V_f = \left[\frac{1}{12}\left(h^2\alpha + \frac{h(2\,N_u + \alpha\sigma_0 h)(\,\alpha + 6\psi)}{(\alpha + 2\psi)}\right) - \frac{1}{6}\left(\frac{(2\,N_u + \alpha\sigma_0 h)^2(\,\alpha + 6\psi\lambda)}{\sigma_0(\alpha + 2\psi)^2}\right)\right]\frac{hN_u}{3l_{sp}}$$

$$for\ \ 0 \leq \alpha < 1\ and\ \ -\frac{N_t}{2} \leq N \leq \psi N_u \quad (15)$$

Where h defines the height of the masonry spandrel, l_{sp} the length of the masonry spandrel, N_u the spandrel compressive ultimate axial force, defined as $N_u = 0.85\ f_{hd}\ h\,t$, with t the width of the masonry spandrel, α the ratio between tensile and compressive strength, ψ refers to the height of the equivalent plastic zone according to the stress-block model ,usually assumed equal to 0.8 the height of a parabolic-rectangular stress diagram, while λ refer to the distance of resultant force from the neutral axis, usually assumed equal to 0.4 the height of a parabolic-rectangular stress diagram. The surface defined by equation (15) is valid for a N compressive load between 0.8 times the compressive ultimate axial force, and half of the spandrel tensile ultimate axial force, defined as $N_t = f_{fttd}\ h\,t$, while for the surface outside this zone, please refer to [70].

The peak strength of the spandrel macroelement was computed as the minimum between those corresponding to toe crushing, sliding along horizontal joints and diagonal stepped cracks, sliding shear and tensile diagonal cracking. Under these assumptions, the resistance of the spandrel for intact URM was estimated to be 33.81 kN for the minimum shear strength as shown from N-V interaction curves drawn for spandrel cross section in Figure 72 .

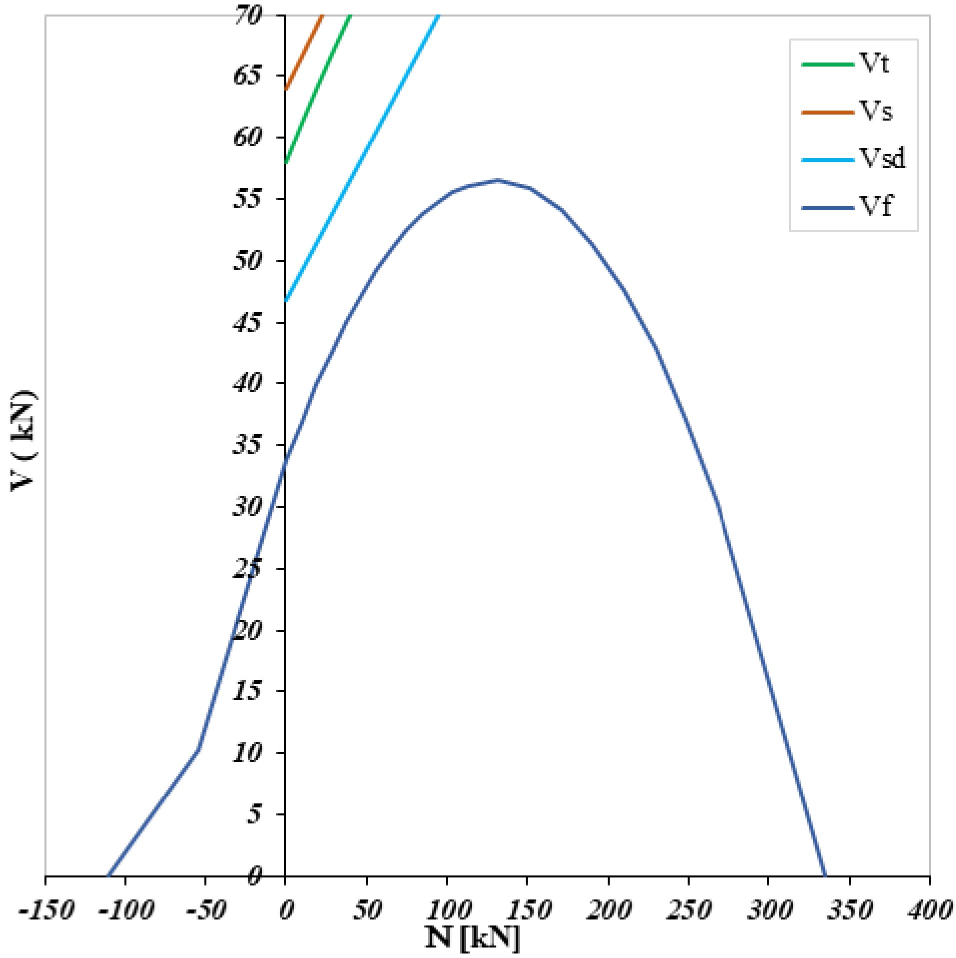

Figure 72. Interaction domain N-V for spandrel cross section intact URM

V_f was the minimum shear strength, the equation used in this study confirmed the flexural cracking failure observed during test on the intact spandrel panel. Equation (15) seems to be best suited for estimating the peak flexural strength. So, when spandrel reached an advanced crack, the two piers behaved as separate cantilevers, bringing the gravitational load, *i.e.,* 200 kN, while spandrel panel turned into a horizontal pendulum. Also for the deteriorated URM, the interaction domain N-V was drawn (Figure 73). For this configuration, the compressive strength of masonry was assumed to be 85% of the actual one, which was on overage equal to $f_c = 2.04\ MPa$ according to the uniaxial compression tests on deteriorated tuff masonry wallets previously shown (see Sect.2.3.4), while for the other mechanical parameters, values of f_{v0} and τ_0 on average was the same of the intact one, as diagonal compression tests revealed in Sect.2.3.6 on deteriorated tuff masonry wallets. Capacity features were computed with reference to the net gross area. Under these assumptions, the resistance of the spandrel for deteriorated URM was estimated to be 25.30 kN for the minimum shear strength as shown from N-V interaction curves. Equation (15) for flexural strength overestimates the experimentally determined flexural strength of the spandrel by approximately 5 kN, which corresponds to approximately 25% of the actual strength.

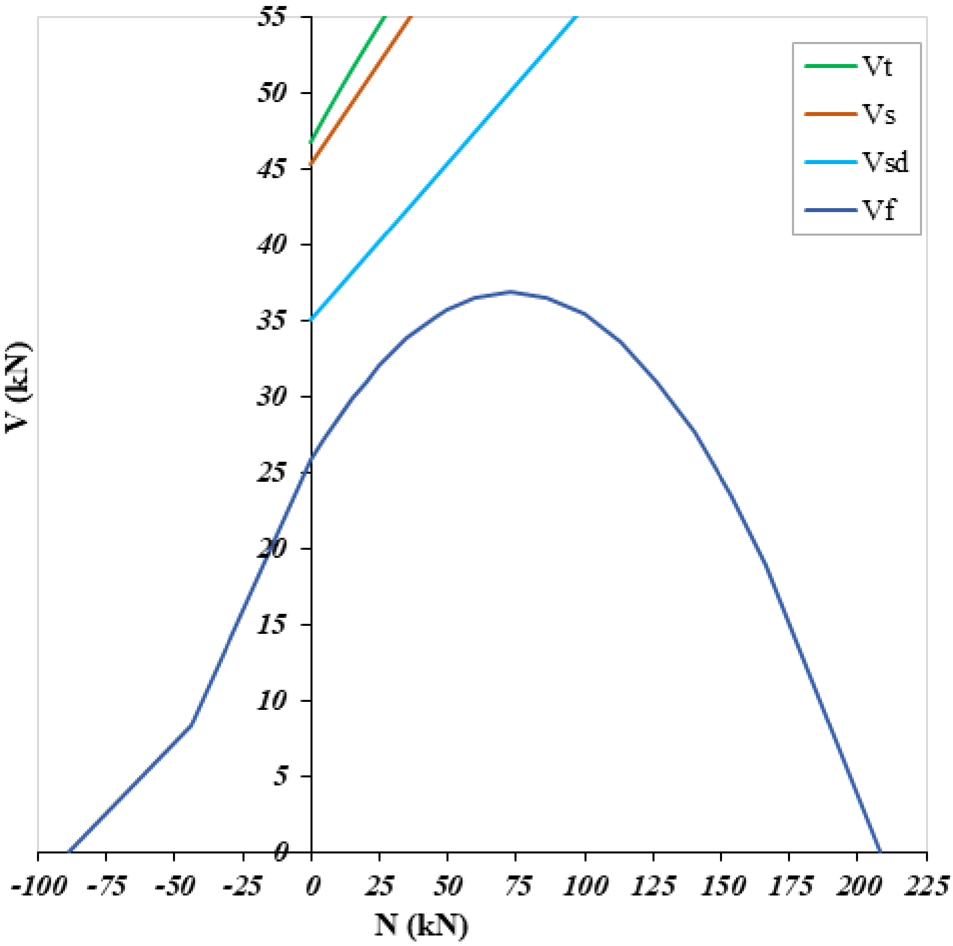

Figure 73 Interaction domain N-V for spandrel cross section deteriorated URM

As previously introduced, the larger initial deformability of mortar joint impacted the response of deteriorated URM in terms of residual strength.

In spite of the fact that cracks pass through many bricks, and the interlocking failure mechanism could be therefore impaired, probably the initial intrinsic deformability of joints yields to limited interlocking of bricks able to activate a strut mechanism, since the beginning of the test.

As the rotations of the interfaces at each crack were partially prevented, a diagonal compression strut gave to URM the residual strength after flexural cracking. For the evaluation of the residual strength different approaches are reported in the literature [67]–[69]

According to Italian code, if the axial force in the spandrels is known, the spandrels are treated like as piers. Conversely, if it is unknown, the capacity of the spandrel can only be considered if a strut-and-tie mechanism can develop*, i.e.,* a tensile resistant member must be present, such as a timber lintel, steel ties or ring beam. If the axial force P_{sp} is known (Figure 74), the shear strength associated with the flexural mechanism of the spandrel can be computed with Eq (16):

$$M_u = P_{sp}\frac{h}{2}\left(1 - \frac{P_{sp}}{(0.85\, f_{hd}\, h\, t)}\right) \quad (16)$$

An equivalent shear strength is computed by assuming that the spandrel is subjected to double bending, as Eq (17):

$$V_P = 2 \cdot M_u / l_{sp} \text{ (17)}$$

Where l_{sp} stands for the spandrel length.

If the axial force is unknown, the flexural capacity is computed by replacing P_{sp} with the minimum of the tensile strength of the horizontal tension elements, and 0.4 $f_{hd}\, h\, t$, that can be seen as a percentage of the compressive failure of the spandrel.

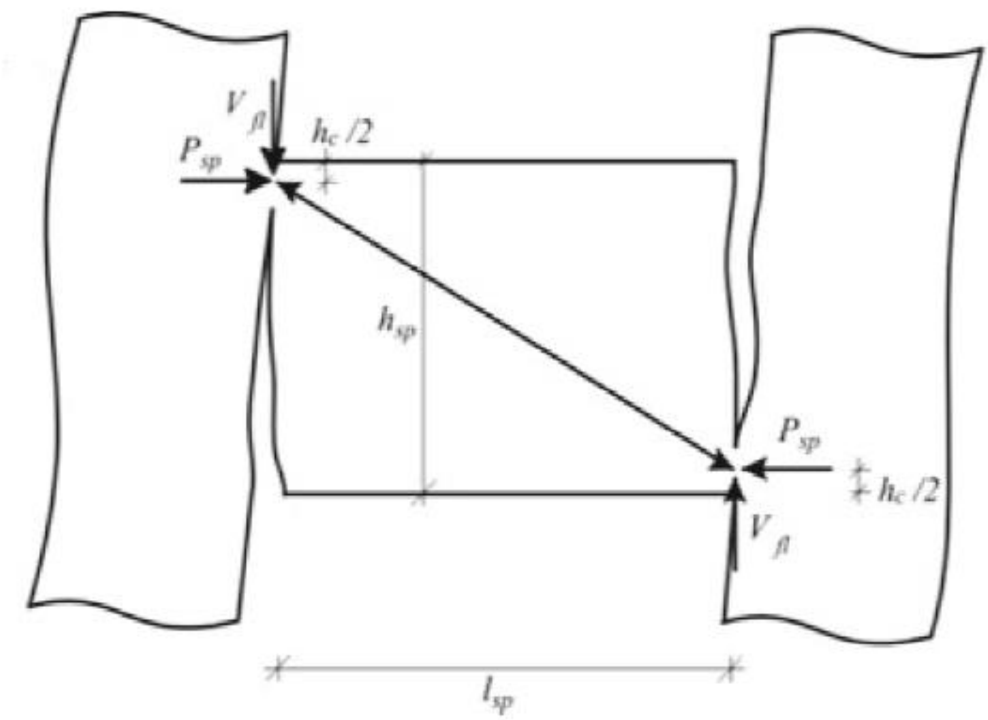

Figure 74. Diagonal compression strut model

P_{sp} was found to be equal to

$$P_{sp} = \min(0.4 \cdot 1.03 \cdot 960 \cdot 250; 3.0 \cdot 25000)N = min(97.92; 75)\ kN \quad (18)$$

where the conventional tensile strength of the timber $f_{t,l}$ is assumed to be a yield strength provided by the bond τ over the anchorage length in the masonry.

A reasonable value for τ is 1.0 MPa, so $f_{t,l}$ is defined as

$$f_{t,l} = \frac{A_l\,\tau}{A_s} = \frac{2 \cdot 250 \cdot 150 \cdot 1.0}{25000} = 3.0\ MPa \qquad (19)$$

With A_l is the anchoring surface along which τ acts, A_s the cross section of timber lintel. Flexural mechanism was equal to:

$$M_u = 75 \cdot \frac{960}{2}\left(1 - \frac{75}{0.85 \cdot 1.02 \cdot 960 \cdot\ 250}\right) = 36.0\ kNm \qquad (20)$$

To evaluate the residual shear strength, after the peak load a double bending behaviour is inconsistent due to the cracks formation at the ends of the spandrel, so the shear is assumed to be

$$V_P = \frac{M_u}{L} = \frac{36}{1.7} = 21.17\ kN \qquad (21)$$

The model proposed by Italian Code, based on a diagonal compression strut, seems to be the most suitable approach for estimating the residual strength after flexural cracking.

In addition, Italian Code and different authors consider also a strength related to sliding failure. Spandrel internal force acts orthogonally to the mortar bed joints and the mortar head joints are not aligned, so bricks tend to prevent sliding failure. Hence sliding failure is considered to be a rare failure mode for spandrels. Magenes and Fontana [69] estimated the spandrel strength as

$$V_s = h\, t\, c_{red} \tag{22}$$

Where $c_{red}$is the reduced cohesion of the mortar bed joints (Mann and Müller [65]):

$$c_{red} = \frac{1}{1+\varphi} c \tag{23}$$

The reduced cohesion according to Mann and Müller, which was used to compute the shear strength according to equation (23), equates to $c_{red} = 0.54c$. To take in account the shape factor b equal to the in-plane slenderness of the panel as the equation of Mann and Muller (14), equation (23) should be rewritten as:

$$V_s = \frac{h\, t\, c_{red}}{b} \tag{24}$$

Using the last equation, the residual strength related to sliding failure was found to be $V_s = \frac{960 \cdot 250 \cdot 0.15}{1.5} = 21.36MPa$

Shear equation (23) matches the residual shear strength of the spandrel so well, as the cohesive strength of the joints would be lost after the joints undergo some sliding movement associated with the shear mechanism.

According to FEMA 306 [72], for a spandrel panel, it should be more correct to associate the ultimate bending moment capacity to the bed-joint sliding strength. The sliding mechanism can control the residual strength of the spandrel once flexural cracking leads to an approximately vertical failure plane. However, in most cases the failure plane is curved (see Figure 45,Figure 46), hence the sliding failure of spandrels is unlikely to occur.

Equation (24) yields to good estimates of the residual shear strength for the deteriorated URM spandrel, however this finding seems somehow contrary to the mechanical understanding, so comparison with other experimental test is required, to validate the last conclusion.

3.3. Theoretical model for out of plane testing

As pointed out by Liu et al [73], in Figure 75 the increase of the axial load increases the out-of-plane strength but also reduces the ductility.

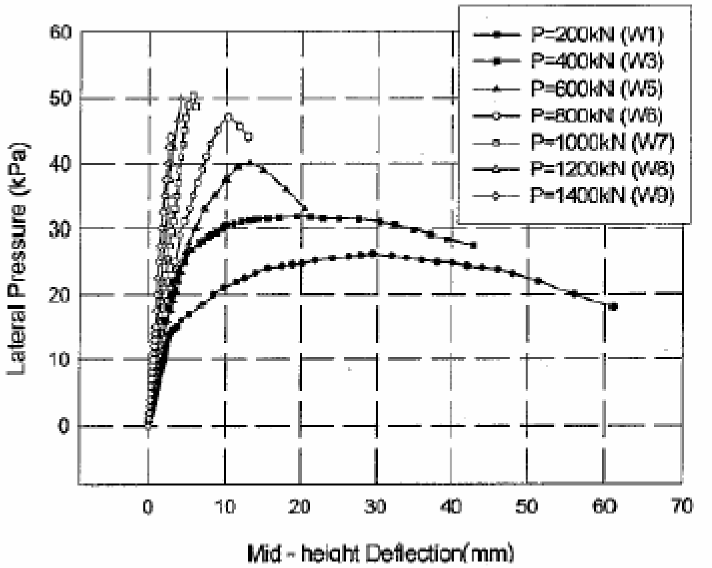

Figure 75. Mid-height deflection vs. lateral pressure measured in reinforced masonry walls (Liu et al [73]**).**

Brittle behaviour exhibited by the degraded URM is compatible with the last remark, with a drop in load capacity after peak load was reached. For the intact URM, peak load is recorded for a considerable displacement, but this is attributable to the splitting phenomenon, which partially interrupted the overturning mechanism (see Figure 68). Deteriorated wall had a proportionally higher axial load ratio, since its vertical capacity is lower.

As in shear walls, where the behaviour is governed by in plane mechanisms as illustrated before, flexural strength of masonry is a central property in the behaviour of walls under out-of-plane loading.

Vertical axial load has implications in the evaluation of the energy absorbed in the bed joints:

Four kinds of joint failure mechanisms, namely bending and torsional failure of bed and head joints, majorly contribute to the force capacity of wall, along a diagonal crack line, as happened in the intact test (Figure 76,Figure 77) :

1) the flexural tensile strength of the head joints ;

2) the torsional capacity of the bed joints;

3) the torsional capacity of the head joints;

4) the flexural tensile strength of the head joints ;

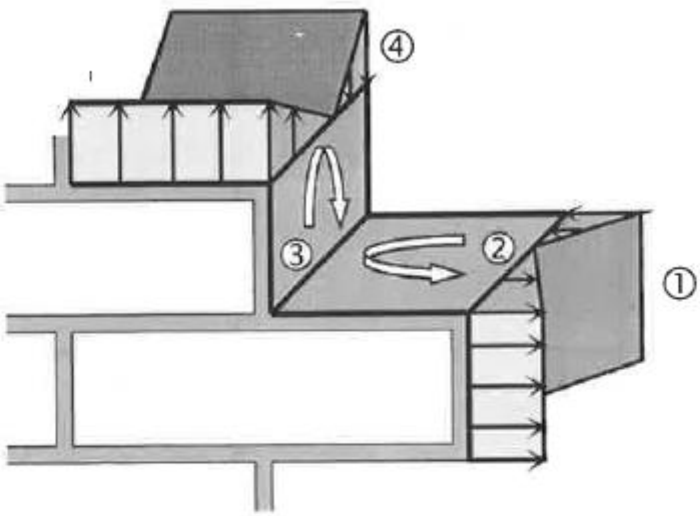

Figure 76. Failure mechanisms contributing to flexural strength.[50]

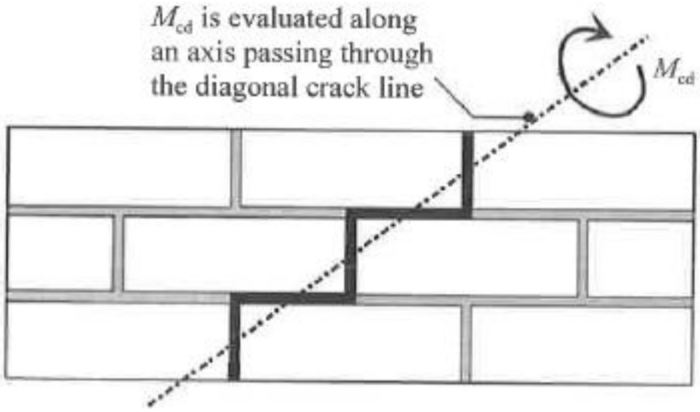

Figure 77. Bending moment along an axis passing through a diagonal crack line[50].

Lang-Zi Chang [74] explained that fracture energy dissipated by all joint failure mechanisms increases as the pre-compression increases.

Intact URM showed a diagonal stepped crack affecting the loaded pier and passing through the whole spandrel thickness due to a clear overturning mechanism. The achievement of flexural tensile strength yields to URM failure. Due to the lack of experimental data on the masonry's flexural strength, for the spandrel it is increased by 1.2 the previously introduced pure tensile strength (see equation 14)

Under these assumptions, the resistance of the spandrel for intact URM is described by interaction domain N-M, where flexural strength V_f defined in equation (15) has been rewritten in the form of bending moment, Figure 78.

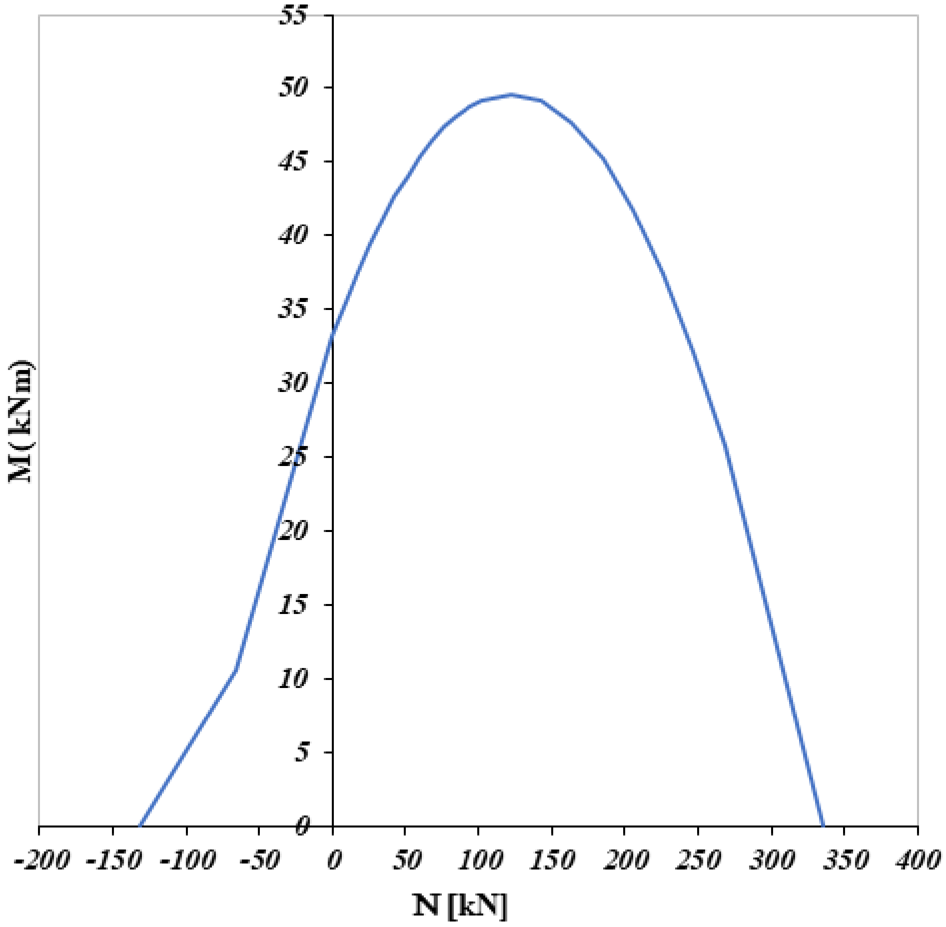

Figure 78. Interaction domain N-M for spandrel cross section intact URM

A first comparison between the maximum bending moment registered during the out-of-plane test and the theoretical one, that can be calculated by using simple analytical formulations, is here presented. Spandrel panel, because of good interlocking at the node panels, can be schematised as a fixed-eng beam with a span equal to the clear span of the opening. In more detail, out of plane failure always occurred due to the tensile failure of masonry in proximity of the top and bottom spandrel sections, where the bending moment demand was maximum, and found to be equal to:

$$M_{sp} = \frac{6\,\delta EI}{{l_{sp}}^2} \qquad (25)$$

where l_{sp} is the length of the masonry spandrel as introduced before, while δ is the out of plane displacement, E and I are respectively the Young's modulus and inertia moment.

At a displacement of 91.50 mm, where the peak out of plane force was reached, the bending moment demand δ was found to be equal to 33.80 kNm reaching the capacity, estimated to be 33.25 kNm.

Also for the deteriorated URM, the final cracking pattern shows a vertical crack from the top towards the bottom near the interface zone between spandrel section and joint panel. In this configuration, joint deformability due to geometric deformation did not allow the flexural resistance to evolve along the diagonal path, but failure occurred when the capacity at the interface is reached. In this case, for the spandrel, vertical flexure strength is equal to the horizontal flexure strength, related to the tensile strength.

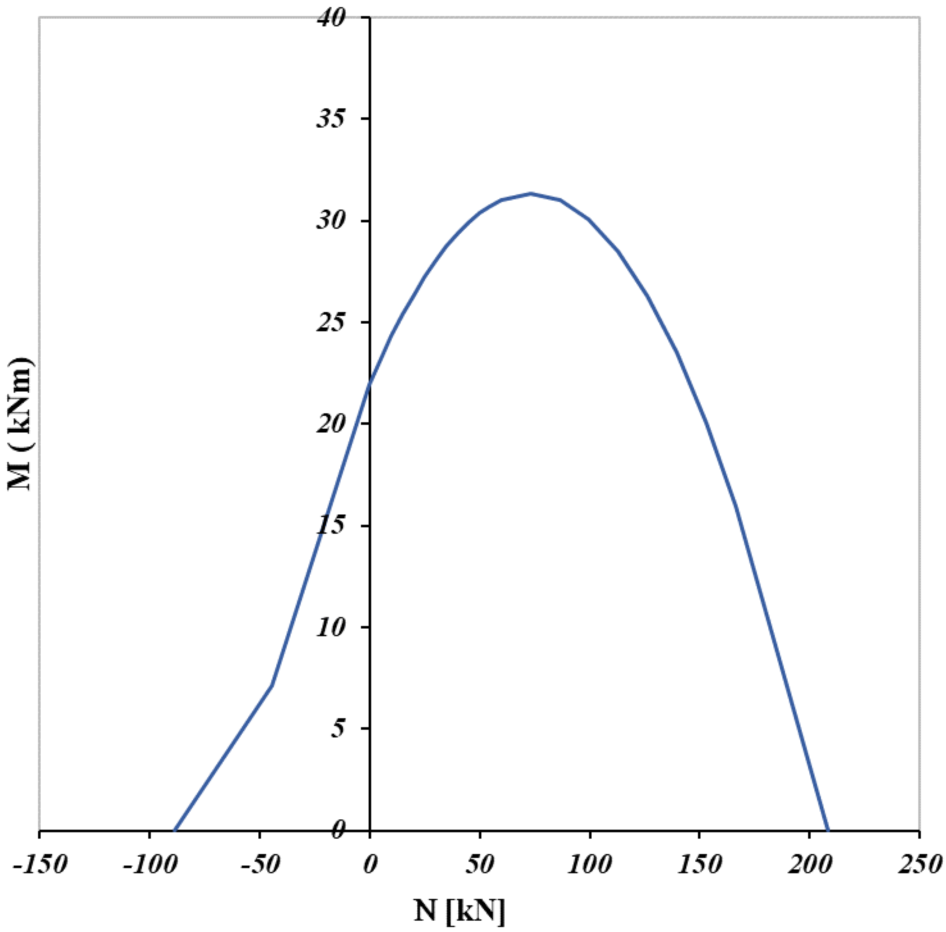

Figure 79. Interaction domain N-M, for spandrel cross section deteriorated URM

For deteriorated URM, the interaction domain N-M was drawn (Figure 79). For this configuration, the compressive strength of masonry was assumed to be 85% of the actual one, which was on overage equal to $f_c = 2.04\ MPa$ according to the uniaxial compression tests on deteriorated tuff masonry wallets previously shown (see Sect 2.3.4) with capacity computed with reference to the net gross area. Under these assumptions, the strength of the spandrel for deteriorated URM was estimated to be 21.96 kNm as shown from N-M interaction curves. At displacement of 55.45 mm, where the peak out of plane force was reached for the deteriorated URM, the bending moment demand estimated by equation (25) was found to be equal to 23.15 kNm being greater than the respective capacity.

Chapter 4

Finite Elements Nonlinear Modelling of Masonry Structures

4.1. Abstract

A relatively simple numerical model, suitably calibrated, is used to analyse the results of the experimental investigation, leading to a validation of the model itself.

The work includes the calibration of numerical microscopic/detailed models considering the masonry units and the mortar joints separately and characterized by different constitutive laws.

Hereafter, as presented in the experimental part, first numerical analyses on bricks and then on tuff masonry are illustrated. The finite element method (FEM) was used to simulate the mechanical behaviour of the walls tested under uniaxial, diagonal compression test and for URM subjected to in and out plane. The experiments were simulated using the FEM software DIANA FEA 10.4

4.2. Numerical modelling for diagonal compression test

The finite element method (FEM) was used to simulate the mechanical behaviour of the walls tested under uniaxial and diagonal compression tests. The diagonal compression experiments were simulated using the FEM software DIANA FEA 10.4 [75], under plane-stress assumption, in displacement control, measuring in-plane stress-deformations.

Two-dimensional numerical model is referred to in order of simulating the nonlinear behaviour of the unreinforced fully filled mortar joints and aged masonry panels. The 2D analysis represents a valid assumption given the geometry of the walls and the in-plane applied loading. The model, initially validated with experimental results on brick stone masonry, is utilized to simulate the experimental nonlinear behaviour for specimens with integrated smart bricks with both fully and not fully filled mortar joints.

Micromechanical modelling of brick and tuff stone masonry was performed defining the mortar and brick elements separately as continuous isotropic elements without friction interfaces between them, assuming a smeared-crack approach. The choice of simple micro-modelling is related not only to the uncertainty in the material properties but also to simulate geometric alteration for mortar joints to describe the behaviour of aged walls.

4.3. Masonry modelling, boundary conditions

Eight-node quadrilateral elements (CQ40S) were used to simulate the brick stone masonry, in micro modelling approaches. The mesh of the FEM model was generated using squared, curved shell CQ40S elements with 8 nodes and isoparametric formulation. The studies were only on the in-plane response of wallets, the choice of curved shell elements used in the FEM model has been made, taking into consideration other load conditions that can be the subject of future studies using the same modelling strategy.

The size of finite elements was equal to the thickness of mortar joints and was selected after a mesh sensitivity analysis.

Tensile strength (f_t), Young's modulus (E), tensile fracture energy (G_f^I) and compressive fracture energy (G_c) and compressive strength (f_c) are the minimum set of data adequate for non-linear analysis of such models, as validated against experimental data in [62], [76], [77] confirming that simple micro-modelling without interface not only allows a good simulation of tuff masonry behaviour but also this allows a trade-off between accuracy and computational cost.

Values assumed for E, ν f_c, f_t, were estimated experimentally with the material properties, while starting from the values of the literature [78] the fracture energies, both in tension and compression, together with the tensile strength, were then adjusted through the diagonal compression tests, in order to minimize the differences between the numerical and experimental average shear stress-strain diagram by least squares best fitting.

A nonlinear, isotropic, constitutive relationship was attributed to each finite element, accounting for strain softening both in tension and compression through fracture energies. The same stress-strain functional forms were assigned to mortar and tuff stones, while considering different values of mechanical properties. More specifically, a nonlinear behaviour was considered in compression, whereas the tensile behaviour was assumed to be linear elastic up to peak strength with post-peak nonlinear softening up to failure as depicted in Figure 80.

An exponential relationship was considered for the behaviour of the material in the post-elastic phase, as exponential softening is one of the most common constitutive laws used for representing the softening behaviour of concrete as shown by Hordijk [79] but also for masonry [76] taking into account the following parameters:

$$\frac{\sigma_{nn}^{cr}(\varepsilon_{nn}^{cr})}{f_t} = \exp\left(\frac{\varepsilon_{nn}^{cr}}{\varepsilon_{nn,ult}^{cr}}\right) \tag{26}$$

$$\varepsilon_{nn,ult}^{cr} = \frac{G_f^I}{h_{cr} f_t} \tag{27}$$

where: σ_{nn}^{cr} is the crack stress, ε_{nn}^{cr} is the crack strain, $\varepsilon_{nn,ult}^{cr}$ is the ultimate crack strain and h_{cr} is the crack bandwidth.

To define the values of compressive fracture energy, a parabolic softening law [80] related to the equation used by DIANA was adopted as follows:

$$\varepsilon_{C/3} = -\frac{1}{3}\frac{f_c}{E} \tag{28}$$

$$\varepsilon_c = -\frac{5}{3}\frac{f_c}{E} = 5\varepsilon_{C/3} \tag{29}$$

$$\varepsilon_u = \varepsilon_c - \frac{3}{2}\frac{G_c}{h_{cr}\, f_c} \tag{30}$$

$$f = \begin{cases} -f_c \cdot \frac{1}{3}\frac{\varepsilon_j}{\varepsilon_{\frac{c}{3}}} & \text{if } \varepsilon_{c/3} < \varepsilon_j \leq 0 \\ -f_c \cdot \frac{1}{3}\left(1 + 4\left(\frac{\varepsilon_j - \varepsilon_{\frac{c}{3}}}{\varepsilon_c - \varepsilon_{\frac{c}{3}}}\right) - 2\left(\frac{\varepsilon_j - \varepsilon_{\frac{c}{3}}}{\varepsilon_c - \varepsilon_{\frac{c}{3}}}\right)^2\right) & \text{if } \varepsilon_c < \varepsilon_j \leq \varepsilon_{c/3} \\ -f_c\left(1 - \left(\frac{\varepsilon_j - \varepsilon_{\frac{c}{3}}}{\varepsilon_c - \varepsilon_{\frac{c}{3}}}\right)^2\right) & \text{if } \varepsilon_u < \varepsilon_j \leq \varepsilon_c \\ 0 & \text{if } \varepsilon_j \leq \varepsilon_u \end{cases} \tag{31}$$

where: $\varepsilon_{C/3}$ is the strain at which one-third of the maximum compressive strength, ε_c is the strain at the maximum compressive strength, and ε_u is the ultimate strain at which the material is completely softened in compression.

Damage due to tensile cracking is modelled using a rotating crack model, in which stress–strain relationships are evaluated in the principal directions of the strain vector so the direction of the cracks changes according to the direction of the principal strain

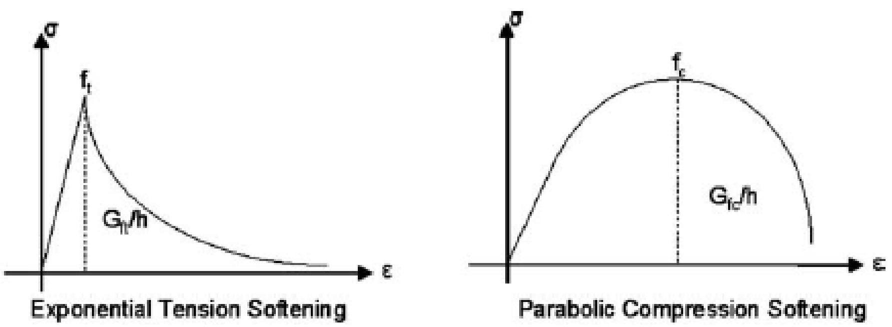

Figure 80. Material model used for mortar and bricks.

Regarding boundary conditions, constraints were assigned to the panel nodes at the base to prevent horizontal and vertical translations. Simplified steel loading shoes have been included at the top to better simulate the load application, modelled as an elastic material.

The simulation of the diagonal compression load has been performed through imposed displacements, with increasing magnitude, in agreement with the testing procedure. The numerical solution was carried out in an incremental manner with a Newton-Raphson method (using the secant stiffness matrix) together with a line-search procedure used to solve the corresponding nonlinear equations.

The average vertical and horizontal strains, $\varepsilon_v, \varepsilon_h$ have been computed as the average displacement along the compressive and tensile diagonals, respectively, over the LVDT's gauge length as in the experimental tests. During the calibration process, the main focus was on the comparison of the experimental and numerical initial stiffness and maximum load.

A different methodology was used for brick diagonal compression tests. The model, initially validated with experimental results on brick stone masonry, is utilized to simulate the experimental nonlinear behaviour for specimens with integrated smart bricks, with both fully and not fully filled mortar joints. From experimental results, briefly, it is noted that unreinforced panels without smart bricks, CB_D_1 and CB_D_1_D were characterized by a similar behaviour up to about 30% of the maximum shear strength (Figure 11) when for CB_D_1_D wallet the mortar geometric variation caused a stiffness drop resulting in higher deformability and shear strength decrease.

For specimens with integrated smart bricks, the load increased almost linearly with the imposed displacement until a sudden load drop occurred. The behaviour of the specimens was similar, with the τ–γ curves that followed one another closely up to the end of the test with difference in shear strength. The geometric defect effect was very limited by smart bricks that have added an inherent weak spot to masonry with a further worsening of shear strength wallet when smart bricks are integrated both in its front and rear sides.

Considering the influence of the smart bricks on the wallet behaviour, FEM model was defined by considering only the net cross section of masonry removing the smart brick length in case of smart bricks specimen both front and rear sides, while half-length in case of aged specimen.

4.4. Comparison of numerical-experimental brick test

The numerical-experimental comparison in Figure 81 shows a satisfactory agreement between the numerical and experimental average shear stress-strain diagram.

The numerical curves, different for intact and deteriorated mortar thickness, with and without smart bricks sensors are always positioned within the two experimental curves well describing the main aspects of τ–γ diagram.

The curve for full mortar thickness has a similar trend to the experimental one, characterized by an almost linear elastic branch until the 75% of the shear strength where first cracks in the mortar were attained, where then cracks appeared almost simultaneously along the full length at peak load.

Curves for specimens with integrated smart bricks were treated (Figure 81.b) separately since the latter experienced a maximum shear stress lower than those of the same geometric mortar joints width. For this reason, two numerical models, for the same geometric mortar configuration, were used on the basis of the experimental behaviour observed to take in account smart bricks influence.

The peak shear stress is 0.25 and 0.27 MPa, respectively for intact and deteriorated specimens, underestimating the experimental value for the latter of the 4% while a well agreement was found for the one with fully filled mortar joint. The numerical curve well describes the peak shear stress of smart bricks test, with a lower stress for specimens with smart bricks placed on both front and rear leaves, so FEM models were able to simulate not only the difference in shear strength but also the limited shear strain.

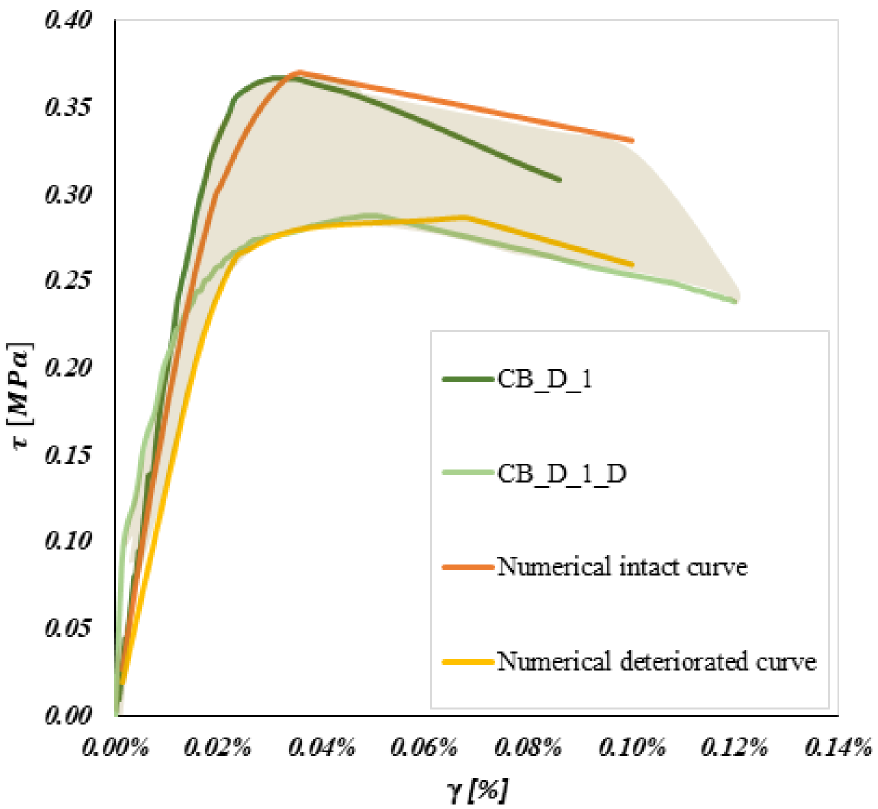

a)

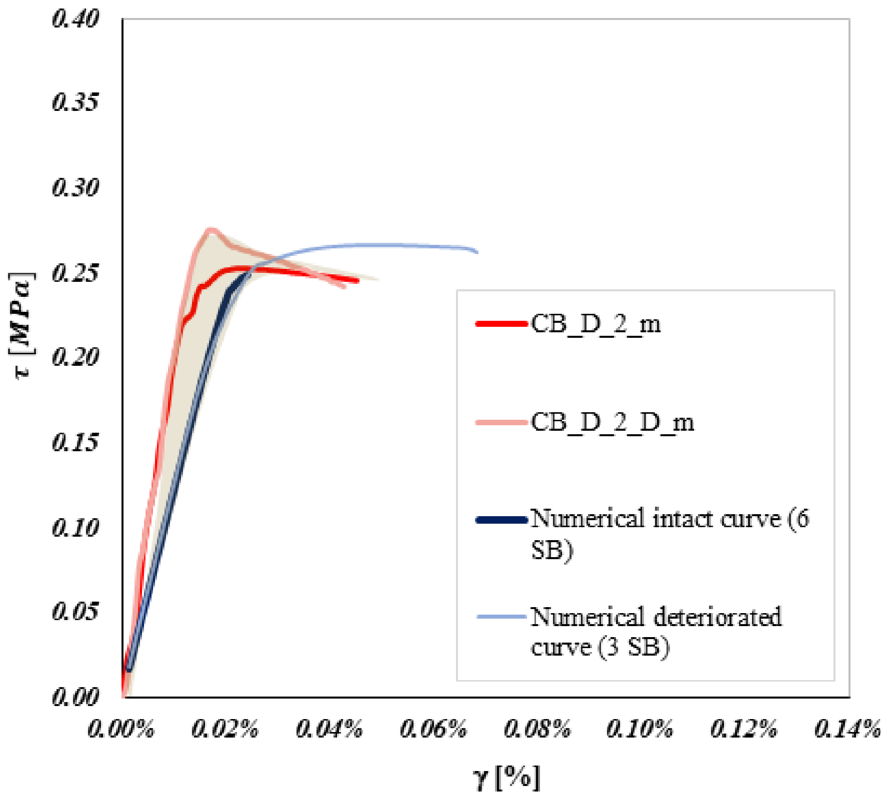

b)

Figure 81. Comparison between numerical and experimental results for a) CB_ D_1 and CB_D_1_D wallets and b) CB_D_2_m and CB_D-2-D-m wallets.

Figure 9 and Figure 10 , (see Sect. 2.2.5), introduced in the experimental section, detail the progress of cracking for experimental wallets, with a satisfactory agreement with the numerical ones (Figure 82and Figure 83)

The URM panels without smart bricks, CB_D_1 and CB_D_1_D were characterized by a similar behaviour, with a final diagonal main crack connecting both loaded corners involving both bed and head joints along the compressed diagonal. On the other hand, smart bricks have added an inherent weak spot to masonry with cracks arising along these planes of weakness, as reproduced by FEM model. (Figure 83)

The plots show where the cracks involved the mortar joints also outside the diagonal courses, with a more widespread distribution that became scattered, only in the case of reduced mortar filling differently from the case of intact ones, where the cracks are concentrated in the central area.

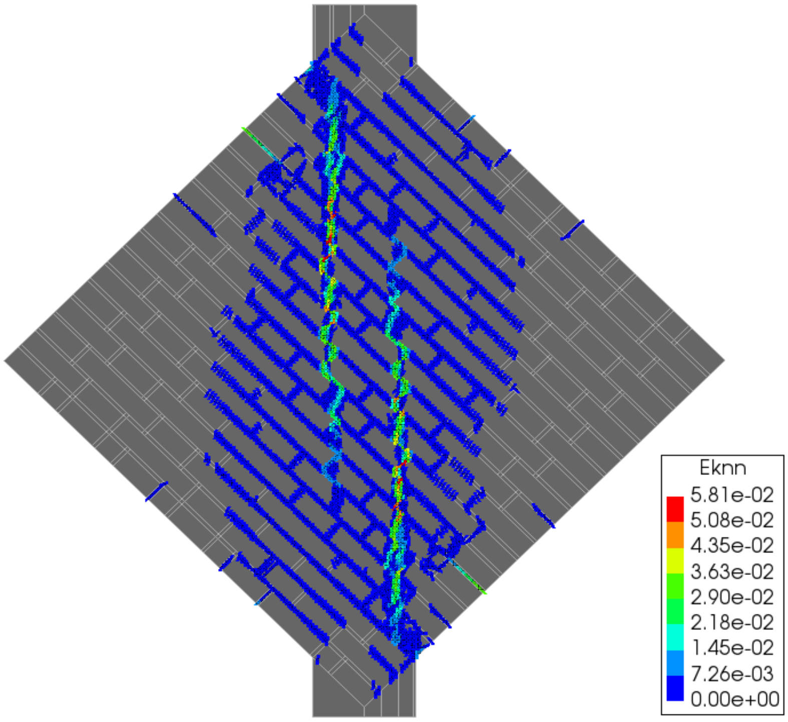

a)

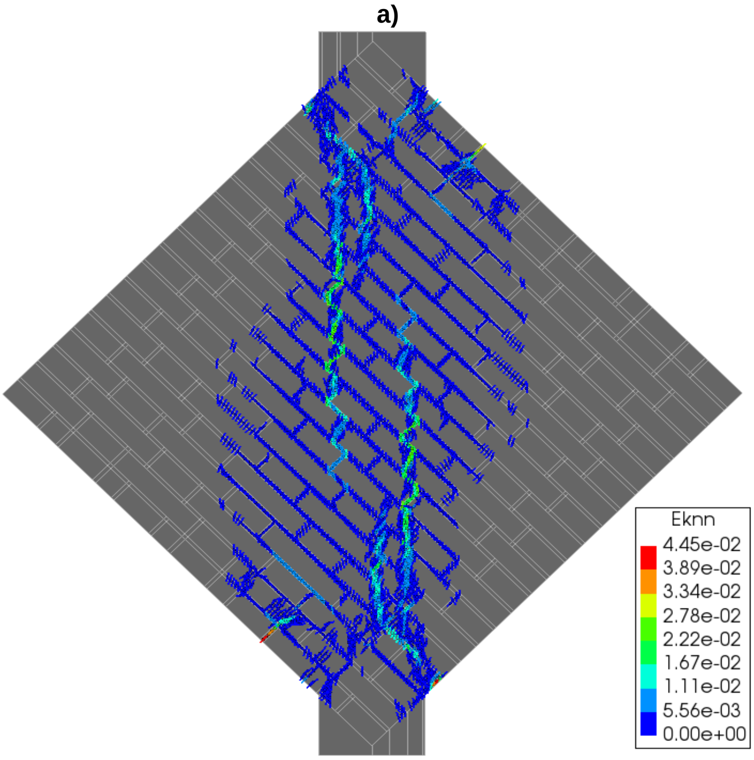

b)

Figure 82. Numerical failure mode for: a) CB_D_1, b) CB_D_1_D

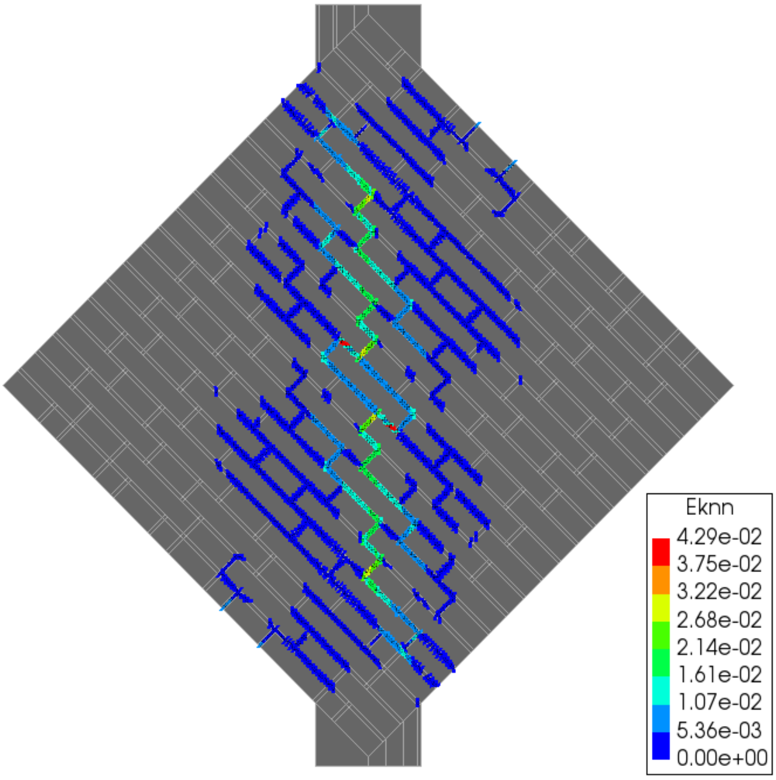

a)

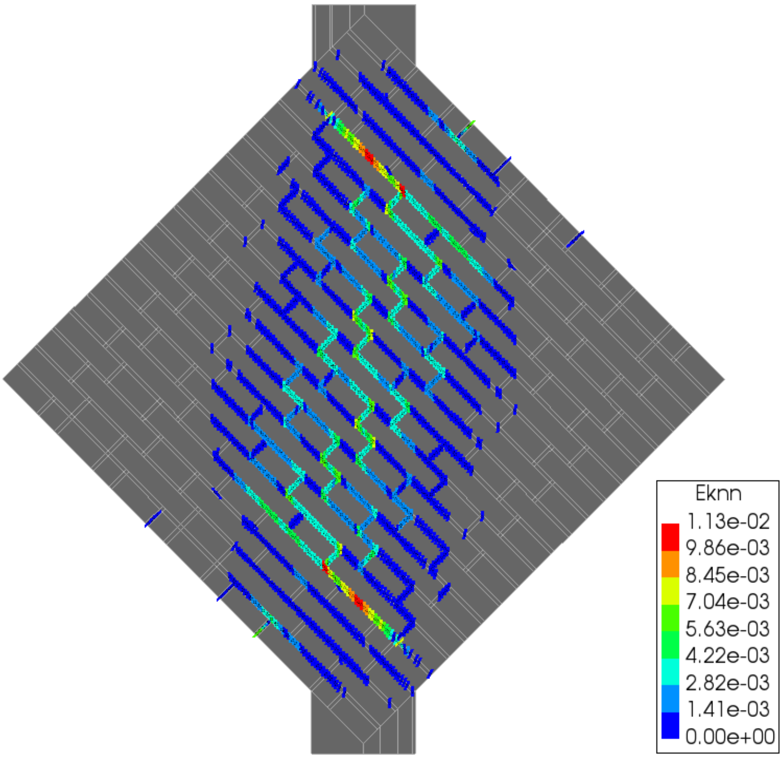

b)

Figure 83. Numerical failure mode for: a) CB_D_2_m, b) CB_D_2_D_m

Observing the maximum principal stress (Figure 84), it can be shown that failure occurs at the attainment of the tensile strength mainly in the central region of the panel while for unfilled joints there is a higher concentration of tensile stresses also along the bed joints and on areas closer to the units.

The main aspects to be noted in the results of the numerical tests on the masonry are:

•the compressive stresses are concentrated in an area more or less coincident with the direction of the compression load except for aged specimen where there are zones with different stress concentrations in the units closer to unfilled mortar joints;

•there is a higher concentration of stresses along the bed joints to panel edge on areas closer to the head joints, especially when these are unfilled (Figure 85);

•in the corners of the masonry wallets a high concentration of stresses and deformation in the units is shown.

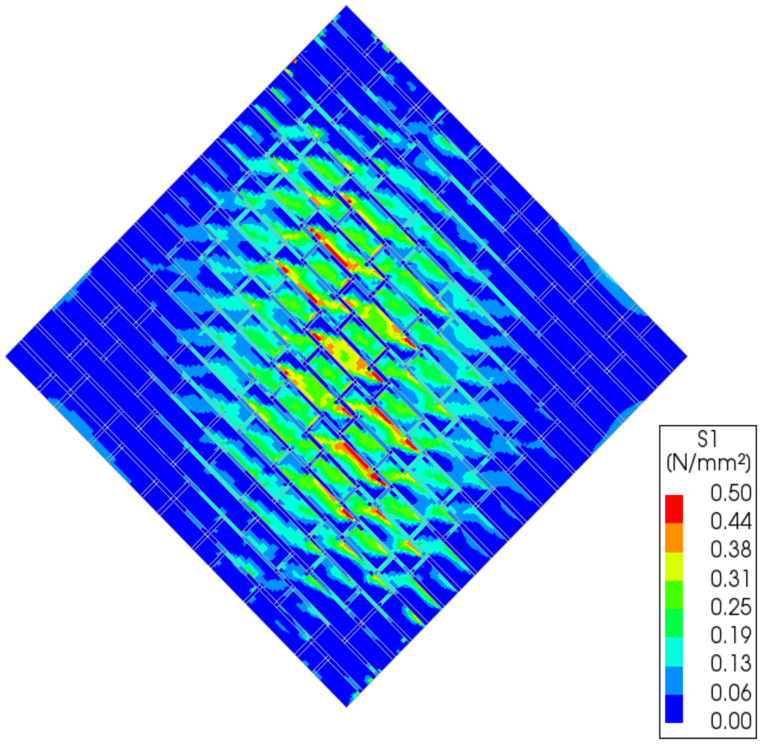

a)

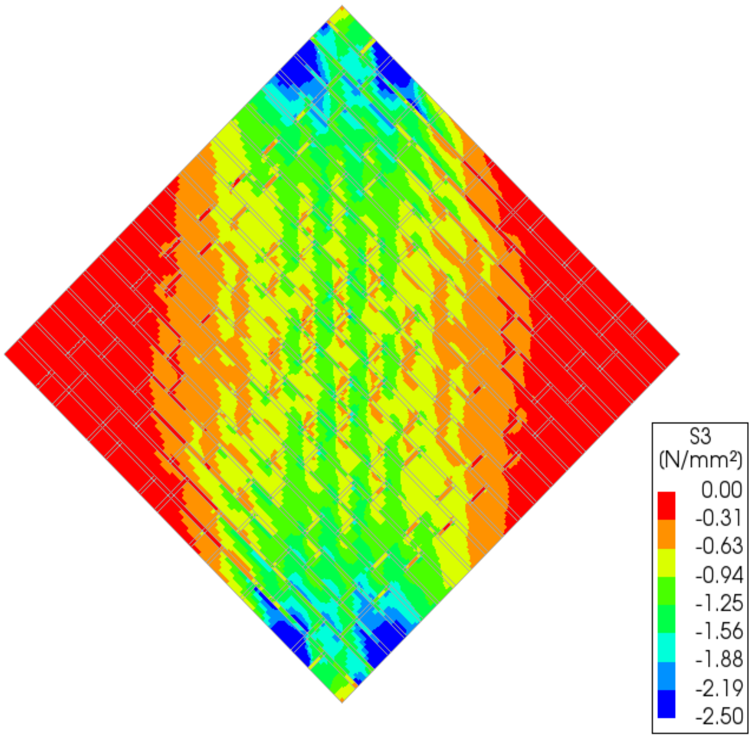

b)

Figure 84.) Picture of a) maximum and b) minimum principal stress for intact panel

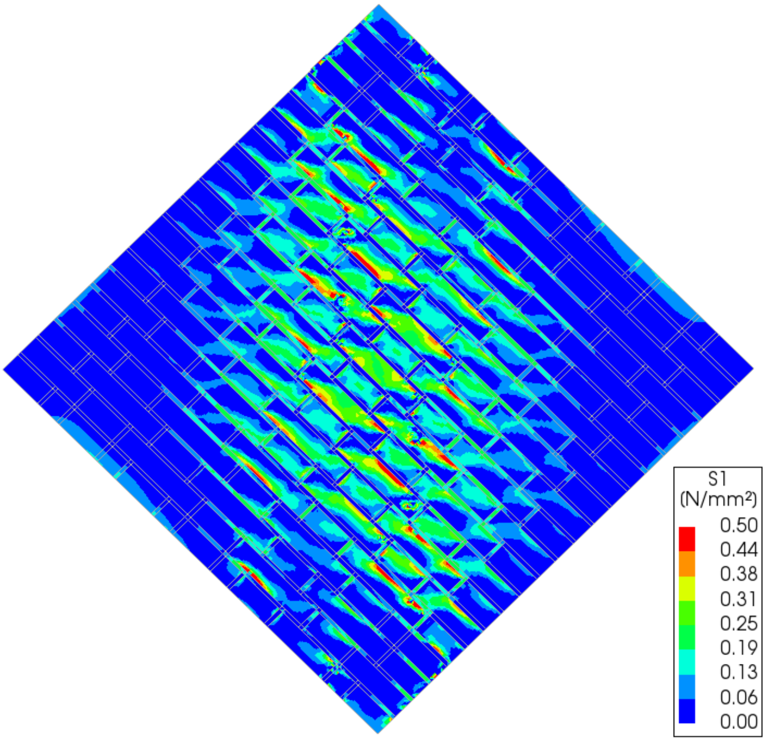

a)

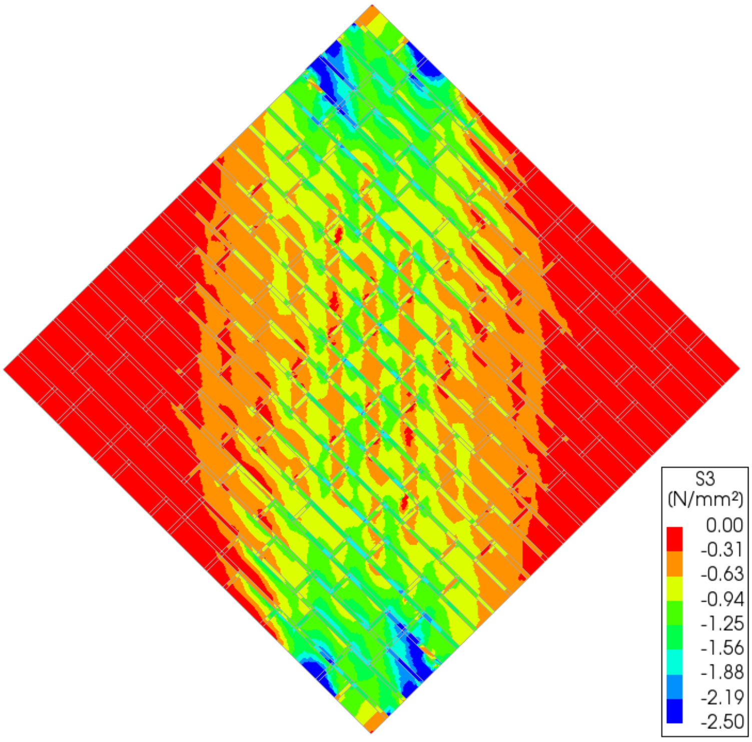

b)

Figure 85. Picture of a) maximum and b) minimum principal stress for deteriorated panel.

Similar results were found for specimens with embedded smart bricks, and Figure 81.b shows the numerical-experimental comparison in terms of shear stress-strain diagrams.

Despite the simplicity of this plane model, it was able to reproduce the stress distribution as shown in Figure 86 and Figure 87 where the maximum and minimum principal stresses, S1 and S3 at the final step of the analysis, are reported.

In the full mortar joints specimen with both front and rear sides placed smart bricks, stresses mainly affect the bricks at the ends as well as in the central area while for specimen joints unfilled stresses spread around the central region affecting especially the bed and head joints.

Compression stress flow away from the region occupied by the smart bricks, with a high concentration of stresses at the corner, and consequently also for strains recorded by smart bricks.

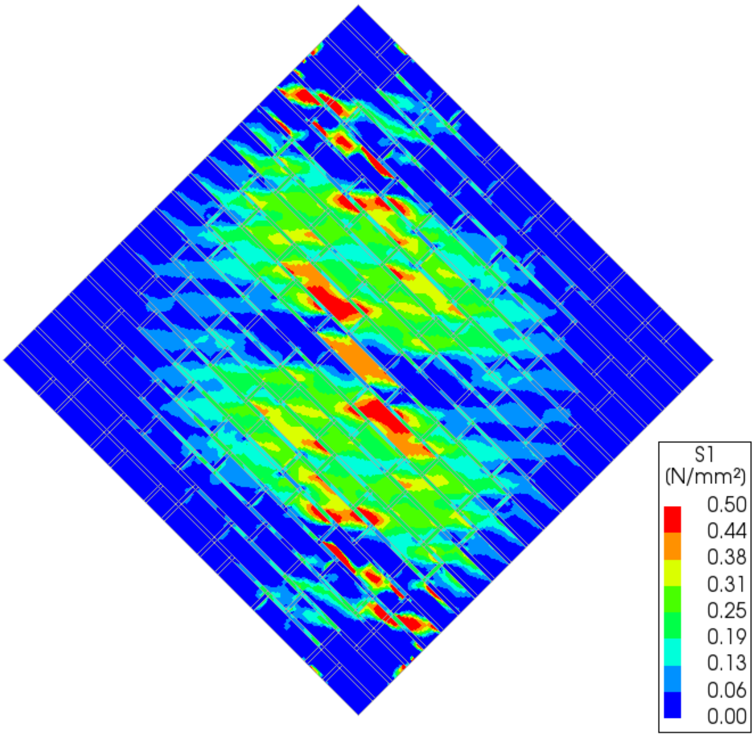

a)

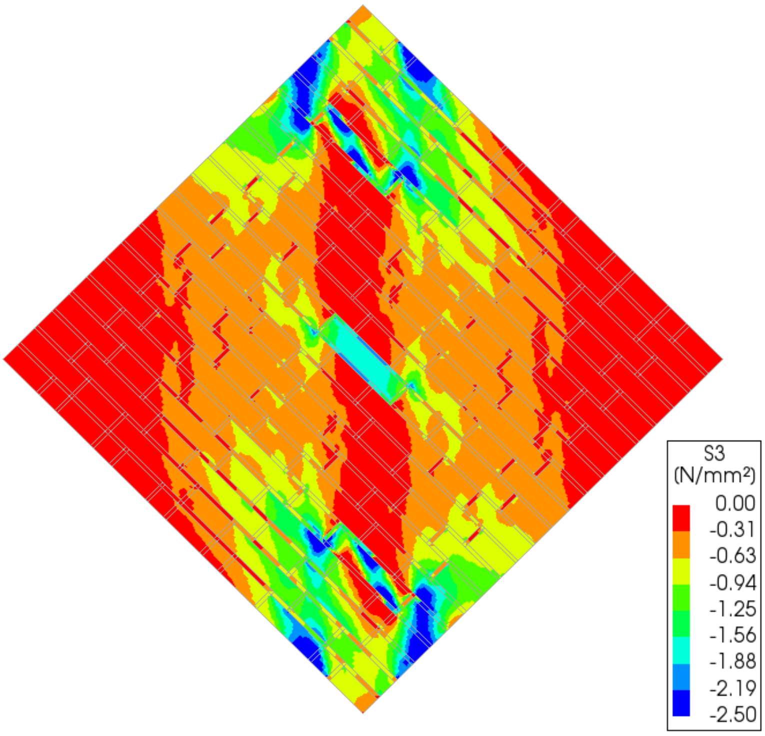

b)

Figure 86. Picture of a) maximum and b) minimum principal stress for intact panel embedded with smart bricks

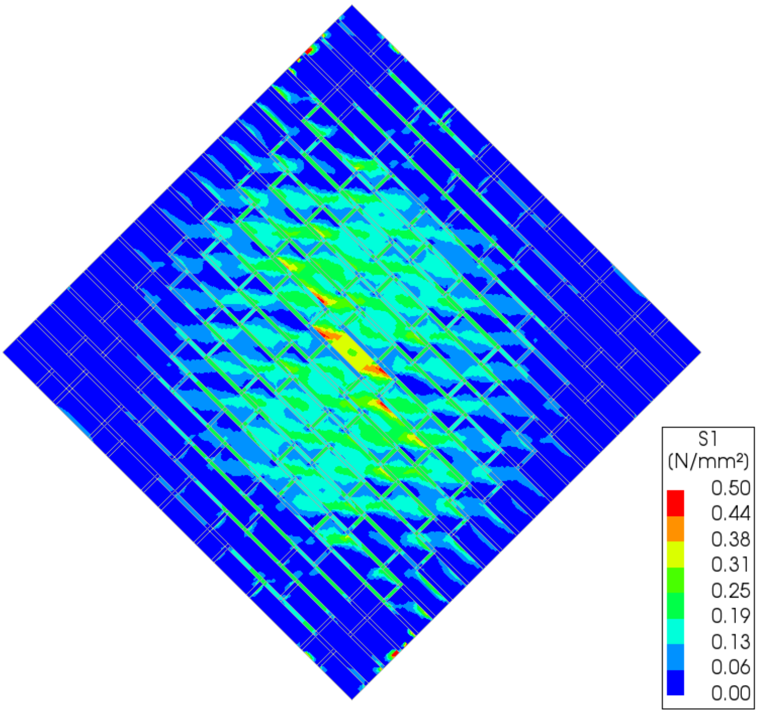

a)

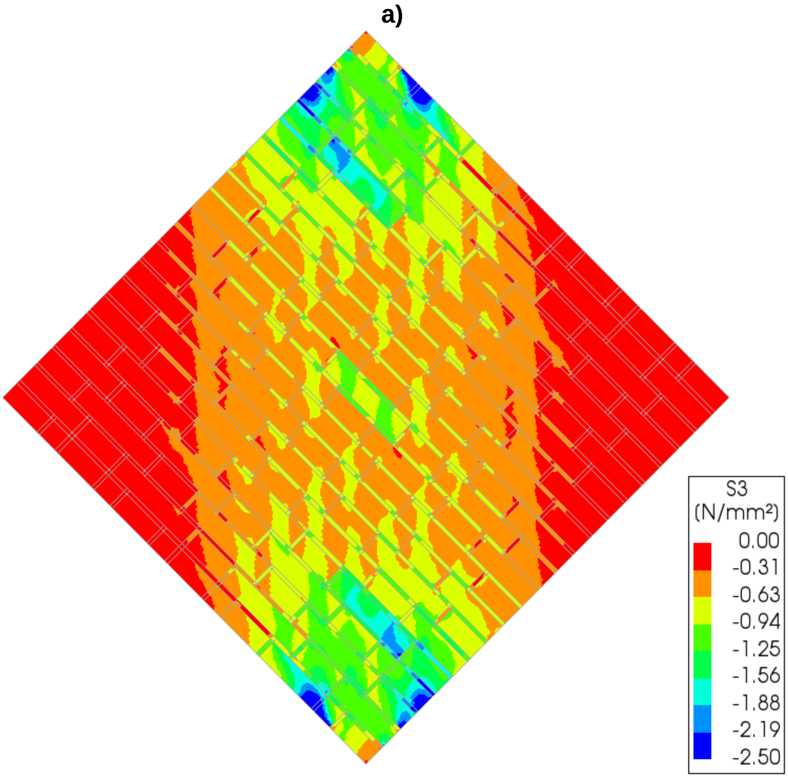

b)

Figure 87.Picture of a) maximum and b) minimum principal stress for deteriorated panel embedded with smart bricks.

4.5. Comparison of numerical-experimental tuff test

The numerical-experimental comparison in Figure 88 and Figure 89 shows a satisfactory agreement between the numerical and experimental average shear stress-strain diagram.

The numerical curves, different for intact and deteriorated mortar joints, are always positioned within the two experimental curves well describing the main aspects of τ–γ diagram. (Figure 89)

As mentioned in the experimental description, specimens couples TM_D_1/TM_D_1_D and TM_D_2/TM_D_2_D have a similar two-by-two behaviour, in terms of elastic stiffness.

From compression test on deteriorated specimens, a limited material ejection was recorded, without occurrence of splitting phenomenon. Considering that splitting failure for this test is due to the difference between elastic properties of masonry units and those of mortar, the greater masonry deformability, due to not fully filled mortar joints, may have not fully involved tuff's stiffness. To account for experimental variability, two numerical models have been adopted, with the difference in tuff elastic modulus passing from 2100 MPa to 1200 MPa, close to mortar's elastic modulus expressed, respectively with T2100 and T1200 both for intact "INT" and deteriorated "DET" numerical models(Figure 88 a and b).

The curve for full mortar thickness has a similar trend to the experimental one, Figure 88a, characterized by a linear elastic branch until the 45% of the shear strength, the latter comparable to the experimental ones.

Anyway, for deteriorated numerical curve, where a similar trend to experimental one was observed, in terms of masonry elastic stiffness for both numerical models, while the latter with tuff elastic modulus value set to 1200 MPa has also a comparable shear strength in Figure 88 b.

From Figure 89 emerges that, with tuff elastic modulus value set (*i.e.* T2100 or T1200) geometric degradation of mortar joint does not weight on masonry initial elastic stiffness, but only lowering shear strength threshold, reproducing the observed experimental behaviour.

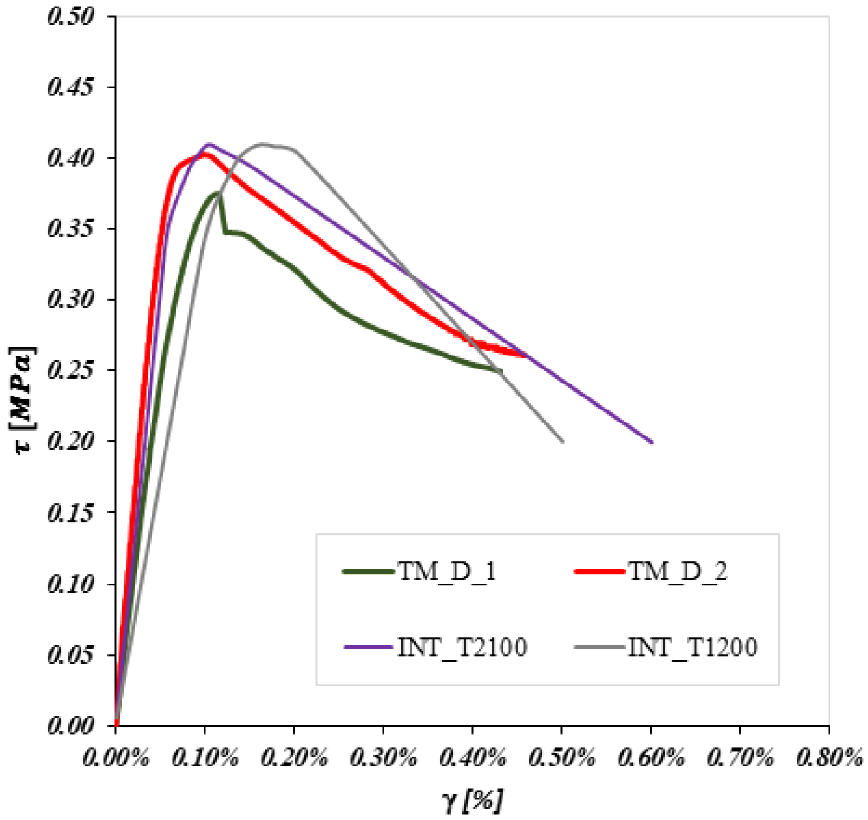

a)

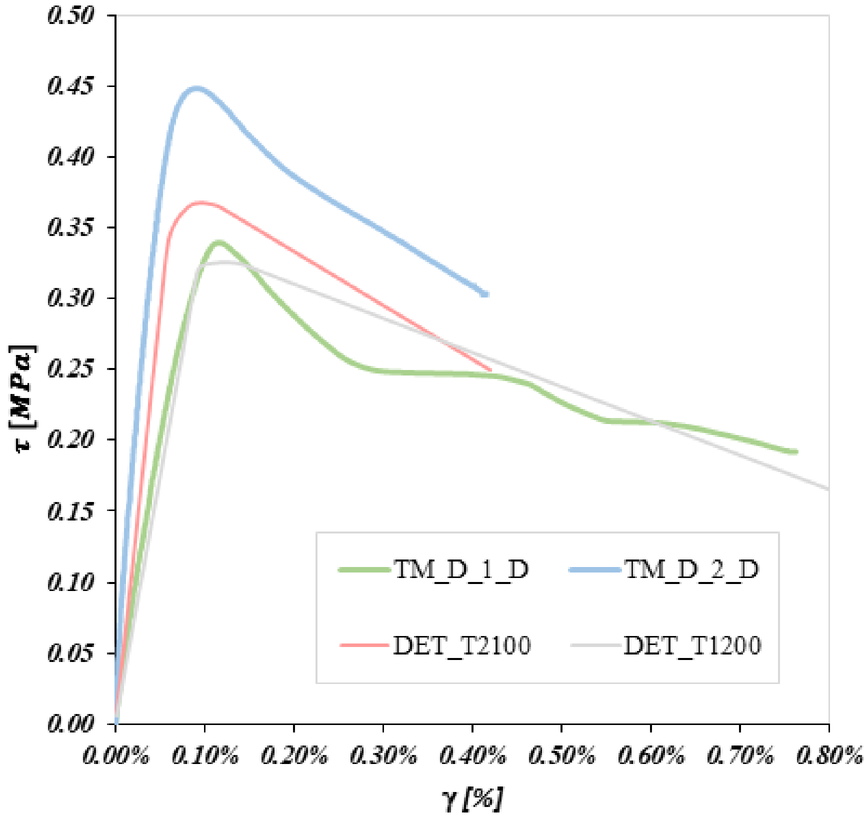

b)

Figure 88. Comparison between numerical and experimental results for a) intact and b) deteriorated wallets.

So FEM models were able to simulate not only the difference in shear strength but also the shear strain.

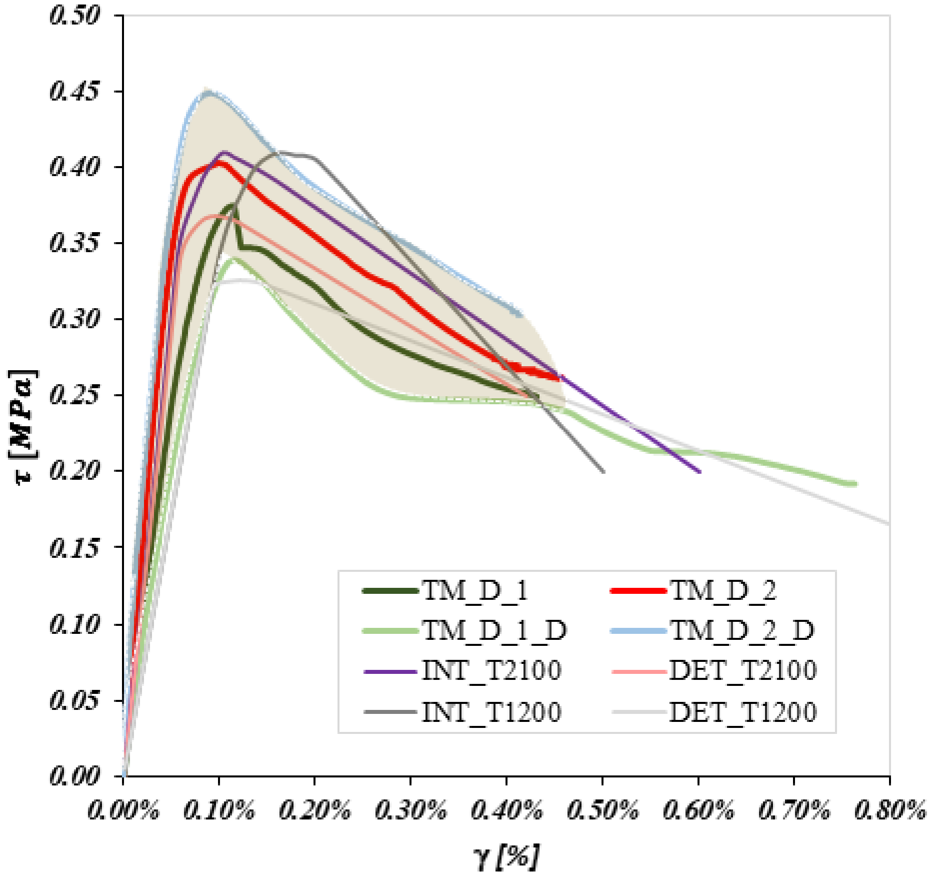

Figure 89. Comparison between numerical and experimental results for both intact and deteriorated wallets

Figure 26, Figure 27, Figure 28and Figure 29 introduced in the experimental section, detail the progress of cracking for experimental wallets, with a satisfactory agreement with the numerical results (Figure 90 and Figure 91)

Intact panels for both tuff elastic modulus series (*i.e.*T2100 and T1200) show a similar failure pattern, with a final diagonal main crack connecting both loaded corners and involving both bed and head joints along the compressed diagonal, accompanied by tensile cracks in the tuff units, with cracks arising along these planes of weakness. (Figure 90.a and Figure 91.a) For series T2100, plot shows mortar joints cracks also outside the diagonal courses.

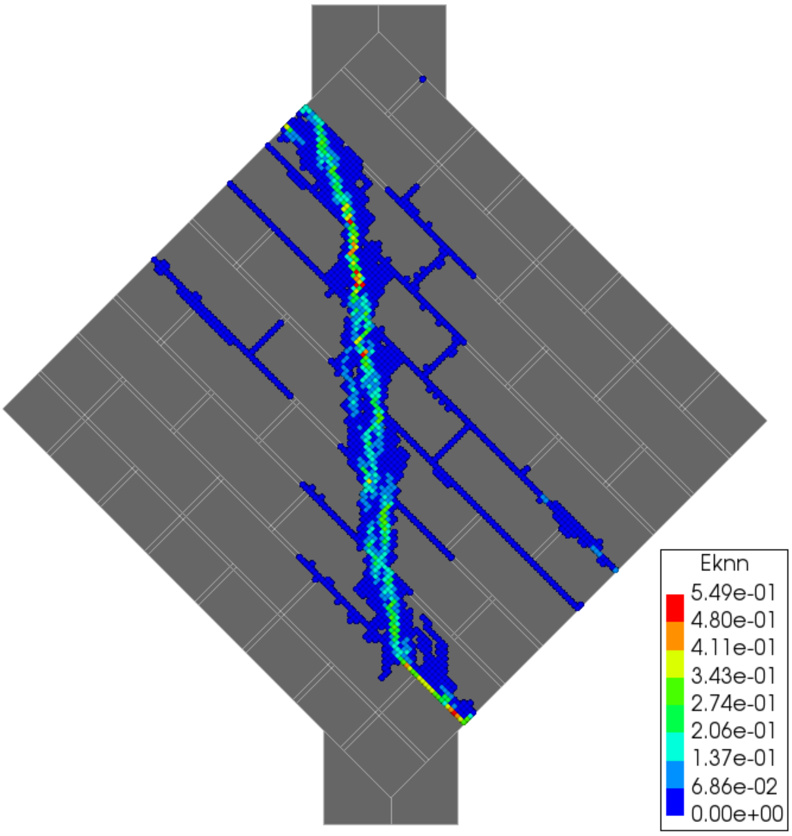

a)

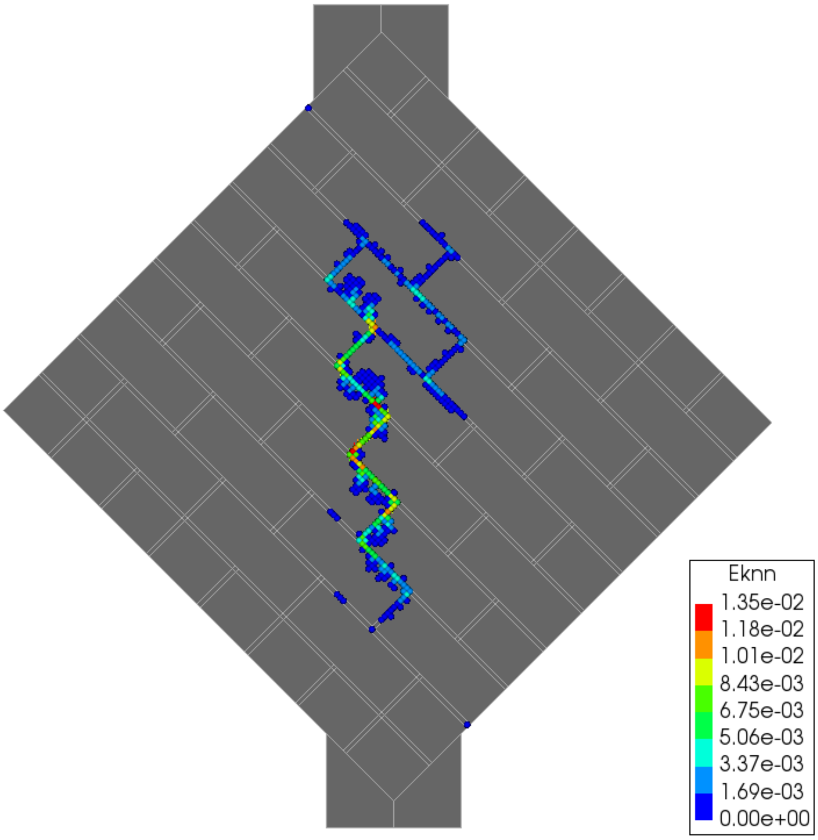

b)

Figure 90 Numerical failure mode for T2100 series a) intact, b) deteriorated configuration.

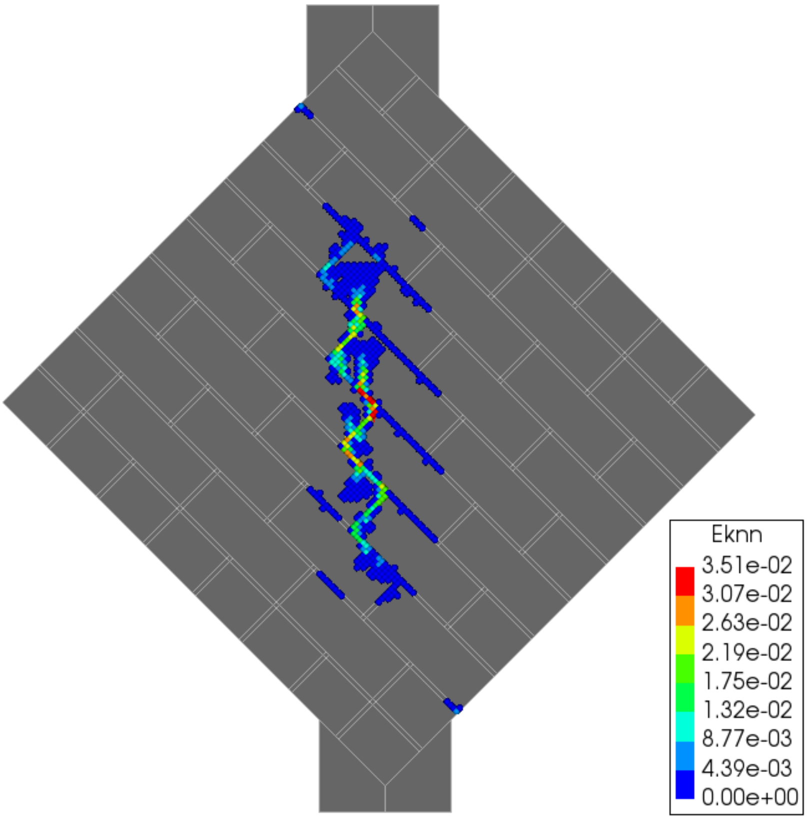

a)

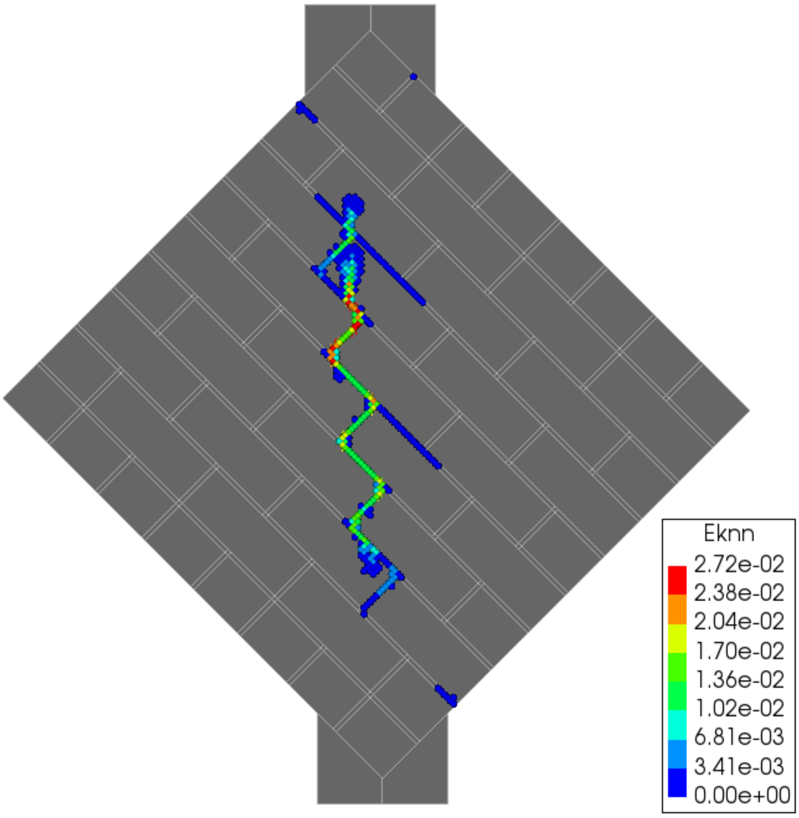

b)

Figure 91. Numerical failure mode for T1200 series a) intact, b) deteriorated configuration.

Deteriorated panels for both tuff elastic modulus series (*i.e.*T2100 and T 1200) exhibit a diagonal main crack involving both bed and head joints along the compressed diagonal, accompanied by few tensile cracks in the stones, reproducing the experimental test well enough (Figure 90.b and Figure 91.b).

As expected, diagonal tension failure mode occurred due to stress concentration along the tensile principal direction. Observing the principal stress, from Figure 92 to Figure 95, it can be shown that wallets failed due to the attainment of the tensile strength mainly in the central region.

For tuff elastic modulus series T2100 a higher concentration of tensile stresses also along the bed joints and on areas closer to unit is showed when geometric degradation of mortar joint was included. Also for intact configuration, non-uniform tensile stresses are present because of different elastic properties of masonry components (Figure 92,Figure 93).

For tuff elastic modulus series T1200 a more even distribution of stresses is shown: tensile stresses tend towards a uniform radial distribution from the central region, while compressive stresses assume an hourglass shape. This trend is partially interrupted, passing from intact to deteriorated configuration because of mortar greater deformability. (Figure 94, Figure 95).

In all cases, compressive stresses are concentrated in an area more or less coincident with the direction of the compression load except for aged specimen where there are zones with different stress concentrations in the units closer to unfilled mortar joints. In addition, in the corners of the masonry wallets, a high concentration of stresses and deformation in the units is shown. For unfilled mortar joints, there is a higher concentration of stresses along the bed joints to panel edge on areas closer to the head joints.

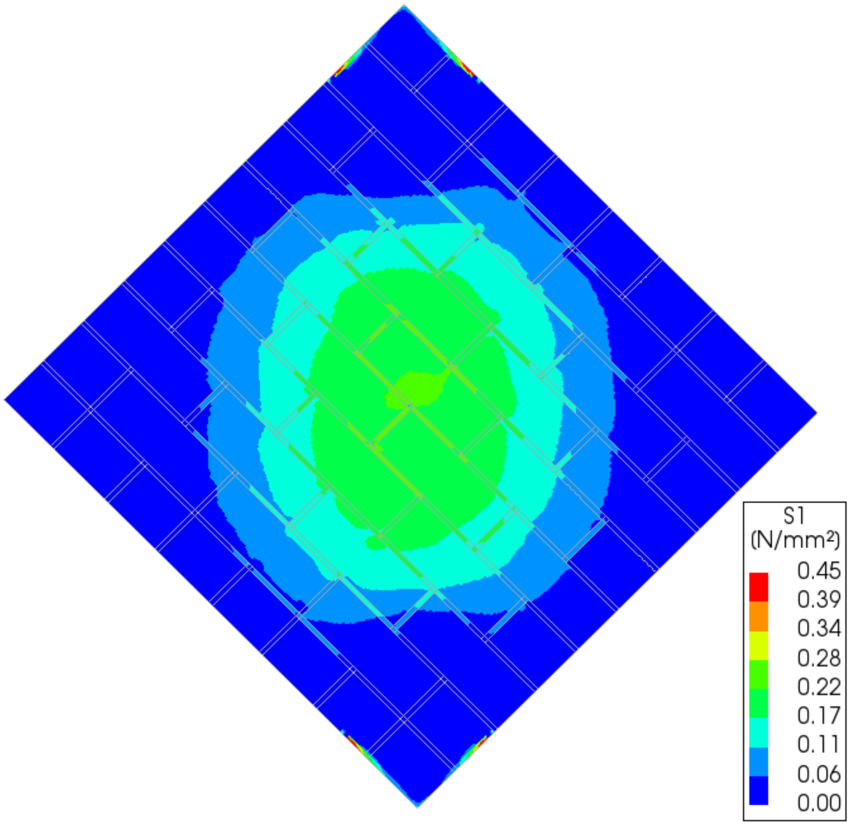

a)

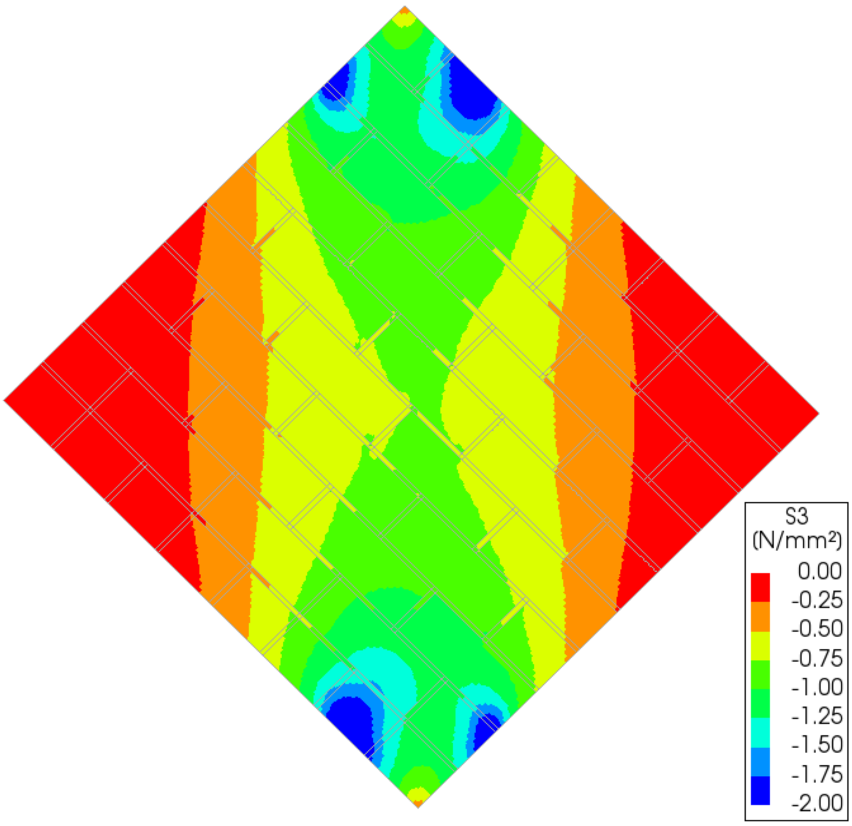

b)

Figure 92 Picture of a) maximum and b) minimum principal stress for T2100 series intact panel.

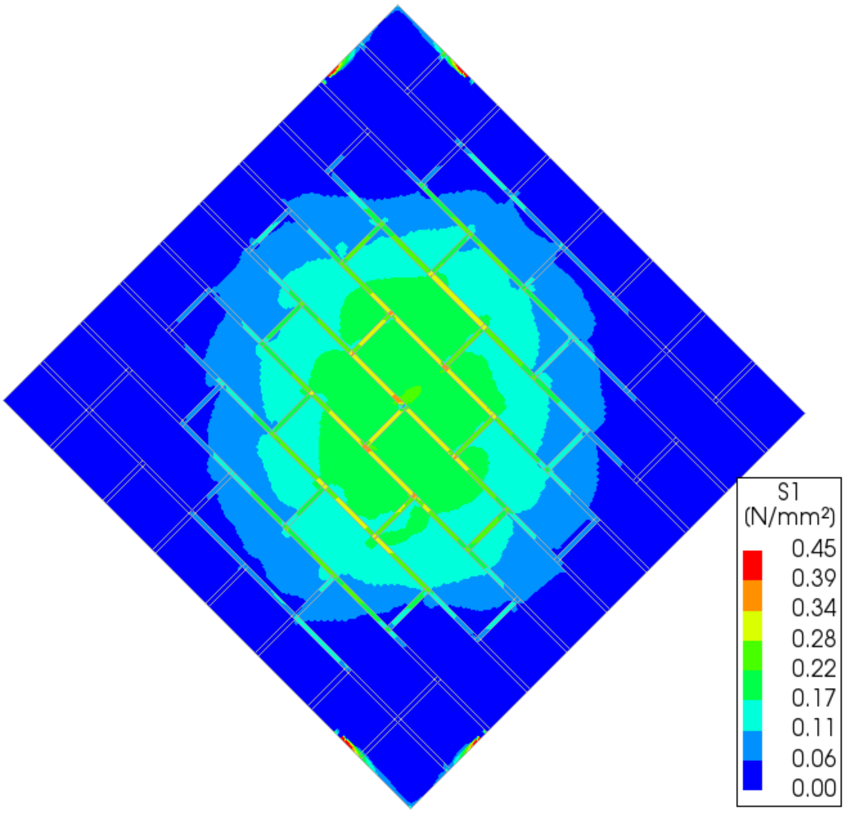

a)

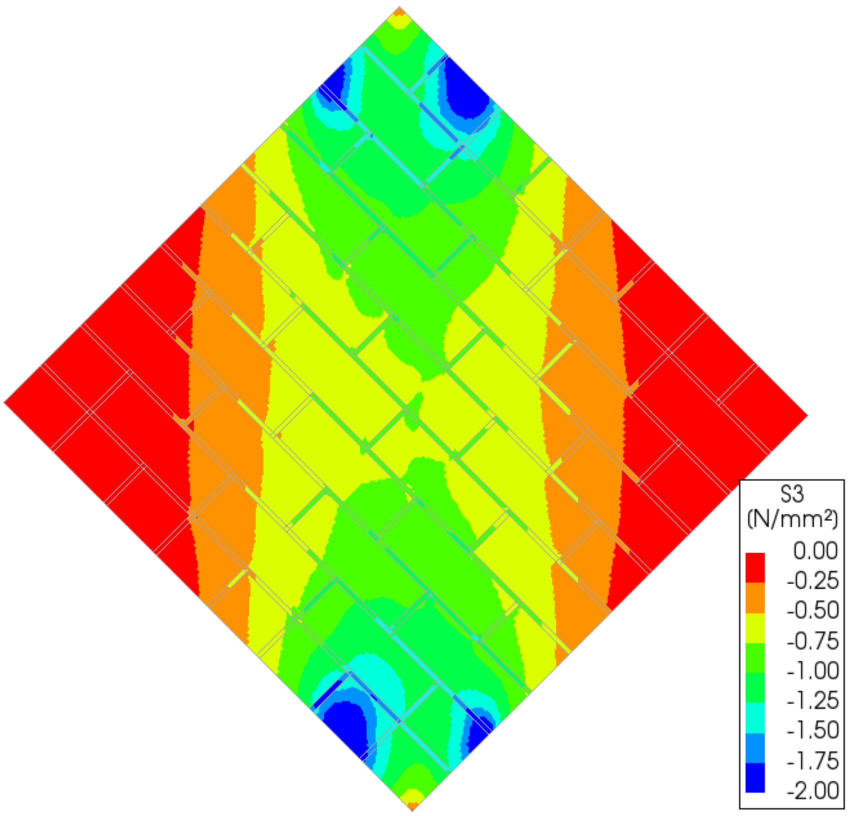

b)

Figure 93) Picture of a) maximum and b) minimum principal stress for T2100 series deteriorated panel.

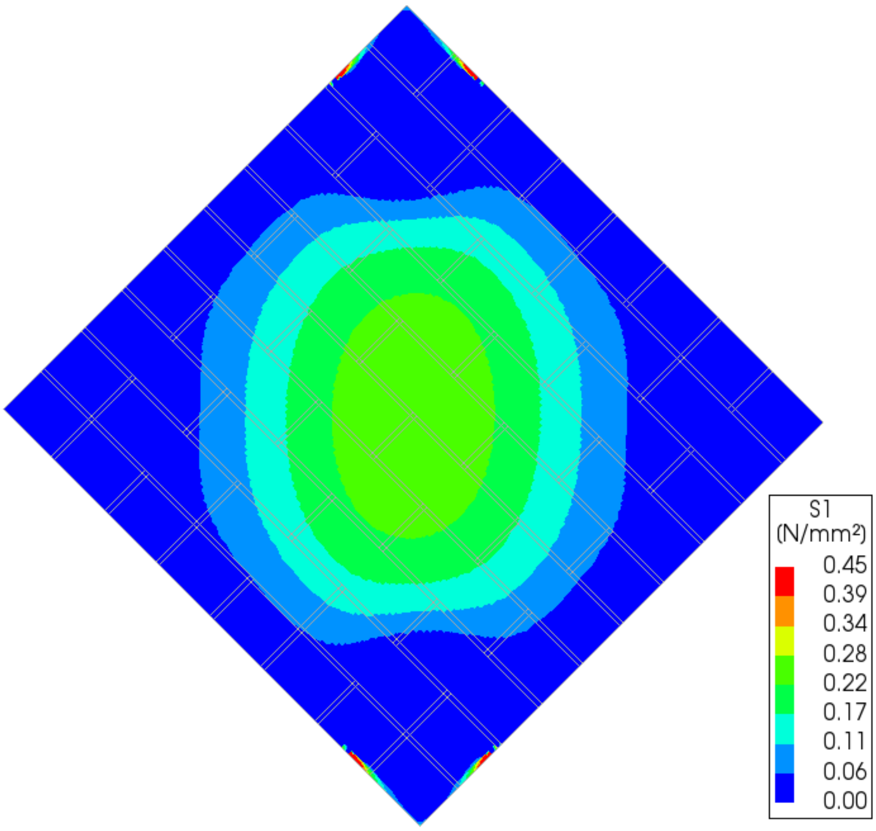

a)

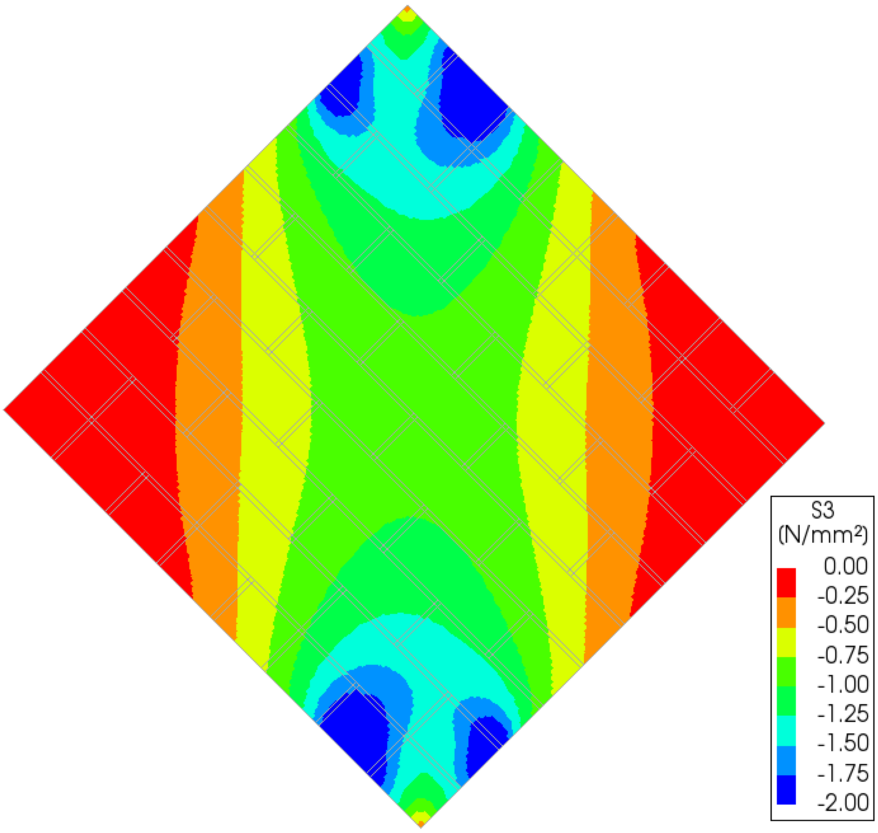

b)

Figure 94. Picture of a) maximum and b) minimum principal stress for T1200 series intact panel

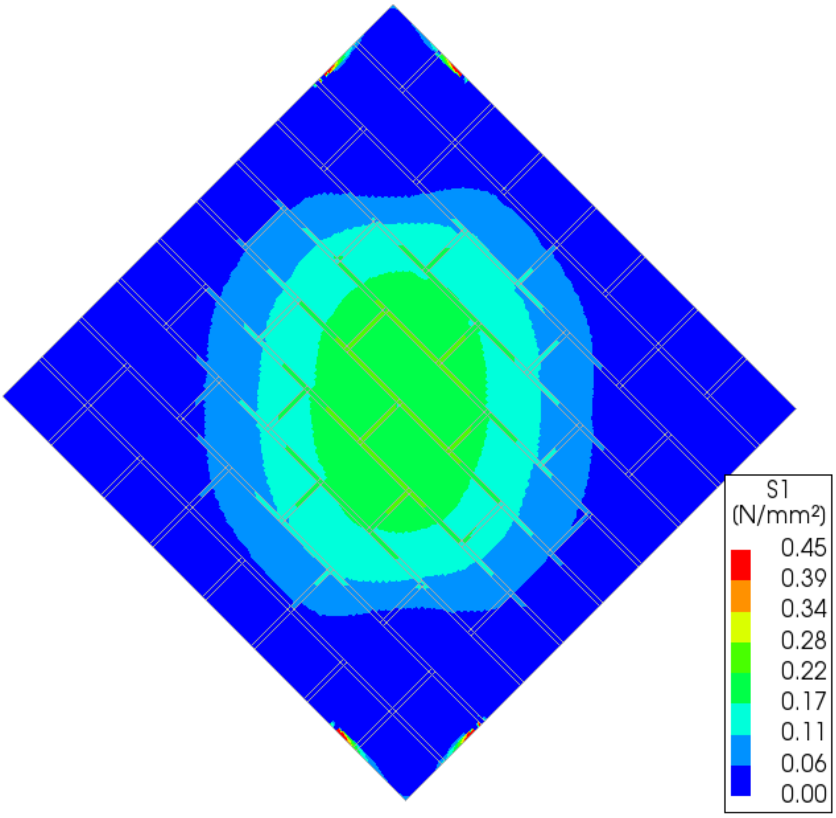

a)

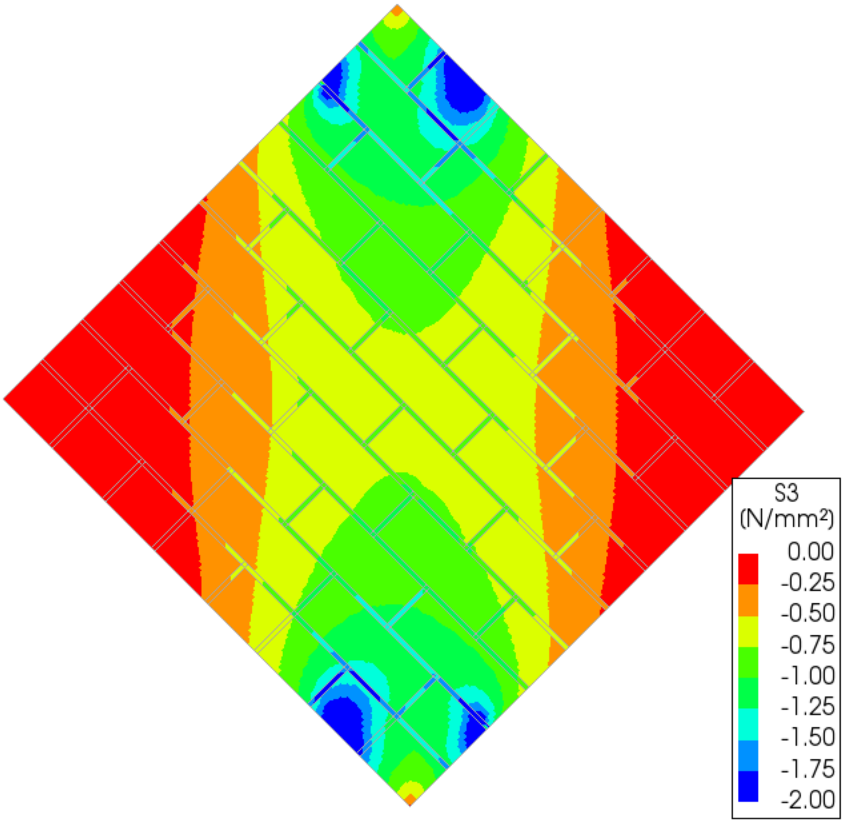

b)

Figure 95. Picture of a) maximum and b) minimum principal stress for T2100 series deteriorated panel.

4.6. Numerical modelling for settlement test

Settlement loading tests on the intact and deteriorated URM were simulated in DIANA. As done for the compression tests previously introduced, eight-node quadrilateral elements (CQ40S) were used to simulate the tuff stone masonry, in micromodelling approaches. The mesh of the FEM model was generated using squared, curved shell CQ40S elements with 8 nodes and isoparametric formulation, representing tuff units and mortar joints without unit-mortar interface elements between them. Although, FEM was used to simulate settlement loading tests, *i.e.,* an in-plane load for the URM, the choice of curved shell elements used in the FEM model has been made to use the same modelling strategy for the out-plane tests on the same URM geometry, described in the next paragraph. The size of finite elements was equal to the thickness of mortar joints and was selected after a mesh sensitivity analysis.

The geometry of the URM wall exactly reflects the dimensions of the tested walls and the numerical models share also the same boundary and loading setup, according to the experimental tests. Steel profile elements are introduced to correctly simulate the bottom boundary conditions, as schematically illustrated (Figure 96). All sensitivity analyses showed a negligible influence of the wooden lintel on the spandrel capacity but only some stress concentrations at the masonry-wood interface, so the lintel was not included in the final numerical model.

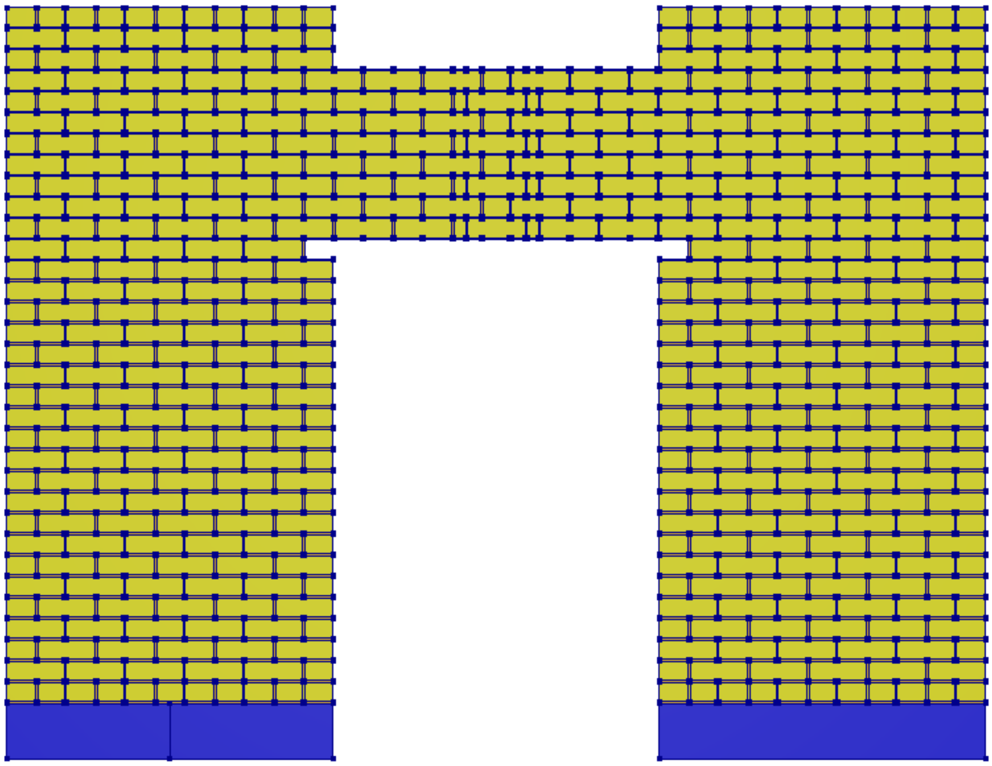

Figure 96. Finite-element model

The collapse of the URM is induced by the uniform settlement of the pier that is introduced in the model through the movable support. A monotonic increasing vertical displacement was prescribed in the middle of the steel plate and displacements were recorded at the corresponding LVDTs locations, while all nodes of the fix pier base sections were pinned, leaving free the pier top sections. Since the intact URM had at the bottom beam PTFE sheets at the screws locations, and the deteriorated URM had an hydraulic jack directly applied at the bottom beam, it was added an horizontal constraint at the bottom beam only in the case of deteriorated test. Vertical loads on the piers were applied with a uniform pressure to provide 200 kN axial forces for each pier and when the vertical pre-compression loads were applied, finally a maximum settlement of 15 mm was applied for the intact URM, while for the deteriorated one was applied a maximum settlement of 35 mm. URM were analysed through displacement-controlled nonlinear analysis based on Newton–Raphson incremental iterative procedure and a mixed force–displacement convergence criterion.

A smeared crack model was employed to simulate the fracture process within tuff masonry. The behaviour of tuff system has been simulated by means of a Total Strain Crack model, which describes the tensile and compressive behaviour of a material by means of a stress-strain relationship as depicted in Figure 80.

In the analysed case of masonry buildings subjected to settlement, the damage is mainly due to tensile and shear stresses, and therefore the focus is on the modelling of tension and cracking modes. For unit tuff and mortar joint defined as isotropic continuum elements, the cracking direction does not necessarily follow the material texture. The models provide crack strains which have to be translated to crack widths via the use of the crack bandwidth h as a finite element discretisation parameter.

The tension softening law was defined by the tensile strength f_t, the fracture energy G_f and the crack bandwidth h, which is related to the element size. The material parameters were obtained from the experimental tests and they are listed in Sections 2.3.4 and 2.3.6.

To account for experimental variability, as well as it was done for the compression tests, two numerical models have been adopted, with the difference in tuff elastic modulus passing from 2100 MPa to 1200 MPa, close to mortar's elastic modulus, expressed, respectively, with T2100 and T1200 both for intact "INT" and deteriorated "DET" numerical models. In fact, according to the previous work by Lignola et al. [81], in the case of tuff masonry, the FE numerical global behaviour of the entire masonry is primarily affected by both the compressive and tensile energy values assigned to tuff stones.

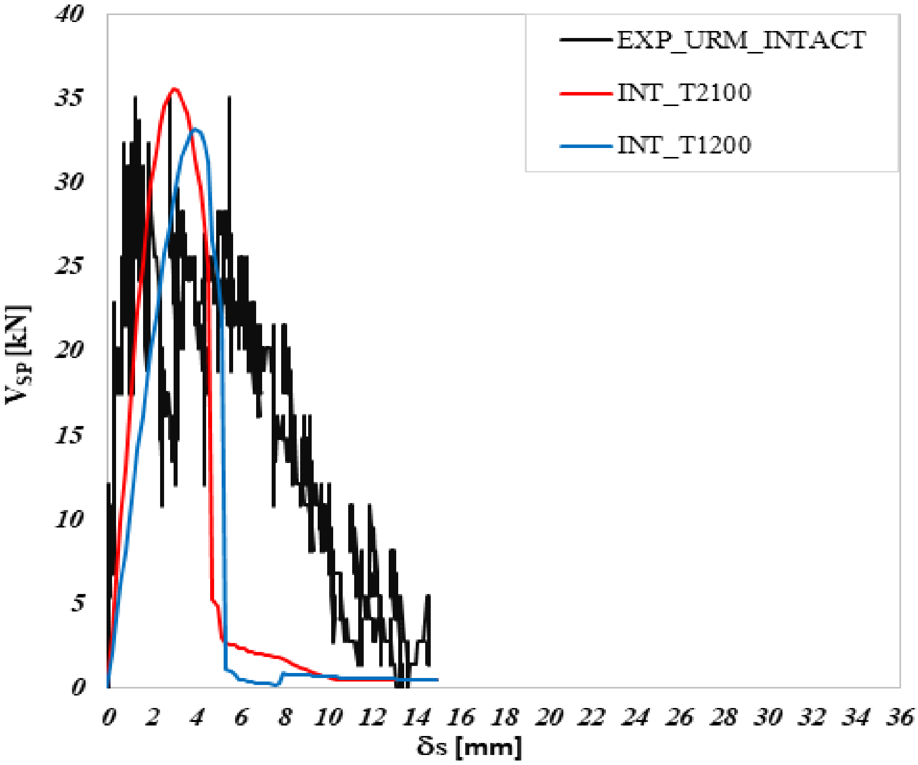

a

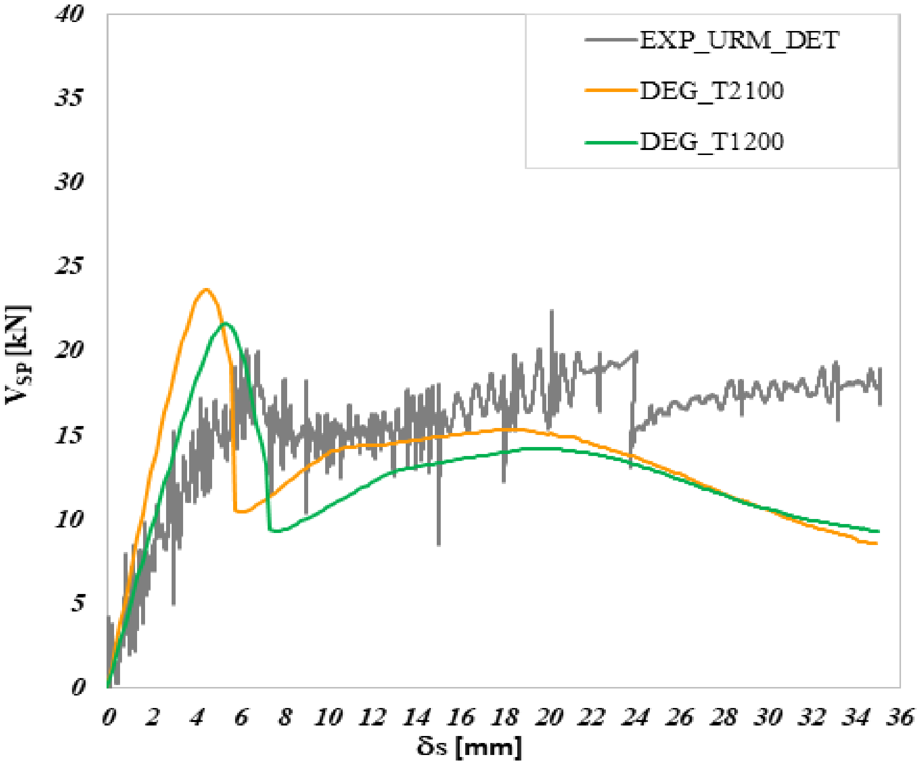

b)

Figure 97. Comparison between numerical and experimental results for a) intact and b) deteriorated URM

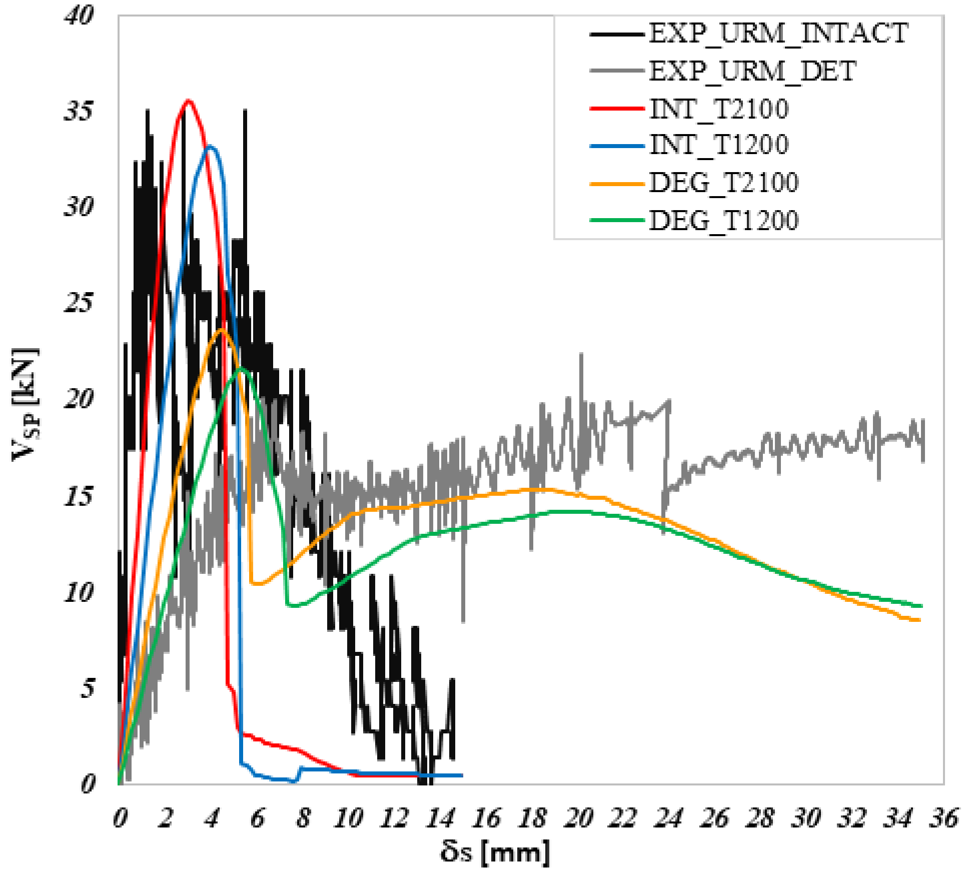

Figure 98. Comparison between numerical and experimental results for both intact and deteriorated URM

In general, a good correlation can be observed from both qualitative (failure mode occurred) and quantitative (predicted value of V_{sp}) points of view. In Figure 97and Figure 98 the performance of the numerical analysis is evaluated in terms of spandrel shear and displacement imposed at the pier base section. Spandrel shear V_{sp} can be defined from a condition of global equilibrium. During the test execution, a vertical force is distributed over the two piers as a result of the deflection set at the spandrel panel. In fact, V_{sp} is considered equal to the axial force N_{pr} acting on the pier subjected to settlement, given by the gravitational force and the load arising as a result of the imposed settlement δs, minus the contribution of the initial load.

A satisfactory agreement between the numerical and experimental spandrel shear displacement diagram was found. The numerical curves, different for intact and deteriorated mortar joints, well described the main aspects of V_{sp} -δ_s diagram (Figure 98).

The curves with full mortar thickness have a similar trend to the experimental one, Figure 97.a, characterized by a linear elastic branch up to the 45% of the shear strength, comparable to the experimental value . Indeed, intact URM for both tuff elastic modulus series (i.e.T2100 and T 1200) match the shear strength of the spandrel so well, especially for T2100 series, showing both spandrel failure after the attainment of the peak force. The numerical T2100 series is also able to match the displacement at which the peak shear was reached, an experimental value between 1.3 and 2.6 mm, taking into account that the axial force acted on piers in intact configuration was obtained by strain gauge calibration and not with the load cell, unlike the deteriorated test, resulting in a discontinuous response. For this reason, stiffness of the intact URM could be lower than recorded. As experimentally noted, the advanced cracking on the end sections of the spandrel, without the development of a residual resistant mechanism in the spandrel, bring URM to turn into two separate cantilevers linked by a horizontal pendulum without any more load carried as the settlement progresses.

Anyway, also for deteriorated numerical curve, a similar trend to the experimental one was observed, with a satisfactory agreement in terms of both masonry stiffness, shear strength and the corresponding displacement, especially for the T1200 series (Figure 97.b).

Both tuff elastic modulus series, after the attainment of the peak force, represent an ascending phase that ends when subassemblage produced masonry cracking in the spandrel and then resulting in a compressed strut within them. Also, the numerical force-displacement curve was able to capture the residual strength for the deteriorated URM corresponding to the diagonal compression strut of the spandrel panel.

From Figure 98 emerges that, with selected tuff elastic modulus values (i.e. T2100 or T1200) geometric degradation of mortar joints impacts on both masonry initial elastic stiffness and the shear strength threshold, reproducing the observed experimental behaviour.

For increasing values of settlement, the combination of tensile stresses induced to the URM and the low material strength causes the masonry damage, as previously described, with URM stiffness reduction.

In Figure 99,Figure 100 the performance of the numerical model is evaluated in terms of resulting crack patterns. The model is able to reproduce all the main cracks leading to the failure mechanisms described along with the experimental results. In particular, the model reproduces the localisation and propagation of bending cracks from the peak load to the end of test. Figure 99,Figure 100 show a classical representation of a smeared cracking strain field according to the adopted numerical modelling strategy. These do not aim to represent effective discrete cracks; but highlight the portions where cracking strains occur numerically.

The FE model shows strain localization at the locations of the observed cracks associated with the flexural cracking at the spandrel panel-pier interfaces because of the low tensile strength of the masonry.

After the attainment of the maximum tensile value at the end section of the spandrel (corresponding also to the attainment of V_{sp}), it is noted here a damage mechanism characterized by the opening of the head joints in the corners in tension (Figure 100.a). Then the spandrel behaves as an equivalent strut, which propagates towards the corners (Figure 100.b). On the contrary, in the case of intact URM, the failure mechanism is only due to flexural behaviour; thus the crack pattern is like the Figure 99.a with the attainment of the maximum tensile value at the end section of the spandrel; this is similar to deteriorated URM spandrel described before, but without the subsequent activation of diagonal compression strut. In fact, due to the moderate compressive stresses acting on the contiguous masonry portions, they cannot rely much on the interlocking phenomena since spandrel is unable to develop a diagonal compression strut.

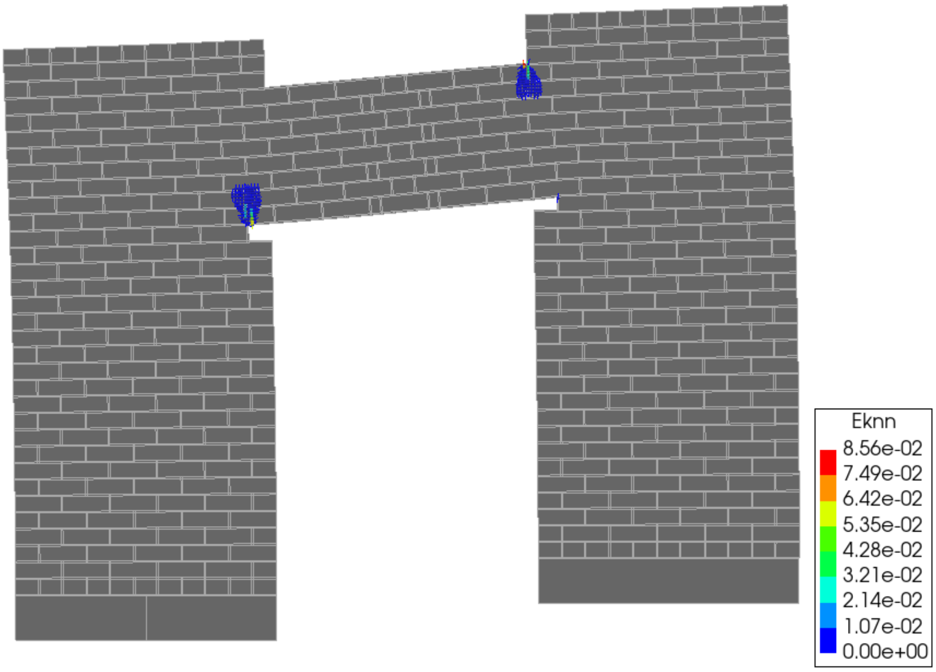

a)

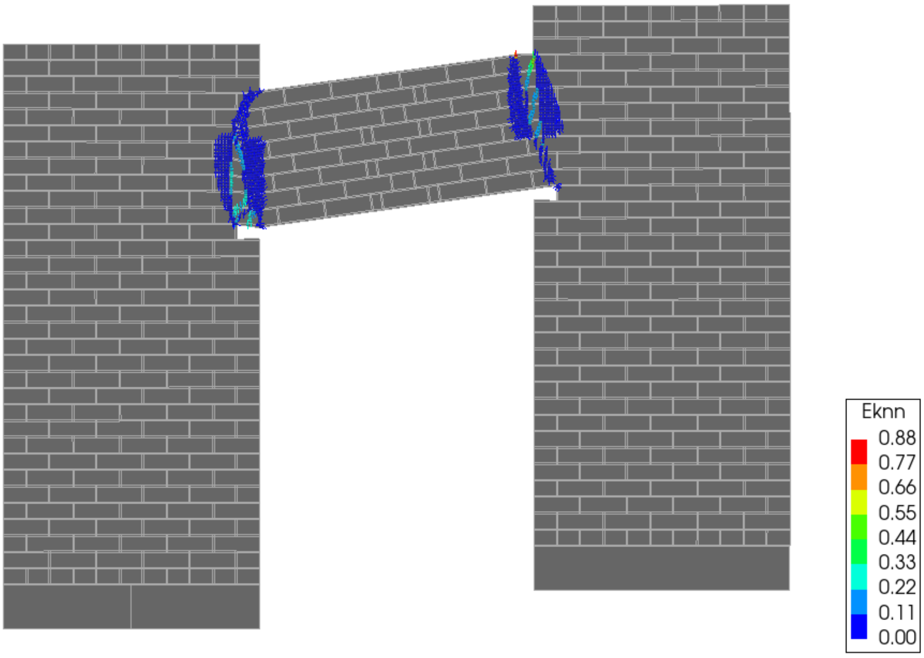

b)

Figure 99. Crack patterns of the intact URM for displacement at a) peak shear strength; b) end test

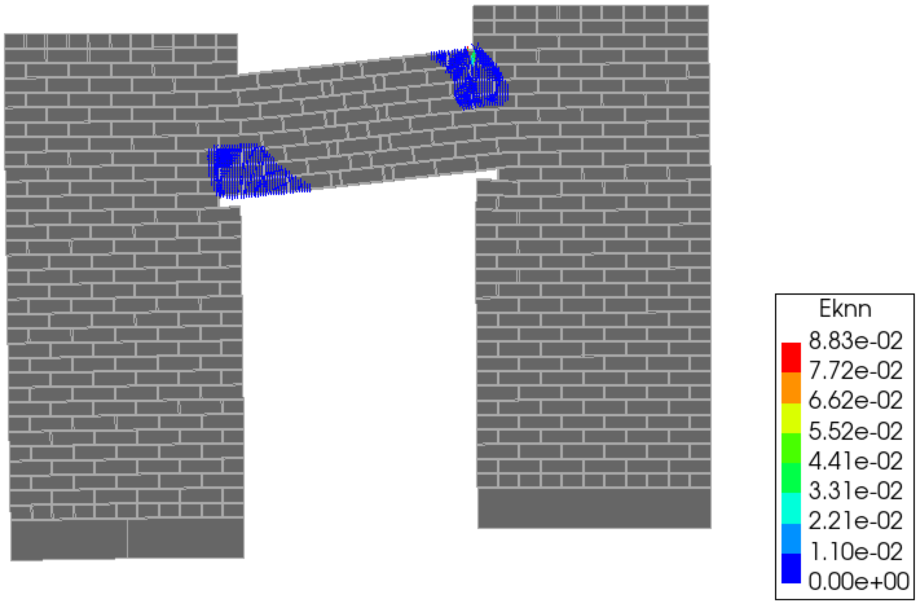

a)

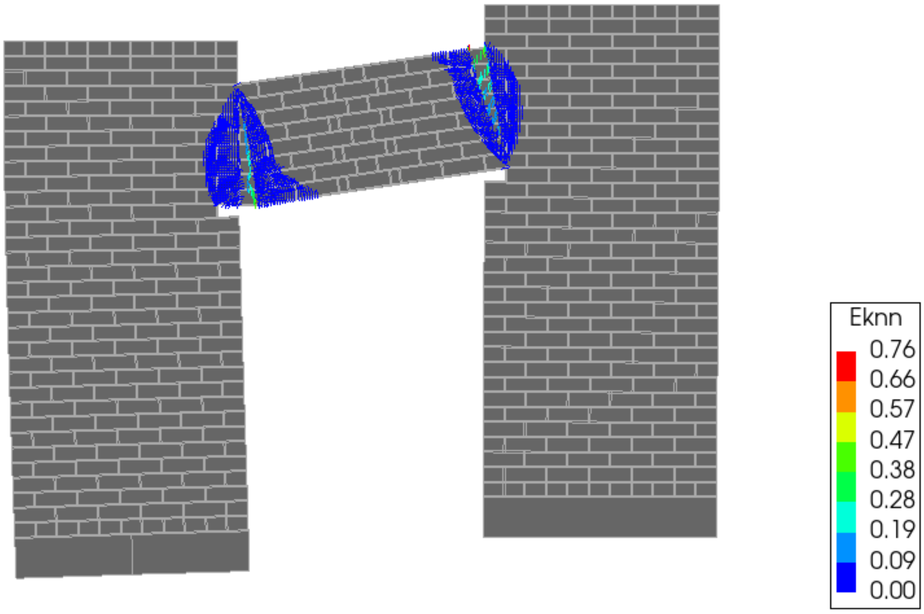

b)

Figure 100. Crack patterns of the deteriorated URM for displacement at a) peak shear strength; b) end test

4.7. Numerical modelling for out plane test

Out of plane loading tests on the intact and deteriorated URM were simulated in DIANA as done for previously introduced URM tests, using eight-node quadrilateral elements (CQ40S) simulate the tuff stone masonry, in micromodelling approaches. The mesh of the FEM model was generated using squared, curved shell CQ40S elements with 8 nodes and isoparametric formulation, representing tuff units and mortar joints without unit-mortar interface elements between them. In this way, same modelling strategy was used to simulate URM geometry subjected to different load conditions, i.e. in and out plane and wallets, as representing parts of the URM, subjected to in-plane load condition.

The geometry of the URM wall exactly reflects the dimensions of the tested walls and the numerical models share also the same boundary and loading setup, according to the experimental tests. Steel plate is introduced to correctly simulate the horizontal actuator, adopted to impose out-of-plane displacements, as schematically illustrated (Figure 101). All sensitivity analyses showed a negligible influence of the wooden lintel on the spandrel capacity, so the lintel was not included in the final numerical model.

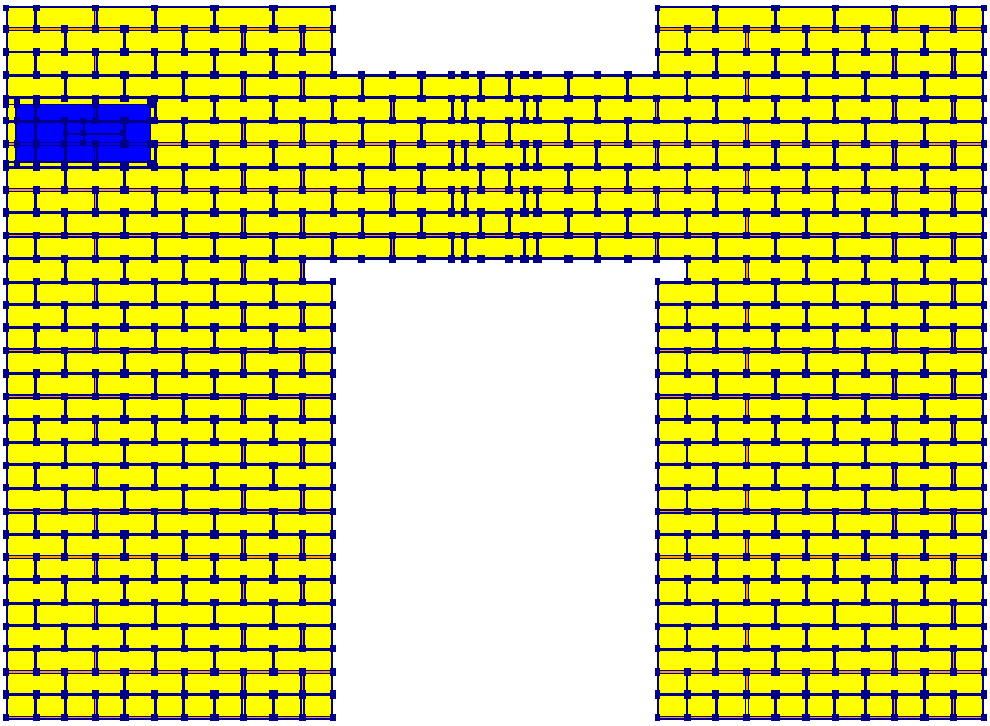

Figure 101. Finite-element model

A monotonic increasing horizontal displacement was prescribed in the middle of the steel plate, while all nodes of the fixed piers base sections were pinned. Since both types of URM configuration, at the end of the test, had PTFE sheets completely crushed between the hydraulic jack and the beam of transverse frames, and the beam of transverse frames prevent rotational displacement, a rotational constraint at the loaded pier top sections was introduced. Vertical loads on the piers were applied with a uniform pressure to provide 400 kN axial forces for each pier and when the vertical pre-compression loads were applied, finally a maximum displacement of 130 mm was applied for the intact URM, while for the deteriorated one a maximum displacement of 90 mm was applied. URM walls were analysed through displacement-controlled nonlinear analysis based on Newton–Raphson incremental iterative procedure and a mixed force–displacement convergence criterion.

A smeared crack model was employed to simulate the fracture process within tuff masonry. The behaviour of tuff system has been simulated by means of a Total Strain Crack model, which describes the tensile and compressive behaviour of a material by means of a stress-strain relationship. Because of displacement at maximum load in the experimental tests is related to crushing of units, and large out of plane displacements are expected [82] elastic–perfectly plastic constitutive laws were assumed for both masonry and mortar in compression, while an exponential softening law was used for representing the softening behaviour in tension.

The material parameters were obtained from the experimental tests and they are listed in Sections 2.3.4 and 2.3.6 as well as for URM subjected to a settlement load.

To account for experimental variability, as well as it was done for the compression tests, two numerical models have been adopted, with the difference in tuff elastic modulus passing from 2100 MPa to 1200 MPa, close to mortar's elastic modulus, expressed, respectively, with T2100 and T1200 both for intact "INT" and deteriorated "DET" numerical models.

The numerical model presented in this thesis is intended for the prediction of the overall flexural response of a masonry wall in terms of a curve representing the lateral force F vs. the lateral displacement δ, and as a support tool in terms of resulting crack patterns.

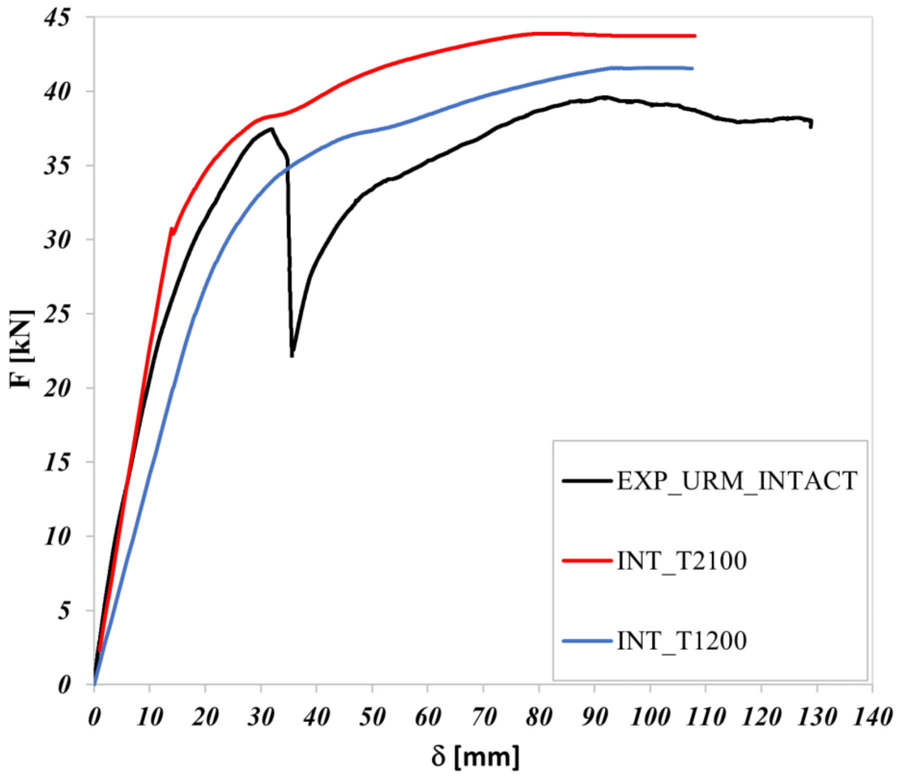

a)

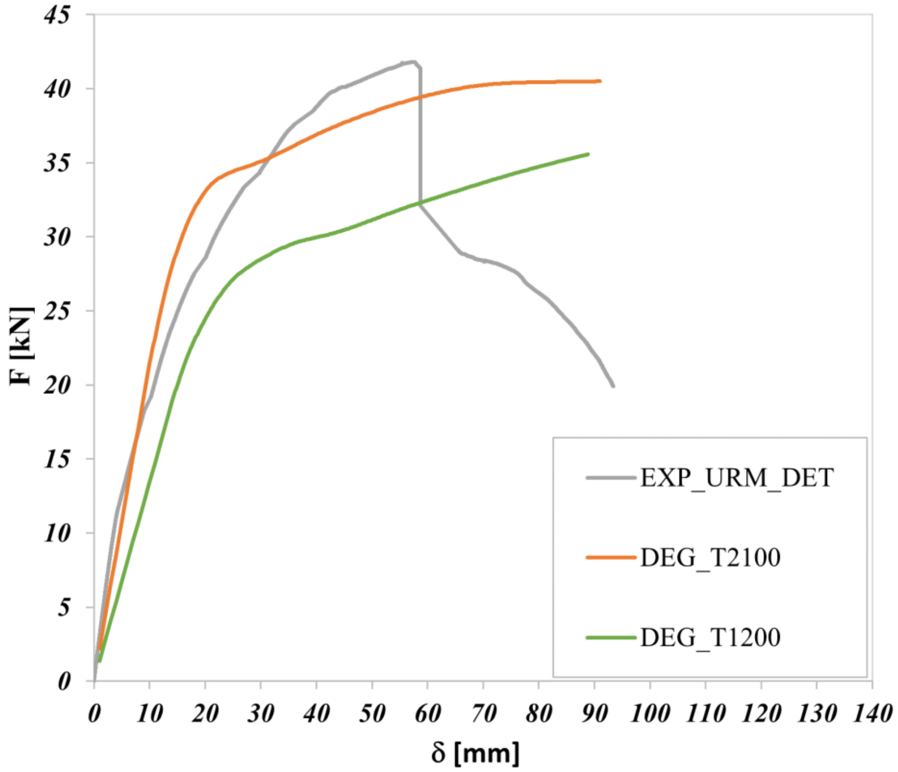

b)

Figure 102. Comparison between numerical and experimental results for a) intact and b) deteriorated URM

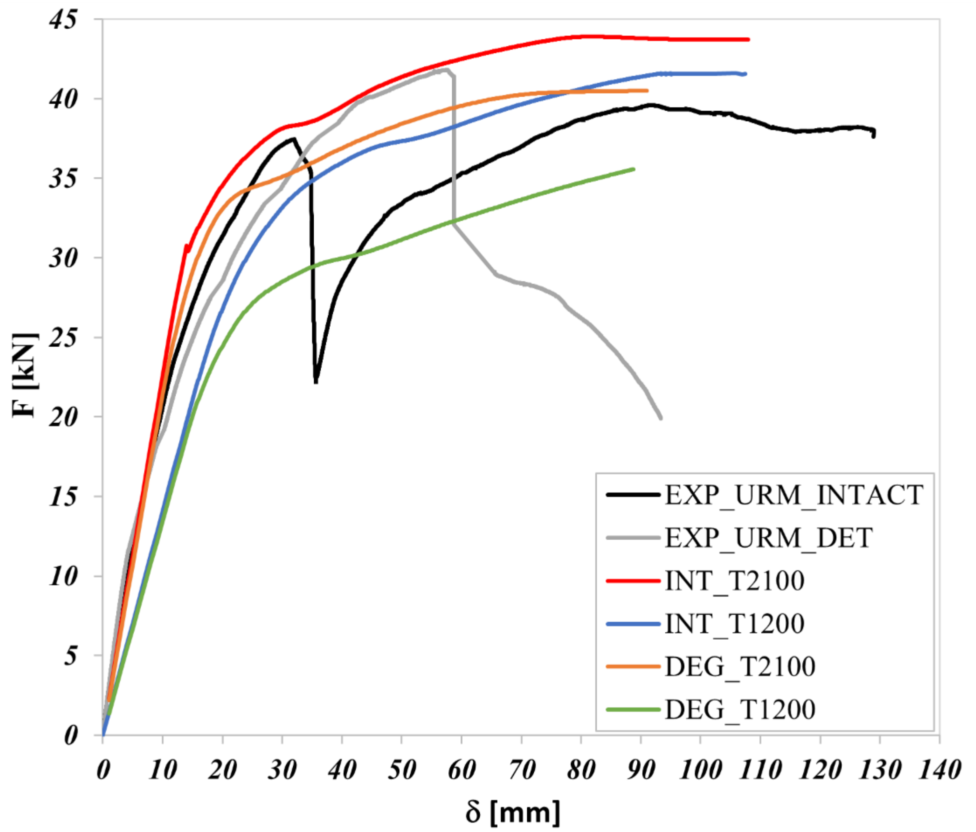

Figure 103. Comparison between numerical and experimental results for both intact and deteriorated URM

A good correlation can be observed from both qualitative, in terms of occurred failure mode, and quantitative, in terms of predicted load value, points of view. In Figure 102 and Figure 103 the performance of the numerical analysis is evaluated in terms of out-of-plane force versus imposed displacement at the steel plate mid hight.

The numerical curves, different for intact and deteriorated mortar joints, well described the main aspects of $F - \delta$ diagram (Figure 103).

The curves with full mortar thickness have a similar trend as the experimental one, Figure 102.a characterized by a linear elastic branch up half of the peak load, comparable to the experimental value. Indeed, intact URM for both tuff elastic modulus series (i.e.T2100 and T 1200) match the load so well, especially for T2100 series, showing both spandrel failure after the attainment of the peak lateral force.

The implemented models did not simulate load degradation related to crushing of units, as the adopted constitutive law did not have a post-peak softening phase in compression. However, also for deteriorated numerical curve, a similar trend to the experimental one was observed, with a satisfactory agreement in terms of both masonry stiffness, peak load, especially for the T2100 series (Figure 102.b) whereas different ultimate deflection of 71.5 mm was recorded at the peak load. The T1200 series, for the deteriorated configuration wasn't able to match neither the lateral force nor the stiffness of the URM.

From Figure 103 emerges that, with selected tuff elastic modulus values (i.e. T2100 or T1200), geometric degradation of mortar joints does not influence on URM initial elastic stiffness, but only lowering lateral force, reproducing the observed experimental behaviour.

The out of plane failure always occurred at the top and bottom spandrel sections, portions, as previously described, where the bending moment demand was such that it developed full flexural strength.

The performance of the numerical model is evaluated in terms of resulting crack patterns in Figure 104 and Figure 105. The model is able to reproduce the main cracks leading to the failure mechanisms described in the experimental results. In particular, the model reproduces the localisation and propagation of bending cracks from the peak load to the end of test. Figure 104 and Figure 105.show a classical representation of a smeared cracking strain field according to the adopted numerical modelling strategy. They do not aim to represent effective discrete cracks; but highlight the portions where cracking strains occur numerically.

Indeed, intact configuration wasn't capable to simulate the diagonal stepped cracks, experimentally observed, because the latter was an overturning mechanism effect, hardly to simulate with the used FEM methodology. However, FEM model shows strain localization at the locations of the observed cracks associated with the flexural cracking at the spandrel panel- which led to the final collapse of the URM.

It is possible to observe the increase in the volume of the masonry panel where the material response reached the tensile strength, producing cracks with increasing length and width. Main cracks are at the base of the pier especially for the loaded one, as experimentally observed, and also for the other pier for excessive displacement.

The plots show where the cracks involved the mortar joints with a more widespread distribution that became scattered, in the case of reduced mortar filling. After the attainment of the maximum flexural strength at the end section of the spandrel, Figure 105.a shows a damage mechanism characterized by the opening of the head joints for deteriorated specimens unlike the intact one (Figure 104.a).

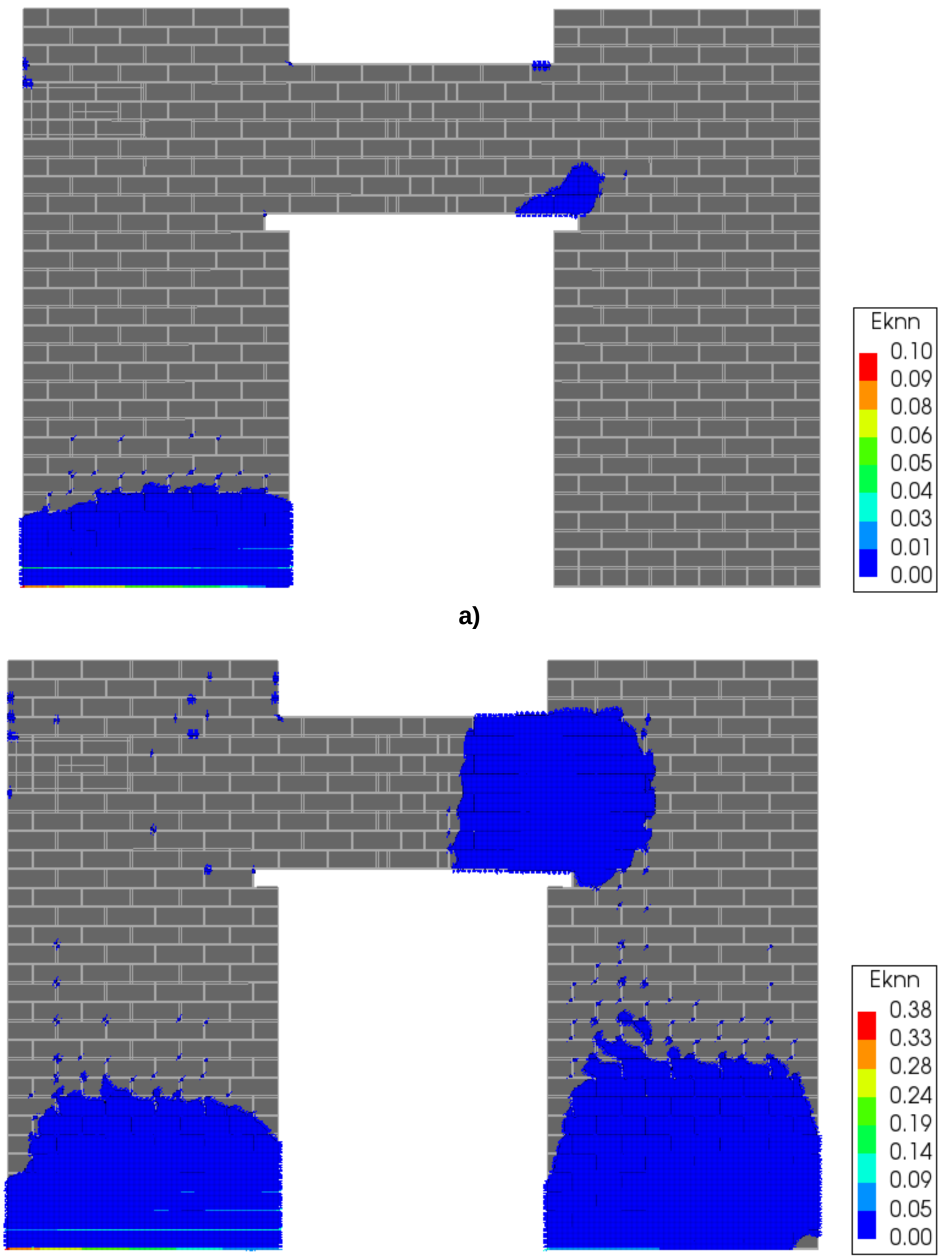

a)

b)

Figure 104. Crack patterns of the intact URM for displacement at a) onset of peak lateral load; b) end test

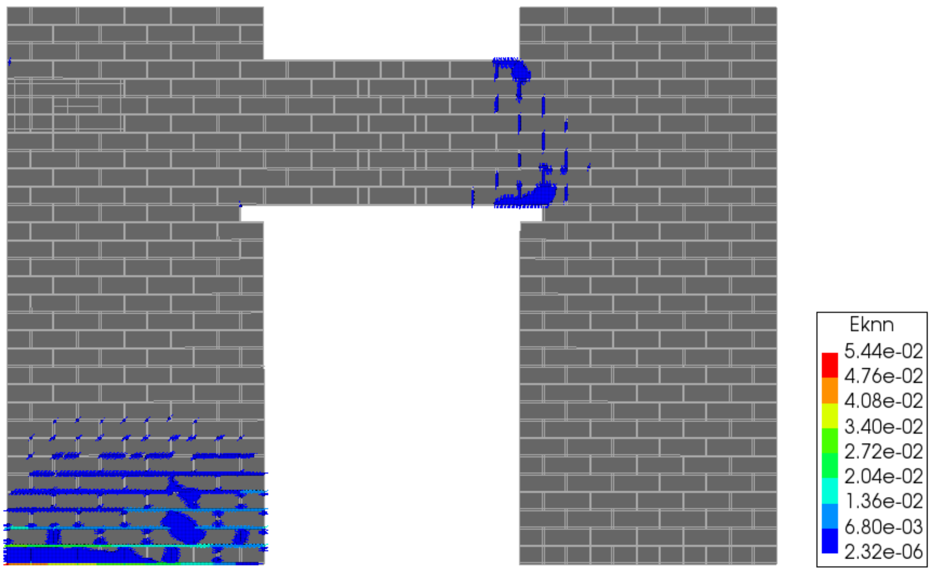

a)

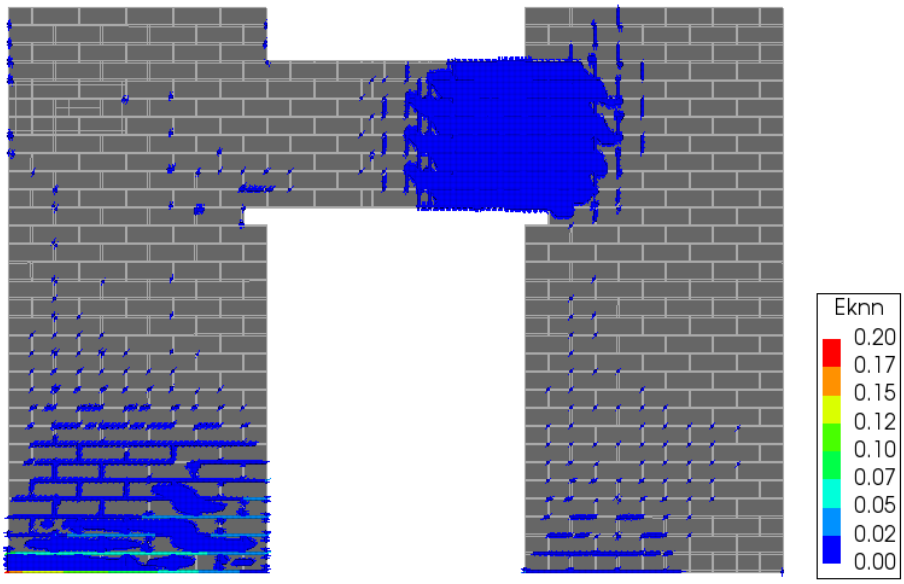

b)

Figure 105. Crack patterns of the deteriorated URM for displacement at a) onset of peak lateral load; b) end test

Chapter 5

Conclusions

Conclusive remarks on the different phases of the developed work are presented in this section. Finally, open issues that resulted from the thesis are described as future developments of research to be pursued.

In this thesis, an experimental program was carried out to assess the behaviour of unreinforced masonry panels and to expand and deepen the knowledge on the static behaviour due to aging and degradation effects passing from small scale wallets to full-scale unreinforced masonry (URM) walls with openings.

These tests were also complemented by a non-destructive investigation and a preliminary program for the characterization of the applied materials, stone and mortar. Tested specimens were divided into two configurations, i.e., intact and deteriorated, to study the influence of aging on crucial factors, such as material properties, pre-compression, aspect ratio and openings.

The F.E.M. analysis of the tested specimens have been performed simulating in detail the nonlinearities, with a calibration based on the experimental results from simple and diagonal-compression tests.

The three parts of this research were fundamental and complementary. Results of experimental tests (chapter 2) and theoretical analyses (chapter 3) were performed to assess the failure mode and the rationale of different behaviours, showing that a good agreement was achieved. Then the experimental data were used to elaborate numerical and simplified models in order to simulate the experimental behaviour of the wallets and walls (chapter 5).

Overall, the geometric degradation effect is strongly linked to the failure mechanism with a connection, sometimes obvious, sometimes not, between local geometric degradation and global degradation in mechanical terms.

For uniaxial and diagonal compression tests on brick and tuff masonry, differences have been noted. For the uniaxial test, for the intact brick specimens, vertical cracks spread along the head joints and bricks starting from the edges of the specimen, when the splitting phenomenon is triggered, up to the inner zone. Conversely, for the deteriorated specimens, extensive cracking occurred in the central zone even in the range of small deformations, Due to the weaker consistence of the masonry.

Tuff specimens showed the same crack pattern except for splitting phenomenon; it was observed less evidently for the intact specimens, while for those deteriorated, only a limited material ejection was recorded. This can be attributed to the different relationship between materials: mortar is clearly weaker than bricks, while in the case of tuff, the behaviour between stone and mortar is less different.

Splitting along the thickness is a failure mode of masonry subjected to axial compression and is due to the difference between elastic properties of masonry units and of mortar. The enhanced masonry deformability, due to unfully filled mortar joints, may have partially engaged the stone response and stiffness.

For diagonal compression tests on bricks, in the case of reduced mortar filling, cracks involved the mortar joints also outside the diagonal courses, with a more widespread distribution that became scattered, while for the deteriorated tuff specimens, this aspect is less pronounced. The reason could be linked to a huge difference in Young's modulus for bricks masonry constituents, which is much smaller in tuff masonry.

In uniaxial load the local degradation of joints plays a direct role on the global response, while in the diagonal compression the degradation of joints is mitigated by the interlocking of blocks, both brick and tuff ,leading to a less significant global degradation, compared to the local degradation of joints.

Local-global data sets were used to develop linear regression models for their use in structural safety assessment of masonry structures, for prediction of the compressive strength reduction and that of elastic modulus given mortar joint filling, and also a regression model to estimate the conditional mean value of reduced elastic modulus given the loss of the compressive masonry strength related to material degradation. Same regression models were introduced for the prediction of shear strength reduction and that of shear elastic modulus and between elastic modulus and shear modulus values due to masonry degradation.

A numerical FEM was calibrated based on the experimental results from simple and diagonal-compression tests.

For tuff masonry, two micro-models with differences in tuff elastic modulus were considered to assess the strength envelope and are useful to evaluate the influence of the mechanical properties of each material on the global behaviour for both intact and deteriorated configurations.

For the two URM configurations, intact and deteriorated walls subjected to a settlement load, showed different behaviours. Although the geometric degradation implies a reduction of the peak load strength, URM exhibits a not negligible residual strength due to mechanical interlocking occurring at the crack interface during the in-plane deformation of the spandrel, with a different behaviour compared to intact URM. The results of the numerical analyses are used to set the framework of an overall damage model which correlates the analysed structural features with the assessment of potential damage of buildings suffering a base settlement.

Particular attention has been paid to the case of existing buildings where the progressive release of steel tying, or the punctual load of arches, pushes URM to an out-of-plane load, resulting in crucial bending mechanism.

This was the starting point for investigating the behaviour of URM subjected to out of plane load, considering also the impact of aging effects with a deteriorated configuration. The geometric degradation impacted the response of deteriorated URM, however a residual shear after the peak lateral load was reached also at significant displacements.

Progressive release of steel tying can be seen also as a degradation effect of previous (historical) retrofit interventions.

FEM was used to simulate the global behaviour of URM walls, allowing force–displacement curves and cracking patterns to be investigated, with a good correlation observed from both qualitative and quantitative, points of view.

It has been highlighted how the common practice of adopting the same capacity models proposed for pier elements can lead to severe underestimations of the strength for spandrel panels. It is founded on the outcome that the response as an “equivalent strut” of the spandrel may also occur by virtue of the interlocking phenomena which can be originated at the interface between its end-sections and the contiguous masonry joint panels.

The next step of future research development could be essentially represented by the capacity investigation of masonry structures subjected to a combination of aging with an in-plane seismic lateral load. The analysis could represent an important development to be faced, in particular, for historical masonry structures. The first topic could be faced with the further possibility to numerically investigate the influence of settlement effects on the seismic capacity of deteriorated masonry structures.

Also, could be useful to evaluate the influence of the compressive vertical load on the flexural masonry strength to define a link between local mechanical properties and the global strength for out of plane loading.

Extending the numerical simulation of the cyclic behaviour of stone masonry walls based on micro and macro-modelling strategies and comparison with experimental results, can be a principal research activity to be further developed. The macro-modelling has a major role in practical applications and can be one of the main tools supporting engineers to assess an acceptable level of safety for aged buildings.

Finally, degradation of previous retrofit interventions will be one of the topics to be further addressed also with reference to the current context of rehabilitation of the Italian building stock.

Bibliography

[1] P. Roca, M. Cervera, G. Gariup, and L. Pela', "Structural analysis of masonry historical constructions. Classical and advanced approaches," *Arch. Comput. Methods Eng.*, vol. 17, no. 3, pp. 299–325, 2010, doi: 10.1007/s11831-010-9046-1.

[2] J. Li, M. J. Masia, M. G. Stewart, and S. J. Lawrence, "Spatial variability and stochastic strength prediction of unreinforced masonry walls in vertical bending," *Eng. Struct.*, vol. 59, pp. 787–797, 2014, doi: 10.1016/j.engstruct.2013.11.031.

[3] J. Li, M. J. Masia, and M. G. Stewart, "Stochastic spatial modelling of material properties and structural strength of unreinforced masonry in two-way bending," *Struct. Infrastruct. Eng.*, vol. 13, no. 6, pp. 683–695, 2017, doi: 10.1080/15732479.2016.1188125.

[4] E. Erduran and E. Martinelli, "Some remarks on the seismic assessment of rc frames affected by carbonation-induced corrosion of steel bars," *fib Symp.*, pp. 395–403, 2021.

[5] L. Berto, R. Vitaliani, A. Saetta, and P. Simioni, "Seismic assessment of existing RC structures affected by degradation phenomena," *Struct. Saf.*, vol. 31, no. 4, pp. 284–297, 2009, doi: 10.1016/j.strusafe.2008.09.006.

[6] C. Wang, Q. Li, and B. R. Ellingwood, "Time-dependent reliability of ageing structures: an approximate approach," *Struct. Infrastruct. Eng.*, vol. 12, no. 12, pp. 1566–1572, Dec. 2016, doi: 10.1080/15732479.2016.1151447.

[7] T. Forgács, V. Sarhosis, and S. Ádány, "Shakedown and dynamic behaviour of masonry arch railway bridges," *Eng. Struct.*, vol. 228, no. November 2020, 2021, doi: 10.1016/j.engstruct.2020.111474.

[8] E. Rirsch and Z. Zhang, "Rising damp in masonry walls and the importance of mortar properties," *Constr. Build. Mater.*, vol. 24, no. 10, pp. 1815–1820, 2010, doi: 10.1016/j.conbuildmat.2010.04.024.

[9] P. Foraboschi and A. Vanin, "Experimental investigation on bricks from historical Venetian buildings subjected to moisture and salt crystallization," *Eng. Fail. Anal.*, vol. 45, pp. 185–203, 2014, doi: 10.1016/j.engfailanal.2014.06.019.

[10] J. Hu and F. Ma, "Sensitivity analysis of the influences of mortar aging and loss on the structural performance of masonry arch aqueducts," *E3S Web Conf.*, vol. 300, p. 01022, 2021, doi: 10.1051/e3sconf/202130001022.

[11] G. Magenes and G. M. Calvi, "In-plane seismic response of brick masonry walls," *Earthq. Eng. Struct. Dyn.*, vol. 26, no. 11, pp. 1091–1112, Nov. 1997, doi: 10.1002/(SICI)1096-9845(199711)26:11<1091::AID-EQE693>3.0.CO;2-6.

[12] V. Turnšek and F. Čačovič, "Some experimental results on the strength of brick masonry walls," *Proc. 2nd Int. Brick Mason. Conf.*, pp. 149–156, 1971, [Online]. Available: http://www.hms.civil.uminho.pt/ibmac/1970/149.pdf.

[13] S. Lagomarsino, "On the vulnerability assessment of monumental

buildings," *Bull. Earthq. Eng.*, vol. 4, no. 4, pp. 445–463, Nov. 2006, doi: 10.1007/s10518-006-9025-y.
[14] N. Gattesco, C. Amadio, and C. Bedon, "Experimental and numerical study on the shear behavior of stone masonry walls strengthened with GFRP reinforced mortar coating and steel-cord reinforced repointing," *Eng. Struct.*, vol. 90, pp. 143–157, May 2015, doi: 10.1016/j.engstruct.2015.02.024.
[15] M. Del Zoppo, M. Di Ludovico, A. Balsamo, and A. Prota, "Experimental In-Plane Shear Capacity of Clay Brick Masonry Panels Strengthened with FRCM and FRM Composites," *J. Compos. Constr.*, vol. 23, no. 5, p. 04019038, Oct. 2019, doi: 10.1061/(asce)cc.1943-5614.0000965.
[16] J. Segura, L. Pelà, S. Saloustros, and P. Roca, "Experimental and numerical insights on the diagonal compression test for the shear characterisation of masonry," *Constr. Build. Mater.*, vol. 287, Jun. 2021, doi: 10.1016/j.conbuildmat.2021.122964.
[17] M. Basili, F. Vestroni, and G. Marcari, "Brick masonry panels strengthened with textile reinforced mortar: experimentation and numerical analysis," *Constr. Build. Mater.*, vol. 227, Dec. 2019, doi: 10.1016/j.conbuildmat.2019.117061.
[18] F. Saviano, F. Parisi, and G. P. Lignola, "Material aging effects on the in-plane lateral capacity of tuff stone masonry walls: a numerical investigation," *Mater. Struct. Constr.*, vol. 55, no. 7, 2022, doi: 10.1617/s11527-022-02032-5.
[19] "UNI EN 8942-3. Test methods for masonry elements. Determination of flexural strength." .
[20] "Eurocode 6: Design of masonry structures - Part 1-1: General rules for reinforced and unreinforced masonry structures) Comité Européen de Normalisation, Bruxelles, Belgium."
[21] Ministero delle Infrastrutture e dei Trasporti., "DM 17.01.2018 'Aggiornamento delle Norme tecniche per le costruzioni' (in Italian)", Italian Ministry of Infrastructures and Transportation, Rome, Italy," *Gazz. Uffic. Rep. Ita.*, pp. 1–198, 2018.
[22] "UNI EN 1015-11. Methods of test for mortar for masonry – Part 1-1: Determination of flexural and compressive strength of hardened mortar." .
[23] N. Augenti and F. Parisi, "Constitutive Models for Tuff Masonry under Uniaxial Compression," *J. Mater. Civ. Eng.*, vol. 22, no. 11, pp. 1102–1111, 2010, doi: 10.1061/(asce)mt.1943-5533.0000119.
[24] American Society for Testing and Materials, "ASTM E 519 Standard Test Method for Diagonal Tension (Shear) in Masonry Assemblages, (2010)."
[25] F. Parisi, I. Iovinella, A. Balsamo, N. Augenti, and A. Prota, "In-plane behaviour of tuff masonry strengthened with inorganic matrix-grid composites," *Compos. Part B Eng.*, vol. 45, no. 1, pp. 1657–1666, 2013, doi: 10.1016/j.compositesb.2012.09.068.
[26] P. Cassese, C. Balestrieri, L. Fenu, D. Asprone, and F. Parisi, "In-plane shear behaviour of adobe masonry wallets strengthened with textile reinforced mortar," *Constr. Build. Mater.*, vol. 306, no. February, p. 124832, 2021, doi: 10.1016/j.conbuildmat.2021.124832.
[27] A. Meoni, A. D'Alessandro, and F. Ubertini, "Characterization of the strain-sensing behavior of smart bricks: A new theoretical model and its

application for monitoring of masonry structural elements," *Constr. Build. Mater.*, vol. 250, Jul. 2020, doi: 10.1016/j.conbuildmat.2020.118907.
[28] A. Meoni, A. D'Alessandro, R. Kruse, L. De Lorenzis, and F. Ubertini, "Strain field reconstruction and damage identification in masonry walls under in-plane loading using dense sensor networks of smart bricks: Experiments and simulations," *Eng. Struct.*, vol. 239, no. February, p. 112199, 2021, doi: 10.1016/j.engstruct.2021.112199.
[29] A. Meoni, A. D'Alessandro, F. Saviano, G. P. Lignola, F. Parisi, and F. Ubertini, "Seismic Monitoring of Masonry Structures Using Smart Bricks: Experimental Application to Masonry Walls Subjected to In-Plane Shear Loading," *Lect. Notes Civ. Eng.*, vol. 253 LNCE, pp. 71–80, 2023, doi: 10.1007/978-3-031-07254-3_8.
[30] A. Meoni, A. D'Alessandro, N. Cavalagli, M. Gioffré, and F. Ubertini, "Shaking table tests on a masonry building monitored using smart bricks: Damage detection and localization," *Earthq. Eng. Struct. Dyn.*, vol. 48, no. 8, pp. 910–928, Jul. 2019, doi: 10.1002/eqe.3166.
[31] European Committee for Standardization (CEN), "EN 1052-1 Methods of test for masonry – Part 1: Determination of compressive strength, (1999)."
[32] A. Brencich and G. de Felice, "Brickwork under eccentric compression: Experimental results and macroscopic models," *Constr. Build. Mater.*, vol. 23, no. 5, pp. 1935–1946, May 2009, doi: 10.1016/j.conbuildmat.2008.09.004.
[33] S. T. Method, "ASTM E 111-04, Standard Test Method for Young ' s Modulus , Tangent Modulus , and Chord Modulus," *Practice*, vol. 03, no. Reapproved 2010, pp. 1–7, 1981, doi: 10.1520/E0111-04R10.
[34] Ministero delle Infrastrutture e dei Trasporti., "Istruzioni per l'applicazione dell' Aggiornamento delle 'Norme Tecniche per le costruzioni' di cui al decreto ministeriale 17 gennaio 2018 (in Italian). ," *Gazz. Uffic. Rep. Ita.*, 2019.
[35] "RILEM TC 76-LUM, Diagonal Tensile Strength Tests of Small Wall Specimens; RILEM Publications SARL: London, UK, 1994."
[36] M.M. Frocht, "Recent advances in photoelasticity and an investigation of thestress distribution in square blocks subjected to diagonal compression, Trans.Am. Soc. Mech. Eng. 53 (1931) 135–153."
[37] C. Calderini, S. Cattari, and S. Lagomarsino, "Identification of shear mechanical parameters of masonry piers from diagonal compression test, 11th Canadian Masonry Symposium, Toronto, Ontario,."
[38] V. Alecci, M. Fagone, T. Rotunno, and M. De Stefano, "Shear strength of brick masonry walls assembled with different types of mortar," *Constr. Build. Mater.*, vol. 40, pp. 1038–1045, 2013, doi: 10.1016/j.conbuildmat.2012.11.107.
[39] G. Crisci, F. Ceroni, and G. P. Lignola, "Comparison between design formulations and numerical results for in-plane FRCM-strengthened masonry walls," *Appl. Sci.*, vol. 10, no. 14, Jul. 2020, doi: 10.3390/app10144998.
[40] M. Corradi, A. Borri, and A. Vignoli, "Experimental study on the determination of strength of masonry walls," *Constr. Build. Mater.*, vol. 17, no. 5, pp. 325–337, Jul. 2003, doi: 10.1016/S0950-0618(03)00007-2.
[41] A. Borri, G. Castori, and M. Corradi, "Determination of Shear Strength of Masonry Panels Through Different Tests," *Int. J. Archit. Herit.*, vol. 9, no.

8, pp. 913–927, Nov. 2015, doi: 10.1080/15583058.2013.804607.
[42] "UNI EN 1926:2007. Natural stone test methods - determination of uniaxialcompressive strength."
[43] "UNI EN 14580:2005 Natural stone test methods - Determination of static elastic modulus." [Online]. Available: www.uni.com.
[44] "UNI EN 12372:2007. Natural stone test methods Determination of flexural strength under concentrated load."
[45] Mastrodicasa Sisto, *Dissesti statici delle strutture edilizie*. .
[46] M. Korff, "Deformations and damage to buildings adjacent to deep excavations in soft soils, literature survey, Delft: Deltares."
[47] P. C. . R. J. G. . T. K. C. van Staalduinen, "Onderzoek naar de oorzaken van bouwkundige schade in GroningenMethodologie en case studies ter duiding vande oorzaken."
[48] M. D. Boscardin and E. J. Cording, "Building Response to Excavation-Induced Settlement," *J. Geotech. Eng.*, vol. 115, pp. 1–21, 1989.
[49] M. Bruneau, "State-of-the-art report on seismic performance of unreinforced masonry buildings."
[50] Craig Robert Willis, "Design of Unreinforced Masonry Walls for Out-of-plane Loading," 2004.
[51] N. Fardis M, "S.O.A. Lecture: Lessons Learnt in Past Earthquakes". Proceedings of the 10th European Conference on Earthquake Engineering,Rotterdam,1995,pp.779-788."
[52] J. N. Priestley, "Seismic behaviour of unreinforced masonry walls, Bulletin of the New Zealand Society for Earthquake Engineering, 1985."
[53] Drysdale R.G., Hamid A.A., and Baker L.R., *Masonry Structures : Behavior and Design*. 1999.
[54] British Standards Institution., *Eurocode 7: Geotechnical design: Part 1, General rules.* BSI, 2004.
[55] Polshin;D and R. Tokar, "Maximum allowable non-uniform settlement of structures, 4th International Conference on Soil Mechanics and Foundation Engineering (London)." [Online]. Available: https://www.issmge.org/publications/online-library.
[56] G. G. Meyerhof, "Limit states design in geotechnical engineering," *Struct. Saf.*, vol. 1, no. 1, pp. 67–71, 1982, doi: https://doi.org/10.1016/0167-4730(82)90015-7.
[57] J. Boscawen Burland, "Settlement of Buildings and Associated Damage." [Online]. Available: https://www.researchgate.net/publication/248646701.
[58] A. W. SKEMPTON and D. H. MACDONALD, "THE ALLOWABLE SETTLEMENTS OF BUILDINGS.," *Proc. Inst. Civ. Eng.*, vol. 5, no. 6, pp. 727–768, 1956, doi: 10.1680/ipeds.1956.12202.
[59] S. Moorak and C. E. J, "Estimation of Building Damage Due to Excavation-Induced Ground Movements," *J. Geotech. Geoenvironmental Eng.*, vol. 131, no. 2, pp. 162–177, Feb. 2005, doi: 10.1061/(ASCE)1090-0241(2005)131:2(162).
[60] G. Giardina, A. Marini, M. A. N. Hendriks, J. G. Rots, F. Rizzardini, and E. Giuriani, "Experimental analysis of a masonry façade subject to tunnelling-induced settlement," *Eng. Struct.*, vol. 45, pp. 421–434, Dec. 2012, doi: 10.1016/j.engstruct.2012.06.042.
[61] G. Ricceri and M. Soranzo, "An analysis on allowable settlements of

structures.," *Riv. Ital. di Geotech.*, vol. vol.4, pp. 177–188, 1985.
[62] F. Parisi, G. P. Lignola, N. Augenti, A. Prota, and G. Manfredi, "Nonlinear Behavior of a Masonry Subassemblage Before and After Strengthening with Inorganic Matrix-Grid Composites," *J. Compos. Constr.*, vol. 15, no. 5, pp. 821–832, 2011, doi: 10.1061/(asce)cc.1943-5614.0000203.
[63] C. Calderini, S. Cattari, and S. Lagomarsino, "In-plane strength of unreinforced masonry piers," *Earthq. Eng. Struct. Dyn.*, vol. 38, no. 2, pp. 243–267, 2009, doi: https://doi.org/10.1002/eqe.860.
[64] G. P. Lignola, ; A Flora, and G. Manfredi, "Simple Method for the Design of Jet Grouted Umbrellas in Tunneling," doi: 10.1061/ASCE1090-02412008134:121778.
[65] W. Mann and H. Muller, "Failure of shear-stressed masonry. An enlarged theory, tests and application to shear walls," in *Proc. Br. Ceram. Soc.*, 1982, no. 30, p. 223.
[66] G. P. Lignola, R. Angiuli, A. Prota, and M. A. Aiello, "FRP confinement of masonry: analytical modeling," *Mater. Struct. Constr.*, vol. 47, no. 12, pp. 2101–2115, 2014, doi: 10.1617/s11527-014-0323-6.
[67] S. Cattari and S. Lagomarsino, "A STRENGTH CRITERION FOR THE FLEXURAL BEHAVIOUR OF SPANDRELS IN UN-REINFORCED MASONRY WALLS."
[68] K. Beyer and S. Mangalathu, "Review of strength models for masonry spandrels," *Bull. Earthq. Eng.*, vol. 11, no. 2, pp. 521–542, Apr. 2013, doi: 10.1007/s10518-012-9394-3.
[69] G. Magenes, "Simplified non-linear seismic analysis of masonry buildings Collection and Organization of Experimental Dataset for the Identification of Deformation and Strength Performance Limits on Masonry Wallets (ReLUIS) View project," 1998. [Online]. Available: https://www.researchgate.net/publication/285075147.
[70] CNR-DT 200 R1/2013, "CNR-DT 200 R1/2013 Istruzioni per la Progettazione, l'Esecuzione ed il Controllo di Interventi di Consolidamento Statico mediante l'utilizzo di Compositi Fibrorinforzati Materiali, strutture di c.a. e di c.a.p., strutture murarie (in italian)," 2013.
[71] G. Ramaglia, "Seismic strengthening of slender masonry barrel vaults: experimental behaviour and analytical modelling,Ph.D.Thesis,."
[72] D. C. Washington, "FEMA 306 Evaluation of earthquake damaged concrete and masonry wall buildingS Basic Procedures Manual Applied Technology Council (ATC-43 Project)," 1998.
[73] Y. . D. J. . M. D. (2004) LIU, "Reinforced masonry concrete block walls under combined axial and uniformly distributed lateral load, Proceedings of 13th International Brick and Block Masonry Conference, Amsterdam, Netherlands, paper nº 216.," 2004.
[74] L. Z. Chang, F. Messali, and R. Esposito, "Capacity of unreinforced masonry walls in out-of-plane two-way bending: A review of analytical formulations," *Structures*, vol. 28, pp. 2431–2447, Dec. 2020, doi: 10.1016/j.istruc.2020.10.060.
[75] "DIANA FEA, 2020. DIANA 10.4 - User's Manual, Delft."
[76] G. P. Lignola, A. Prota, and G. Manfredi, "Nonlinear analyses of tuff masonry walls strengthened with cementitious matrix-grid composites," *J. Compos. Constr.*, vol. 13, no. 4, pp. 243–251, 2009, doi: 10.1061/(ASCE)CC.1943-5614.0000007.

[77] N. Augenti, F. Parisi, A. Prota, and G. Manfredi, “In-Plane Lateral Response of a Full-Scale Masonry Subassemblage with and without an Inorganic Matrix-Grid Strengthening System,” *J. Compos. Constr.*, vol. 15, no. 4, pp. 578–590, 2011, doi: 10.1061/(asce)cc.1943-5614.0000193.
[78] P. B. Lourenço, “Recent advances in masonry modelling: micromodelling and homogenisation,” in *Multiscale Modeling in Solid Mechanics*, vol. Volume 3, IMPERIAL COLLEGE PRESS, 2009, pp. 251–294.
[79] “Hordijk DA. 1991. Local Approach to Fatigue of Concrete.PhD thesis, Delft University of Technology.” .
[80] G. Mininno, B. Ghiassi, and D. V. Oliveira, “Modelling of the in-plane and out-of-plane performance of TRM-strengthened masonry walls,” in *Key Engineering Materials*, 2017, vol. 747 KEM, pp. 60–68, doi: 10.4028/www.scientific.net/KEM.747.60.
[81] G. P. Lignola, R. Cuzzilla, A. Prota, and G. Manfredi, “Non linear modelling of masonry: effect of different brickworks and specific energy of materials. 14th European Conference on Earthquake Engineering, Ohrid (FYRoM), 29 August – 4 September 2010, paper # 630.”
[82] C. D’Ambra, G. P. Lignola, and A. Prota, “Multi-Scale Analysis of In-plane Behaviour of Tuff Masonry,” *Open Constr. Build. Technol. J.*, vol. 10, no. 1, pp. 312–328, Jun. 2016, doi: 10.2174/1874836801610010312.